POLITECNICO DI TORINO

Corso di Laurea in Ingegneria Aerospaziale

Tesi di Laurea Magistrale

Mars Drone Design & Thermal Analysis

Relatore
Prof. Paolo Maggiore

Correlatore:
Prof. Domenic D'Ambrosio

Laureando
Fabio Acquaviva
matricola: 242090

Supervisori aziendali
Thales Alenia Space Italia
Head of Thermal & Environmental Control Design Engineering Unit,
Expert for ATCS design:
Ing. Massimo Antonacci
Senior Thermal Designer:
Ing. Valter Perotto

Alla mia famiglia,
che mi ha sempre sostenuto più di ogni forza esistente in natura.

Sommario

L’argomento di questa tesi è studiare la fattibilità del volo e la sopravvivenza di un drone su Marte dal punto di vista termico. Su questo pianeta lo scambio di calore è ostacolato dalla bassissima densità dell’atmosfera e le temperature ambientali variano tra estremi intollerabili per molti componenti elettronici e meccanici.
Un design preliminare del drone, in particolare del gruppo propulsivo motore-rotore, è stato svolto attingendo sia dalla letteratura che dai risultati di alcuni test svolti in TAS-I. Successivamente ci si è soffermati sul processo di **analisi termica ed energetica** attraverso il software ESATAN-TMS e sulle soluzioni di protezione termica dei componenti del drone per mantenerli entro i requisiti di temperatura operativa.

Summary

The aim of this work is to study the feasibility of the flight and the operation of a drone on Mars from the thermal point of view. On this planet the thermal exchange is hampered by the very low density of the atmosphere and environmental temperatures vary between extremes which are dangerous for most of the electronic and mechanical components.
Since a conceptual design of a Martian quadcopter does not exist a drone preliminary design is proposed gleaning information from both literature and TAS-I tests. Then we focused on the **thermo-energetic analysis** of the whole drone with a detailed ESATAN-TMS model and some thermal control solutions were assessed in order to maintain the drone components within their operative temperature limits.

Contents

List of Tables

List of Figures

Nomenclature

α_S Solar absorptance [ ]

β Isobaric coefficient of thermal expansion, $[1/K]$

$\Delta n/\Delta M$ Slope of the M-n curve $[rpm/mNm]$

$\dot{q}$ Power flux, $[W/m^2]$

ϵ Emissivity [ ]

η Efficiency, [ ]

Γ Circulation, $[m^2/s]$

γ Specific heat ratio, [ ]

κ Induced power factor, [ ]

μ Dynamic viscosity, $[Pa \cdot s]$

ν Cinematic viscosity, $[m^2/s]$

Ω Rotational speed, $[rad/s]$

ω Vorticity, $[rad/s]$

ϕ Inflow angle, $[rad]$

ρ Density, $[kg/m^3]$

σ Stephan-Boltzmann constant, $[W/(m^2 \cdot K^4)]$

τ Time constant, $[s]$

Θ Pitch angle, $[°]$

ξ Motor throttle, [ ]

A Rotor disk area, $[m^2]$

a Speed of sound, $[m/s]$

C Thermal capacitance $[J/K]$

c Chord $[m]$ or Specific heat capacity $[J/(kg \cdot K)]$

C_M Torque coefficient, [ ]

C_P Power coefficient, [ ]

C_T Thrust coefficient, [ ]

D Diameter, $[m]$

E_B Battery energy, $[Wh]$

F Prandtl factor, [ ]

G Glauert loading parameter, [ ]

g Gravitational acceleration, $[m/s^2]$

GL Linear thermal conductance, $[W/K]$

GR Radiative thermal conductance, $[W/K^4]$

Gr Grashof number, [ ]

h Convective heat transfer coefficient $[W/(m^2 \cdot K)]$

I Motor current, $[A]$

i Reduction ratio, [ ]

I_0 No-load current, $[A]$

$[K]$ Internal conductances matrix

k Thermal conductivity, $[W/(m \cdot K)]$

k_M Torque constant, $[mNm/A]$

k_V, k_n Velocity constant, $[rpm/V]$

L Characteristic or motor length $[m]$

l_{gap} Gap between blades, $[m]$

M Mach number [ ] or Torque $[Nm]$

m Mass, $[kg]$

N Number of rotors or number of nodes, [ ]

n Rotational speed, $[rpm]$

Nu Nusselt number, [ ]

P Power, $[W]$

p Pressure, $[Pa]$

Pr Prandtl number, [ ]

Q Input power, $[W]$

Q_S Solar flux, $[W/m^2]$

QS Solar power absorbed (ESATAN), $[W]$

R Rotor radius, $[m]$

r Radial coordinate, $[m]$

Ra Rayleigh number, [ ]

Re Reynolds number, [ ]

T Temperature $[K]$ or Thrust $[N]$

t Time, $[s]$

u Rotor induced tangential velocity, $[m/s]$

V Velocity $[m/s]$ or Tension $[V]$

v Rotor induced vertical velocity, $[m/s]$

v_l Landing velocity, $[m/s]$

V_s Motor voltage, $[V]$

V_{tip} Rotor tip speed, $[m/s]$

z Altitude, $[m]$

$\boldsymbol{M}$ Molar mass, $[kg/mol]$

$\boldsymbol{R}$ Specific gas constant $[J/(kg \cdot K)]$

Acronyms

BLDC	Brushless Direct Current
CFD	Computational Fluid Dynamics
CPU	Central Processing Unit
ECM	Electronics Core Module
EDM	Entry, Descent & landing demonstrator Module
EOP	Extreme Operative Point
ESA	European Space Agency
ESATAN	European Space Agency Thermal Analysis Network
FM	Figure of Merit
FoV	Field of View
GB	Gearbox
GL	Linear thermal conductance
GMM	Geometrical Mathematical Model
GR	Radiative thermal conductance
HD	High Definition
IAS	Induced Air Speed
IR	Infra Red
JPL	Jet Propulsion Laboratory
LMD	Laboratoire de Météorologie Dynamique
LPTN	Lumped Parameters Thermal Network
LS	Solar Longitude
MHS	Mars Helicopter Scout

MLS	Martian Solar Longitude
MOLA	Mars Orbiter Laser Altimeter
PoliTO	Politecnico di Torino
RHU	Radioactive Heating Unit
Sol	Martian day
TAS-I	Thales Alenia Space Italia
TCS	Thermal Control System
TMM	Thermo Mathematical Model
TMS	Thermal Modelling Suite

Chapter 1

Introduction

This thesis starts with a question: **Why do we want to fly on Mars?**
There are several answers but the main reason is that we want to improve our knowledge of Mars by exploring large portions of its surface in a fast and efficient way. Rovers running on the surface of the red planet are forced to go very slowly because they must prevent accident on their way; in fact they are driven from the Earth once images taken by orbiters and from the rovers themselves are received and processed. Since 2004, three exploration rovers have successfully landed on the Martian surface. Yet, only about sixty kilometres have been explored on 21,000 km of the planet's circumferential path. The slow exploration rate is mainly due to a lack of visibility on the ground [1]. Aerial exploration of Mars with airborne support could provide mission capabilities that go far beyond that of orbiting satellites. The aerial images resolution would be comparable to rovers one and much better than satellites one. Furthermore a drone could access and land at targets that can't be reached by rovers. With this kind of features a fast scouting of the near-rover surface could be achieved and the exploration of the planet would drastically improve in speed.
Another interesting feature is that they can be used for the retrieval of small scientific samples to be returned to Earth in missions like Mars Sample Return (ESA).

1.1 Flying on Mars

Martian atmosphere will be better explained in Chapter "*Martian Environment*" but the biggest challenge to fly is the thin carbon dioxide atmosphere with its very low density and lower speed of sound compared to Earth's one. This is a huge drawback in terms of generating thrust. Hence, a new aerodynamic domain is explored:
compressible and ultra-low Reynolds number flow.
Lower thrust to area ratio implies bigger rotor dimensions but this is not always compatible in terms of drone accommodation inside the vehicle launched to Mars and in terms of Mach number, so the maximum dimension of the drone may be imposed. This leads to a higher rotor rotational speed needed in order to archive the required thrust to hover and control the drone. A proper electrical motor must be found. This motor will face quite high torque (versus its maximum limit) and high rpm so an

overheating is to be expected and solved, if necessary, with a proper thermal design. Overcooling is expected at rest due to the Martian nights extreme conditions, therefore it is necessary to use motors with a large range of operative temperature and, if not enough, to provide a specific thermal control design.

1.2 Different types of architectures

Many ideas have been proposed in order to achieve the aerial exploration of the Martian surface:

1. Helicopter

Figure 1.1: NASA's Mars Helicopter Scout.

2. Drone

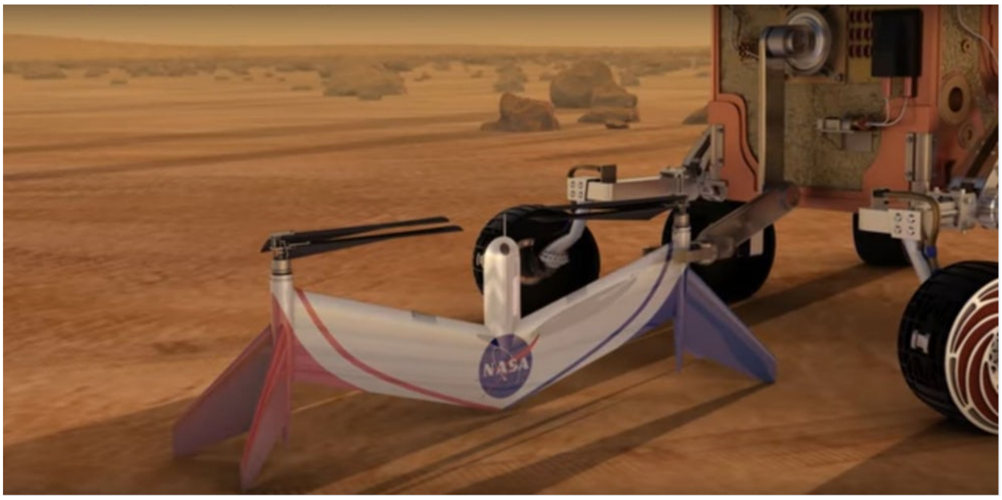

Figure 1.2: NASA's drone (concept).

3. Airplane

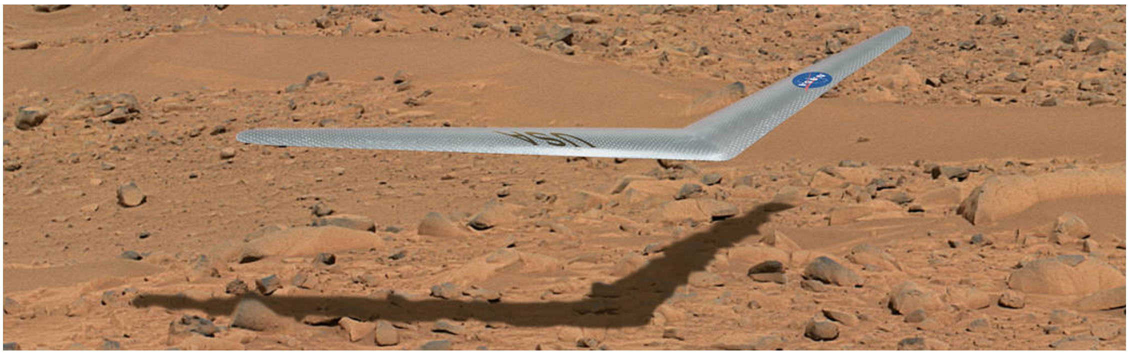

Figure 1.3: NASA's Mars Airplane (concept).

4. Balloon

Figure 1.4: The Mars Society Balloon (rendering).

Among all these proposed solution only the NASA's Mars Helicopter Scout has been actually designed and it is supposed to fly on Mars as a technology demonstrator of Mars aerial mobility within the mission "*Mars 2020*".

1.3 NASA's solution

Since the beginning of the 2000s NASA started to focus on the development of an airborne system able to scout the Martian surface. In August 2013 a technology development project at NASA's Jet Propulsion Laboratory (JPL), together with Caltech, proved that big things could come in small packages. In 2014 a first conceptual design was proposed [3]. The result of the team four years of design, testing and re-design weighs gave birth to the **Mars Helicopter Scout (MHS)** [4]. Its fuselage is about the size of a softball (15x15x15 cm), and its twin, coaxial, counter-rotating rotors will bite into the thin Martian atmosphere at about 3000 rpm, 10 times the rate of a helicopter on Earth. The helicopter also contains built-in capabilities needed for operation at Mars (Figure 1.9), including solar cells to charge its lithium-ion batteries (Figure 1.10), and a **heating mechanism to keep it warm through the cold Martian nights**. The total weight is 1.8 kg (upper mass limit) [10].

MHS known specifications:

- Mass: 1.8 kg [10], [25]
- Battery Mass: 273 g [10]
- Height: 0.8 m [26]
- Coaxial rotor diameter: 1.2 m [26]
- Revolutions/min: 1900 $\div$ 2800 rpm [27]
- Blade tip speed: $<$ Mach 0.7
- Chassis dimension: $\sim$ 15x15x15 cm
- Power: 220 W
- Flight time: up to 90 s [10]
- Operational time: $\sim$ 5 flights in $\sim$ 30 days
- Maximum range: 600 m per flight
- Maximum speed [4]:
  - Horizontal 10 m/s
  - Vertical: 3 m/s
- Payload: High resolution and Navigation cameras. [26]

Figure 1.5: NASA's Mars Helicopter Scout (rendering).

A coaxial helicopter with counter-rotating rotors does not need a tail rotor and stabilizers to counteract the reaction torque generated by the main rotor and thus it's smaller than a classic helicopter. The main drawbacks of this solution are the complicated swashplate mechanisms (with its 6 small motor dedicated system, 3 for each swashplate [10]), the necessity of using two different motors, one for each rotor (Figure 1.11) and the mechanisms dust protection.

MHS gallery

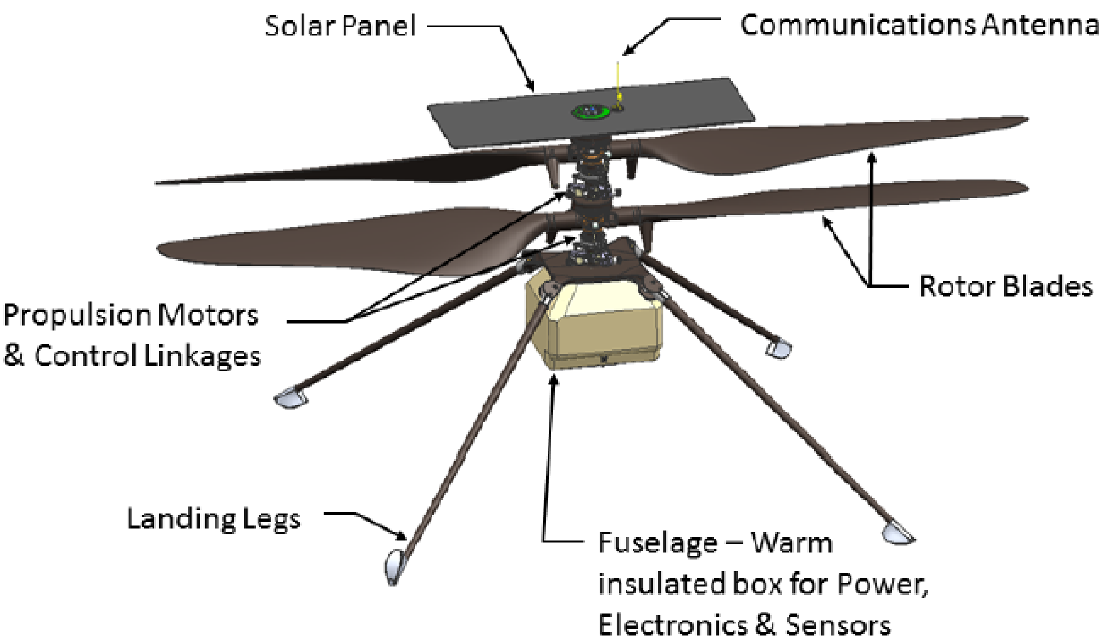

Figure 1.6: NASA's Engineering Demonstration Model Design [10].

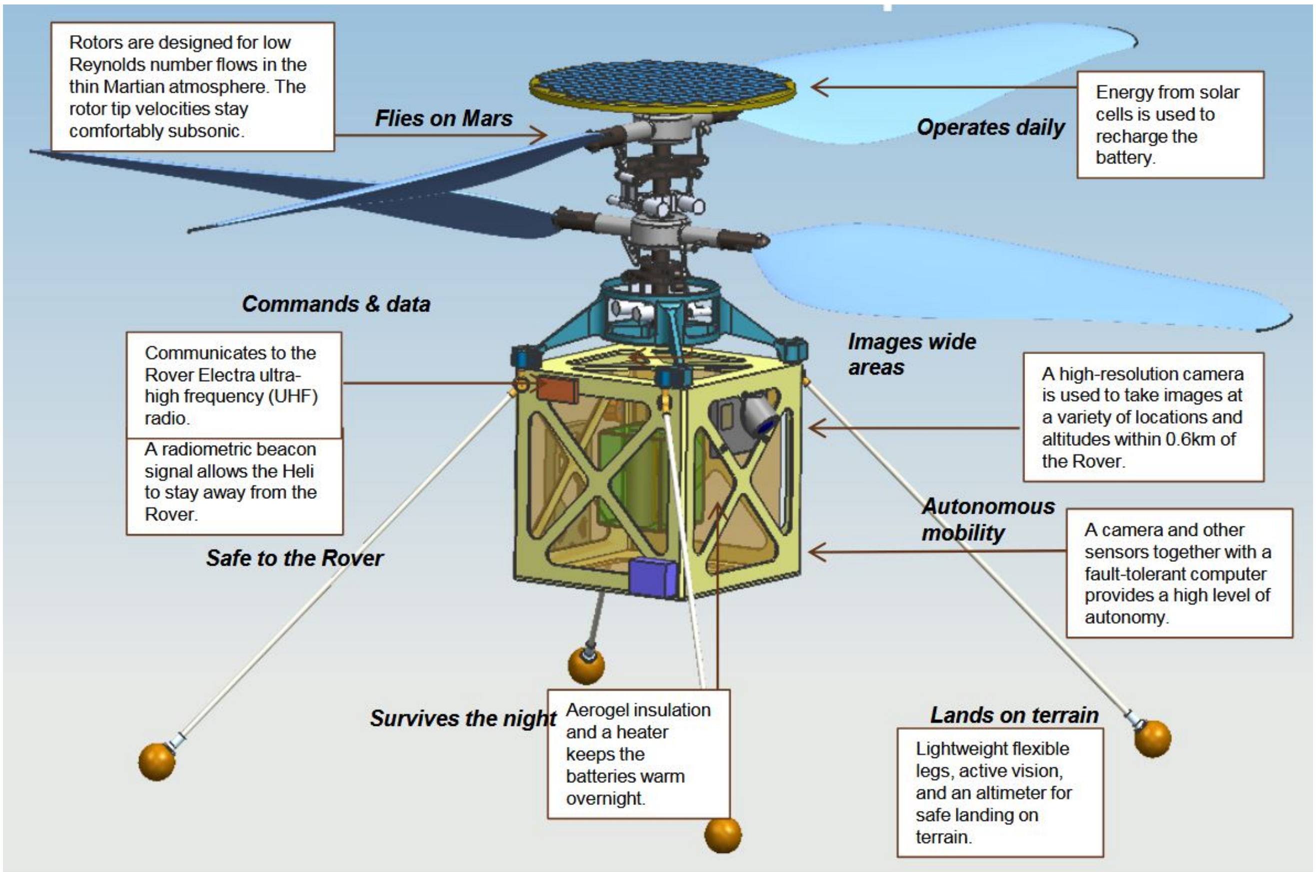

Figure 1.7: NASA's Mars Helicopter Scout details.

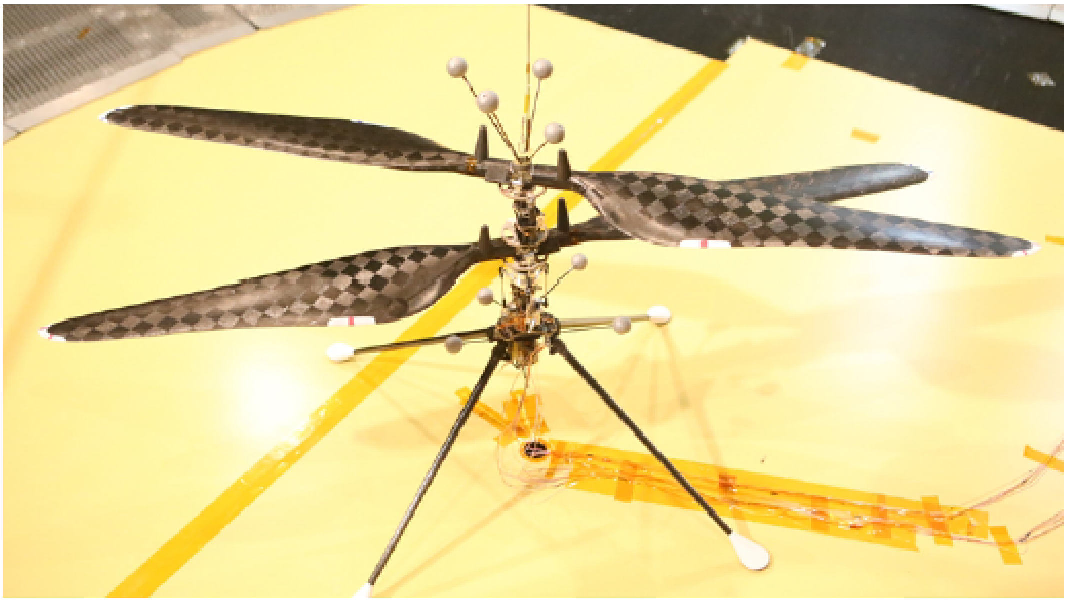

Figure 1.8: NASA's Mars Helicopter full-scale prototype [10].

MHS in Figure 1.8 is shown with safety tether which is removed for free-flight tests, moreover it is possible to see Vicon tracking targets and electrical lines to off-board power and avionics.

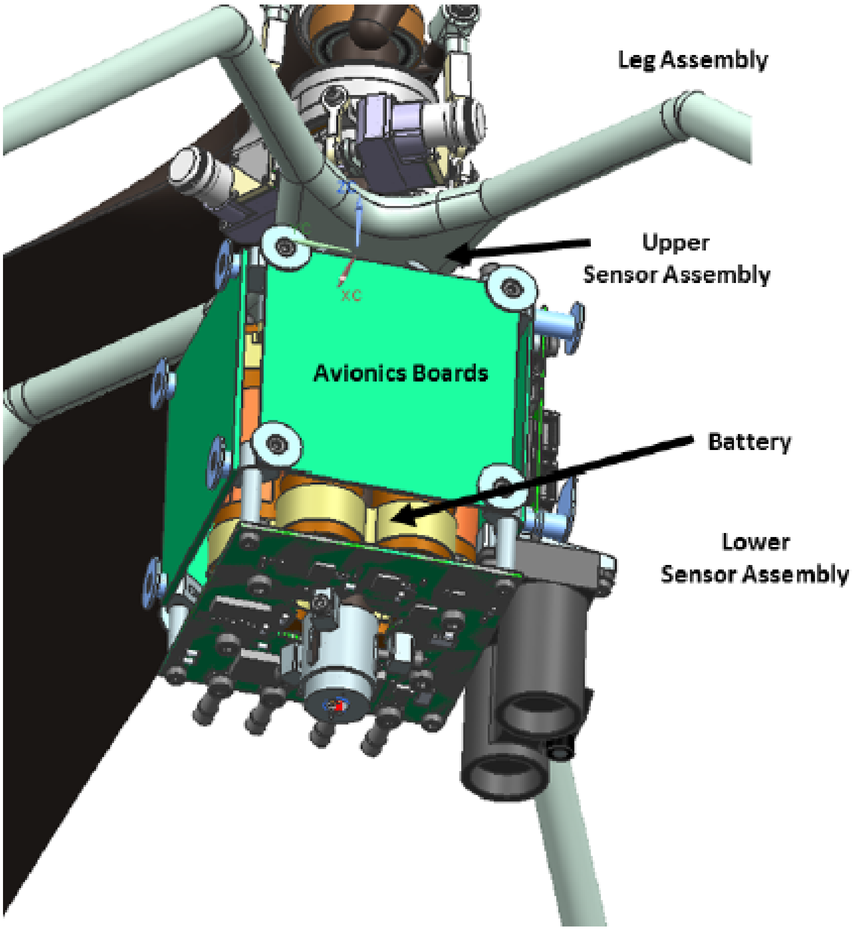

Figure 1.9: MHS Electronics Core Module (ECM) [10].

ECM figure shows configuration of battery surrounded by avionics boards and attached sensor assemblies.

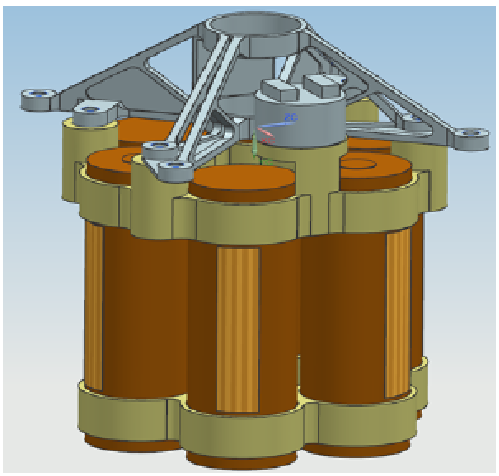

Figure 1.10: MHS Battery assembly: Li-Ion cells, bonded thermostat and heaters [10].

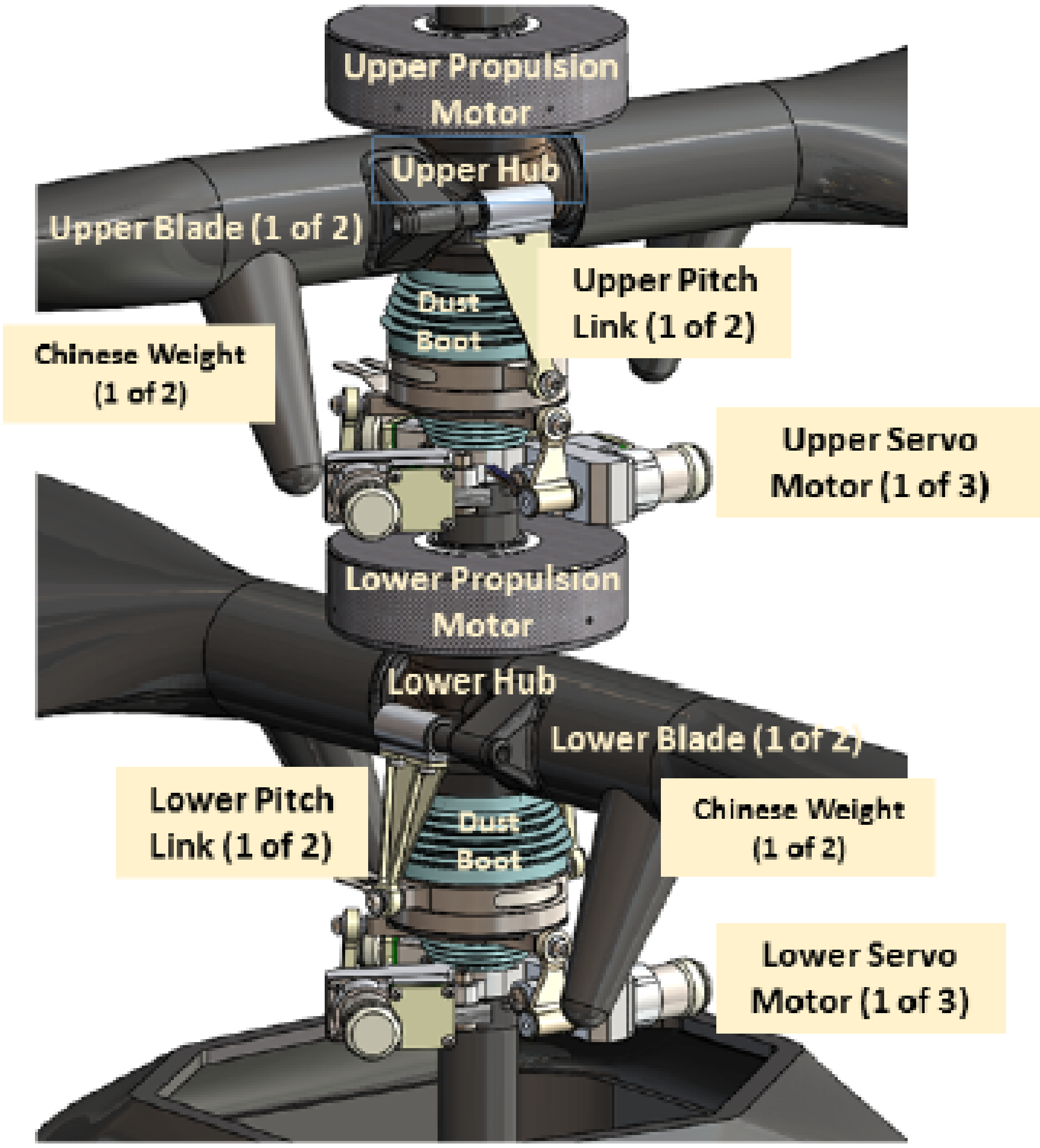

Figure 1.11: MHS Rotor assembly [10].

Recent studies in Europe (ESA) and TAS-I about automated optical landing and attitude control software of drones developed through Vicon tracking targets, together with the complexity of the swashplate and dust protection suggested to study a different solution:
a quadcopter scout.

1.4 Thesis content

The present thesis consists of a feasibility study and conceptual design of a Martian drone intended to hover and explore the planet surface for some minutes and then return to a base for data downloading and battery recharging. The total mass was the main requirement since it comes from the launcher.
The approach used in this work is presented in the flow chart below:

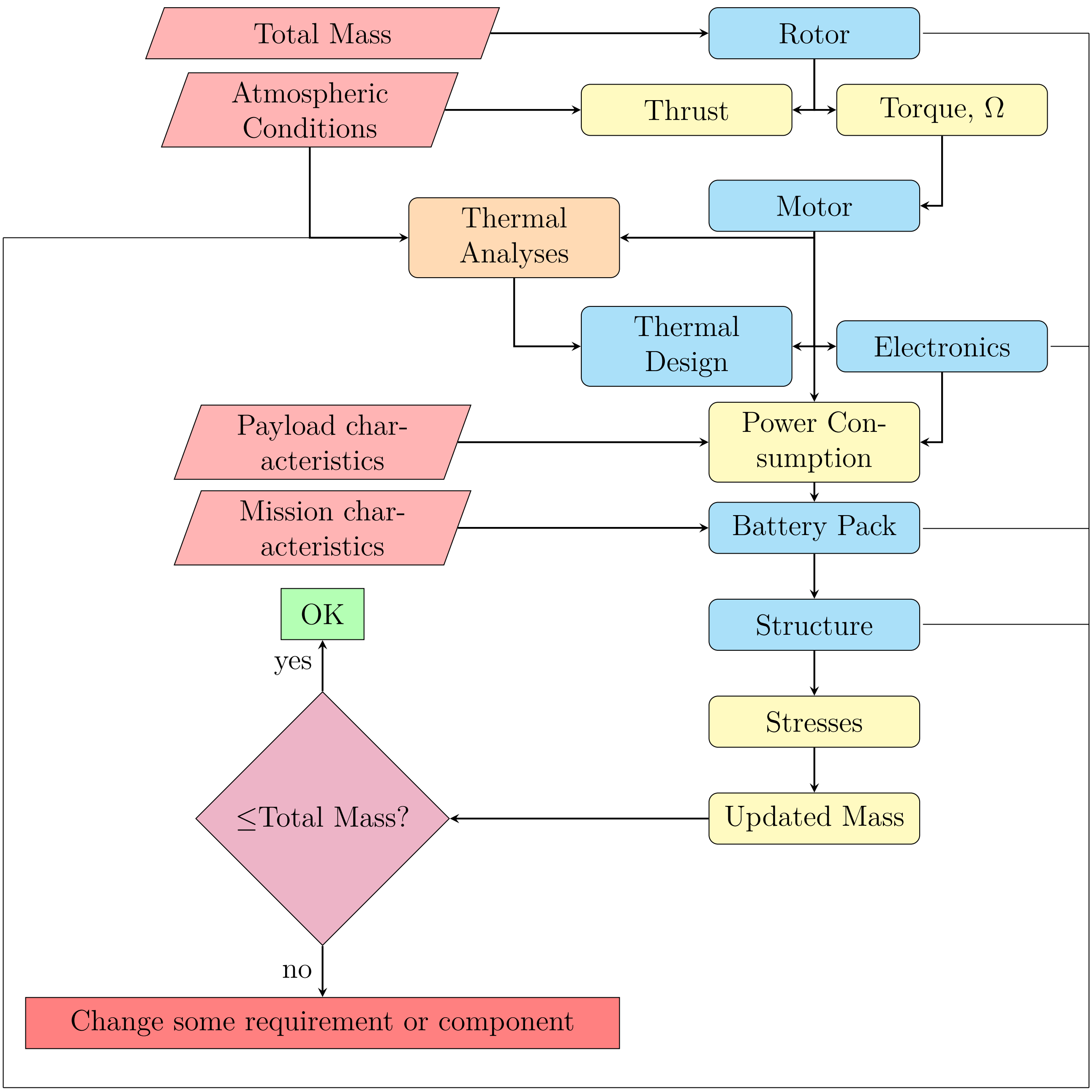

There are five types of boxes:

1. **Light Red Boxes** represent the most important design and **mission requirements**, coming from a search about what other companies, universities, Politecnico di Torino and TAS-I are doing about extra-terrestrial drone application.

2. Cyan Boxes are related to the design or the choice of a component.

3. Yellow Boxes indicate "simulations", using models and engineering tools.

4. ***Orange Box***, *represents the* ***main focus of the thesis***.

The main focus of the thesis was the development of a *Thermo-Aerodynamic Model* of the motor-rotor couple, and of a *Thermal-Energy Model* of the whole drone.
The starting point of all the work was the data analysis and post-processing of the performances of a rotor identic to the one developed by the University of Maryland [6] (the most important known study on the subject of a Martian rotor), and tested in TAS-I with a preliminary motor.
Once analysed the rotor thrust and torque it was evident that the tested motor was not the best choice for that kind of applications and a new one was necessary, coupled with an **optimized rotor** whose features were identified in a past thesis [7].
Even if the first motor was not the best fit for the Maryland/TAS-I rotor it was possible to acquire some temperature data from thermocouples placed on the motor itself during TAS-I tests. This was the first step towards the development of the thermo-aerodynamic model in MATLAB of the motor-rotor couple which was correlated versus the tests data and **provided the heat transfer coefficients between air (at Martian density) and the motor surfaces.**
This was an important input for a more detailed thermal model of the whole drone developed in ESATAN-TMS, calculating the temperature and electrical energy balance of the main components (structure, motor, electronics, battery...) for the expected mission profile on Mars, and consequently enabling the identification of the thermal design solution (e.g. insulations, heaters...) and the verification of the power subsystem design (battery size, recharge solutions...).

In order to better understand the thesis logical process another flow-chart is shown:

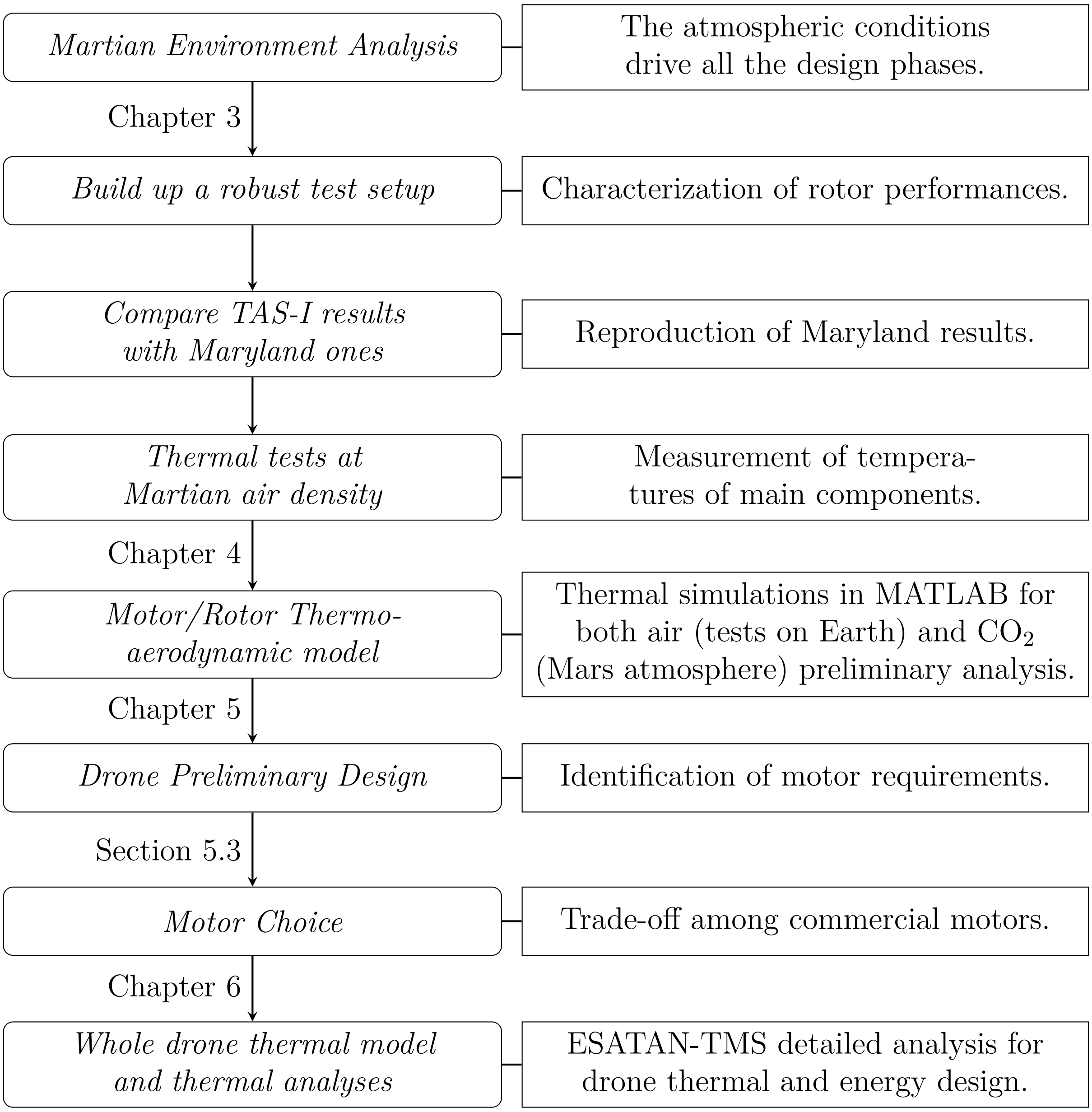

Main Chapters summary:

- *Chapter 3 and 4:* In these chapters rotor analyses and motor thermal tests led to the development of thermo-aerodynamic and motor power consumption routines.
- *Chapter 5 and 6:* Drone preliminary design together with motor choice led to a first drone configuration which was simulated with ESATAN-TMS from the thermal and energy point of view.

Chapter 2

Martian Environment

2.1 Main characteristics

The Martian atmosphere is composed by:

Element	%
Carbon Dioxide	95.32
Nitrogen	2.7
Argon	1.6
Oxygen	0.13
Carbon Monoxide	0.08

Table 2.1: Mars Atmosphere Composition. [5]

The resultant molar mass is $\boldsymbol{M}$=43.34 g/mol and the specific heat ratio γ is equal to 1,289.

Temperatures have been measured by NASA's landers, they vary a lot during the day (called Sol), seasons, with latitude and terrain characteristics. We can expect temperature variation between -143 °C and +35 °C [1].

Pressure (p) and Density (ρ) also vary accordingly to the *Ideal Gas Law*. Averaged values for p,T,ρ,μ are reported in Table 2.2.

Temperature, $\boldsymbol{T}$	-51.6 °C
Pressure, $\boldsymbol{p}$	7.16 mbar
Density, $\boldsymbol{\rho}$	0.0171 kg/m^3
Dynamic viscosity, $\boldsymbol{\mu}$	1.130e-5 Pa·s

Table 2.2: Mars averaged Atmosphere Condition. [4]

[1] -89 to -31 °C on Viking 1 Lander site. [5]

Some other useful thermodynamic characteristics are here summarized:

Specific heat ratio, γ	1.289
Specific gas constant, $\boldsymbol{R} = R/M$	188.9 J/kgK
Speed of sound, $\boldsymbol{a}$	232.26 m/s

Table 2.3: Mars Atmosphere useful characteristics. [4]

Density on Earth is $\rho_E = 1.225\ kg/m^3$ [2] at sea level and standard conditions so Mars' atmosphere density is about 1÷2% of Earth's one.

Mars' gravity is 3.71 m/s^2 [4] so it's about 1/3 of Earth's one.

	Grav. Acc. $[m/s^2]$	**Density** $[kg/m^3]$	**Speed of sound** $[m/s]$
Mars	3.71	0.0167	232.26
Earth	9.81	1.225	340.26
Ratio M/E	0.378	0.0136	0.683

Table 2.4: Earth vs Mars gravitational acceleration, density and speed of sound.

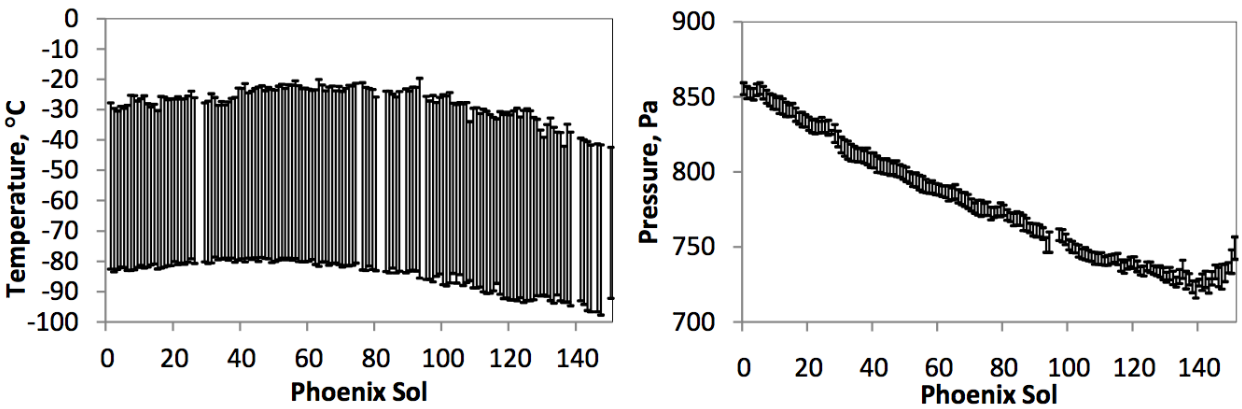

Figure 2.1: Temperature and pressure data collected by the Phoenix lander in 2008.

2.1.1 Martian surface

Height

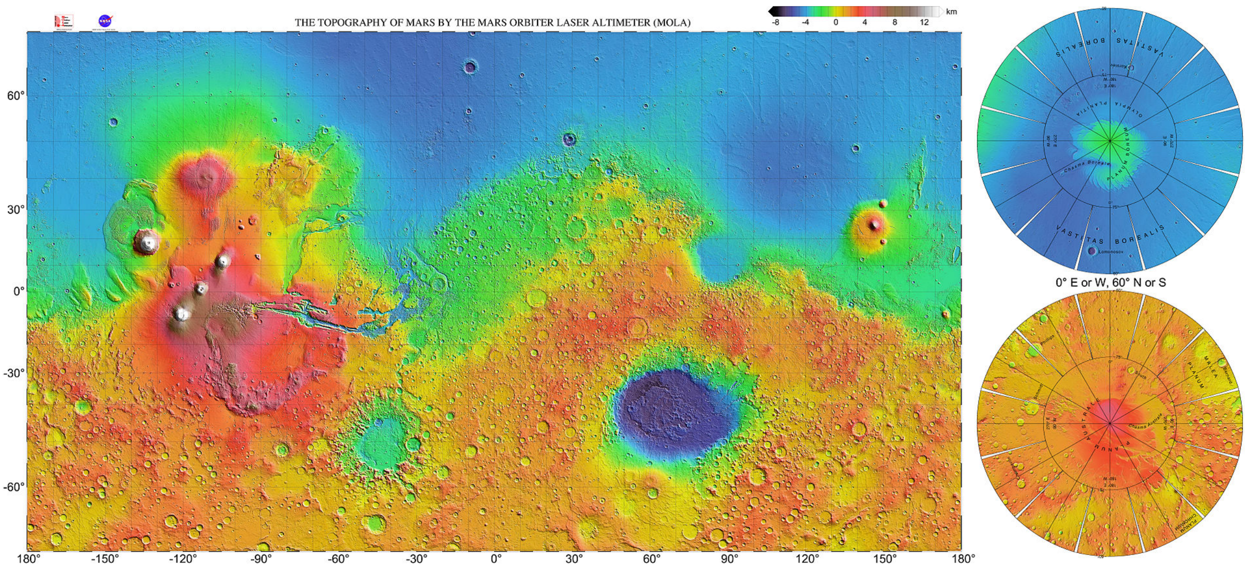

Figure 2.2: Very high resolution topographic shaded relief map of Mars.

Figure 2.2 is based on the Mars Orbiter Laser Altimeter (MOLA) data set from the Mars Global Surveyor spacecraft. The map has a resolution 0.125° (300 dots per inch) and is shown as a Mercator projection to latitude 70° north and south.

Day and Night Temperatures

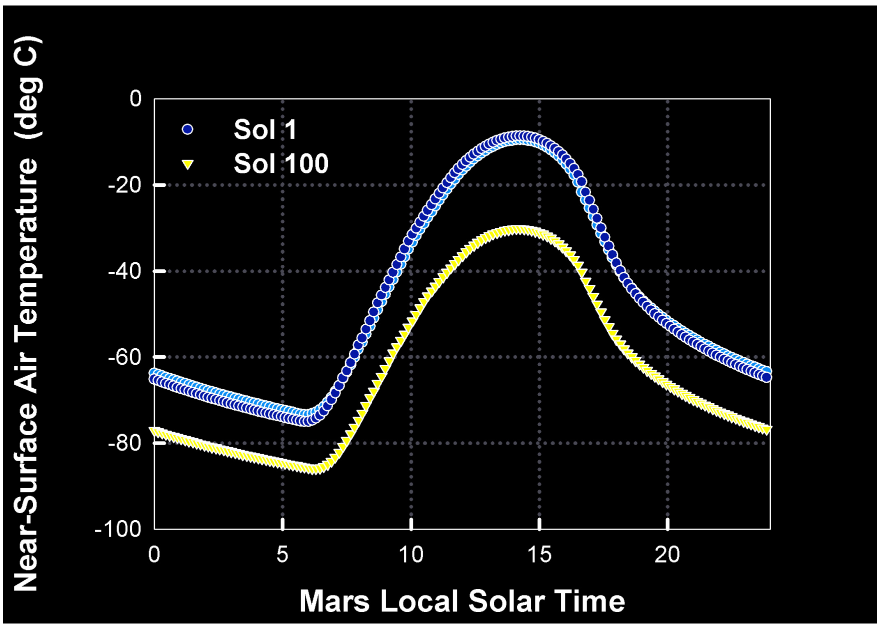

Figure 2.3: Mars CO_2 temperature on ground in different seasons.

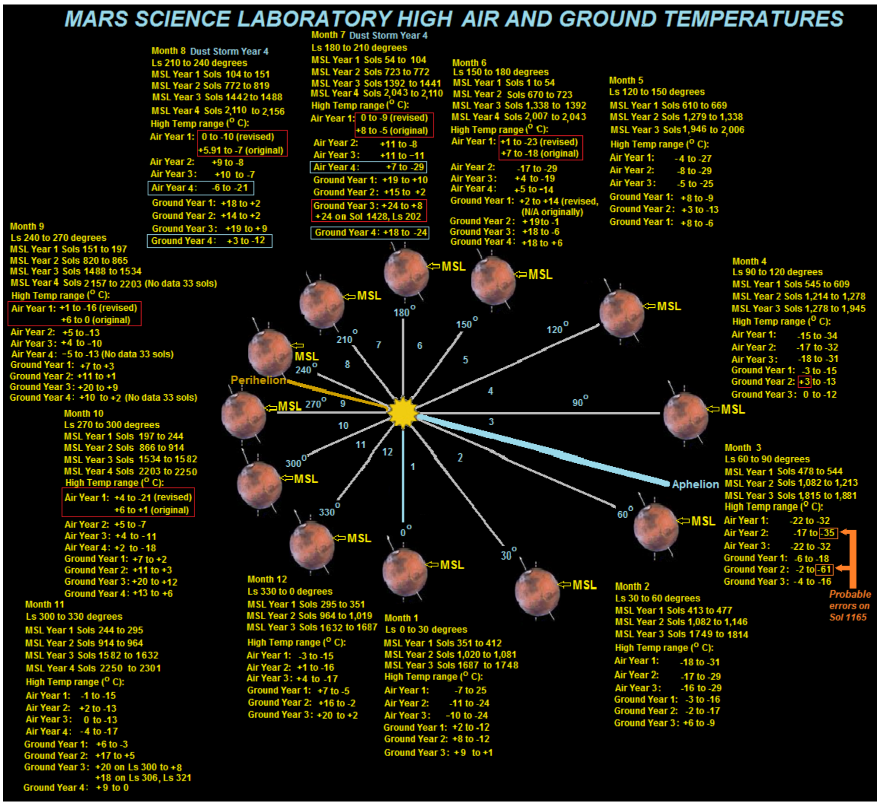

(a) *Day.*

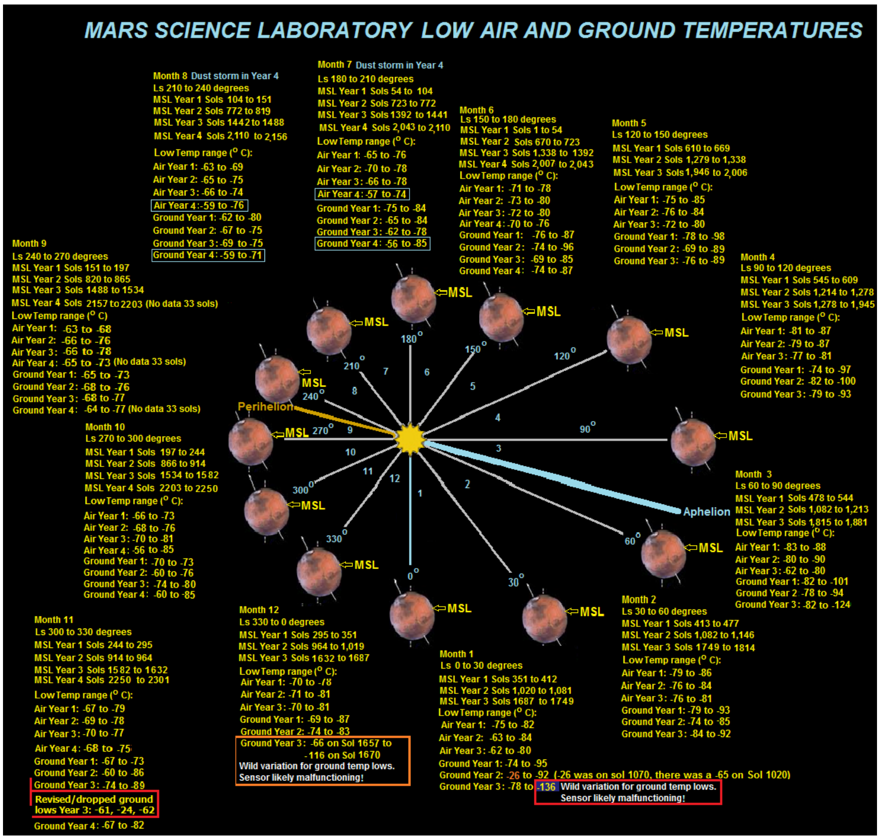

(b) *Night.*

Figure 2.4: Day and Night temperatures depending on MLS.

2.1.2 Mars' orbit

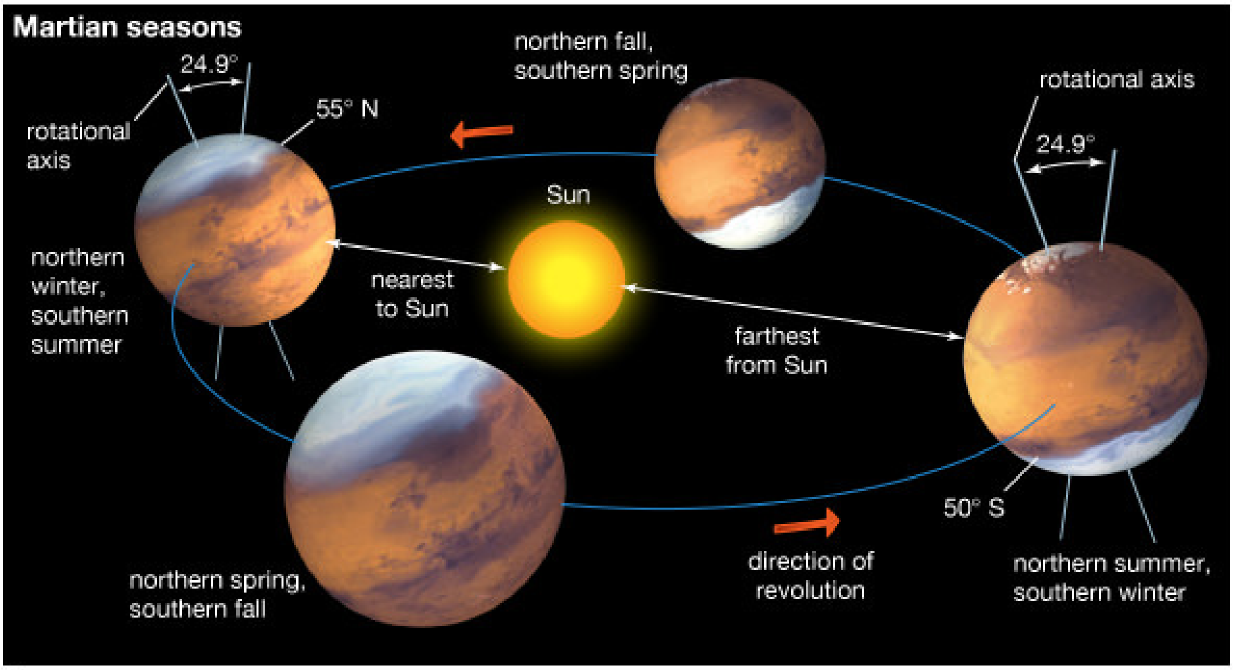

Figure 2.5: Mars' Orbit.

- Semi major axis: 227.9 [Gm]
- Perihelion: 206.7 [Gm]
- Aphelion: 249.2 [Gm]
- Average: 228.9 [Gm]
- Orbital circumference: 1429 [Gm]
- Closest approach to Earth: 55.76 [Gm]
- Farthest distance from Earth: 400.2 [Gm]
- Eccentricity: 0.0934 [ ]
- Inclination: 1.850°
- Orbital period: 687.0 [days]
- Synodic period (apparent orbital period from Earth): 779.9 [days]
- Average speed: 24.1 [km/s]
- Maximum speed: 26.5 [km/s]
- Minimum speed: 22.0 [km/s]

2.1.3 Cold and Hot environmental case

It is important for the thermal design to determine the two extreme operative conditions in terms of environmental characteristics.
These two cases are called **cold** and **hot environmental case**.
• The *cold case* represents the coldest conditions faced by the drone in terms of ambient temperature and external heat fluxes (solar and planet heat fluxes). This case is represented by the Martian night where the external temperatures are very low and the solar and planet fluxes are zero (solar) or negligible (planet). Even if the drone is not operative it's important to verify if it can survive to the cold case and perform a new mission.
• The *hot case* represents the hottest possible operative conditions in terms of ambient temperatures and incident heat fluxes. In this scenario it is important to verify if the motor and avionics will not overheat.

2.2 Aerodynamic problems

It is evident from table 2.4 that we need less thrust to lift-off the same mass on Mars than on Earth but the very low density plays a more important role since

$$T = m \cdot g \propto \rho\, \Omega^2 R^4 \cdot C_T \tag{2.1}$$

where:

- T is the required thrust [N]
- m is the mass to hover [kg]
- g is the gravitation acceleration [m/s^2]
- ρ is the atmospheric density [kg/m^3]
- Ω is the rotational speed [rad/s]
- R is the rotor radius [m]
- C_T is the thrust coefficient [ ]

Through this equation we can estimate the rotational speed needed on Mars to lift-off the same weight with the same propeller characteristics R and C_T than on Earth:

$$\Omega_M = \sqrt{\frac{\rho_E}{\rho_M} \cdot \frac{g_M}{g_E}} \cdot \Omega_E \approx 5.27 \cdot \Omega_E$$

so using a propeller with the same radius and the same aerodynamic load it is necessary to rotate 5 times faster then on Earth to lift-off the same mass. This is a problem in terms of Mach number. In fact the tip of the propeller on Mars would experience a Mach number 46.5% higher than on Earth rotating at the same speed and with the same radius, but rotating 5 times faster means the propeller tip would easily be supersonic and this is not acceptable.

$$\frac{M_M}{M_E} = \frac{\Omega_M \cdot R_M}{a_M} \cdot \frac{a_E}{\Omega_E \cdot R_E} = \frac{\Omega_M}{\Omega_E} \cdot \frac{a_E}{a_M} \approx 7.721$$

A better solution is to choose a bigger and more efficient propeller.
Supposing the same rotational speed Ω and the same C_T the increase in radius to lift-off the same mass will be

$$R_M = \left[\frac{\rho_E}{\rho_M} \cdot \frac{g_M}{g_E}\right]^{1/4} \cdot R_E \approx 2.295 \cdot R_E$$

$$\frac{M_M}{M_E} = \frac{\Omega_M \cdot R_M}{a_M} \cdot \frac{a_E}{\Omega_E \cdot R_E} = \frac{R_M}{R_E} \cdot \frac{a_E}{a_M} \approx 3.362$$

In this way we will have a Mach number roughly three times than on Earth, allowing to design a non-supersonic propeller tip. This fact supports the statement *"compressible and ultra-low Reynolds number flows"* in the introduction. *Compressible* is for the high Mach number involved.
Ultra-low Reynolds number is easily explained too:

$$Re = \frac{\rho c V}{\mu} \tag{2.2}$$

where

- ρ is the atmospheric density,
- c is the airfoil chord (characteristic length),
- V is the relative velocity between the airfoil and the air/CO_2,
- μ is the atmospheric dynamic viscosity.

Assuming a chord of 5 cm and a relative speed of 100 m/s the Reynolds number is:

- on Earth: Re $\sim$ 300000,
- on Mars: Re $\sim$ 7000

Since the Reynolds number is proportional to the ratio between inertial forces and viscous forces, an airfoil on Mars experiences a much more "viscous velocity field" than on Earth. The problem of evaluating and improving performances of a rotor in such a motion field has been investigated in a thesis strictly related to this one, made by Davide Bergamino in TAS-I (Thales Alenia Space Italia).

Chapter 3

Characterization of the rotor performances

The objective of this test campaign, started by Andrea Botta during his master thesis and stage and concluded with data acquisition and analysis, was to test a suitable Martian propeller and motor and to define a reliable testing methodology for different kind of rotors in a Mars-like environment (ρ - like atmosphere) on Earth. This was possible using a vacuum chamber called PHASE (Appendix C).
Once built up, the setup was used to characterize a rotor identic to the one used in a similar research activity made by the University of Maryland [6] and to test the motor thermal behaviour.

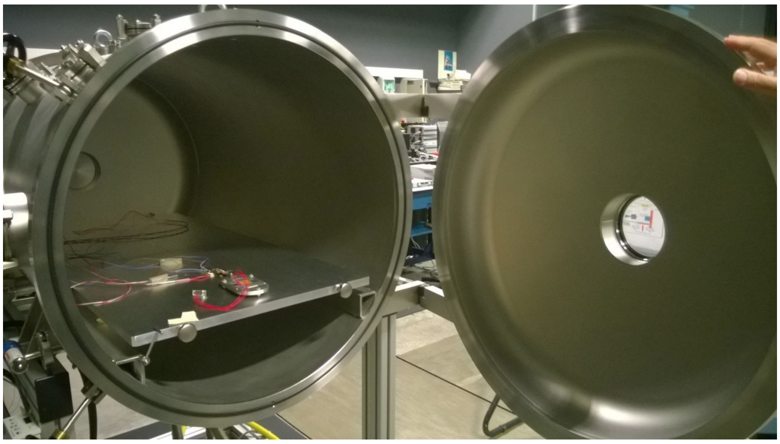

Figure 3.1: PHASE vacuum chamber (Appendix C).

From the thermal point of view mechanical data were important for the purpose of determining the rotor M-n curve and therefore to calculate the motor power dissipation. **These results were the baseline to determine a motor matching the propeller and then to study it with a detailed thermal analysis.**

3.1 TAS-I vs Maryland test setup

The purpose of the research activity was to test a rotor identical to the University of Maryland one. The two rotors are represented in Figure 3.16 and Figure 3.17. Even if the two rotors are almost identical the test setup is different. In fact the **University of Maryland** setup was a **vertical setup** which used a sled and a load cell to acquire thrust data and the motor was matched to the rotor with a 4:1 planetary gearbox in order to reduce the rotational speed at the rotor shaft.
In **TAS-I** a **horizontal setup** was used and no gearbox was needed. Moreover the thrust data were acquired through a load cell connected to the support of the propulsive group by a stiff, nylon wire. All the support was suspended like a pendulum to minimize friction. TAS-I setup is here schematized:

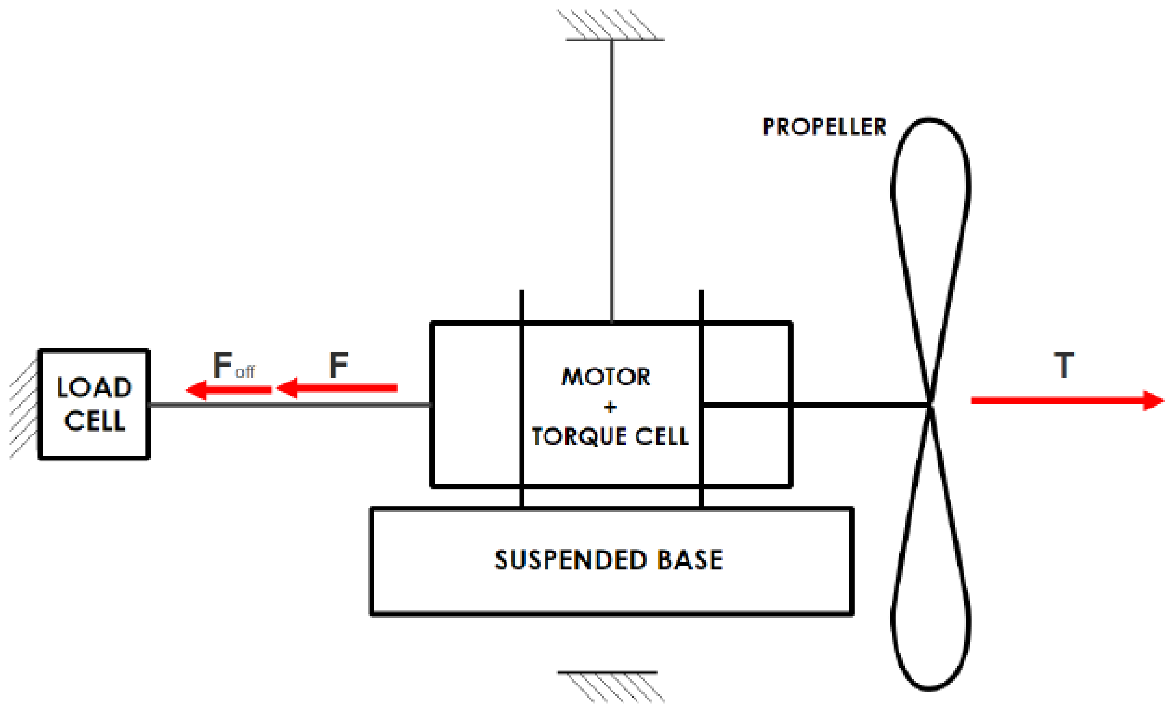

Figure 3.2: Scheme of TAS-I horizontal setup.

where:

- **T** is the rotor Thrust,
- $\mathbf{F}_{off}$ is the offset tension needed to pre-tension the nylon wire,
- **F**=T=$F_{measured} - F_{off}$,
- $\mathbf{F}_{measured}$ is the actual acquired Thrust data.

Pictures of the two setup are here reported:

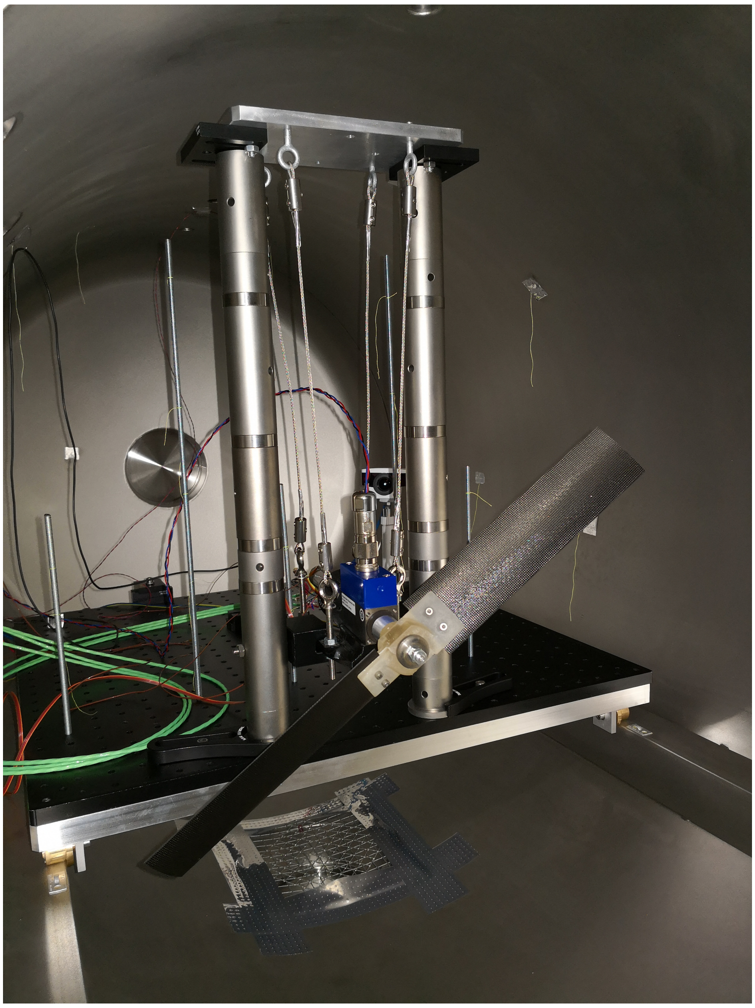

Figure 3.3: TAS-I horizontal setup.

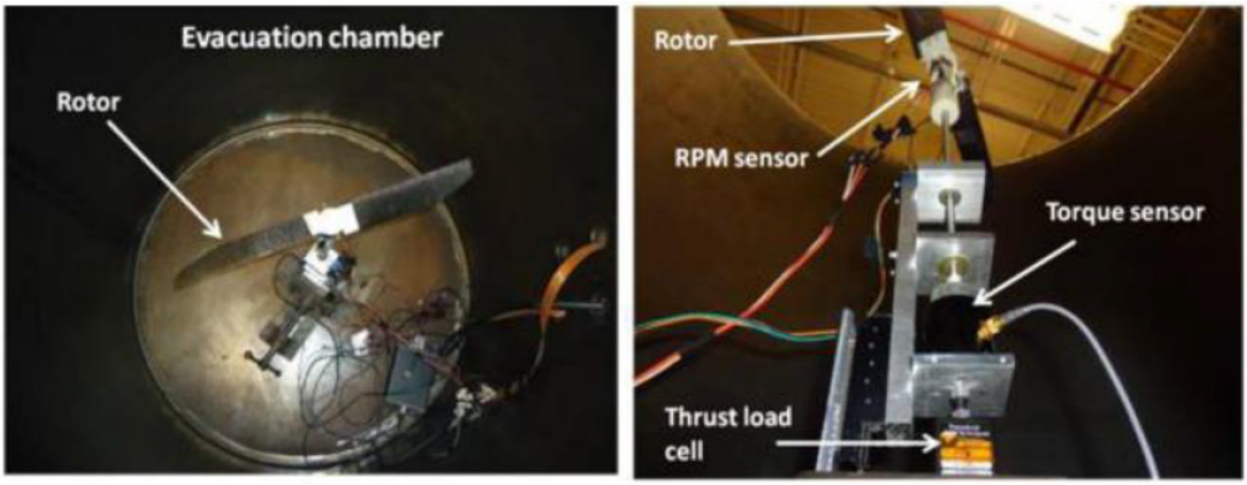

Figure 3.4: University of Maryland vertical setup [6] .

Another scheme of the TAS-I setup is shown in Figure 3.5.

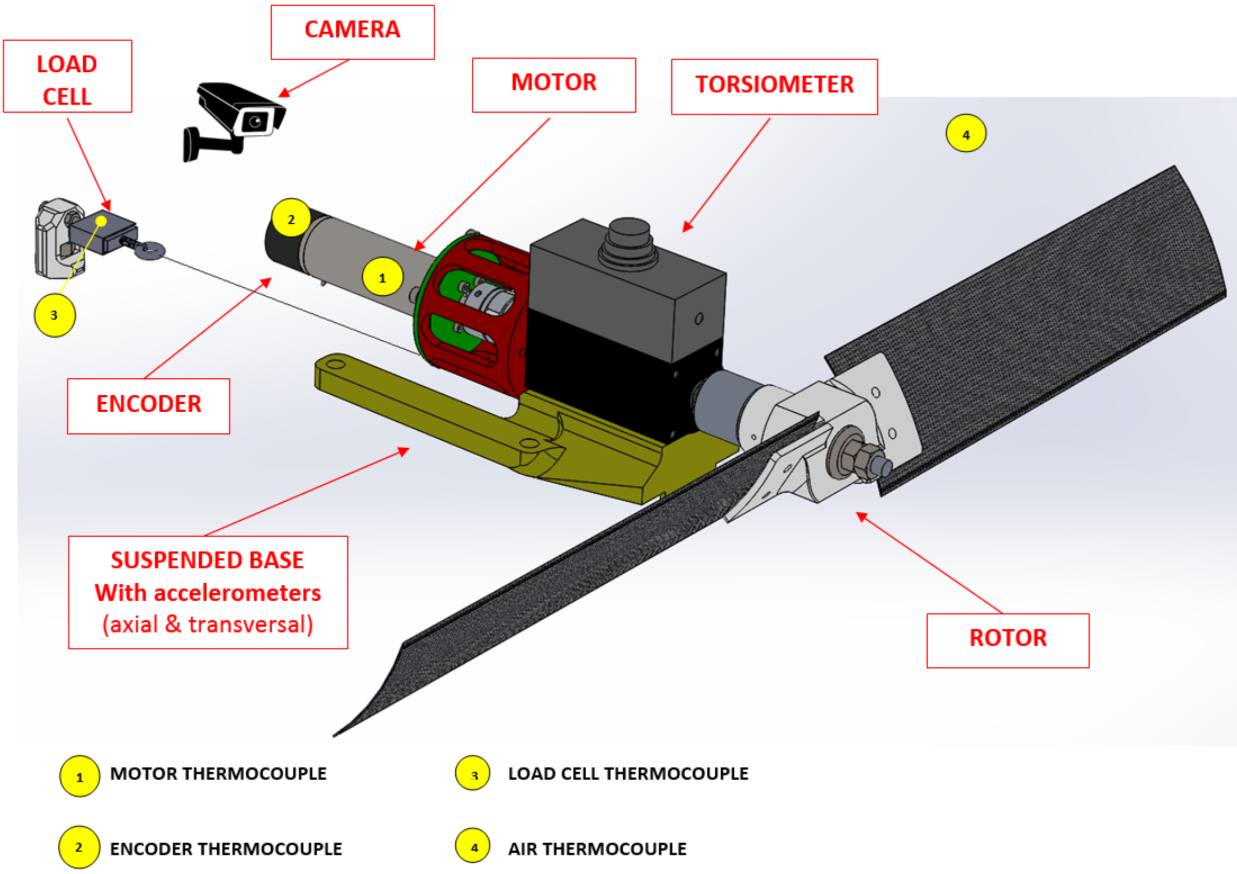

Figure 3.5: TAS-I setup scheme.

In Figure 3.5 are visible the **four thermocouples used during the test campaign**. The most important is the number 1, placed on the motor.
There is only one thermocouple on the motor because during the first tests two thermocouples where placed on the motor but the acquired temperatures where almost the same, meaning that the motor housing is quite isothermal.

3.2 Maryland campaign & results

When testing a new object it is common trying to reproduce known results. In our case they are represented by those obtained by the University of Maryland in 2015 [6]. Their study was in response to the increased interest towards assessing the feasibility of a small-scale autonomous helicopter (gross weight less than 1 kg) for Martian exploration. Here University of Maryland results are briefly summarized:

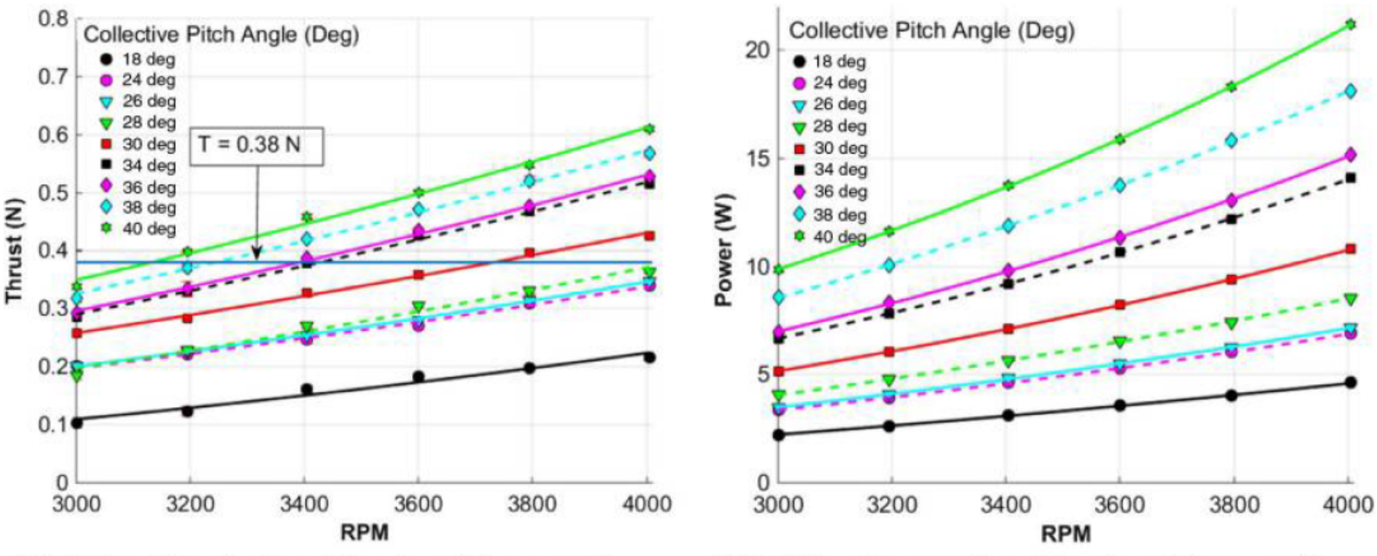

Figure 3.6: Maryland Thrust vs rpm, Power vs rpm for different pitch angles [6].

There is a trend in increasing thrust and power performances with the increase in pitch angle but efficiency must be considered; for rotors efficiency is called *Figure of Merit*.

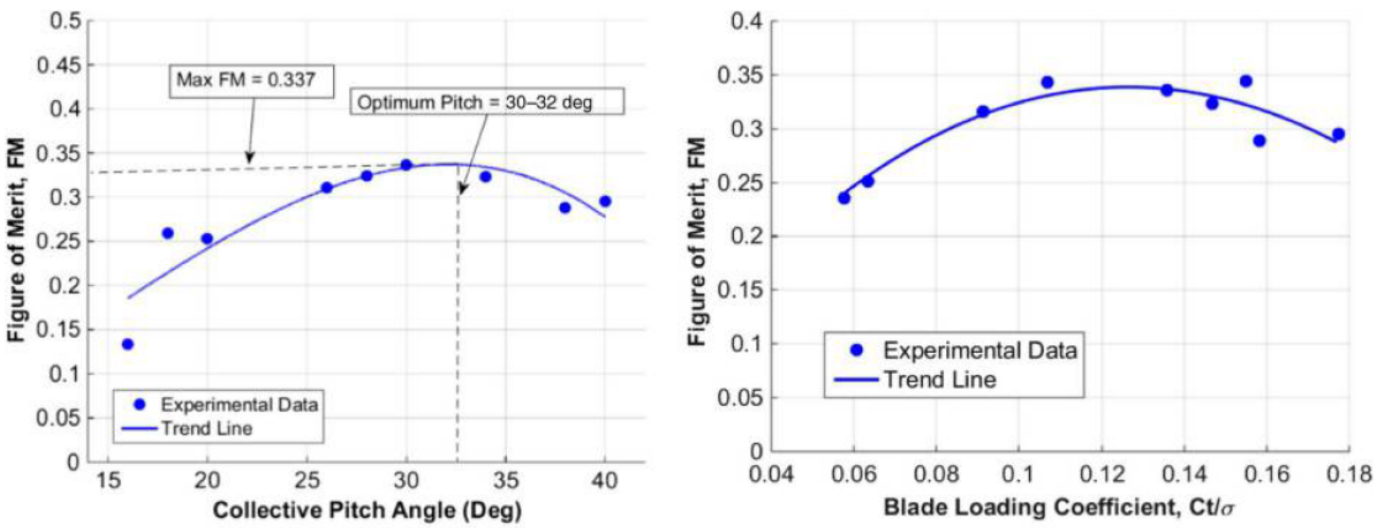

Figure 3.7: Maryland Figure of Merit [6].

The best Figure of Merit (FM) is achieved at $\Theta = 30 \div 32°$ as showed in Figure 3.7.

Figure of Merit is a good efficiency metric to measure the rotor hover performance. This is the ratio of the ideal power required to hover over the actual power required (Actual Induced Power + Profile Power):

$$FM = \frac{\text{Ideal Induced Power}}{\text{Actual Induced Power + Profile Power}}$$

The Actual Induced Power may be written as ($\kappa \cdot$ Ideal Induced Power), where κ is the *Induced Power Factor*. This is an empirical constant that accounts for the induced aerodynamic losses and non-ideal effects. The actual induced power is higher than the ideal power because of non-ideal effects such as non uniform inflow, viscous losses, induced tip losses, etc. Profile Power is the power required to overcome the rotor aerodynamic drag force.
Since we measure the actual power required we can define the Figure of Merit from the blade-element theory as:

$$FM = \frac{C_T^{3/2}/\sqrt{2}}{C_{P_{measured}}} \tag{3.1}$$

Once the pitch from the FM evaluation is chosen as 30° we can focus on the performances of the propeller (Figure 3.8).

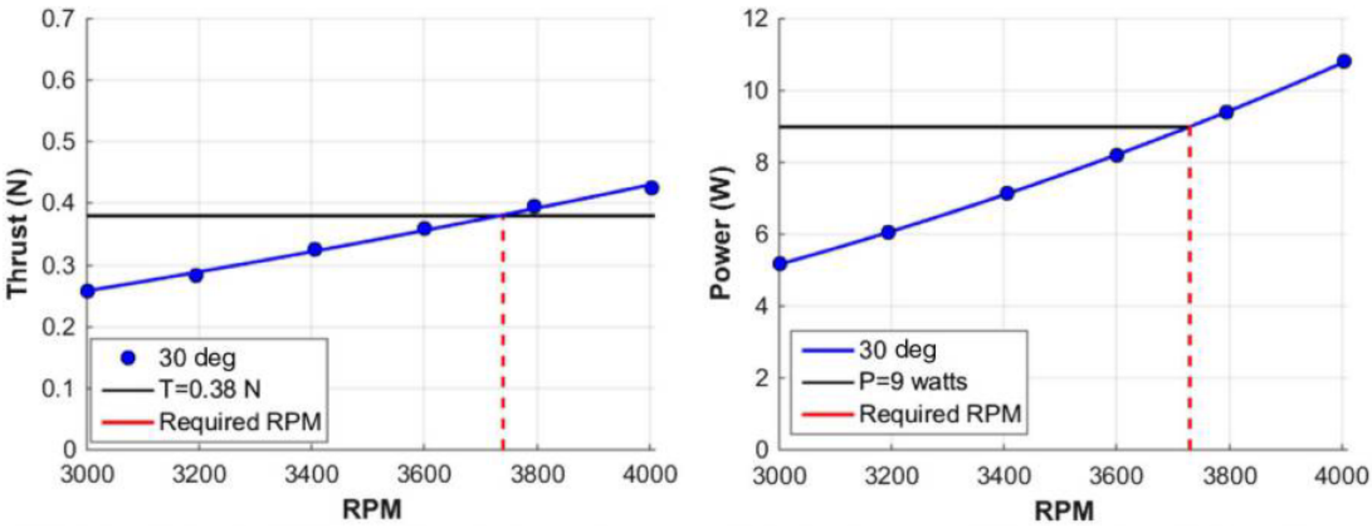

Figure 3.8: Maryland Thrust vs rpm, Power vs rpm for pitch angle=30° [6].

These curves (Figure 3.8) are assumed as benchmark to validate our test setup. To be precise the exact reference curves are slightly higher since **our rotor blades have a pitch angle of 32°.**

University of Maryland characteristic coefficients C_T and C_P are:

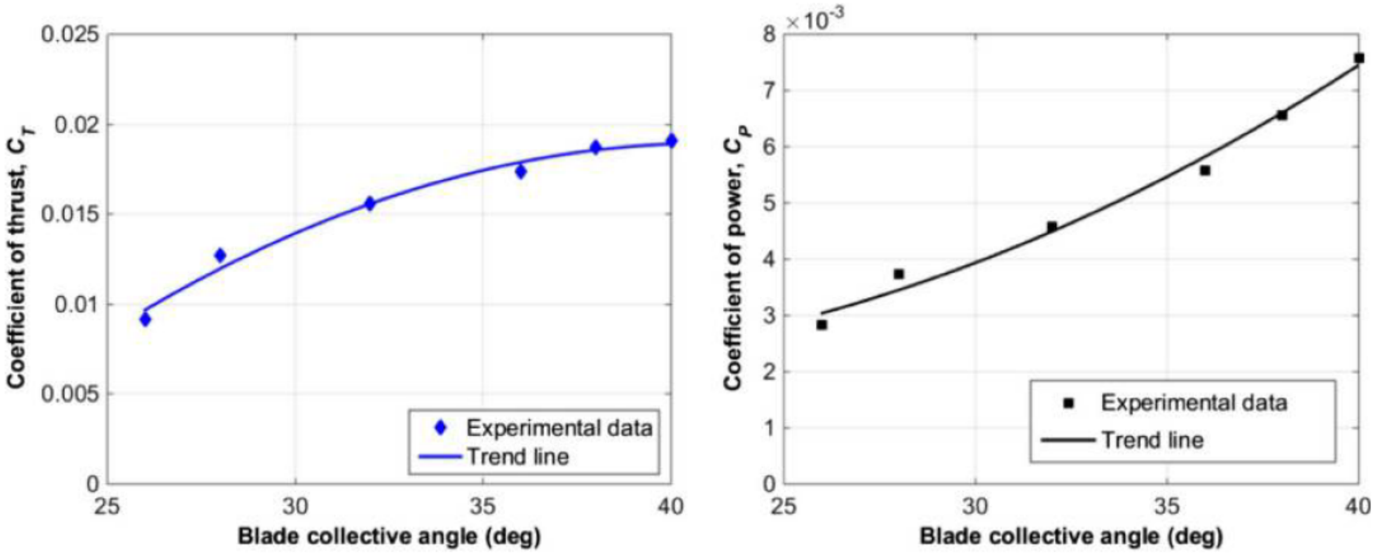

Figure 3.9: Maryland Thrust and Torque Coefficients for different pitch angles [6].

From Figure 3.9 we can extrapolate, for $\Theta = 32°$:

$$C_T \approx 0.016 \qquad\qquad C_P \approx 0.0045$$

Authors don't explain how they obtained these values so a different way to proceed is to compute C_T and C_P for every point of the ideal curve between $\Theta = 30°$ and $\Theta = 34°$, from 3000 to 4000 rpm (Figure 3.8), and than assume a mean C_T and C_P. In this way:

$$C_T = 0.017693 \qquad\qquad C_P = 0.0047744 \tag{3.2}$$

These coefficients are used to reproduce Maryland results in the following sections.

The Maryland University used this definition for C_T and C_P:

$$C_T^{(A)} = \frac{T}{\rho A R^2 \Omega^2} \tag{3.3}$$

$$C_P^{(A)} = \frac{P}{\rho A R^3 \Omega^3} \tag{3.4}$$

$$C_M^{(A)} = C_P^{(A)} \tag{3.5}$$

where:

- T is the output thrust,
- P is the required mechanical power,
- ρ is the atmospheric density,
- A is the rotor disc area,

- R is the rotor disc radius,
- Ω is the rotor angular speed.

Since $P = M \cdot \Omega$ and $M \sim T \cdot R$ we see that in the case of Maryland University $C_P = C_M$, the power coefficient is equal to the torque coefficient.
In literature it is easy to find different definitions for C_T, C_M, C_P so it is important to do the appropriate conversions before comparing results. For example it is easy to find these definitions:

$$C_T^{(B)} = \frac{\pi^2}{4} \cdot \frac{T}{\rho R^4 \Omega^2} \tag{3.6}$$

$$C_M^{(B)} = \frac{\pi^2}{8} \cdot \frac{M}{\rho R^5 \Omega^2} \tag{3.7}$$

$$C_P^{(B)} = \frac{\pi^3}{4} \cdot \frac{P}{\rho R^5 \Omega^3} \tag{3.8}$$

$$\tag{3.9}$$

Conversions between the two definitions called (A) and (B) respectively are:

$$C_T^{(B)} = \frac{\pi^3}{4} \cdot C_T^{(A)} \tag{3.10}$$

$$C_M^{(B)} = \frac{\pi^3}{8} \cdot C_M^{(A)} \tag{3.11}$$

$$C_P^{(B)} = \frac{\pi^4}{4} \cdot C_P^{(A)} \tag{3.12}$$

$$\tag{3.13}$$

3.3 TAS-I experimental campaign

Several tests were made in order to verify the repeatability of the measures and to investigate the performances with respect to air density variations. Here are the results of the reference test. Another test with a little density variation is discussed in Section 3.4.

◇ **Thrust Results**

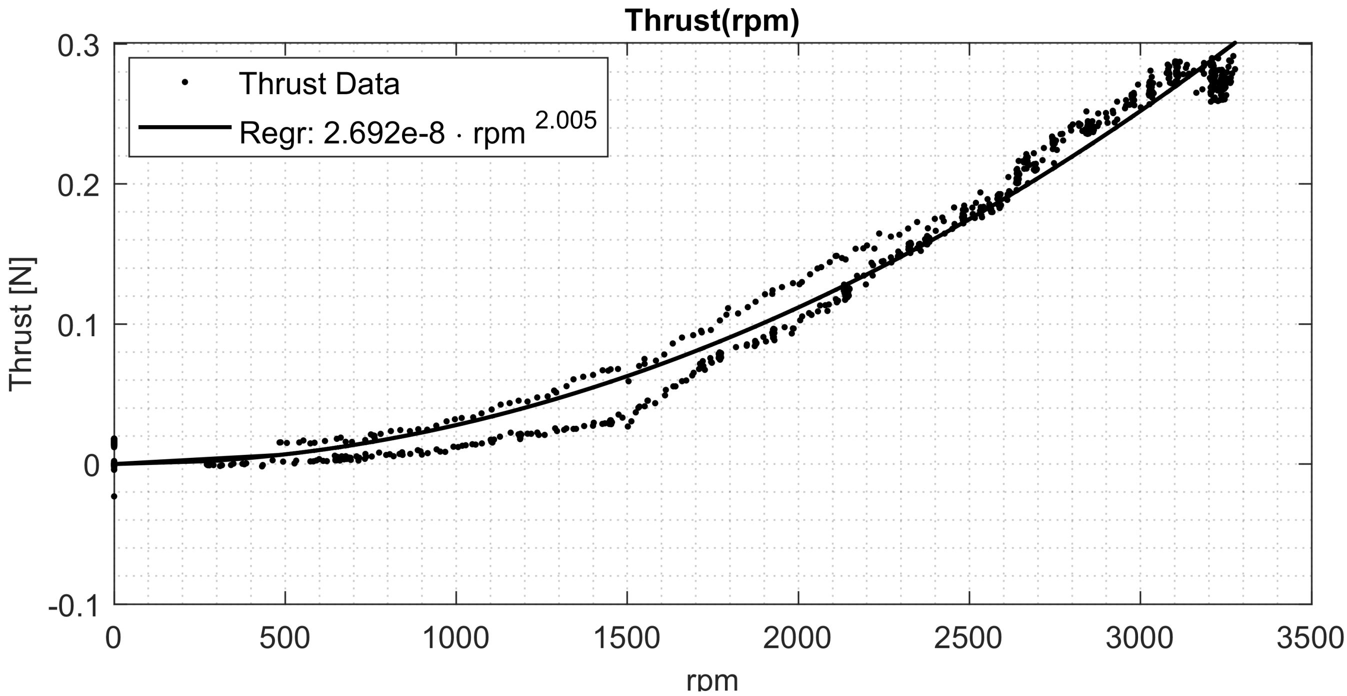

Figure 3.10: TAS-I Experimental results - Reference Thrust.

Figure 3.10 shows an hysteresis between the loading phase and the unloading phase due to wires friction. In fact when the propeller pulls the mechanism forward the wires creep on the breadboard and during the unloading phase the friction determines an increase in tension offset, notwithstanding the exponent of the power regression is 2 as expected. The thrust of the propeller is correlated with the rotational speed by this relation:

$$T = 2.692 \cdot 10^{-8} \cdot n^{2.005} \tag{3.14}$$

The coefficient $2.692 \cdot 10^{-8}$ is proportional to $(\rho \cdot R^4 \cdot C_T)$.

Comparing our results with the Maryland ones:

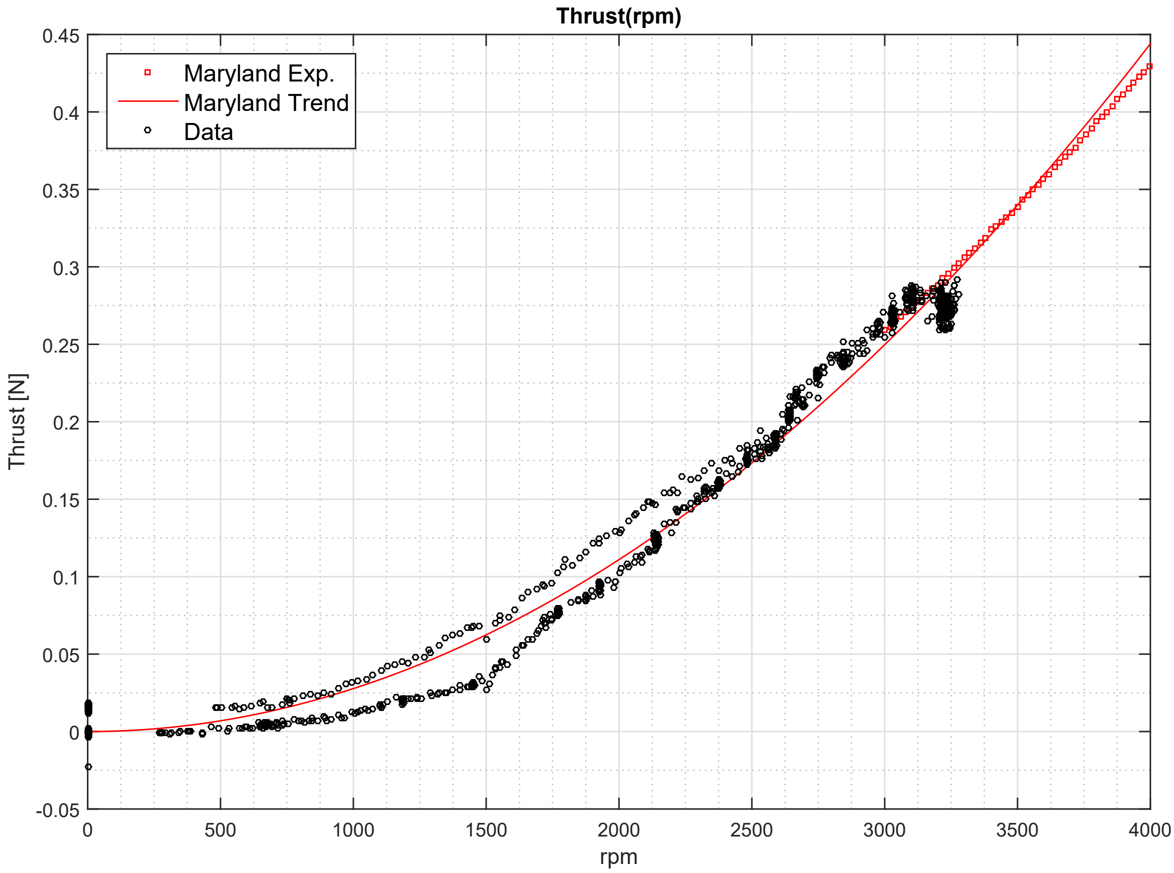

Figure 3.11: Thrust comparison TAS-I vs Maryland.

There is a good matching between our results and those of Maryland. The latter have been modelled assuming constant C_T (Values 3.2).

◇ Torque Results

In Figure 3.12 the Torque data and the relative power regression are shown:

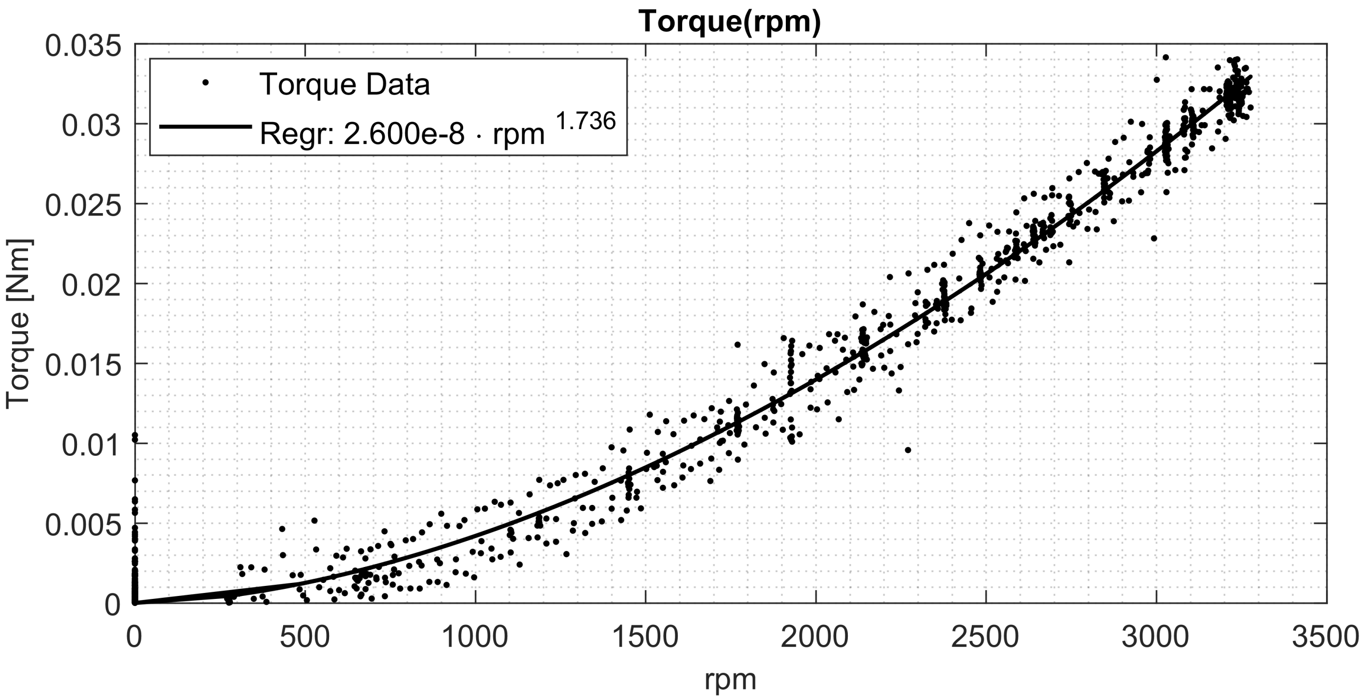

Figure 3.12: TAS-I Experimental results - Reference Torque.

In this case we don't have hysteresis like for the thrust but there is much more dispersion in raw data (every dot in the picture is a mean value of 100 samples).
The Torque-Speed correlation is:

$$M = 2.600 \cdot 10^{-8} \cdot n^{1.736} \tag{3.15}$$

The coefficient $2.600 \cdot 10^{-8}$ is proportional to $(\rho \cdot R^5 \cdot C_M)$.

It is evident the importance of having a benchmark, in fact we see an high divergence between our data and Maryland ones (Figure 3.13). A power coefficient equal to 2 was expected, like in Thrust results, but we got 1,736.

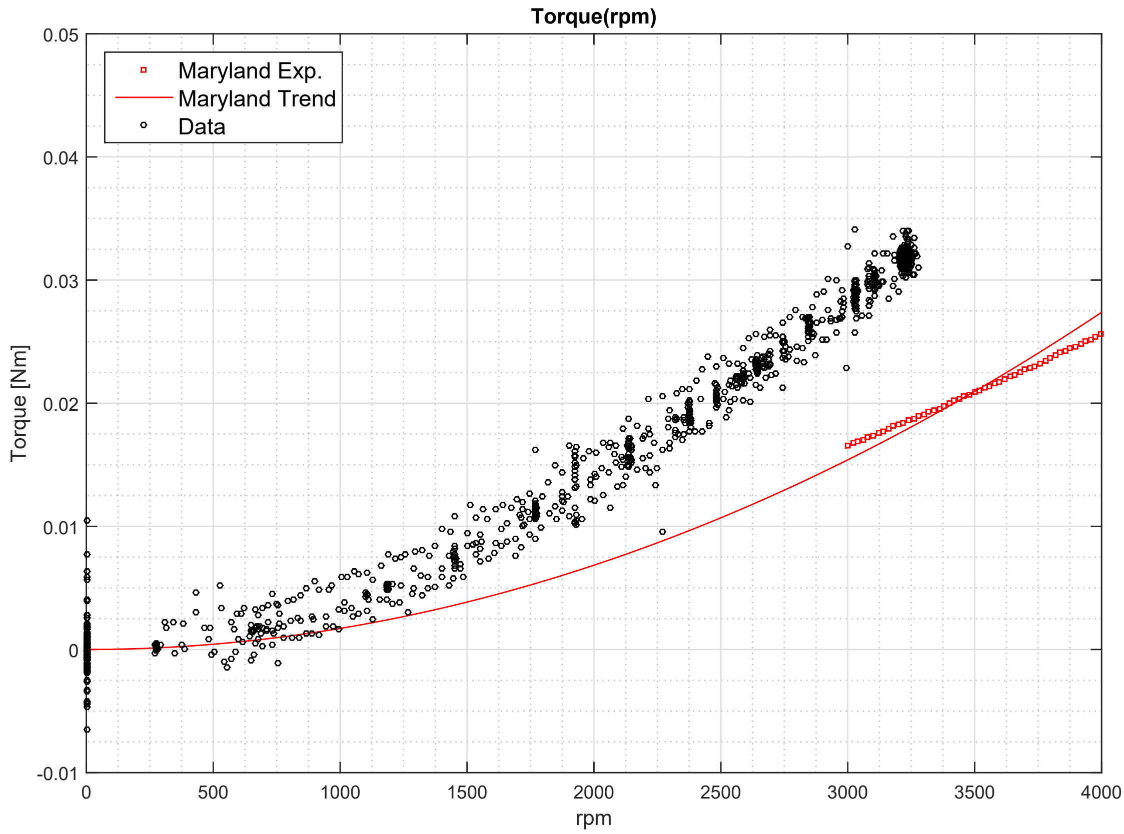

Figure 3.13: Torque comparison TAS-I vs Maryland.

Even in this case we assumed a constant C_M to represent Maryland results (Values 3.2).
It is clear that something went wrong during the acquisition of torque data. They are quite good at very low rpm and then there is a divergence increasing with rotational speed. A torque two times higher means a power two times higher as if our rotor, that is identical to the Maryland one, would need twice the power to produce the same thrust.

To investigate the source of the error and to develop a more reliable testing methodology a new test campaign is ongoing. Moreover we found out that the torsiometer *HBM T21WN (0.1 Nm)* was not vacuum certified.
In future torque data will be acquired separately from thrust data using a new torsiometer. For a lower resolution analysis, during thrust measurements, the motor drained current will be acquired and from the motor characteristics it will be possible to obtain torque results.

$$I = I_0 + \frac{1}{k_M} \cdot M \quad \rightarrow \quad M = k_M \cdot (I - I_0)$$

◇ Coefficients Results

In terms of coefficients the goodness of the thrust results are supported by a similar C_T compared to the Maryland one, while the Torque coefficient is about two times the Maryland one. Reference values were:

$$C_{T_{ref}} = 0.017693$$
$$C_{P_{ref}} = C_{M_{ref}} = 0.0047744$$

We obtained (Figure 3.14):

$$C_T = 0.017900$$
$$C_P = C_M = 0.0096818$$

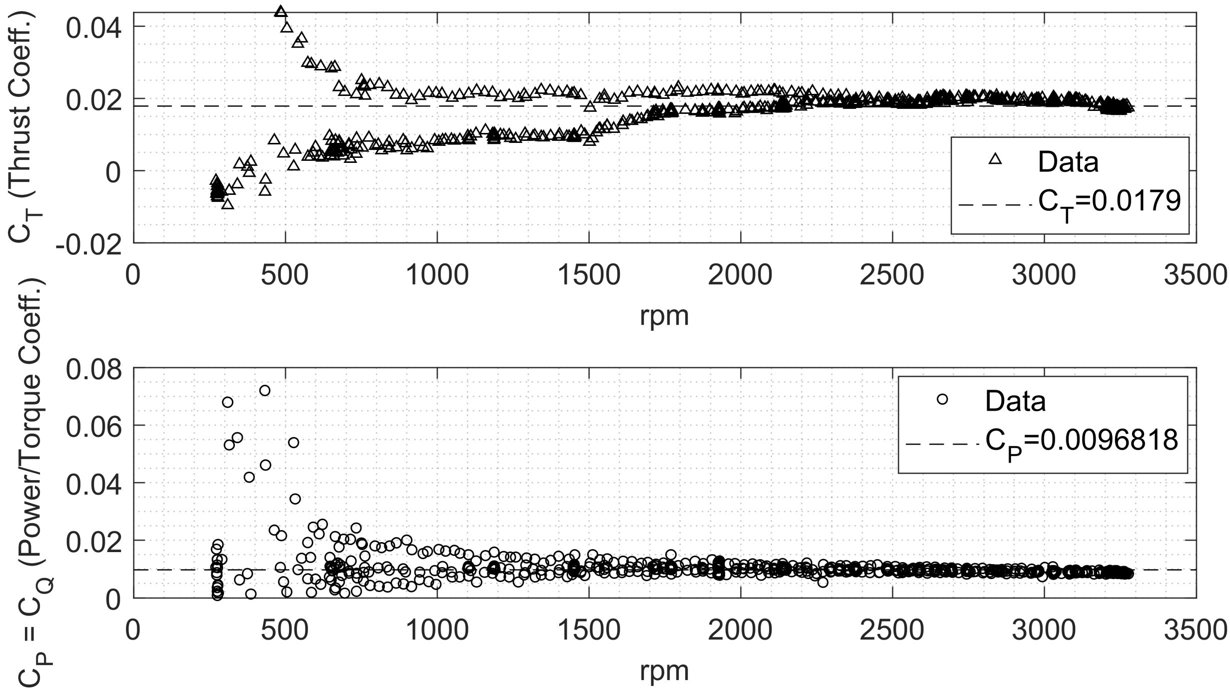

Figure 3.14: TAS-I Coefficients.

Coefficients tends to stabilize when increasing the rotational speed which means that **if the rotational speed is high enough one can assume C_T and C_M constant**. Since usually drone rotors spins faster than 3000 rpm this feature is very important and was used in the Preliminary Design Chapter.

Comparing our results with Maryland ones we have:

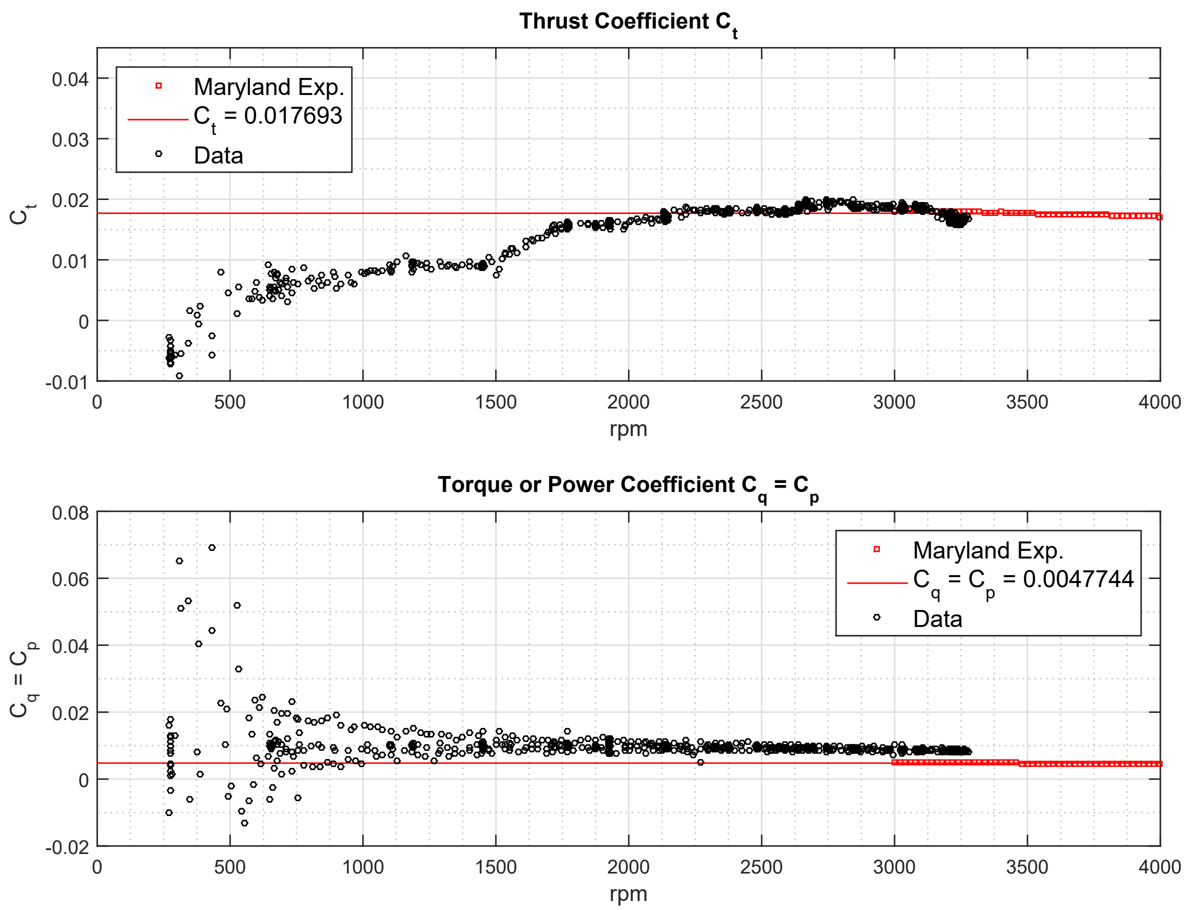

Figure 3.15: TAS-I vs Maryland Coefficients.

Here it is figuratively remarked that there is a very good agreement in C_T while the C_P, C_M is approximately twiced.
The Figure of Merit using our results is $FM = 0.1749$ while using the Maryland one is $FM_{ref} = 0.3486$ that is in good agreement with Figure 3.7.

Due to this non conformity in torque results (that are very important for the motor choice) and since this rotor has not been optimized for this peculiar case (very low Reynolds and high Mach number) it was decided to perform the preliminary design adopting a semi-optimized rotor [7].

"Semi-optimized" means that the airfoil used to obtain the blades is the same in shape span wise but the Reynolds number varies a lot moving from the root to the tip so a further step could be necessary in order to optimize the rotor.

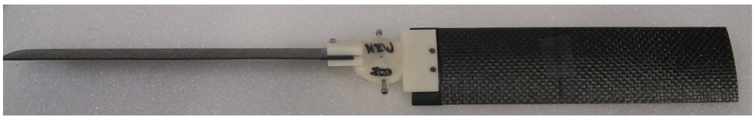

Figure 3.16: Maryland rotor [6].

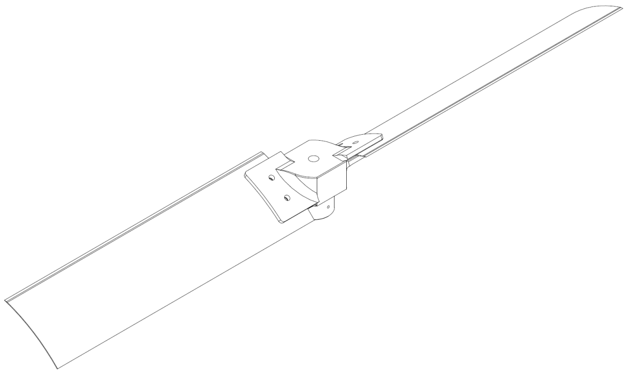

Figure 3.17: TAS-I rotor [8].

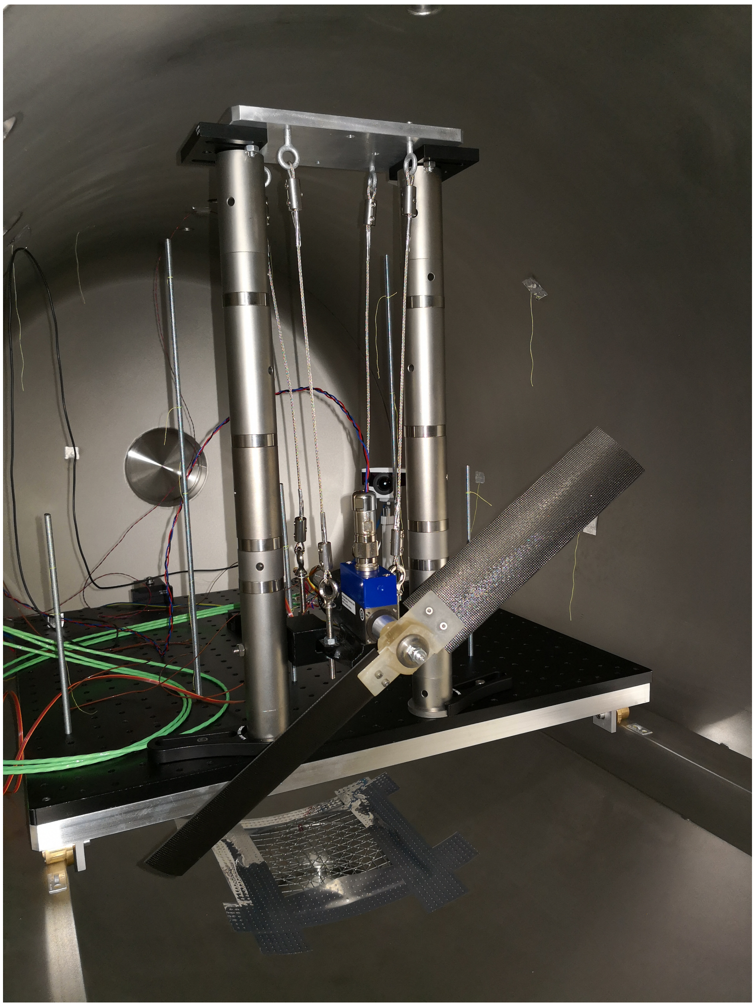

Figure 3.18: TAS-I test setup.

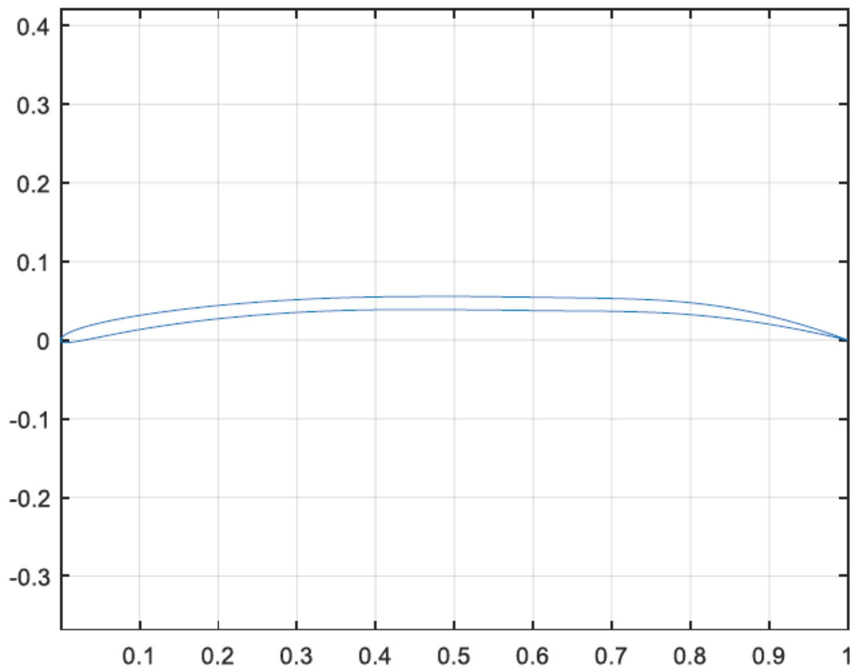

Figure 3.19: PoliTO Optimized airfoil [7].

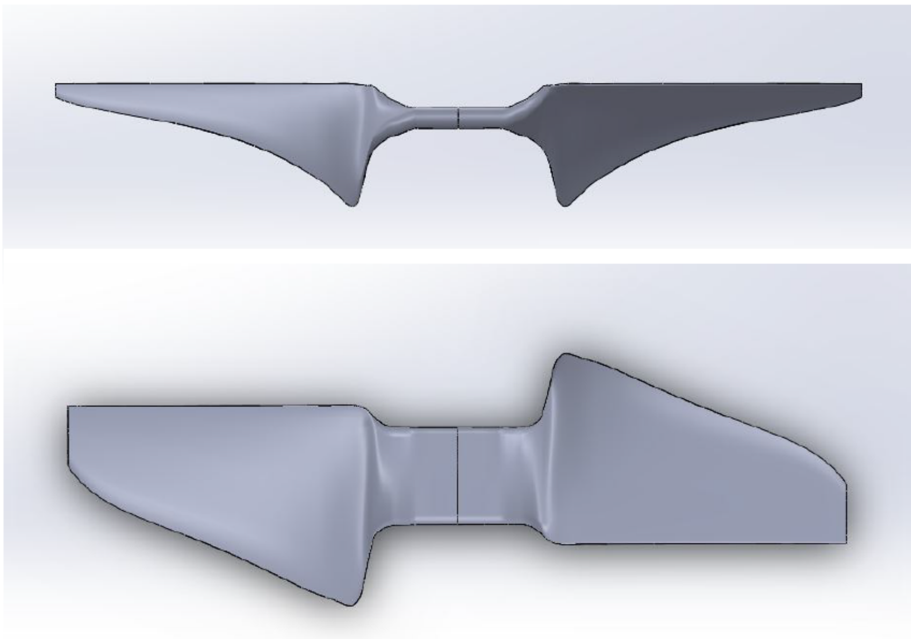

Figure 3.20: PoliTO Semi-optimized rotor [7].

3.4 Effect of density variation

Here we show the results of a test made at a lower density than the reference one, a situation that is worst in terms of required rotational speed. In fact with lower density, if we keep Ω constant assuming that C_T and C_M do not vary much (this is verified in Figure 3.14) we would have less thrust. To compensate we must rotate faster but this means a higher power consumption because:

$$\frac{T}{T_{ref}} = 1 = \frac{\rho}{\rho_{ref}} \cdot \left(\frac{\Omega}{\Omega_{ref}}\right)^2 \rightarrow \left(\frac{\Omega}{\Omega_{ref}}\right)^2 = \frac{\rho_{ref}}{\rho}$$

$$\frac{M}{M_{ref}} = \frac{\rho}{\rho_{ref}} \cdot \left(\frac{\Omega}{\Omega_{ref}}\right)^2 \rightarrow \frac{M}{M_{ref}} = 1$$

$$\rightarrow \frac{P}{P_{ref}} = \frac{M}{M_{ref}} \cdot \frac{\Omega}{\Omega_{ref}} = \frac{\rho}{\rho_{ref}} \cdot \left(\frac{\Omega}{\Omega_{ref}}\right)^2 \cdot \frac{\Omega}{\Omega_{ref}} = \sqrt{\frac{\rho_{ref}}{\rho}}$$

taking into account that:

- Reference test density $\rho = 0.01584 \ kg/m^3$
- Actual density $\rho = 0.01398 \ kg/m^3$
- $\rho/\rho_{ref} = 0.8824$ (12 % lower density)

the power consumption will be

$$\boldsymbol{P/P_{ref} = (0.01584/0.01398)^{1/2} = 6.5\% \ \text{higher.}}$$

In Figures 3.21 and 3.22 it is possible to observe this performance variation with density. To hover we need to rotate faster with the same torque and this means a higher output power which leads to a lower hovering time. To withstand this non-uniformity in power consumption the flight time was computed using only the maximum rotor power at nominal atmospheric density.

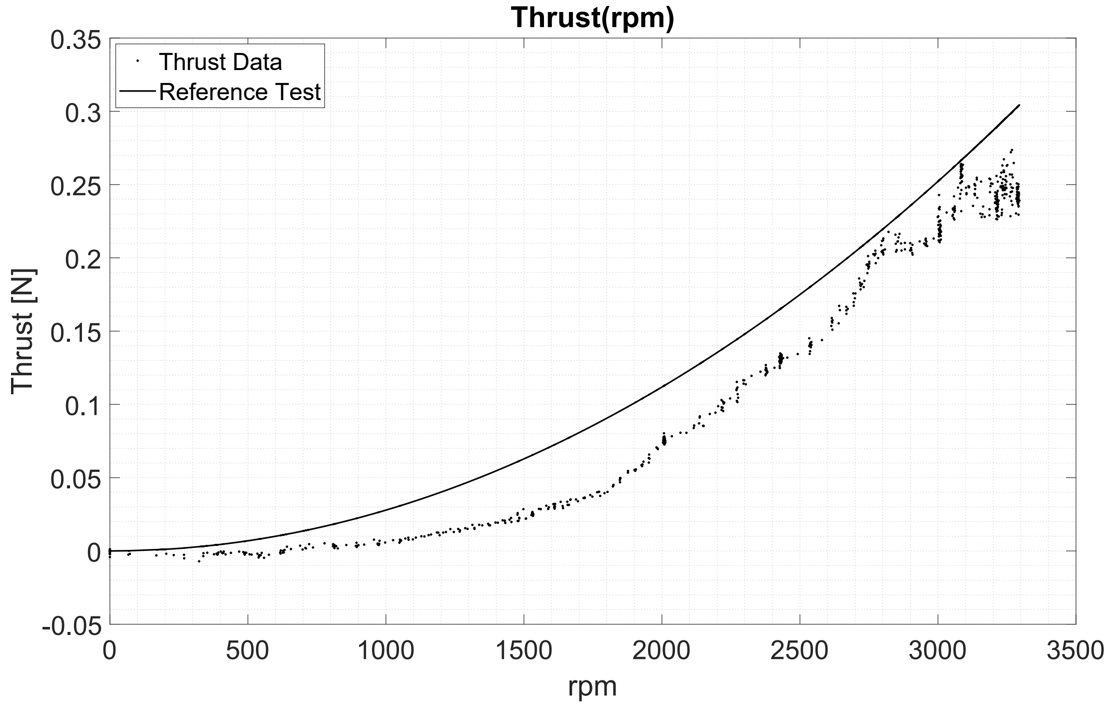

Figure 3.21: Thrust results - $\rho/\rho_{ref} = 0.8824$.

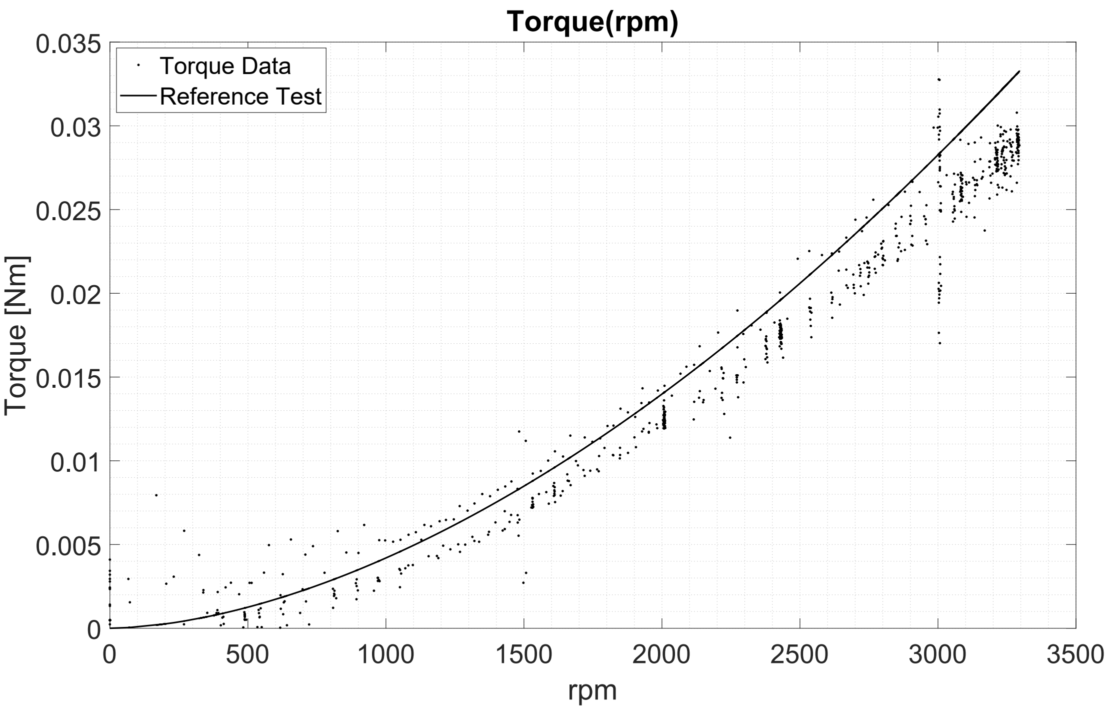

Figure 3.22: Torque results - $\rho/\rho_{ref} = 0.8824$.

3.5 Thermal behaviour

During the performance tests 4 thermocouples were mounted inside the PHASE vacuum chamber to acquire the temperature of:

- the air inside the chamber,
- the BLDC motor,
- the encoder,
- the load cell.

Forgetting about the load cell thermocouple that was placed in order to verify thrust thermal deviation (if thrust measurements were influenced by temperature), the others were helpful to show how fast the temperature of the components increase. During the reference test trends in Figure 3.23 were obtained:

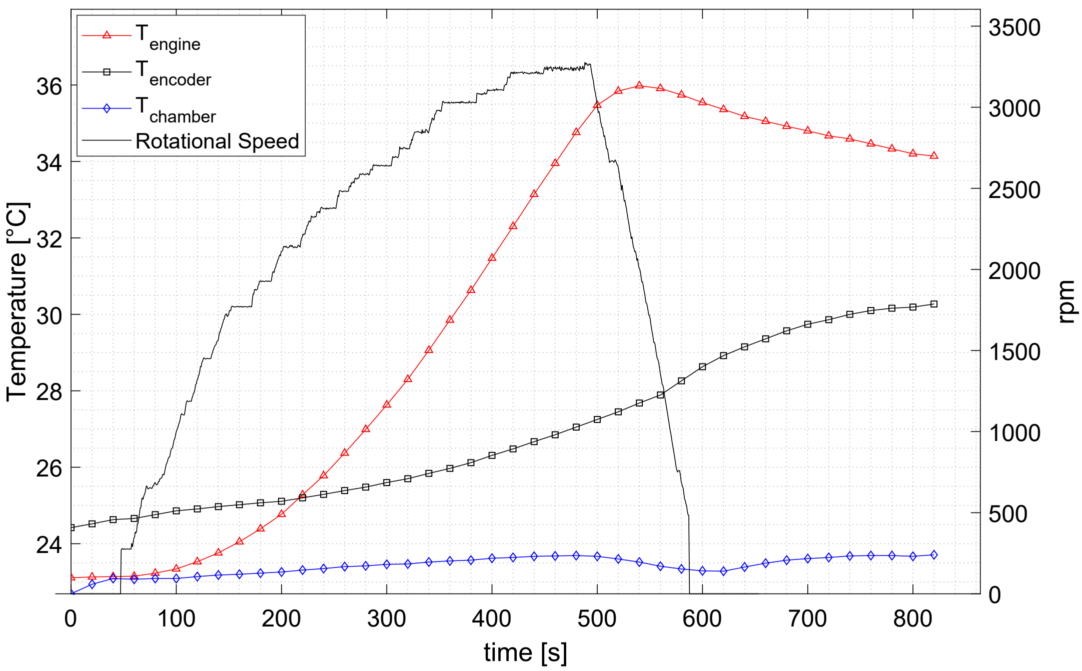

Figure 3.23: Thermal results - Reference test.

Figure 3.23 shows how fast the BLDC motor temperature increases while the air temperature is quite stable. This means that **only a little part of the thermal power from the motor is transferred to the air by convection.** It is important to quantify this effect because convection is the most important way to dissipate power in presence of a fluid motion over a hot surface. In background it's reported the rotational speed profile.
A test is planned to reach this target, meanwhile the convective heat transfer is evaluated with a function developed in MATLAB (Chapter 4).

The aforementioned test would have consisted of:

- Some step tests[1] at different but constant rotational speed with the normal setup, that is with motor directly cooled by air.
- A second phase at same speeds but with the motor insulated, to reduce the effect of convection.

The differences between two tests at the same speed would represent the effect of convection and we would be able to identify a mean heat transfer coefficient correlation. As already mentioned we were able to do only two thermal tests with the normal setup at 1200 and 3000 rpm. Unfortunately this gives only few information about the thermal behaviour. These tests results are shown in Figure 3.24 and Figure 3.25.

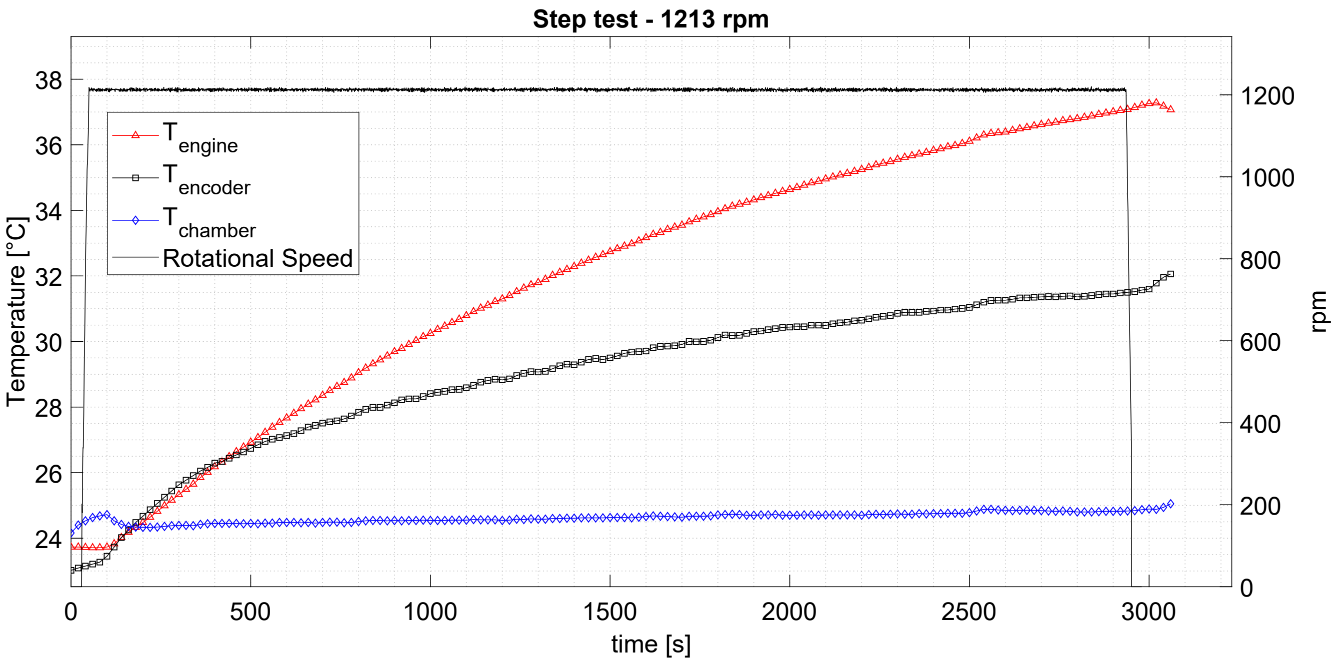

Figure 3.24: TAS-I Thermal results - Step test 1213 rpm.

[1]Step test means a test where the rotational speed of the rotor in achieved in a very short time with respect to the total duration of the test and this velocity is held constant till the end of the test.

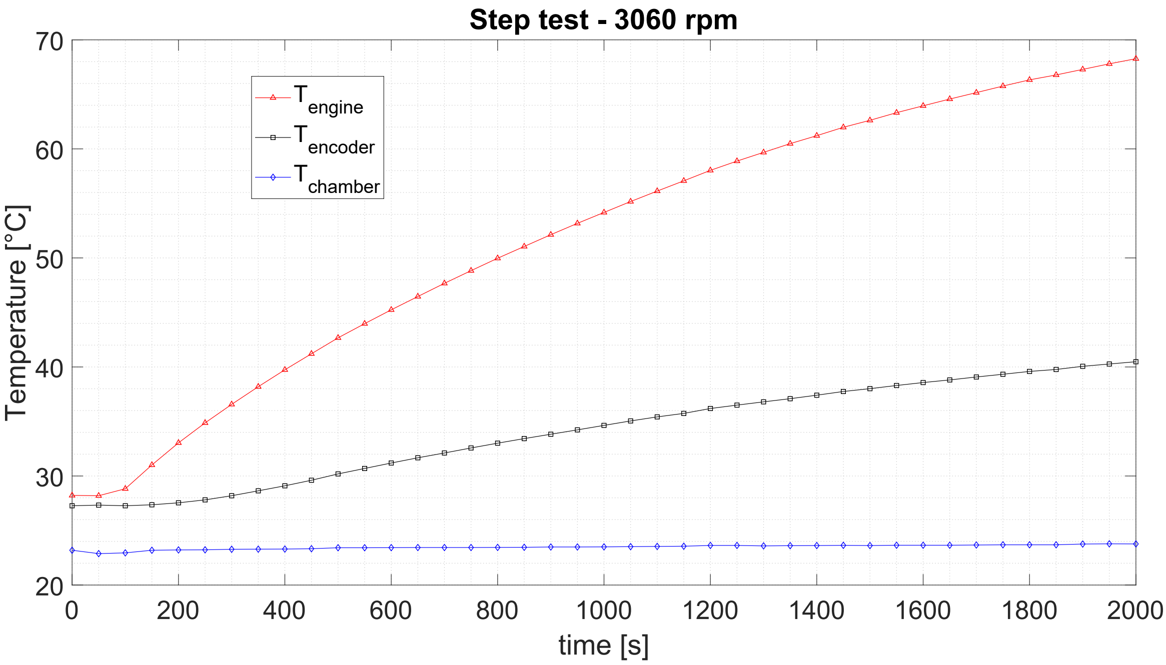

Figure 3.25: TAS-I Thermal results - Step test 3060 rpm.

In both cases (3.24 and 3.25) it is visible a first order system response in accordance to the equation that describes the diffusive heat transfer [9]

$$\rho c \frac{\partial T}{\partial t} = \nabla \cdot k \nabla T + \dot{q} \tag{3.16}$$

Here it is not included the effect of convection but since we deal with solid medium (BLDC motor) the term $\dot{q}$ can include the convection effect as well as radiation effect and internal heat sources.

The most important thing is that the external temperature does not increase too fast, in fact 2000 s correspond to a time of flight that the drone will never experience on Mars because of the battery energy limitation.
The manufacturer datasheet reports a maximum temperature limit for the external case so a simplified model could be used to predict this temperature and to discard a priori solutions that exceeds this limit.
The fact that the external case does not reach a critical temperature does not mean that the internal components will do the same, in fact the windings, that are the sources of the internal heating, could be hotter than the housing, so a more accurate analysis is needed (Chapter 6).

Chapter 4

First thermo-aerodynamic MATLAB model

The **MATLAB** preliminary **model** was used to simulate the motor thermal behaviour. This model takes into account the radiative heat transfer with a field of view (FoV) between motor surfaces and vacuum chamber walls always equal to 1 and natural/forced convection heat transfer as well as internal conductive heat transfer between the motor nodes. Forced convection heat transfer coefficient is computed from the actual rotational speed of the rotor. It is also possible to include the solar heat flux but this must be computed externally.
Validation of the model is presented in Section 4.2.

4.1 MATLAB model description

The MATLAB-based model was developed because there are too many unknowns both in the thermal data (such as single component thermal capacitance, geometry and thermal conductance) and in the aerodynamic field of motion.
This model allows to evaluate some of the most important parameters needed to describe and solve the Motor Lumped Parameter Thermal Network (LPTN) in Figure 4.1, such as convective heat transfer coefficient h, from TAS-I tests.
Only a few parameters are requested and the results are the temperature and the thermal balance of each motor node.
The required data are:

◇ ***INPUT data***:

1. Number of motor Nodes N (axially distributed),
2. Initial Temperature T_0 (if different from ambient temperature),
3. Ambient Temperature T_{amb} (boundary condition),
4. Rotor Diameter D_{prop},
5. **Rotor Performances Correlations Thrust T(n), Torque M(n).**
   From TAS-I tests:

$$T(n) = 2.692 \cdot 10^{-8} \cdot n^{2.005}$$
$$M(n) = 2.600 \cdot 10^{-8} \cdot n^{1.736}$$

In addition **it is necessary to specify the rotational speed profile n(t) and the relative time vector with the proper sample frequency, in this way it is possible to compute the instant power dissipation from the BLDC Motor equations and datasheet informations and the heat transfer coefficient from the Induced Axial Speed function.** The **simulation time and the time step are obtained from the mission profile.** If we want to simulate a time higher than the flight time we just need to set $n(t > t_{flight}) = 0$.

◇ ***BLDC Motor data***:

- **BLDC Motor Thermal Capacitance** (computed as $C = m_e \cdot c_{copper}$ where m_e is the engine mass and c_{copper} is the copper specific heat capacity),
- **BLDC Motor internal thermal conductivity $\boldsymbol{k_e}$** ($k_e = k_{steel}$),
- **BLDC Motor Emittance $\boldsymbol{\epsilon}$**,
- **BLDC Motor Solar Absorptance $\boldsymbol{\alpha_S}$**,
- BLDC Motor Diameter D,

- BLDC Motor Length L,
- Maximum allowable temperature T_{max},
- Minimum allowable temperature T_{min},
- No-load current I_0,
- Torque constant k_M,
- Velocity constant k_V,
- Slope of n-M curve dn/dM.

The four motor data in bold are not known from datasheet so they are assumed from experience provided by TAS-I. The emittance and absorptance are obtained from metal optical properties table choosing the proper material and surface finish (or texture) similar to the motor ones.

Motor thermal capacitance can be also and more properly approximated as $C_{motor} \approx \tau_{motor} \cdot GL_{motor-air}$ if τ_{motor} (τ = time constant) is known (GL motor-air is always given for Earth standard conditions). Sometimes datasheets only report $\tau_{winding}$ and $\tau_{housing}$. In this case it is possible to compute thermal capacitance in this way:

$$C_{winding} \approx \tau_{winding} \cdot GL_{winding-housing} \tag{4.1}$$

$$C_{housing} \approx \tau_{housing} \cdot \frac{1}{\frac{1}{GL_{housing-air}} + \frac{1}{GL_{winding-housing}}} \tag{4.2}$$

It is possible to operate in this way because, for a single two node system composed by motor and air we have:

$$\begin{aligned} & C\frac{dT}{dt} = GL \cdot (T_B - T) + Q \\ \text{Laplace transf.} \quad \rightarrow \quad & Cs\tilde{T} - CT_0(=0) = GL \cdot \tilde{T_B} - GL \cdot \tilde{T} + \tilde{Q} \\ & \tilde{T} = \frac{\tilde{Q}}{sC + GL} + \frac{\tilde{T_B} \cdot GL}{sC + GL} \\ & \tilde{T} = \tilde{Q} \cdot \frac{1/GL(=\mu)}{1 + s \cdot C/GL(=\tau)} + \tilde{T_B} \quad (T_B \text{ supposed to be constant}) \end{aligned}$$

where μ is the "gain" and can be intended as a thermal resistance [K/W], GL=$1/\mu$ is the thermal conductance [W/K], τ is the thermal time constant [s] and Q is the dissipated power [W]. (Example:
-Data: m=140 g, $\tau_w = 7$ s, $\tau_h = 693$ s, $GL_{w-h} = 0.833$ W/K, $GL_{h-a} = 0.0833$ W/K.
-Results: $C_w = 5.83$ J/K, $C_h = 52.48$ J/K, $C_{tot} = 58.31$ J/K.
-Approximation: $C_{approx} = 0.140 \cdot 380 = 53.2$ J/K, $\Delta = 8.76$ %).

Changing these parameters means to change the motor, so it is simple to test different products.

◇ ***Environmental data***:

- External heat sources if known Q_{ext} (default =0),
- Density ρ,
- Pressure p,
- Speed of sound a,
- Dynamic viscosity μ,
- Air/CO_2 thermal conductivity k_{ext},
- Gravitational Acceleration g,
- Prandtl Number Pr.

Changing these parameters allow us to switch between Earth and Mars conditions and from cold to hot cases.

MOTOR THERMAL NETWORK:

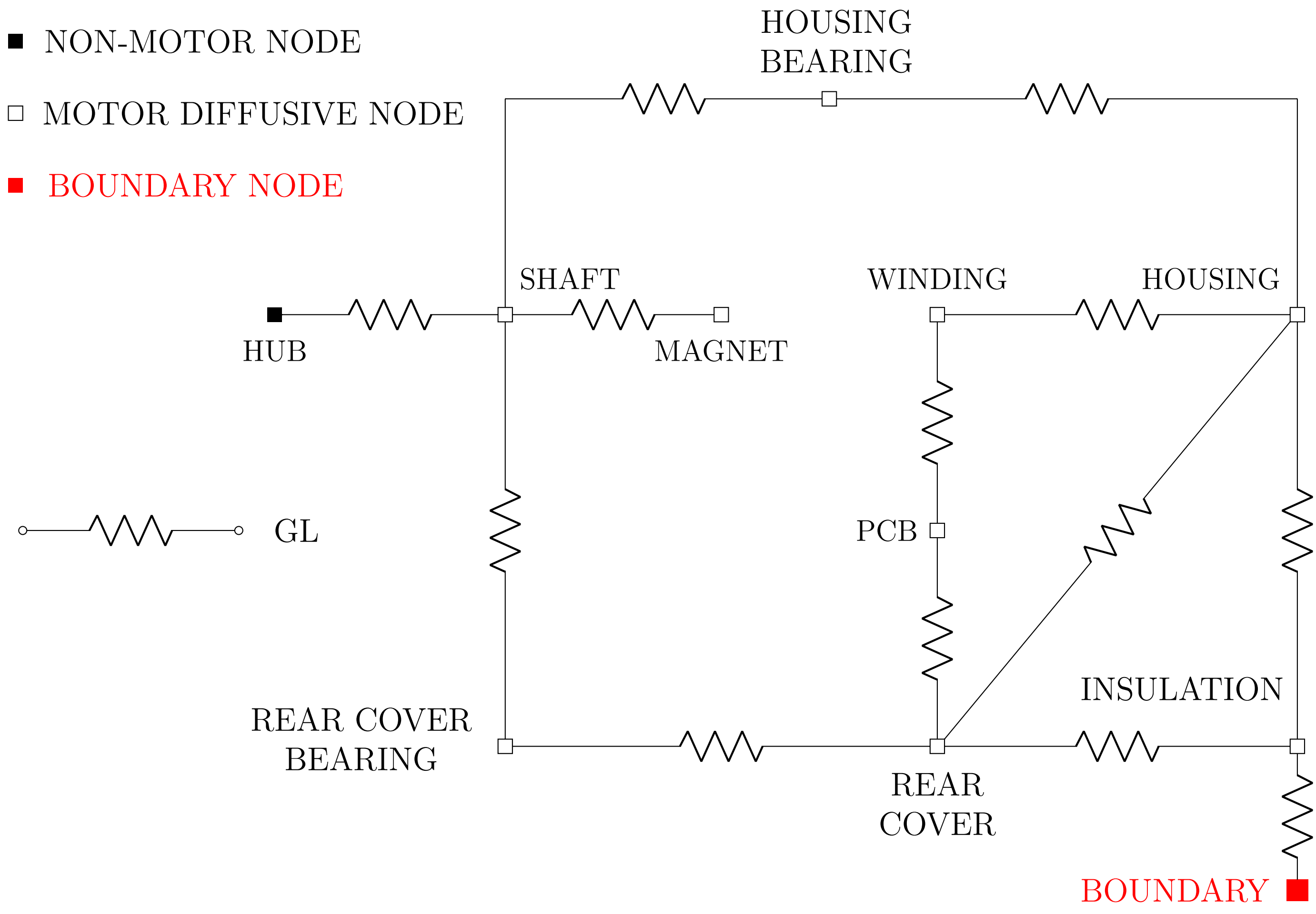

Figure 4.1: Motor Lumped Parameter Thermal Network.

How the code works

Receiving in input all the information about rotor, motor and environment the code builds all the necessary matrices to run the simulation. Some of them can be computed at the beginning of the simulation and remain always constant, some others must be computed step by step in the time march function. Here all the operations are explained in detail.

◇ PRE-PROCESSING

The code initializes the temperatures matrix and builds the surfaces vector A, the thermal capacitances vector C, the internal conductances matrix $[K] \neq [K](t)$ and writes a reminder file of the initial conditions.

The initialized temperature matrix T is zero everywhere except in the first line where:

$$T_i = T_0 \quad \text{, for i=1,...,N-1 if initial temperature is controlled.} \tag{4.3}$$
$$T_i = T_{amb} \quad \text{, for i=1,...,N-1 if initial temperature is not controlled.} \tag{4.4}$$
$$T_N = T_{amb} \quad \text{The last column contains the boundary node temperature.} \tag{4.5}$$

The surfaces vector A is:

$$A_{1\&N-1} = \frac{\pi D^2}{4} + \pi D L_{1,N-1} \quad \text{, for the first and last motor node.} \tag{4.6}$$
$$A_i = \pi D L_i \quad \text{, for } 2 \leq i \leq N-2 \text{ (inner nodes).} \tag{4.7}$$

The thermal capacitance vector C is:

$$C_i = C_{engine} \cdot \frac{V_i}{V_{tot}} = C_{engine} \cdot \frac{L_i}{L} \quad \text{, for i=1,...,N-1.} \tag{4.8}$$
$$C_N = Inf \quad \text{, for i=N. Boundary node has C=}\infty. \tag{4.9}$$

The internal thermal conductances matrix is (for $1 < i < N-1$):

$$K_{i,j} = k_{eng} \cdot \frac{\pi D^2/4}{dx_i} \quad \text{, for } j = i-1:2:i+1 \tag{4.10}$$
$$K_{i,2} = k_{eng} \cdot \frac{\pi D^2/4}{dx_i} \quad \text{, if } i = 1 \tag{4.11}$$
$$K_{i,N-2} = k_{eng} \cdot \frac{\pi D^2/4}{dx_i} \quad \text{, if } i = N-1 \tag{4.12}$$

where dx_i is the distance between nodes i and $i+1$.

[K] matrix has non-zero elements on its $+1, -1$ diagonals except in the last row and column. [K] is shown in Figure 4.2. This happens because there is only an axial discretization so each node is in contact only with the upper and the lower one. The last motor node (N-1) is not connected to the last one (N), that is boundary, by conduction, this explains why the last row and column are empty.

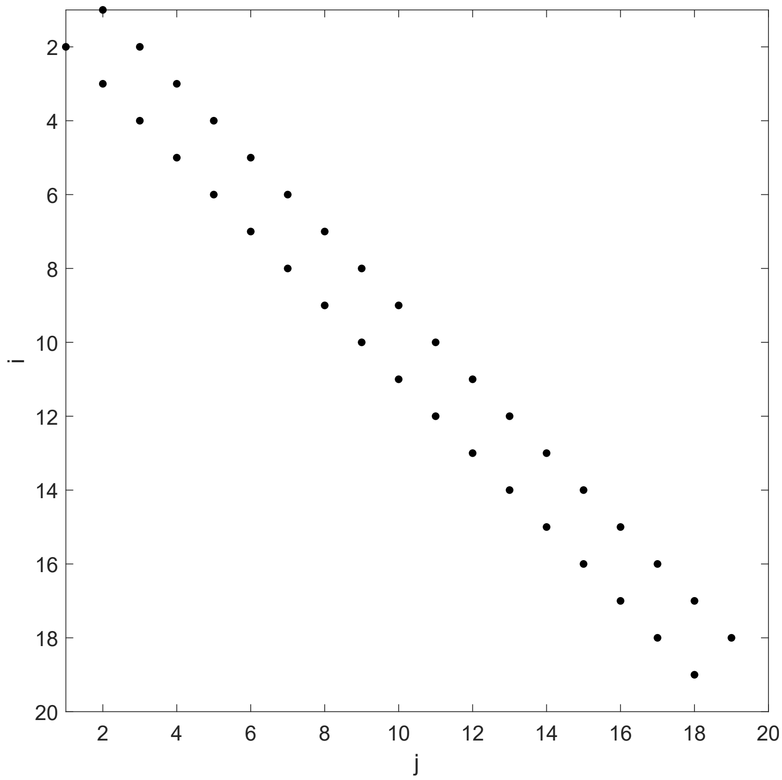

Figure 4.2: [K]-matrix for N=20.

◇ TIME MARCH

The actual time dependent solution is computed with this function. It basically needs the rotational speed of the rotor and its geometry informations, the performance characteristics and the motor datasheet constants. With these parameters it is possible to evaluate the heat transfer factor h in both forced or natural convection through the IAS function that will be described in a dedicated paragraph.

The first step is to compute the rotor Thrust and Torque from the characteristic equations:

$$T = 2.692 \cdot 10^{-8} \cdot n^{2.005} \quad [N] \tag{4.13}$$

$$M = 2.600 \cdot 10^{-5} \cdot n^{1.736} \quad [mNm] \tag{4.14}$$

then through the IAS function it is possible to evaluate the rotor induced air velocity which cools down the motor.
◇ **If this velocity is equal to 0** the heat transfer coefficient is evaluated using the **NATURAL CONVECTION** equations,
◇ **if this velocity is NOT equal to 0** the heat transfer coefficient is evaluated using the **FORCED CONVECTION** Nusselt-based correlations.

1. **Natural Convection** [12]
   Here are reported the steps followed to calculate the natural convection heat transfer coefficient (*this procedure works for every gas because its effect is included in Gr and Nu numbers*):

$$\nu = \frac{\mu}{\rho} \qquad \text{cinematic viscosity} \tag{4.15}$$

$$\overline{T_e} = \frac{1}{N-1} \cdot \sum_{i=1}^{N-1} T_i \qquad \text{motor averaged temperature} \tag{4.16}$$

$$T_m = \frac{1}{2}(\overline{T_e} + T_{amb}) \tag{4.17}$$

$$\beta = \frac{1}{T_m} \qquad \text{isobaric coefficient of thermal expansion} \tag{4.18}$$

$$Gr_L = \frac{g\beta(\overline{T_e} - T_{amb})L^3}{\nu^2} \qquad \text{Grashof number} \tag{4.19}$$

$$\overline{Nu} = \frac{4}{3} \cdot \left[\frac{7Gr_L Pr^2}{5(20+21Pr)}\right]^{\frac{1}{4}} + \frac{4(272+315Pr)L}{35(64+63Pr)D} \qquad [13],[14] \tag{4.20}$$

$$\overline{h_i} = \frac{Nu \cdot k}{D} \qquad \text{i=1,...,N-1} \tag{4.21}$$

$$\overline{h_N} = 0; \tag{4.22}$$

   The Nusselt number equation (4.20) is evaluated with the Le Fevre & Ede correlation [12],[13],[14], obtained through an integral solution of the boundary layer equation, because it is in good accordance with experimental results (Figure 4.3) for aspect ratio L/D equal to the one of all the BLDC Motors found. The most common motors aspect ratio varies between $2 \div 4$.

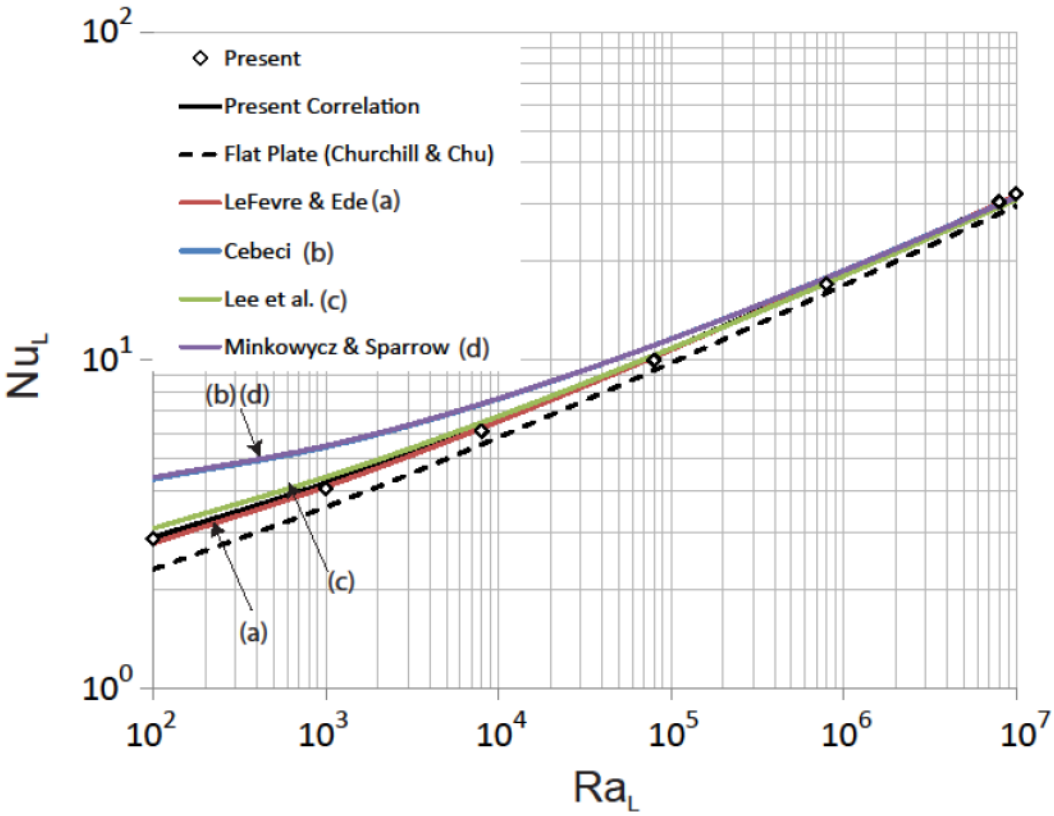

Figure 4.3: Le Fevre & Ede correlation vs experimental data for AR=2 [15].

2. **Forced Convection**
   For axial velocity greater than 0 the following steps are followed:

$$Re_D = \frac{\rho D V_i}{\mu} \quad V_i = \text{induced axial velocity} \tag{4.23}$$

$$\overline{Nu} = Corr_l \cdot 0.134 \cdot Re_D^{0.668} \quad \text{if laminar flow [16]} \tag{4.24}$$

$$\overline{Nu} = Corr_t \cdot 0.155 \cdot Re_D^{0.674} \quad \text{if turbulent flow [16]} \tag{4.25}$$

$$\overline{h_i} = \frac{Nu \cdot k}{D} \qquad \text{i=1,...,N-1} \tag{4.26}$$

$$\overline{h_N} = 0; \tag{4.27}$$

where $Corr_l$ and $Corr_t$ are corrections for laminar and turbulent field of motion obtained from thermal step tests (*in air*) in Figure 3.24, 3.25. Their importance is shown in Figures 4.4, 4.5 and Figures 4.6, 4.7.

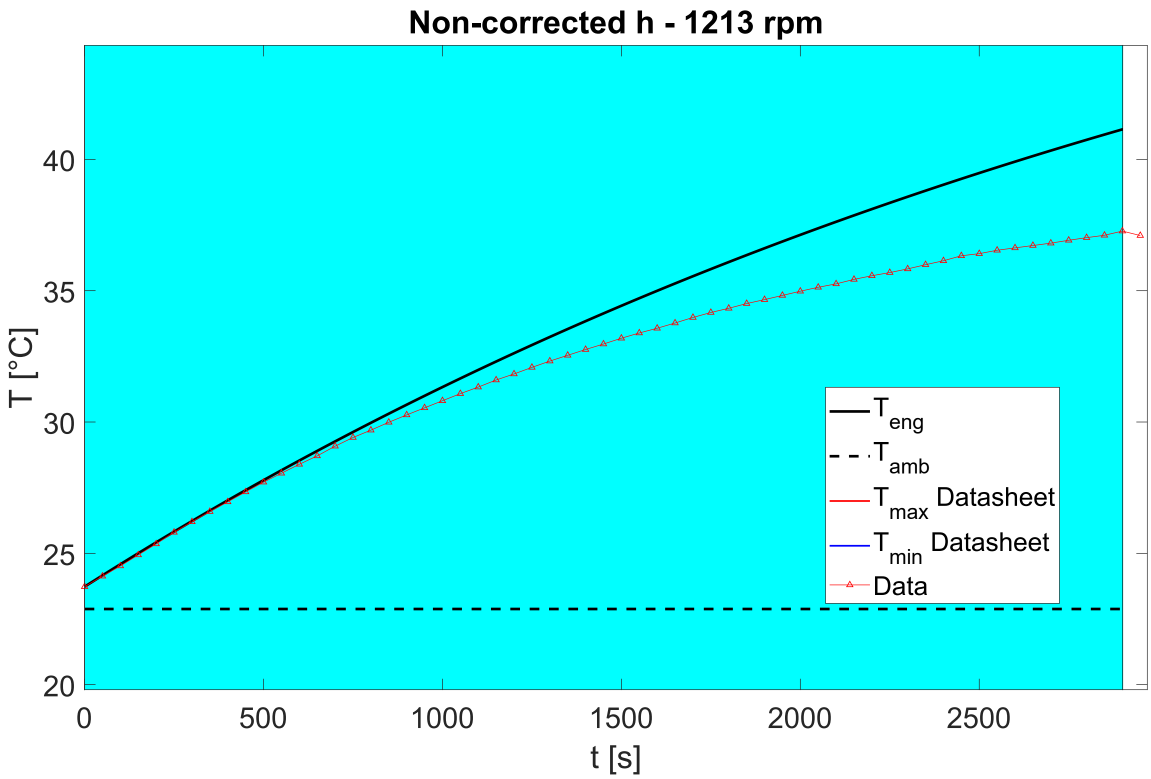

Figure 4.4: Model prediction without corrections for $\Omega = 1213$ rpm.

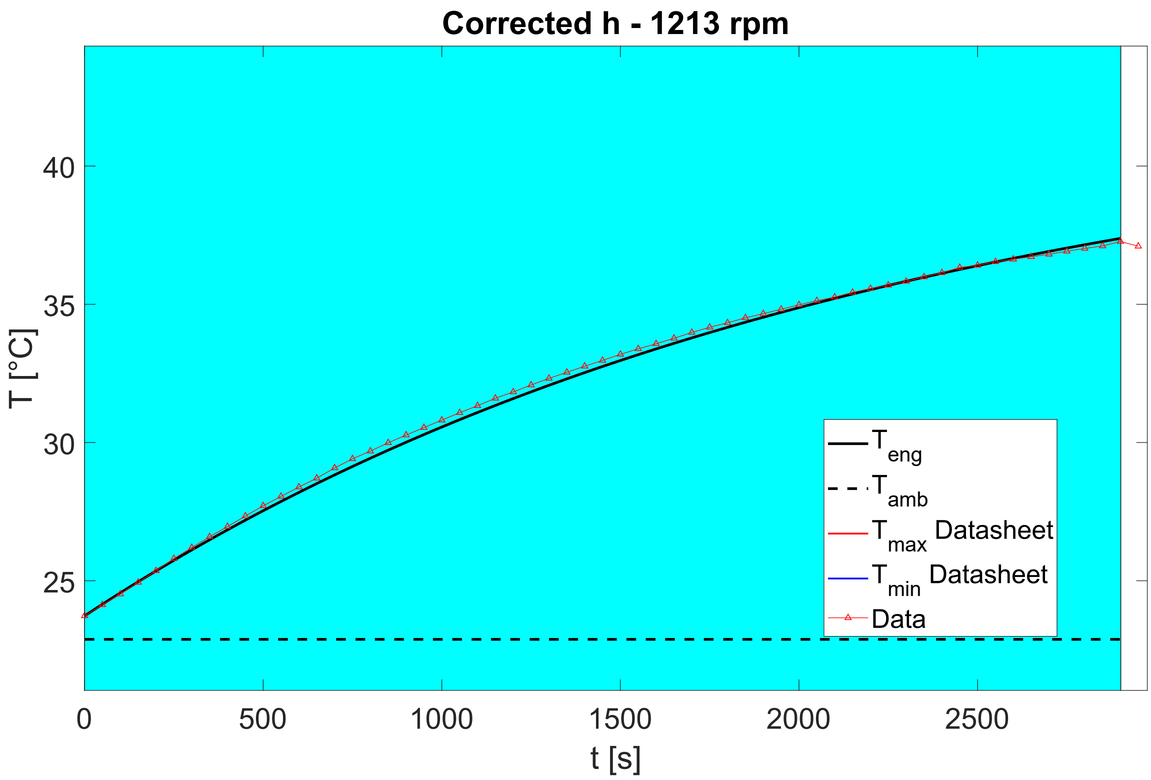

Figure 4.5: Model predictions with corrections for $\Omega = 1213$ rpm.

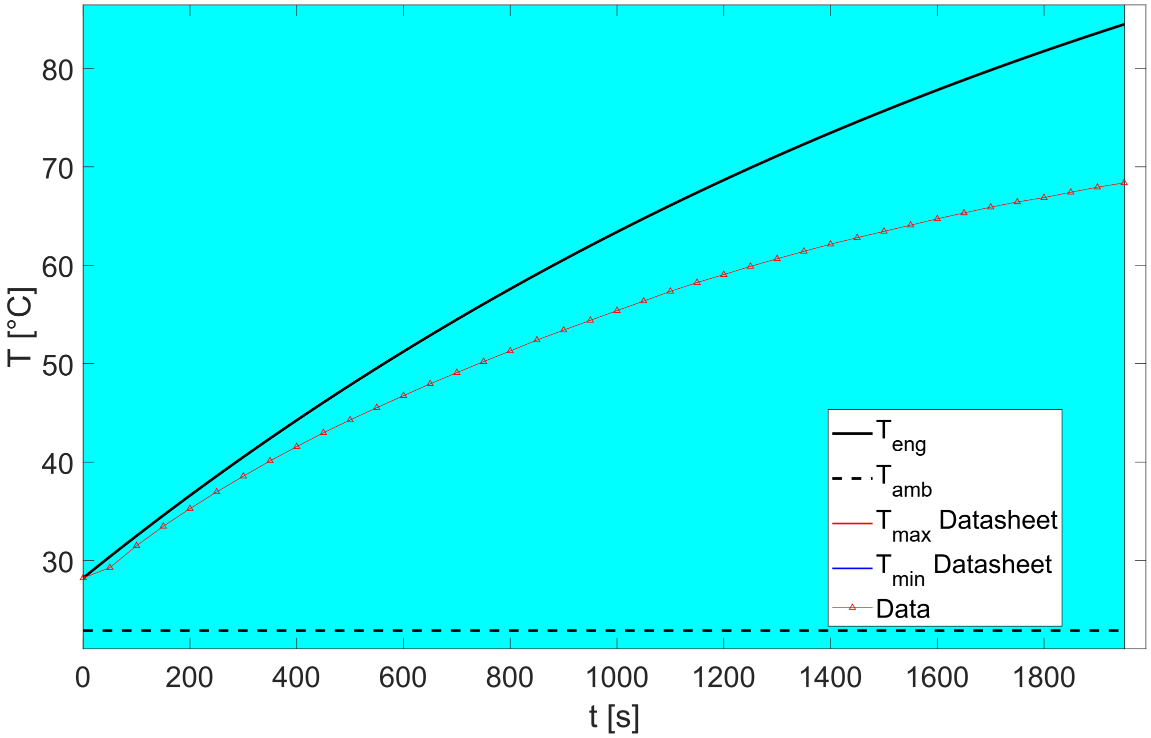

Figure 4.6: Model prediction without corrections for $\Omega = 3060$ rpm.

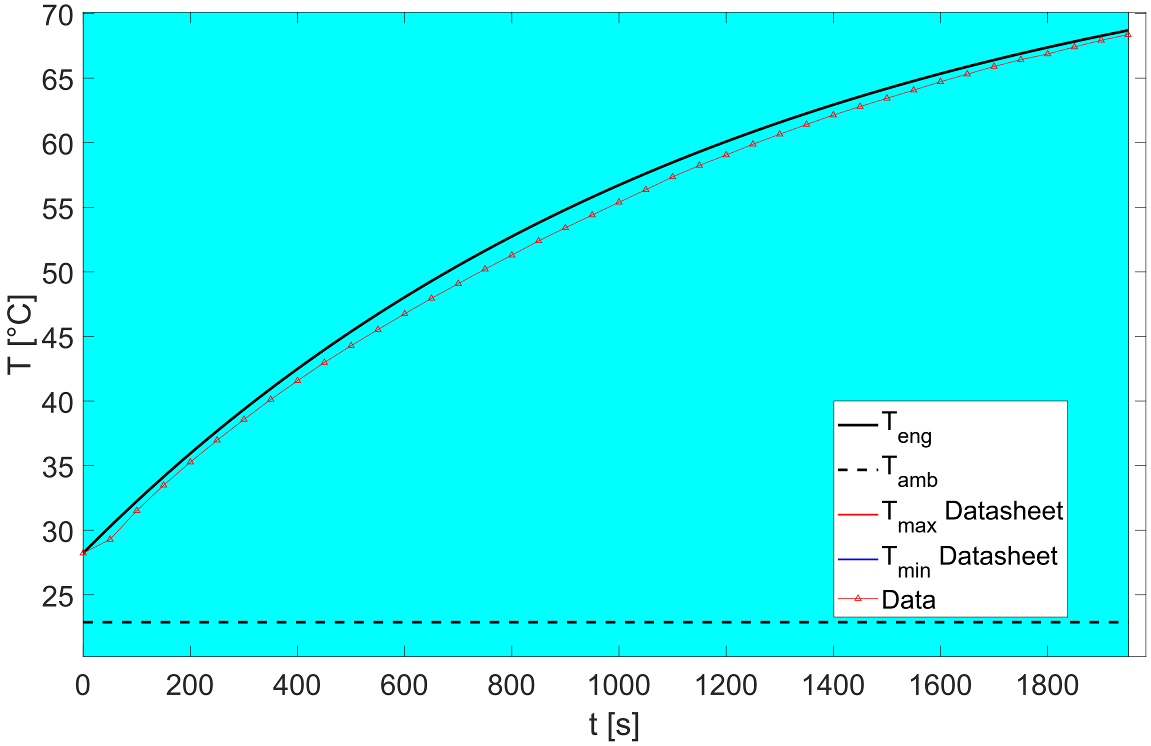

Figure 4.7: Model prediction with corrections for $\Omega = 3060$ rpm.

The correction coefficients are linear with rotational speed and expressed as:

$$Corr_l(n) = 1.8671629 + 2.7071 \cdot 10^{-5} \cdot n \tag{4.28}$$

$$Corr_t(n) = 1.636875 + 1.08284 \cdot 10^{-5} \cdot n \tag{4.29}$$

Their variation with rotational speed is here shown:

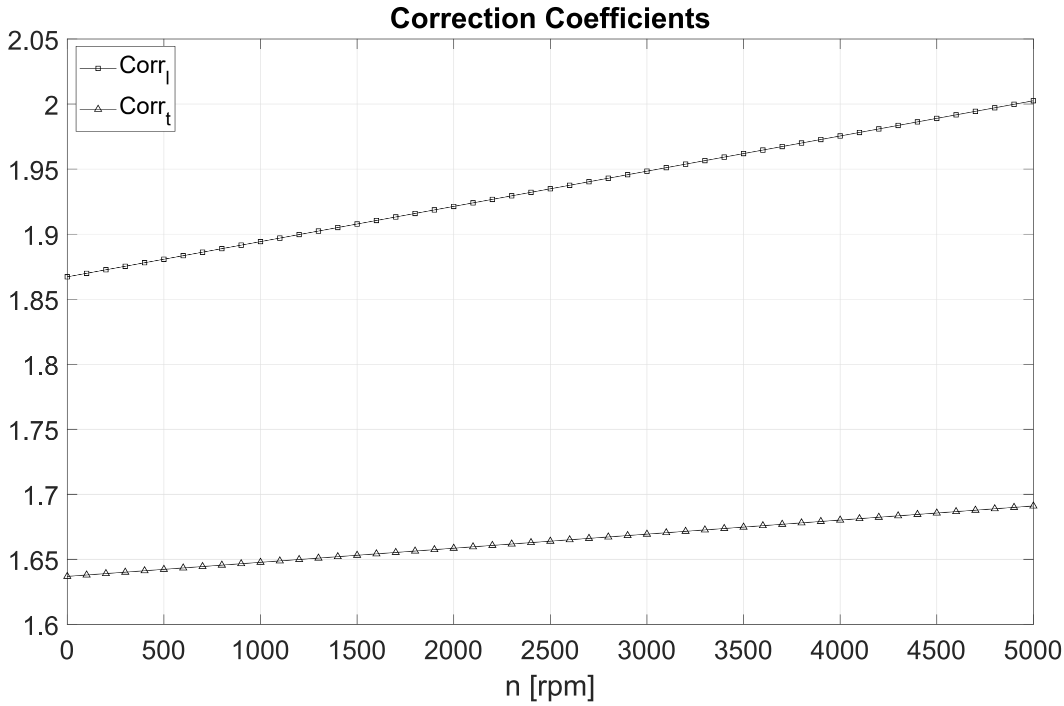

Figure 4.8: Correction coefficients for both laminar and turbulent field of motion.

It is mandatory to introduce these corrections because the induced axial velocity is calculated with the *"optimized rotor hypothesis"* and because in literature no correlations about such a low Reynolds number ($\sim 100 \div 1000$) and geometry were found. In fact the correlations in equations 4.24 and 4.25 are obtained for a cylinder in axial laminar or turbulent flow with no rotors or objects in front of it and for standard atmosphere which means a much higher Reynolds number ($\sim 10^4 \div 10^5$).
Strictly speaking these correction are true only for air and for our test setup geometry.

It would be very interesting and important for future planetary missions to deeply investigate the effect of convection for this kind of geometries (e.g. vertical cylinder and similar) in different density, gas composition and Reynolds conditions.

Once evaluated the heat transfer coefficient h the time march function computes the dissipated power for each node:

$$P_{prop} = M \cdot \Omega = \frac{M}{1000} \cdot \frac{\pi n}{30} \quad \text{Rotor power} \tag{4.30}$$

$$I = I_0 + \frac{1}{k_M} \cdot M \quad \text{Motor current} \tag{4.31}$$

$$V_s = \frac{1}{k_V}\left(n + \frac{dn}{dM}M\right) \quad \text{Motor voltage} \tag{4.32}$$

$$Q_e = V_s \cdot I - P_{prop} \quad \text{Motor dissipated power} \tag{4.33}$$

$$Q_{in} = Q_e + Q_{ext} \quad \text{Total input power} \tag{4.34}$$

$$Q_i = \frac{Q_{in}}{N-1} \quad \text{i=1,...,N-1 dissipated power for each node} \tag{4.35}$$

$$Q_N = 0 \tag{4.36}$$

At this point all the necessary informations are available and it is possible to carry out the time march with the **Eulero method**.

$$T_i^{(k+1)} = T_i^{(k)} + \frac{\Delta t}{C_i}\left(KT_i^{(k)} - \dot{q}_{c_i}^{(k)} - \dot{q}_{r_i}^{(k)} + Q_i^{(k)}\right) \quad \text{i=1,...,N-1} \tag{4.37}$$

where:

- $T_i^{(k+1)}$ is the new temperature for the i-th node [K]
- $T_i^{(k)}$ is the old temperature of the i-th node [K]
- Δt is the time step [s]
- C_i is the i-th node thermal capacitance [J/K]
- $KT_i^{(k)} = \sum_{j \neq i} K_{ij}(T_j - T_i)$ is the conductive power flux [W]
- $\dot{q}_{c_i}^{(k)} = h^{(k)}A(T_i^{(k)} - T_{amb})$ is the convective power flux [W]
- $\dot{q}_{r_i}^{(k)} = \epsilon\sigma A(T_i^{4^{(k)}} - T_{amb}^4) \cdot FoV$ is the radiative power flux [W]
- $Q_i^{(k)}$ is the internal power [W]

Repeating this cycle for each time step the thermal time history is obtained.

◇ IAS FUNCTION

In order to determine the **induced axial speed (IAS)** at the rotor disc height the ***Vortex Theory*** ([17], [22]) for the **optimum rotor** were used. The TAS-I rotor used during tests (Figure 3.17) was not an optimized rotor, the latter should be much similar to that in Figure 3.20. This choice was done in order to make the model much robust, fast and easy to use because **it does not need any geometry input file** of the actual rotor but it supposes to simulate a setup with optimized blades. The only parameter requested is the rotor diameter. With this assumption we do not need a CFD analysis to correlate the induced axial speed with the rotational speed of the rotor and, waiting for the actual rotor that will be used for the drone, lots of different motors can be thermically simulated with a cooling velocity that is the same for all the motors and it is supposed to be similar to the one predicted by this model.

The hypothesis of the vortex theory are: ideal fluid, high inflow rotor and constant density. The first and the latter ones are not properly satisfied because

$$Re \sim 7000, \quad M_{tip} \approx \frac{\Omega R}{a} = \frac{\pi \cdot 4000 \cdot 0.3}{30 \cdot 232{,}26} = 0.54$$

but most of the analytical models are based on these hypothesis or, if not, they are too complex to be used for the purpose of this function.
The governing laws for vorticity in the Vortex Theory are:

- Helmholtz Theorems
- Kelvin Theorem
- Kutta-Joukowski Theorem
- Vorticity Equation
- Biot-Savart Law

Historically N. E. Joukowski laid the foundations for Vortex Theory from 1912 to 1929. He investigated the induced velocity due to the helical wake system of a propeller, but had to use the infinite blade model because of the mathematical complexities. The results of momentum theory were duplicated using the vortex theory and actuator disk analysis. In 1918, Joukowski proposed the use of airfoil characteristics for a cascade of two-dimensional airfoils with the induced velocity taken from vortex theory. This approach essentially gave the elements of modern blade element theory since the cascade effect is negligible for helicopter rotors.
In 1919, A. Betz [21] analysed the vortex system of the propeller wake in detail, determining the minimum power and best thrust distribution by vortex theory. In an appendix to Betz's paper, **L. Prandtl gave an approximate correction for the tip effect on the thrust distribution of a rotor with a finite number of blades; this correction is used in the IAS function.**
The Betz' work was extended by H. Glauert in 1934 for rotors with any kind of load

condition, and this is possible introducing the Glauert loading parameter G [22].

Through the use of these theories it is possible to compute the optimum circulation $\Gamma(r)$ on the blades (lowest power to archive a given thrust) and then the induced axial velocity v_i which is the result we are looking for.
In the Glauert's Vortex Theory [22] for an infinite number of blades the optimum circulation for the **hovering condition** is given by

$$\overline{\Gamma}(r) = \frac{\Gamma(r)}{2\pi\Omega R^2 G^2} = \overline{\omega}\frac{r^2}{R^2G^2} = \overline{\omega}\tilde{r}^2 \tag{4.38}$$

where:

$$\Gamma(r) \quad \rightarrow \quad \text{Optimum circulation distribution} \tag{4.39}$$
$$r \quad \rightarrow \quad \text{radial coordinate} \tag{4.40}$$
$$\omega \quad \rightarrow \quad \text{wake rotational speed} \tag{4.41}$$
$$G \quad \rightarrow \quad \text{Glauert loading parameter} \tag{4.42}$$
$$\tilde{r} = \frac{r}{RG} \tag{4.43}$$
$$\theta = cos^{-1}\left(\frac{\tilde{r}^6 + 3\tilde{r}^4 + 3\tilde{r}^2 - 1}{\tilde{r}^6 + 4\tilde{r}^4 + 3\tilde{r}^2 + 1}\right) \tag{4.44}$$
$$\overline{\omega} = \frac{\omega}{\Omega} = \frac{6}{5 + \tilde{r}^2 + 2(1 + \tilde{r}^2)cos(\theta/3)} \tag{4.45}$$

Since G is not known at first iteration it is possible to assume a little first try value << 1 (for example G=0.0001) and to compute the total thrust. If the residual $T_{expected} - T_{computed} > 0$, G is increased until $T_{expected} = T_{computed}$, where $T_{expected}$ is the thrust calculated with equation 4.13. This is possible because G is a monotone function for high inflow rotors.
Guessing a value for G leads to the determination of v_0 which is the axial speed at which the wake seems to move with reference to the rotor disc.

In fact, for the hovering condition:

$$\overline{\omega}(G) = \frac{2v_0^2}{(\Omega r)^2 + v_0^2} \tag{4.46}$$

and, inversely:

$$v_0(G) = \Omega r\sqrt{\frac{\overline{\omega}(G)}{2 - \overline{\omega}(G)}} \tag{4.47}$$

The Glauert's second approximation to momentum theory implies that the induced flow at the rotor disk is parallel to the local thrust vector, so the inflow angle ϕ **in hovering condition** is:

$$\phi = tan^{-1}\left(\frac{v_0}{\Omega r}\right) \tag{4.48}$$

At this point it is necessary to introduce the **corrections for the finite number of blades N and tip losses** (Prandtl).
The *corrective Prandtl Factor F(r)* is [21]:

$$F(r) = \frac{2}{\pi}cos^{-1}\left(e^{\frac{N}{2}\frac{r-R}{r\phi}}\right) \tag{4.49}$$

Finally from equation 4.38 and Prandtl's correction:

$$\overline{\Gamma}_{corr}(r) = F(r) \cdot \overline{\omega}\tilde{r}^2 \tag{4.50}$$

Once calculated both G and v_0 it is possible to compute the tangential velocity at disc rotor $u(r)$

$$u(r) = \frac{\Gamma_{corr}}{2\pi r} = \frac{\overline{\Gamma}_{corr} \cdot 2\pi\Omega R^2 G^2}{2\pi r} \tag{4.51}$$

and, at the end, the elemental thrust is given by [22],[24]:

$$dT = 2\pi\rho\left[\left(\Omega r - \frac{u}{2}\right)ur\right]dr = 2\pi\rho\left[\left(\Omega - \frac{\omega}{2}\right)\omega r^3\right]dr \tag{4.52}$$

which can be rewritten in the form (from eq. 4.51 and eq. 4.52)

$$dT_{N=2} = 2\pi\rho\left(\Omega r - \frac{\overline{\Gamma}_{corr}\Omega R^2 G^2}{2r}\right) \cdot \overline{\Gamma}_{corr}\Omega R^2 G^2 dr \tag{4.53}$$

The total thrust, or $T_{computed}$ to be compared with $T_{expected} = T(n)$ is:

$$T = N \cdot \int_0^R dT_{N=2}(r)dr \tag{4.54}$$

When $T_{computed} = T_{expected}$ the value of $v_i(r)$ will be the induced axial velocity we were looking for, computed as follows:

$$v_i(r) = \frac{1}{2}\sqrt{\frac{\Gamma_{corr}(r) \cdot \Omega}{\pi}} \tag{4.55}$$

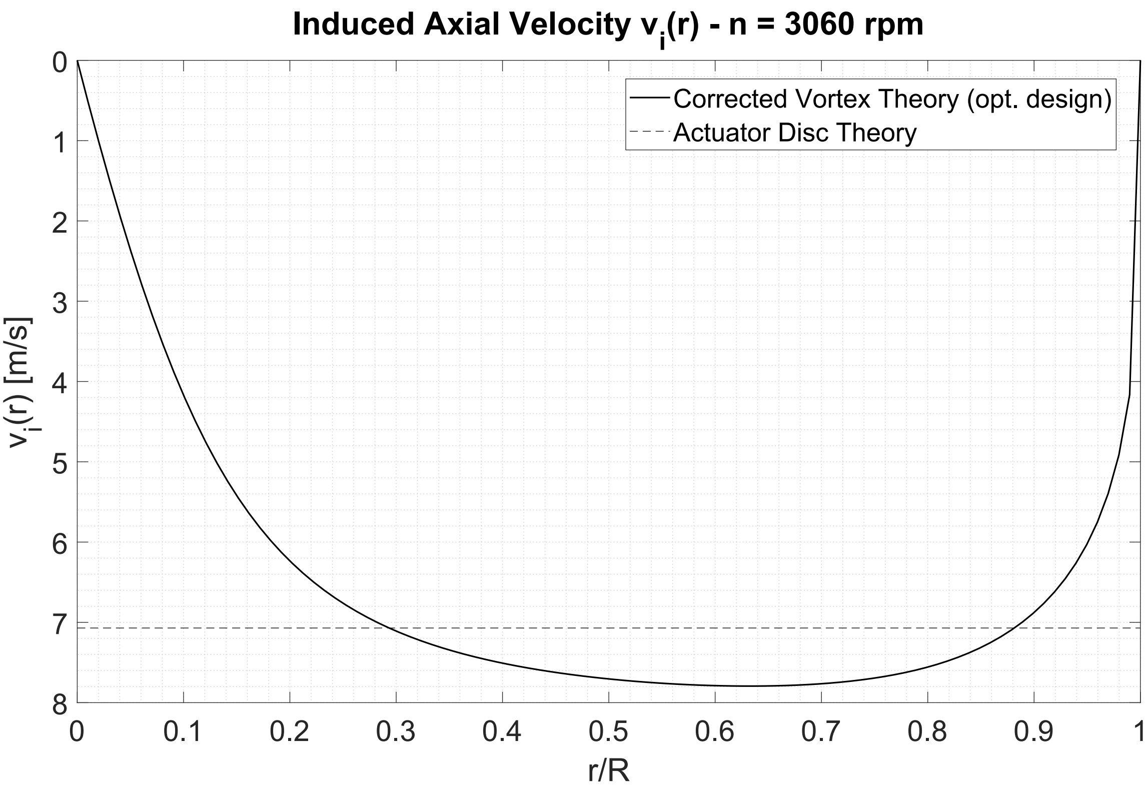

Figure 4.9: Example of induced axial velocity for n=3060 rpm.

The induced axial speed at reference test rotational speed ($\Omega = 3060$ rpm) is shown in Figure 4.9.

For 0.3 < r/R < 0.9 the vertical induced axial speed v_i assumes a value of about 7÷8 m/s which is consistent with the CFD detailed analysis performed in TAS-I.

A detailed design is therefore impossible to perform without a complex thermo-aerodynamic model, but for a preliminary MATLAB analysis the mean v_i value between 0 < r/R < 0.3 gives an adequate approximation for the convective heat transfer through Equations 4.24, 4.25.

4.2 MATLAB model validation

Through the *"optimized rotor hypothesis"* and the use of corrections in equations 4.28 and 4.29 it is possible to simulate a non-constant rotational speed profile such as the reference tests.
To validate the model the reference test in figure 3.23 was simulated in MATLAB with its rotational speed profile. The result is:

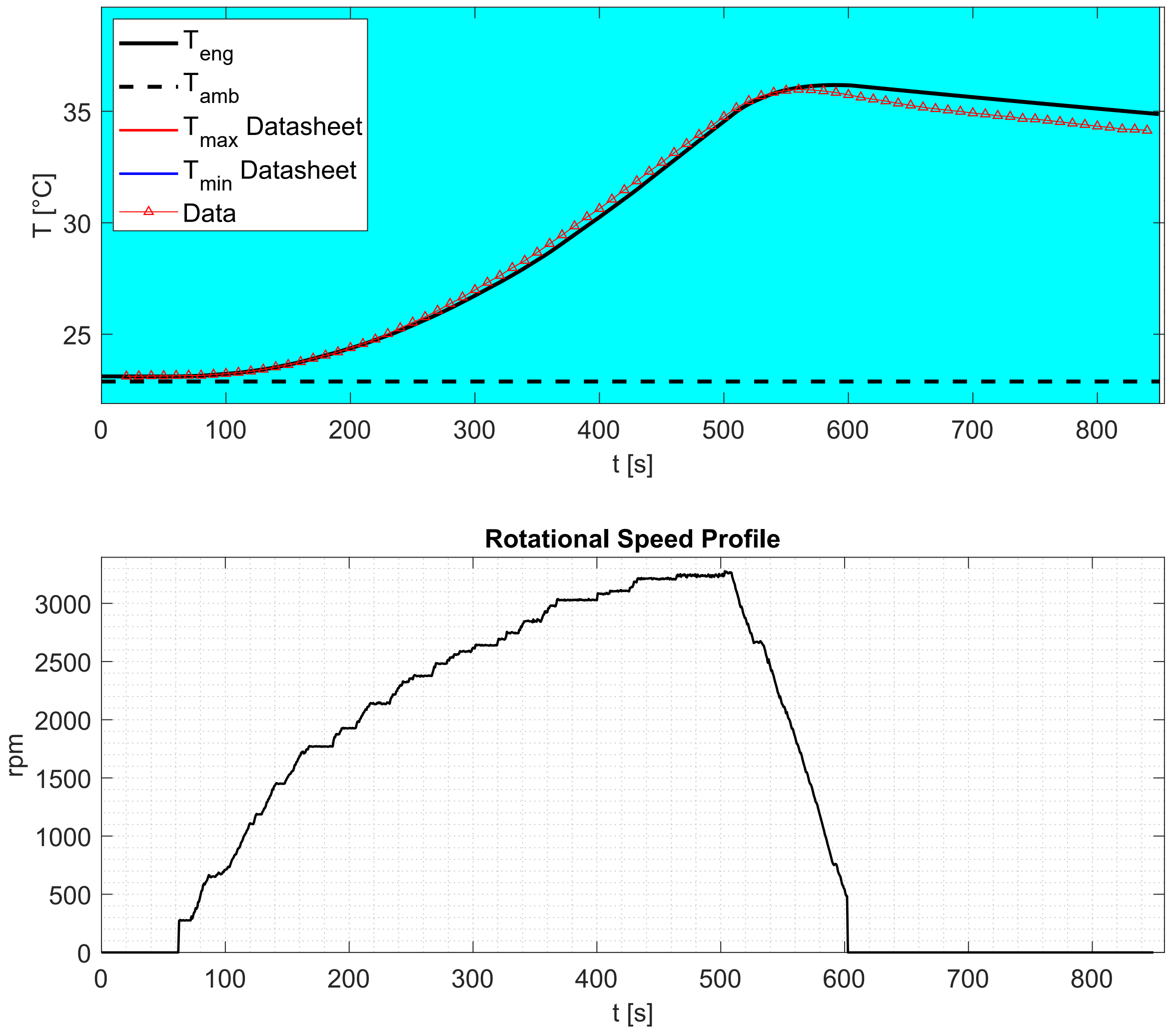

Figure 4.10: Validation of the MATLAB model with the reference test data.

The maximum ΔT between experimental data and model results is +0.21758 °C.

Looking at Figure 4.10 it is possible to state that ***the MATLAB model is a good tool to simulate the motor thermal behaviour in TAS-I PHASE vacuum chamber.***
Changing the atmospheric conditions and the velocity profile it is possible to study an hypothetical operation in Mars' atmosphere.

Since no data are available in order to obtain new correction coefficients for the averaged Nusselt number correlations and then for the forced convection heat transfer coefficient, the same values obtained for the TAS-I tests will be used in the Martian CO_2 MATLAB thermal model.

In Figure 4.11 is reported the convective averaged heat transfer coefficient.

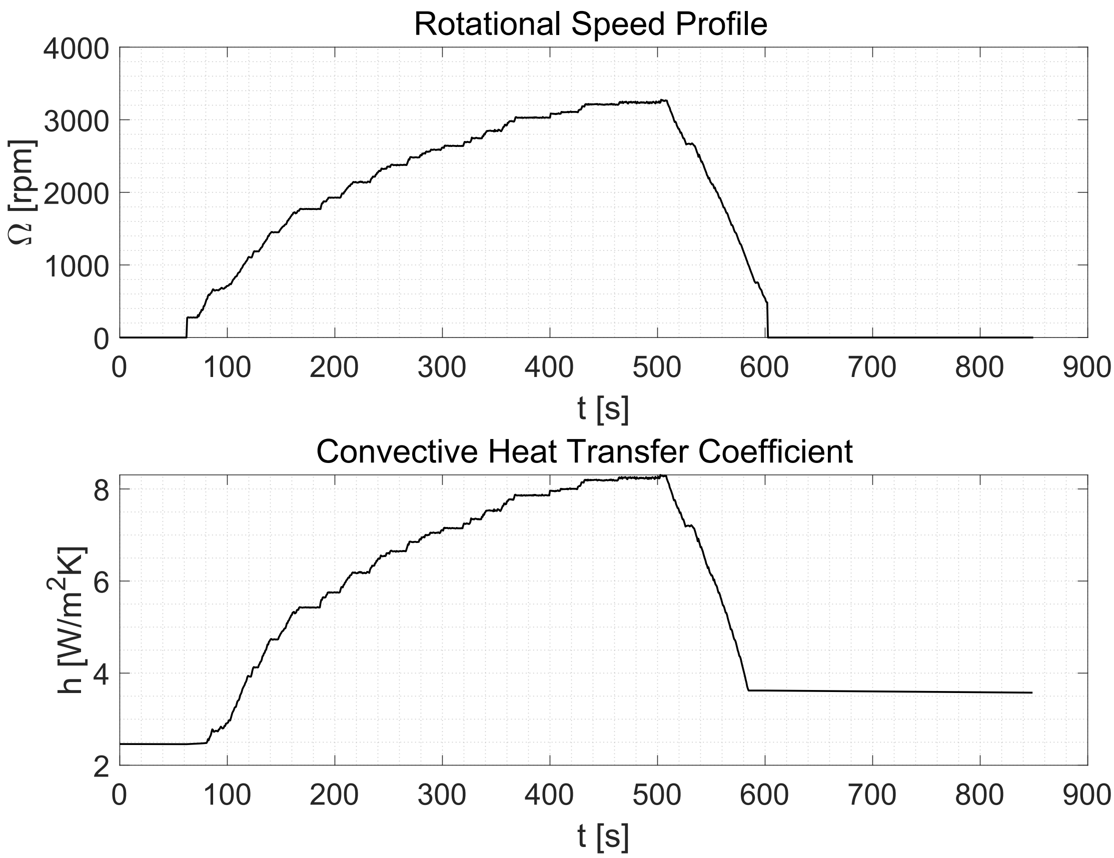

Figure 4.11: Convective heat transfer coefficient h.

The maximum computed forced convection heat transfer coefficient for the reference test is $h = 8.31\ W/m^2K$ at the highest Ω while the maximum natural convection heat transfer coefficient is $h = 3.62\ W/m^2K$ and it is higher than the initial value $h = 2.46\ W/m^2K$ because at the end of the simulation the motor temperature has increased. On Mars lower values are achieved.

4.3 Thermal sensitivity

An analysis very useful to understand which physical phenomena affect the results is the *Sensitivity Analysis*.
The procedure of the analysis consists of generating the set of nominal results and then to produce N new sets, each one with one input parameter modified.

In our case we were interested in motor temperature variations with time and thermal heat fluxes (radiative heat flux and convective heat flux) so the input parameters, for a given geometry, were:

- Environmental characteristics (cold case and hot case),
- Motor thermal capacitance C,
- Motor optical coating (ϵ and α),
- Motor efficiency η (power dissipation),
- IAS cooling effect h.

The MATLAB model validated for the air environment at Martian density conditions, updated for CO_2, was used and the above mentioned parameters were changed as follows:

1. Nominal values - COLD CASE,
2. Nominal values - HOT CASE,
3. Motor thermal capacitance C $\pm 10\%$,
4. Optical coating emissivity ϵ $\pm 10\%$,
5. Optical coating absorptance α $\pm 10\%$,
6. Power dissipation (efficiency) Q_{in} $\pm 10\%$,
7. IAS cooling effect, h $\pm 10\%$,
8. WORST CASE, defined by previous analyses.

The determination of HOT and COLD cases were performed with LMD tool which receives in input the coordinates of the location (latitude and longitude) and the day of interest (in our case LS=244, just before the Mars' perihelion LS=251 and the winter solstice LS=270), and gives back the environmental parameters. Possible scenery were identified by ESA. The environmental analysis was done to design the EDM (Entry, Descent & landing Demonstrator Module) of Mars 2020.

1. CASE 1: COLD CASE

Cold case is represented by these environmental characteristics:

- $T_{amb} = -93.65$ [°C], Ambient Temperature
- $T_{ground} = -98.64$ [°C], Ground Temperature
- $T_{sky} = -144.00$ [°C], Sky Temperature
- $Q_s = 0$ [W/m^2], Solar Flux

Temperatures and solar flux vary during a Sol (Martian day) but, to be conservative in terms of coldest environment, minimum values are used. Results are:

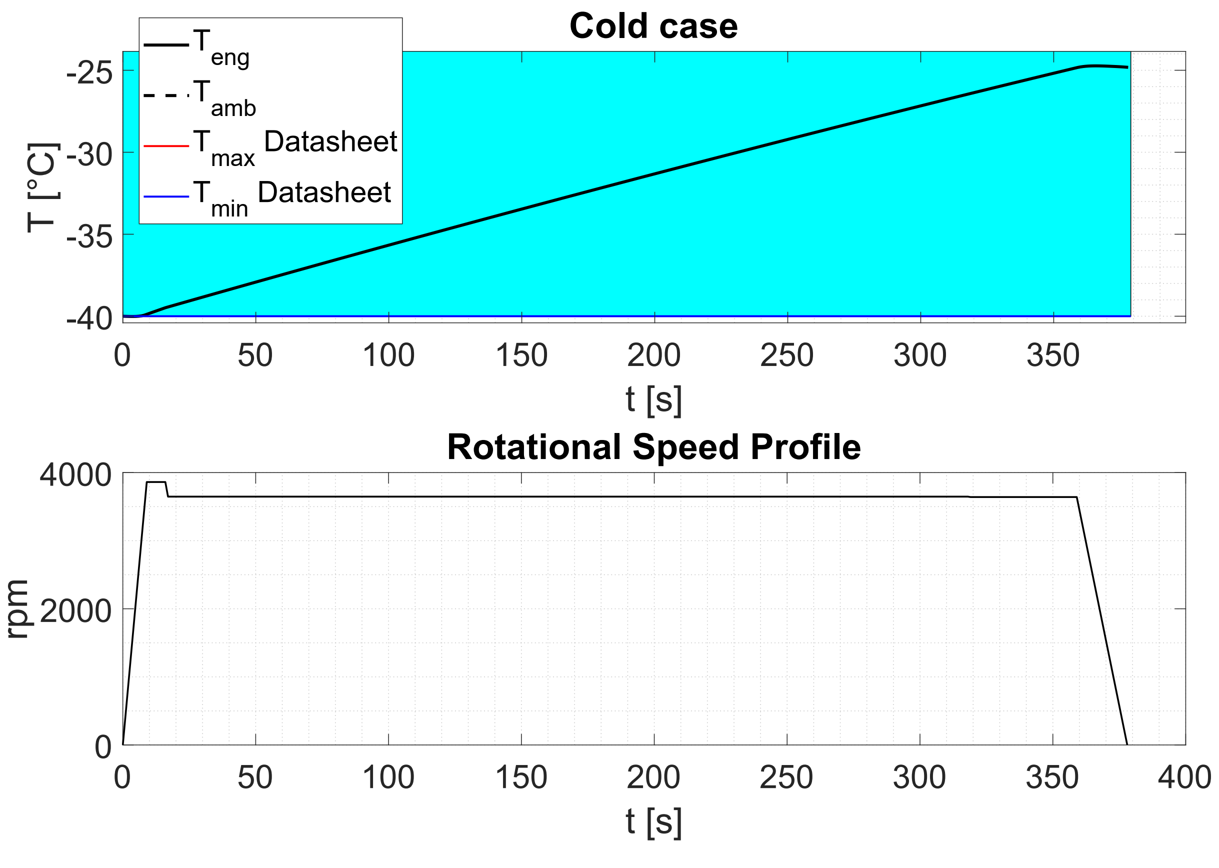

Figure 4.12: Cold case.

Note that it is supposed to start the transient analysis from a temperature of -40 °C that is the minimum allowable temperature for the motor, obtained from datasheet. This means that the temperature is somehow maintained at that value. The maximum temperature reached is -24.6407 °C.

2. **CASE 2: HOT CASE**

Hot case is represented by these environmental characteristics:

- $T_{amb} = 2.40$ [°C], Ambient Temperature
- $T_{ground} = 31.07$ [°C], Ground Temperature
- $T_{sky} = -73.07$ [°C], Sky Temperature
- $Q_s = 557.94$ [W/m^2], Solar Flux

Temperatures and solar flux vary during a Sol (Martian day) but, to be conservative in terms of hottest environment, maximum values are used. Results are:

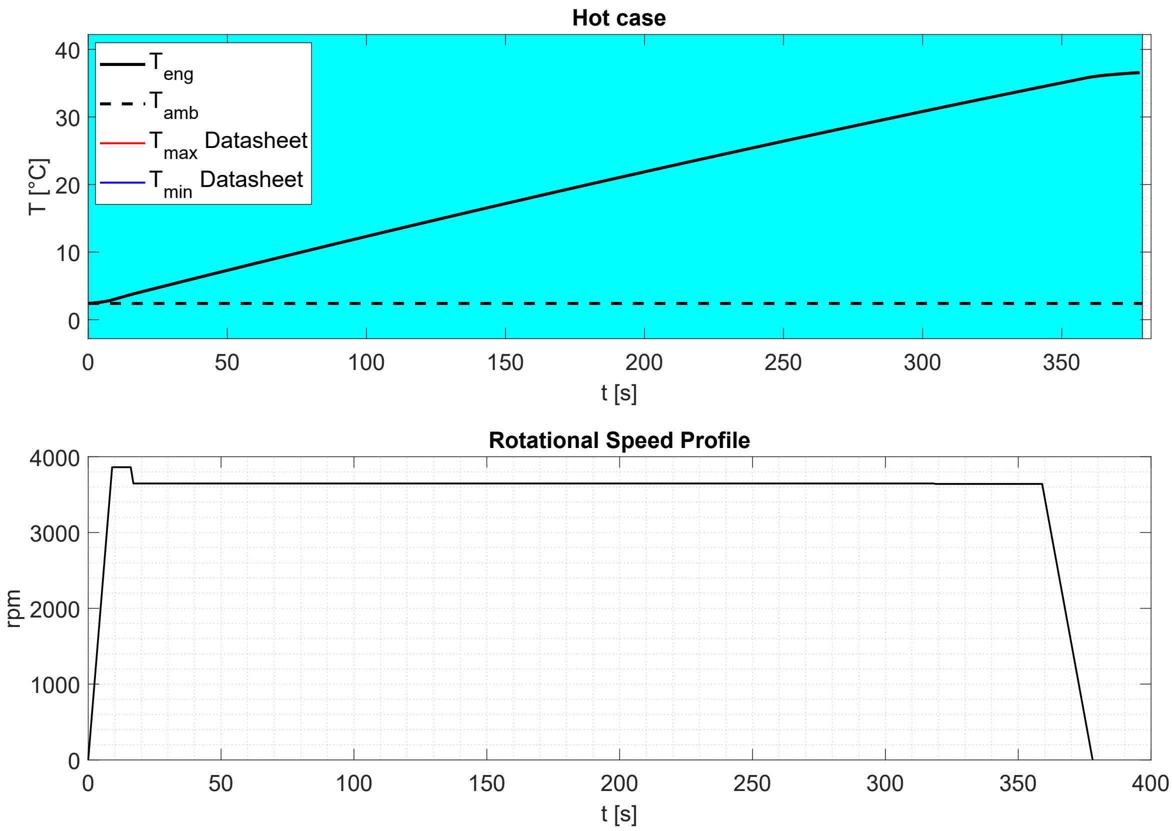

Figure 4.13: Hot case.

In this case the starting temperature is the ambient one because the latter is higher than the minimum allowable motor temperature and therefore there is no necessity to control the starting temperature. In this case the maximum motor temperature reached is +36.6024 °C.
Table 4.1 reports all the results for the sensitivity analysis compared to these reference cases.

3. **CASE 3: Motor Thermal Capacitance C ± 10%**

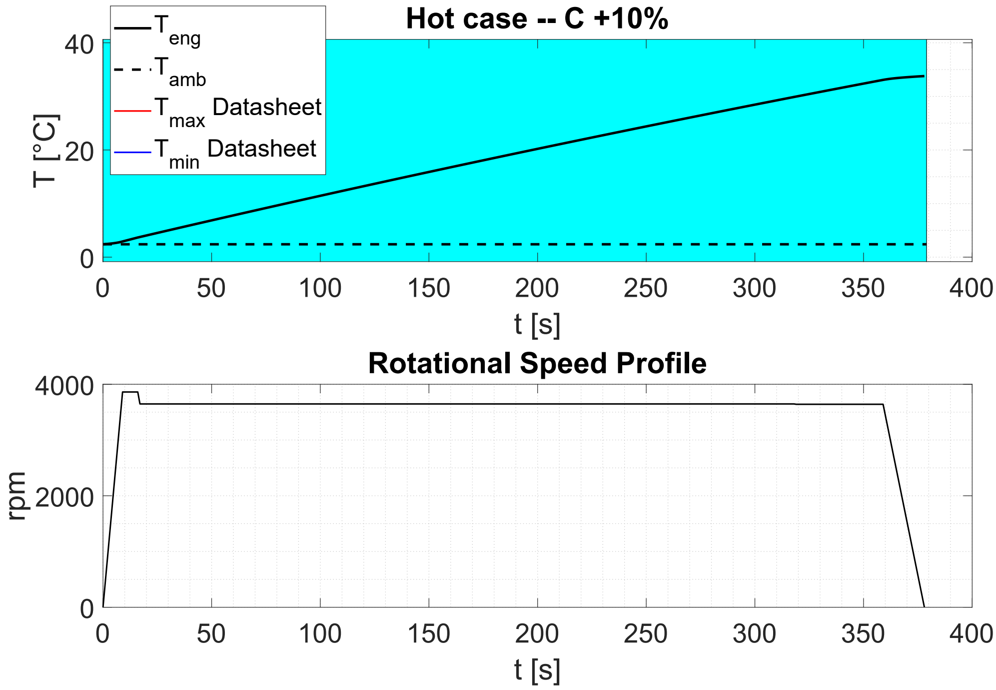

Figure 4.14: A) Hot case with increased motor thermal capacitance.

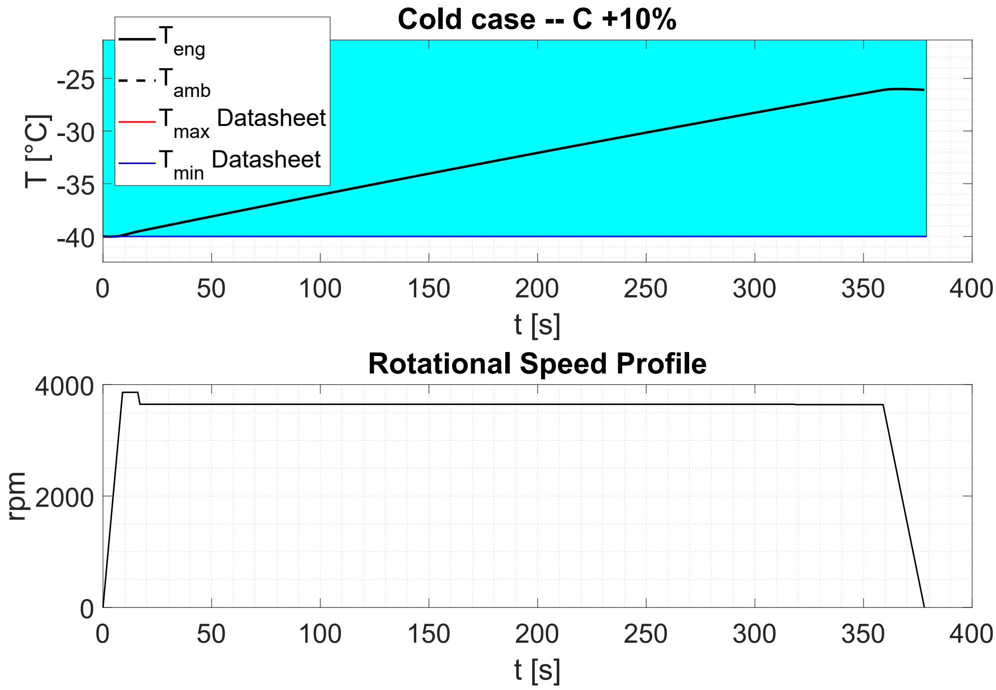

Figure 4.15: B) Cold case with increased motor thermal capacitance.

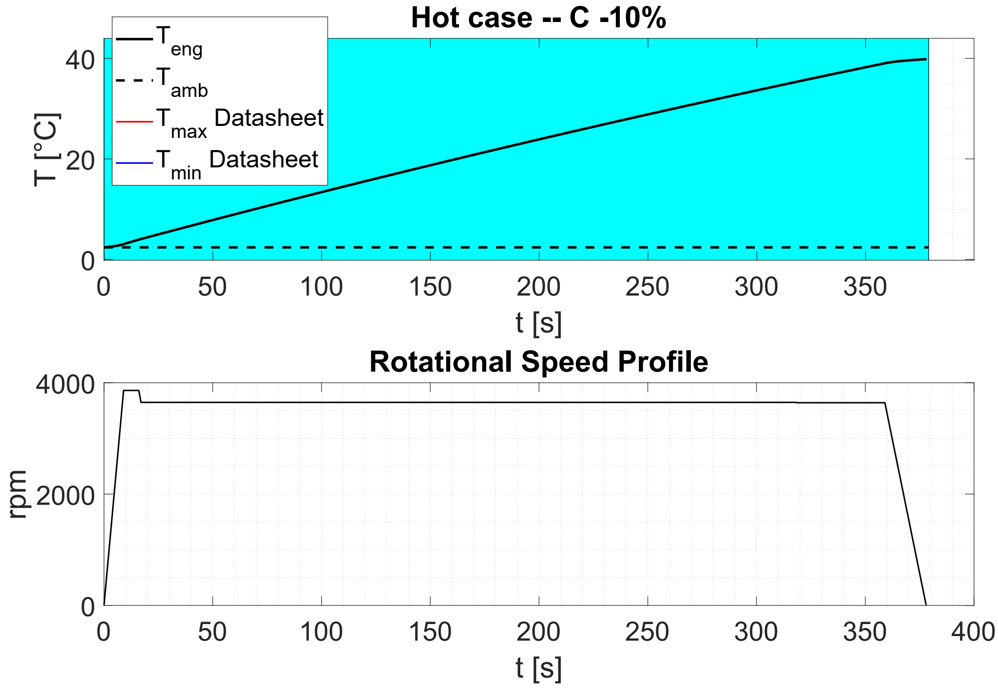

Figure 4.16: C) Hot case with decreased motor thermal capacitance.

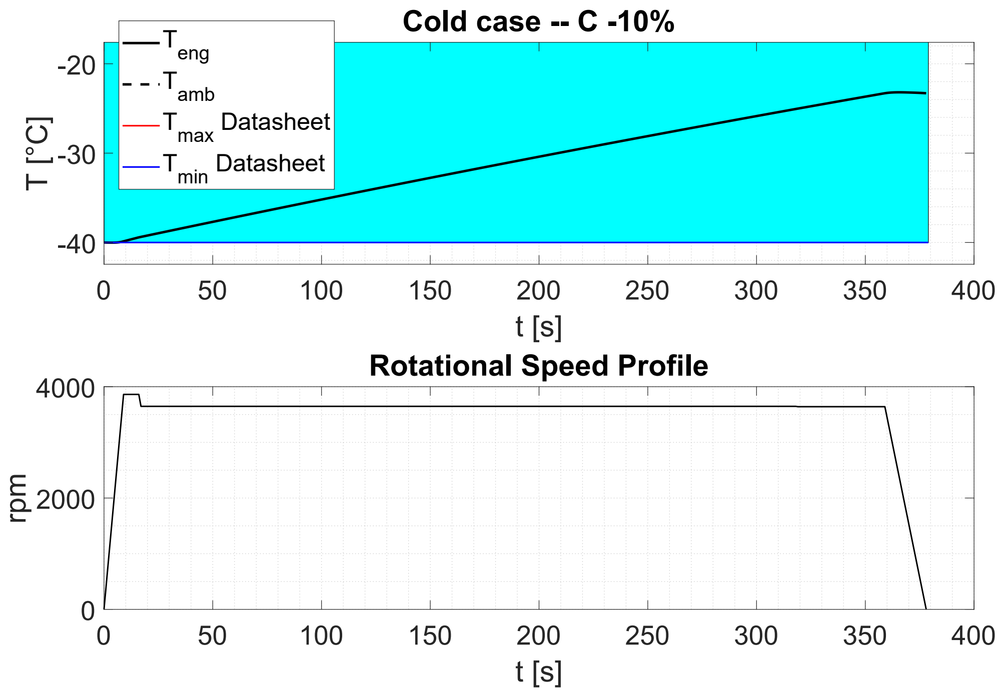

Figure 4.17: D) Cold case with decreased motor thermal capacitance.

4. **CASE 4: Optical Coating emissivity $\epsilon\pm$ 10%**

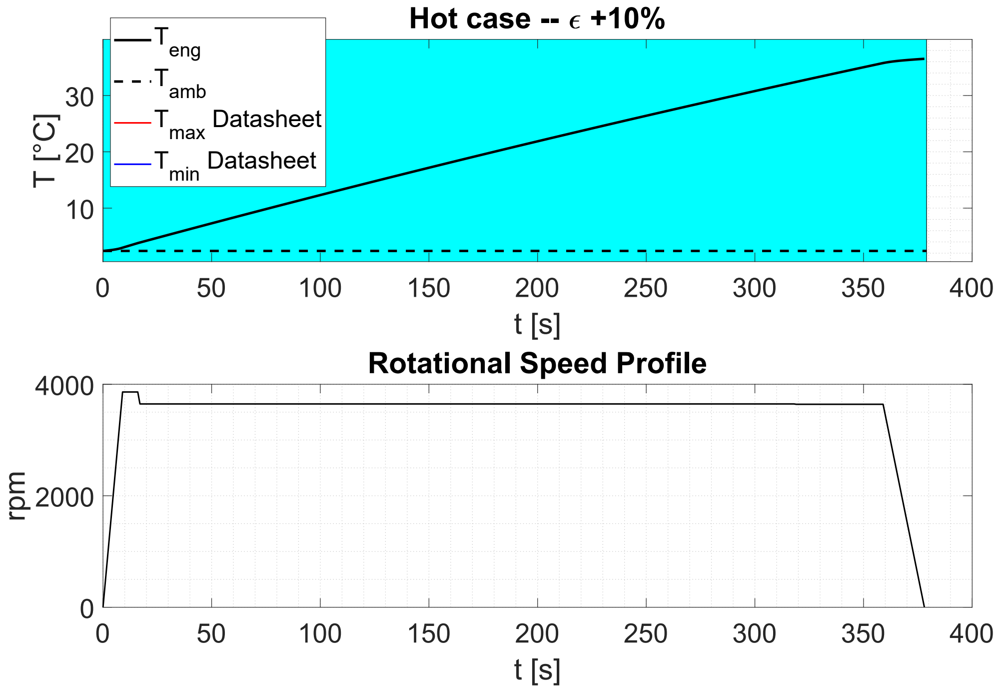

Figure 4.18: A) Hot case with increased motor IR emissivity.

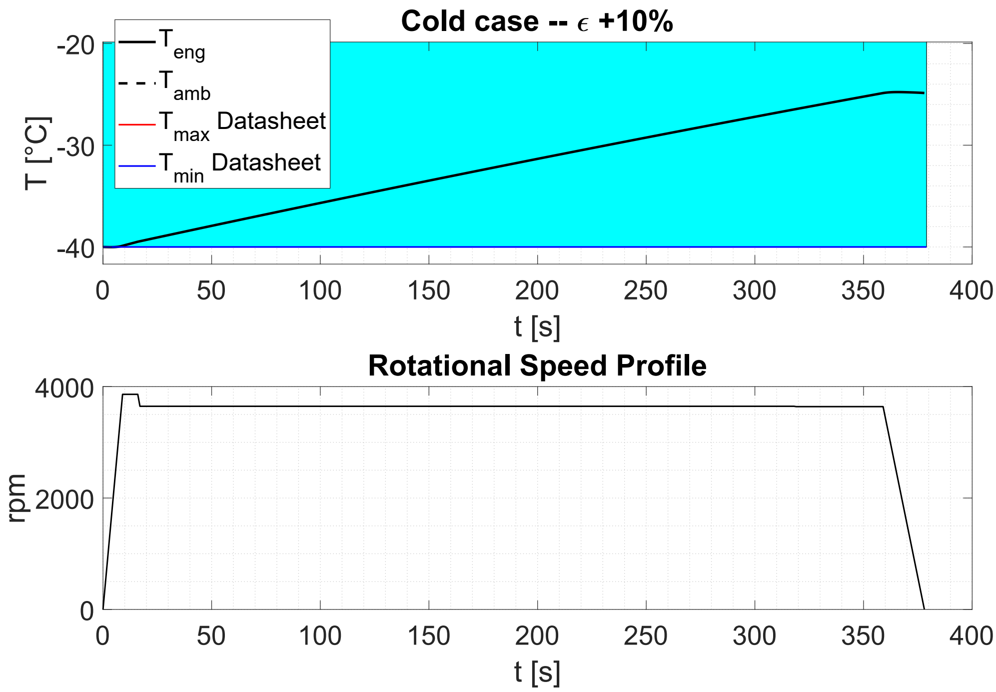

Figure 4.19: B) Cold case with increased motor IR emissivity.

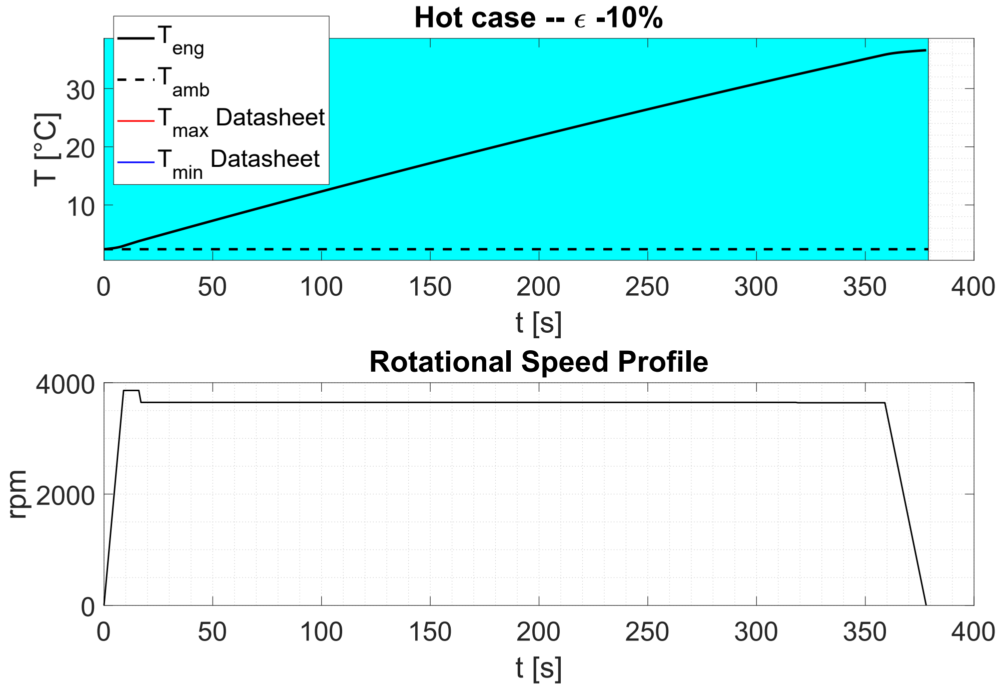

Figure 4.20: C) Hot case with decreased motor IR emissivity.

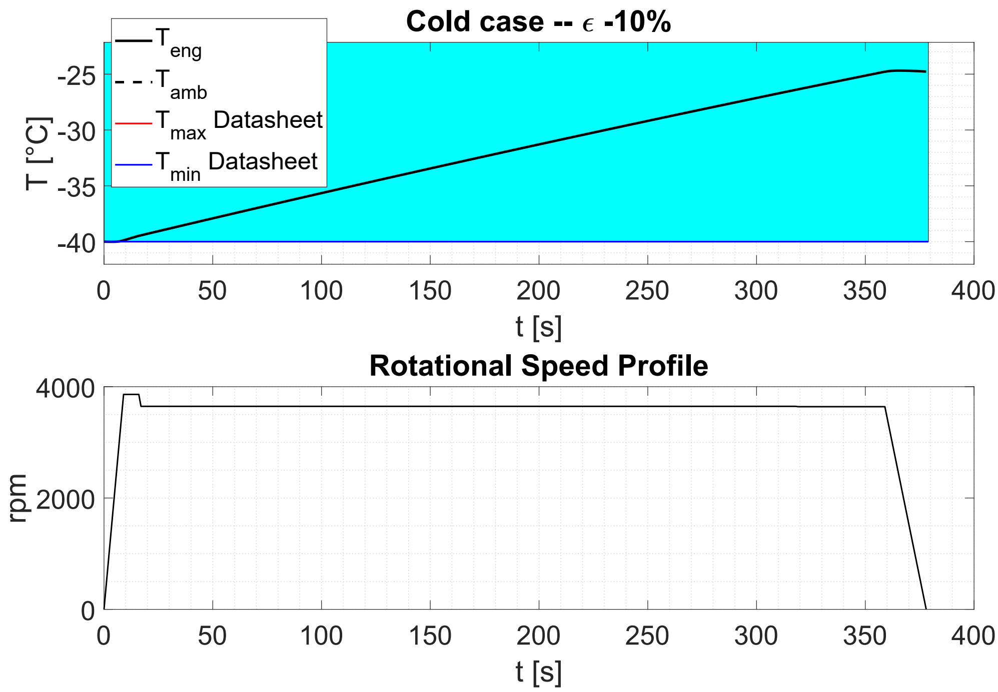

Figure 4.21: D) Cold case with decreased motor IR emissivity.

5. **CASE 5: Optical Coating Absorptance $\alpha\pm$ 10%**

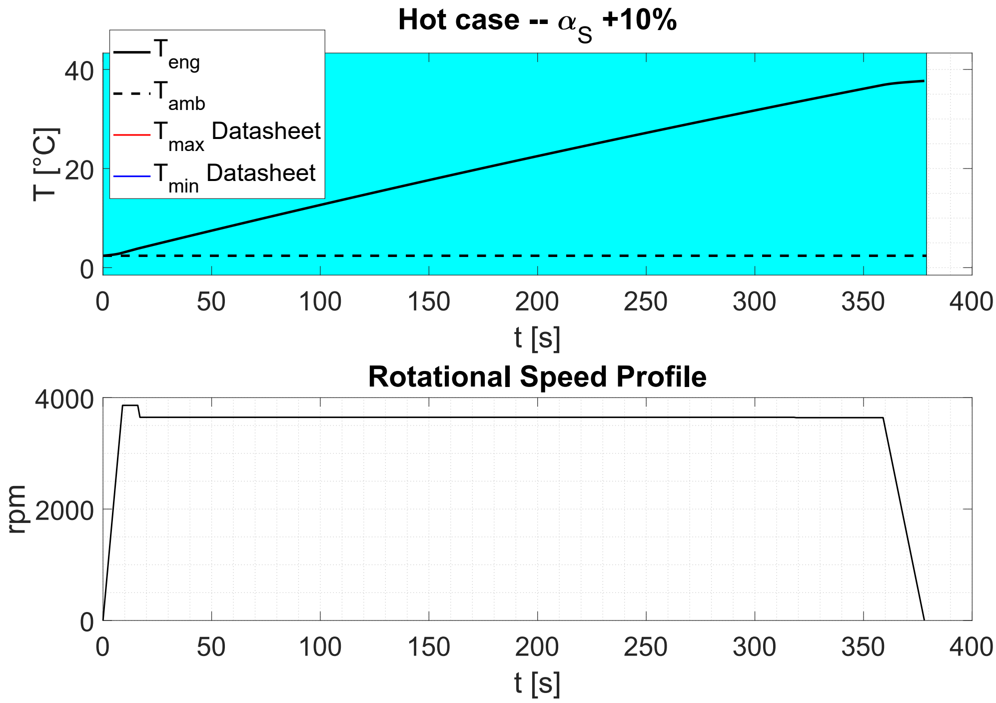

Figure 4.22: A) Hot case with increased motor solar absorptance.

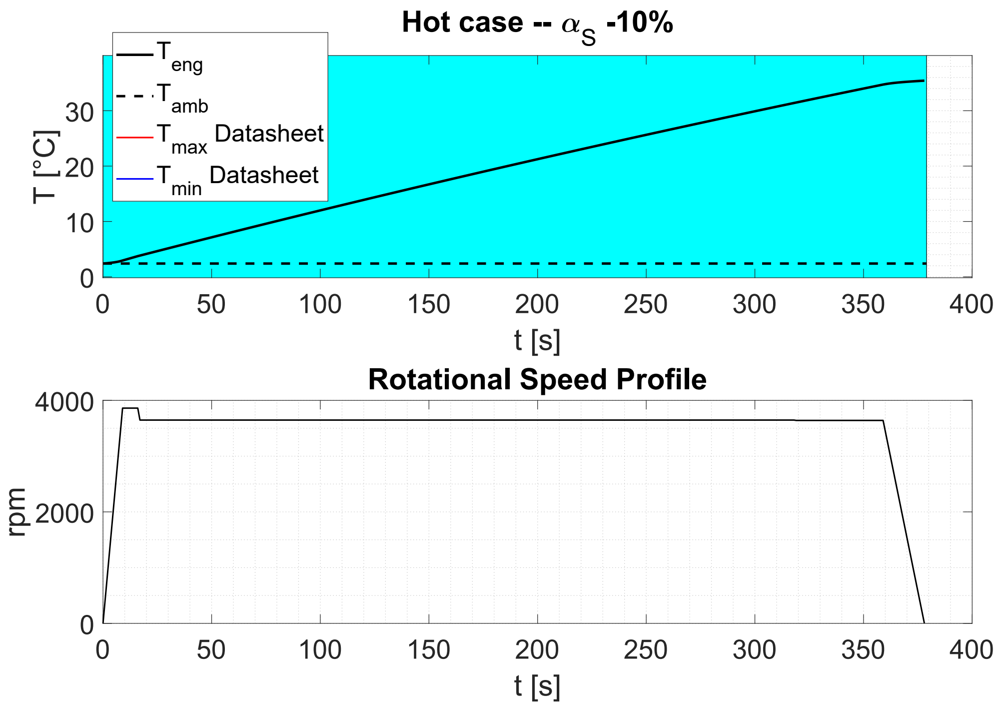

Figure 4.23: B) Hot case with increased motor solar absorptance.

6. **CASE 6: Power Dissipation $Q_{in}\pm$ 10%**

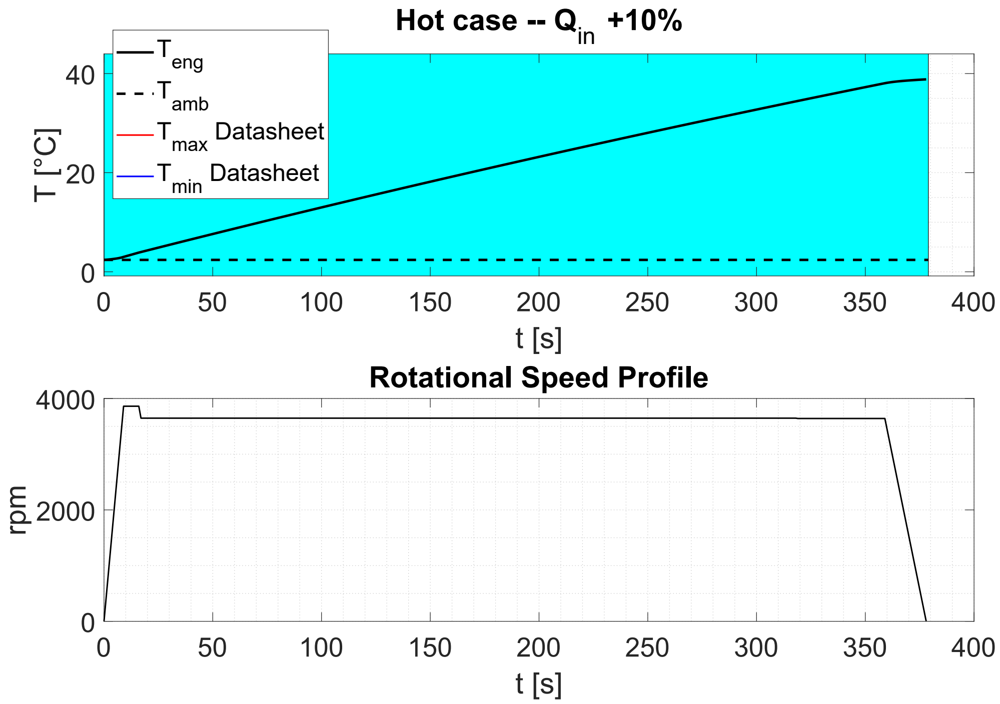

Figure 4.24: A) Hot case with increased motor power dissipation.

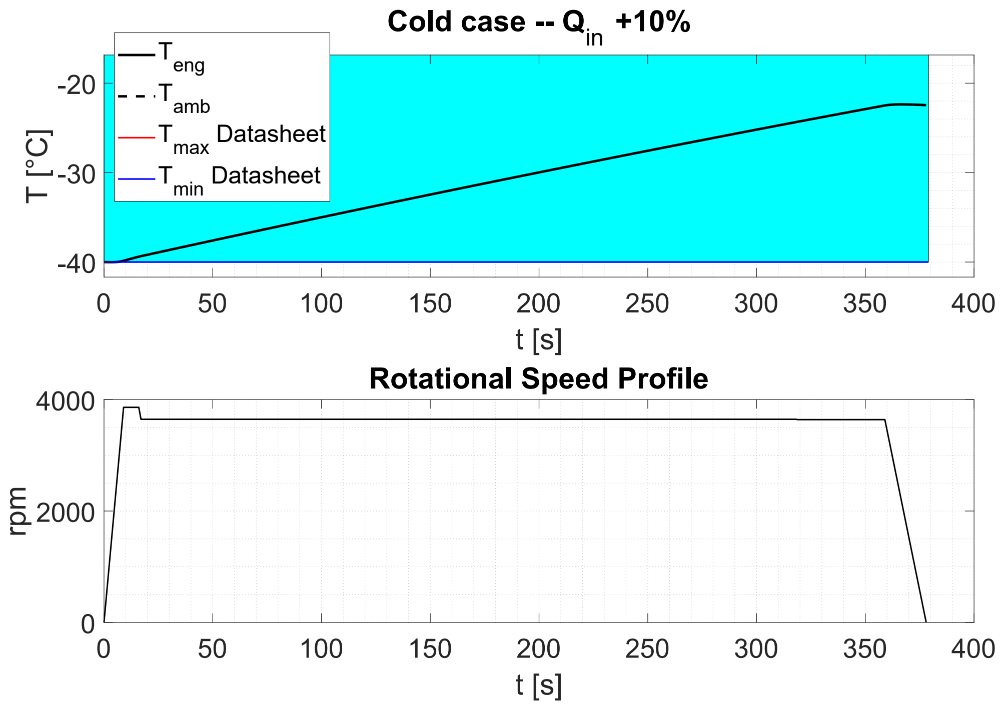

Figure 4.25: B) Cold case with increased motor power dissipation.

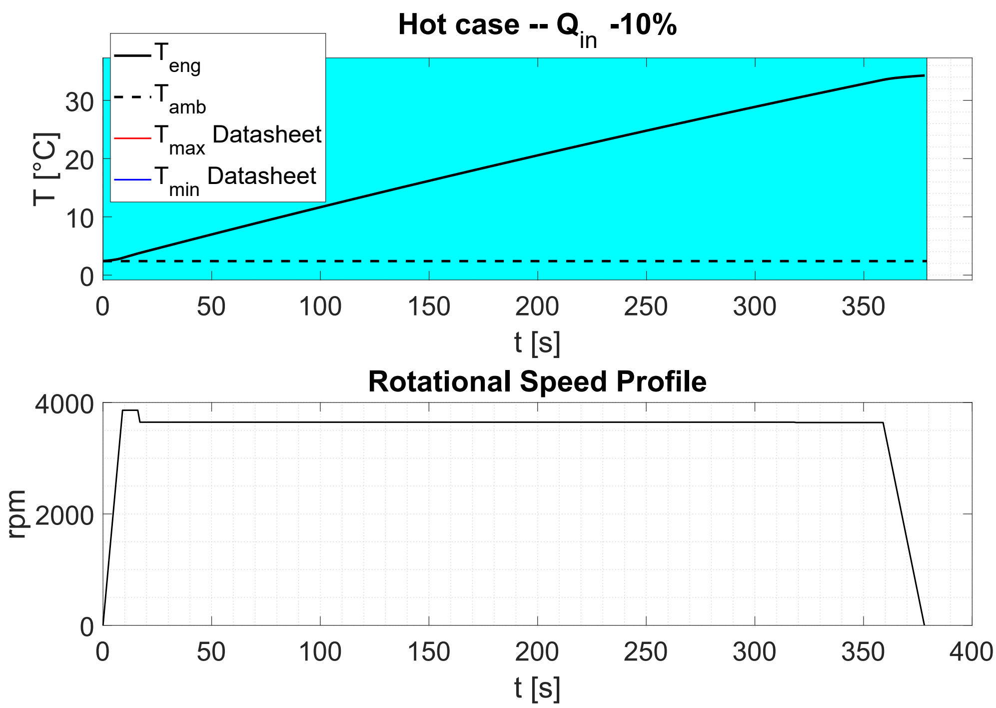

Figure 4.26: C) Hot case with decreased motor power dissipation.

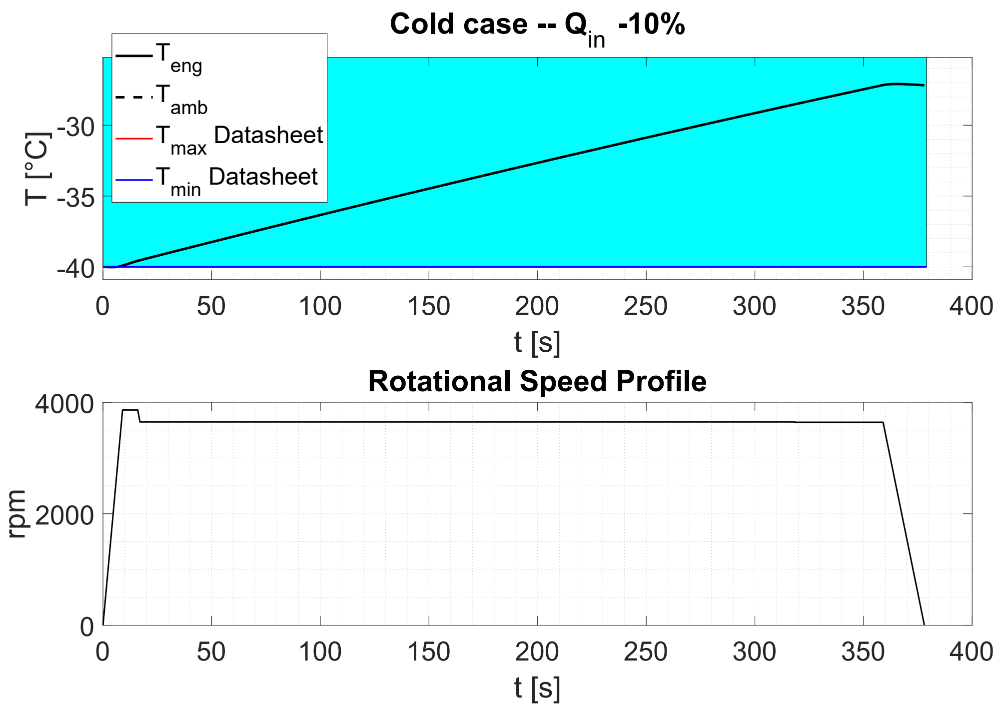

Figure 4.27: D) Cold case with decreased motor power dissipation.

7. **CASE 7: IAS cooling effect, h ± 10%**

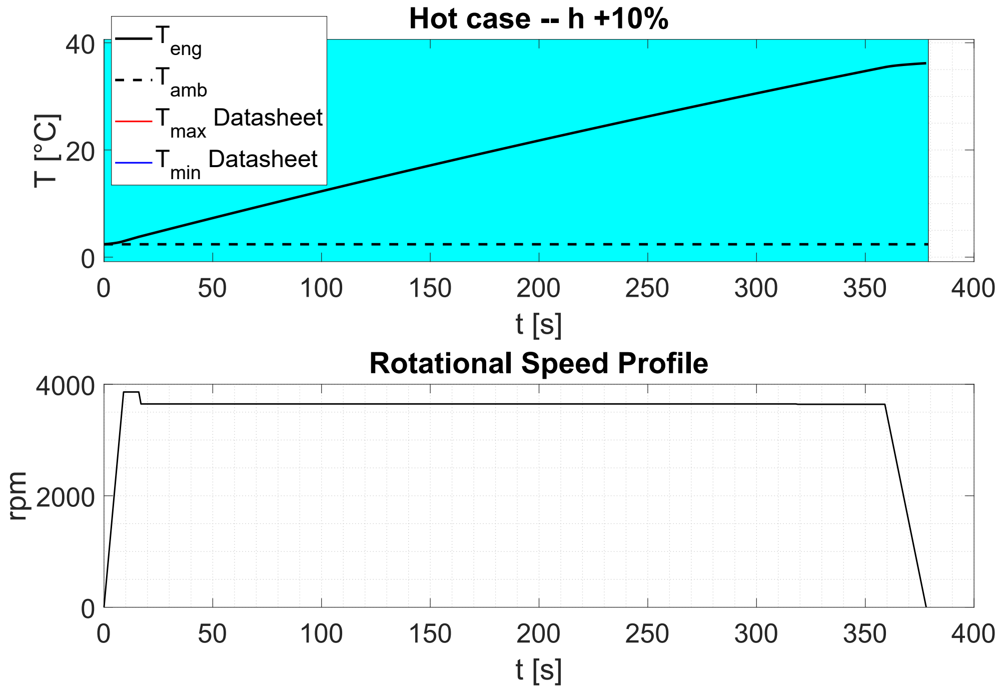

Figure 4.28: A) Hot case with decreased motor power dissipation.

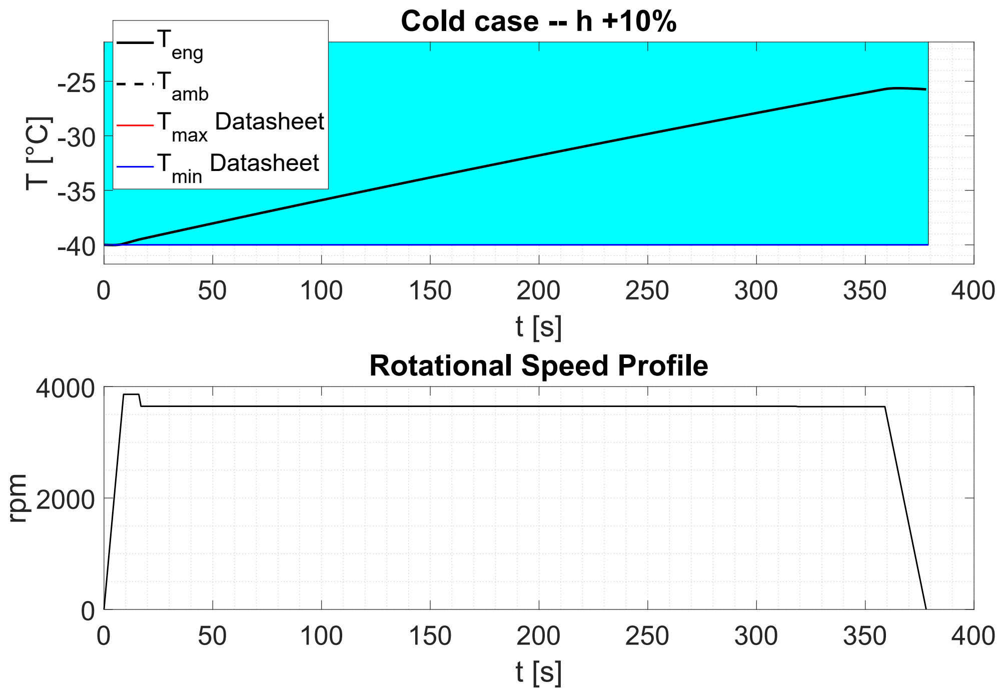

Figure 4.29: B) Cold case with decreased motor power dissipation.

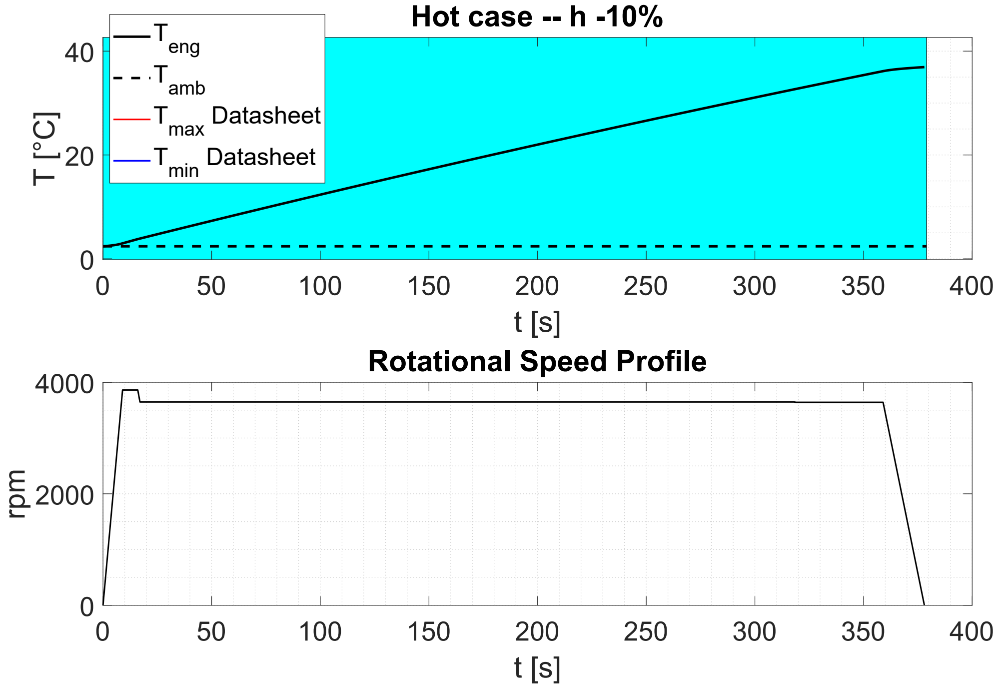

Figure 4.30: C) Hot case with decreased motor power dissipation.

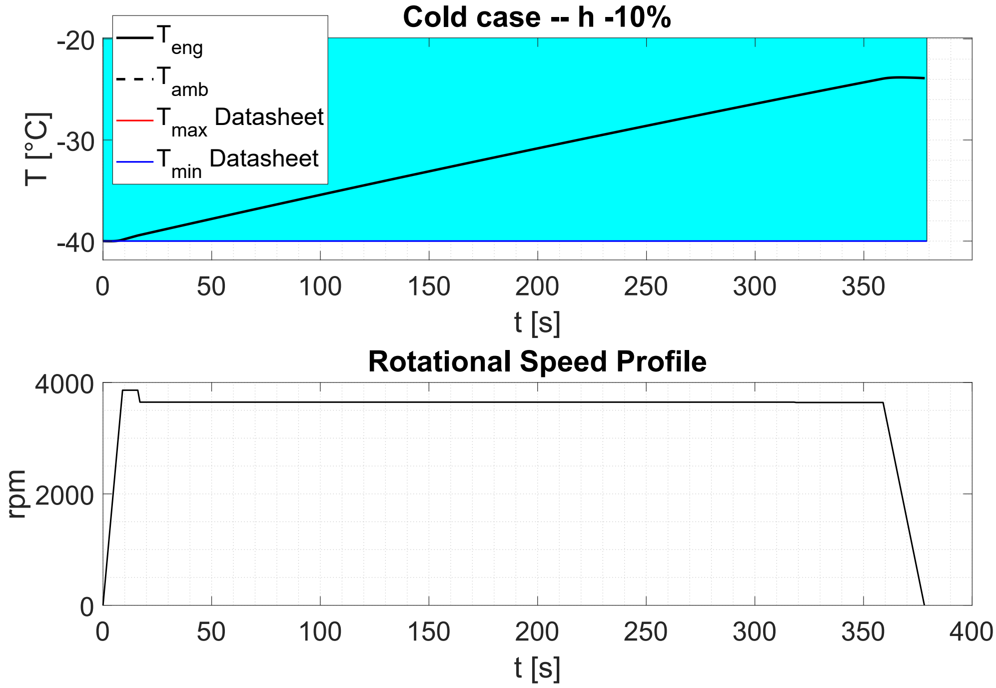

Figure 4.31: D) Cold case with decreased motor power dissipation.

8. **CASE 8: WORST CASE**

In order to determine the worst hot and cold cases it is useful to summarize the previous results in a table:

CASE	Subcase	T_{max} [°C]	$(T-T_0)_{max}$ [°C]	$(T-T_{amb})_{max}$ [°C]	Delta %
1	Standard Cold	-24,6407	15,3593	69,0093	0
2	Standard Hot	36,6024	34,2024	34,2024	0
3	A) C+10%	33,834	31,434	31,434	-7,56344
	B) C+10%	-25,9231	14,0769	67,7269	5,204398
	C) C-10%	39,9006	37,5006	37,5006	9,010885
	D) C-10%	-23,1003	16,8997	70,5497	-6,25145
4	A) ϵ_{IR}+10%	36,5665	34,1665	34,1665	-0,09808
	B) ϵ_{IR}+10%	-24,6881	15,3119	68,9619	0,192365
	C) ϵ_{IR}-10%	36,6384	34,2384	34,2384	0,098354
	D) ϵ_{IR}-10%	-24,5932	15,4068	69,0568	-0,19277
5	A) α_S+10%	37,7323	35,3323	35,3323	3,086956
	B) α_S-10%	35,4723	33,0723	33,0723	-3,0875
6	A) Q_{in}+10%	38,8873	36,4873	36,4873	6,242487
	B) Q_{in}+10%	-22,2782	17,7218	71,3718	-9,5878
	C) Q_{in}-10%	34,317	31,917	31,917	-6,24385
	D) Q_{in}-10%	-27,0019	12,9981	66,6481	9,58252
7	A) h+10%	36,2419	33,8419	33,8419	-0,98491
	B) h+10%	-25,5385	14,4615	68,1115	3,643565
	C) h-10%	36,9681	34,5681	34,5681	0,999115
	D) h-10%	-23,7276	16,2724	69,9224	-3,70566

Table 4.1: Sensitivity Table.

The percentage variation indicates that the parameters which most influence the thermal behaviour are the thermal capacitance and the motor dissipated power, therefore they must be asked to the manufacturer or assumed carefully.
The second most important parameter, the dissipated power, is easily obtainable from datasheet coefficients and rotor performance correlations.

• Solar absorptance is important only in the hot case, when the sun illuminates the motor: its effect is not so strong because not the entire motor is exposed to the sun, but most of the motor surfaces are shaded by the rotor or by the structure. The effect of radiative environment was better investigated with ESATAN-TMS.

• Convective heat transfer is very important in cold case because of the high ΔT between motor surface and CO_2 but, when the ΔT is not so relevant, its effect is much less evident.

• The infra-red emissivity seems negligible but the standard value was only 0.11 so a 10% variation is almost irrelevant. Since ϵ can easily assume high values through the use of paintings or coatings a new case was included.
Assuming $\epsilon = 0.9$ results are:

- HOT CASE: T_{max} = 34.1604 °C, $Delta\%$ = -6.6717
- COLD CASE: T_{max} = -27.9038 °C, $Delta\%$ = 13.2427

An increment from 0.11 to 0.9 is very important, so ϵ becomes one thermal design parameter.

In summary:

- The most important thermal parameter is the thermal capacitance C and must be obtained accurately,
- Power dissipation (or efficiency) is the second most important parameter but can be easily computed,
- Solar absorptance can be quite important but it must be better investigated with ESATAN-TMS, in particular for cool down analysis,
- A small variation in convective heat transfer coefficient does not affect the result significantly if the ΔT is not too high. This means that a complex aerodynamic model is useless for a preliminary design, it is important for a detailed phase analysis,
- Radiative heat transfer can be important as much as convective heat transfer, in particular for the cold case.

Concerning to the motor it is possible to identify two scenarios:

(a) MOTOR HEATING

- FAST: for the purpose of heating up the motor fast, with a given motor power, it is necessary to have: low thermal capacitance, low IR emissivity, high solar absorptance, cover up the motor from the rotor induced velocity or insulate the motor at all ($h \approx 0$).
- SLOW: for the purpose of heating up the motor slowly, with a given motor power, it is necessary to have: high thermal capacitance, high IR emissivity, low solar absorptance, place the motor where the rotor induced velocity is higher ($h = h_{max}$).

(b) MOTOR COOLING

- FAST: for the purpose of cooling down the motor fast it is necessary to have: low thermal capacitance, high IR emissivity, low solar absorptance (if there is solar radiation).
- SLOW: for the purpose of cooling down the motor slowly it is necessary to have: high thermal capacitance, low IR emissivity, high solar absorptance (if there is solar radiation). Best is to insulate the motor.

Analysing the motor heating, the WORST POSSIBLE HOT CASE is the hot case with: low C, low ϵ, high α, high Q_{in} and low h. Combining cases 3C, 4C, 5A, 6A, 7C we have:

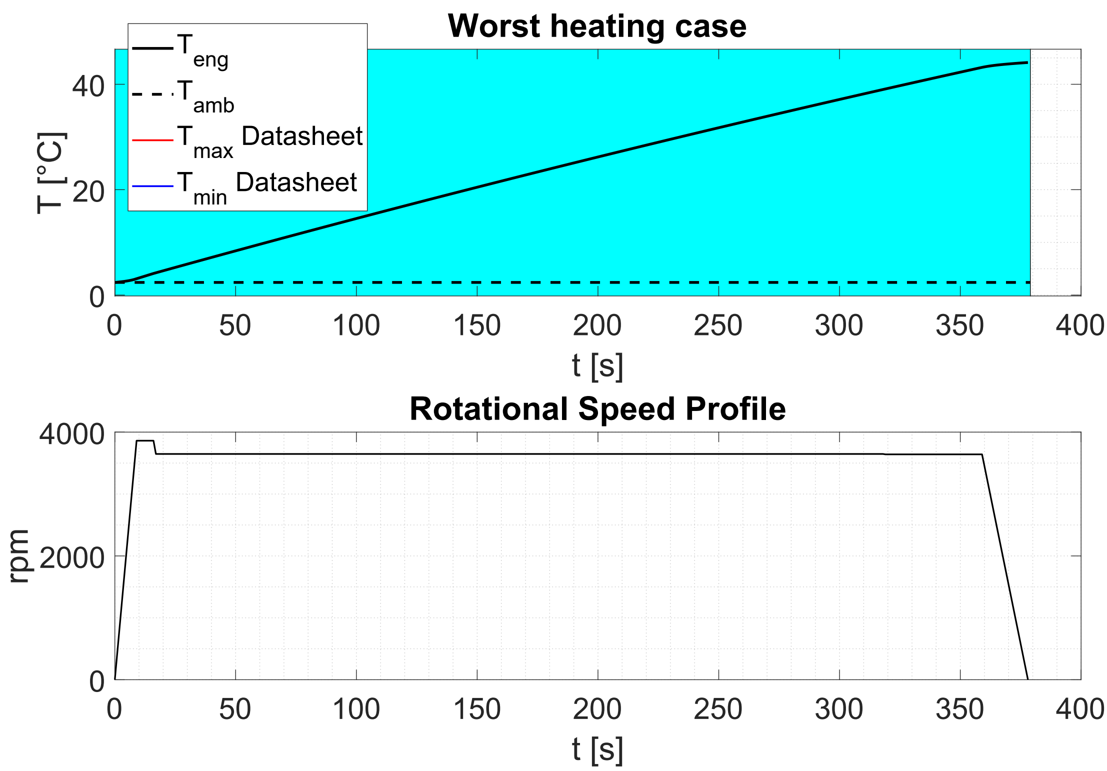

Figure 4.32: Worst heating case.

In Figure 4.32 the temperature limit of 125 °C is never reached so it is possible to state that there is no overheating. Maximum temperature is T = +44.1819 °C which is 20.71% (7.6 °C) higher then the standard hot case.

The above cold cases were analysed with a controlled initial temperature of -40 °C which is the minimum allowable temperature from motor datasheet. How is it possible to keep that temperature constant if the motor is not running? How much power is needed? To give an answer to these questions a cool down analysis was done, consisting of 1 hour cooling in the coldest environment for both "slow cooling" and "fast cooling" scenarios. Moreover it will be simulated a "very worst" heating case with insulated motor ($h \approx 0$) and, if temperature limit is not reached, a cool down analysis with insulated motor will be run.

- FAST COOLING (WORST COLD CASE): C -10%, $\epsilon = 0.9$

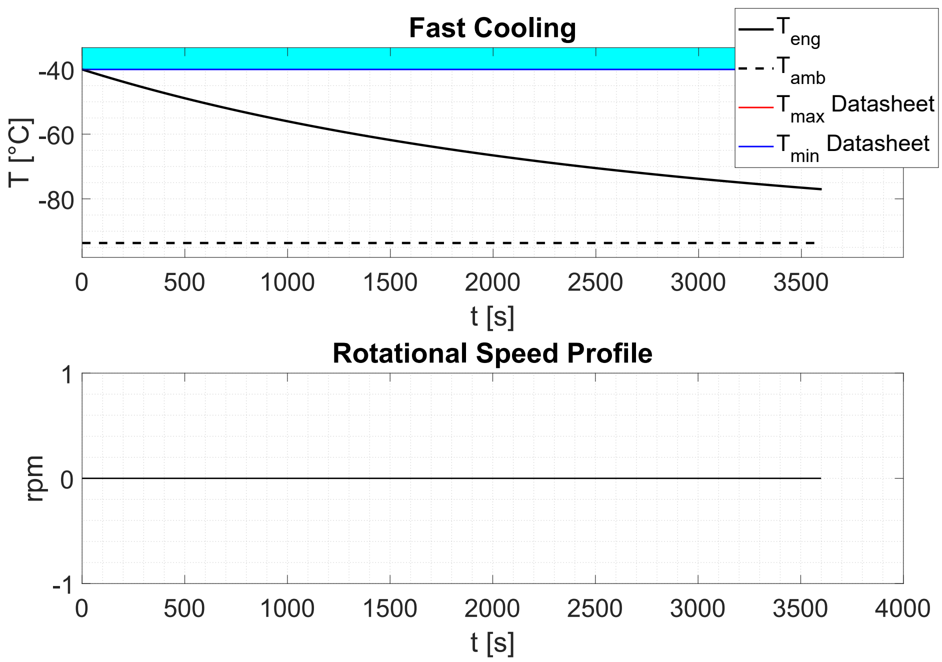

Figure 4.33: Fast Cooling Analysis.

The motor surface temperature after 1 hour in the coldest environment is -77.03 °C. To maintain the temperature to -40 °C it is necessary to heat the motor with a heater of 0.955 W of power.

Fast cooling results:

(a) $T_{min} = -77.03$ °C,

(b) $P_{heater} = 0.955$ W

- SLOW COOLING: C +10%, $\epsilon = 0.1$

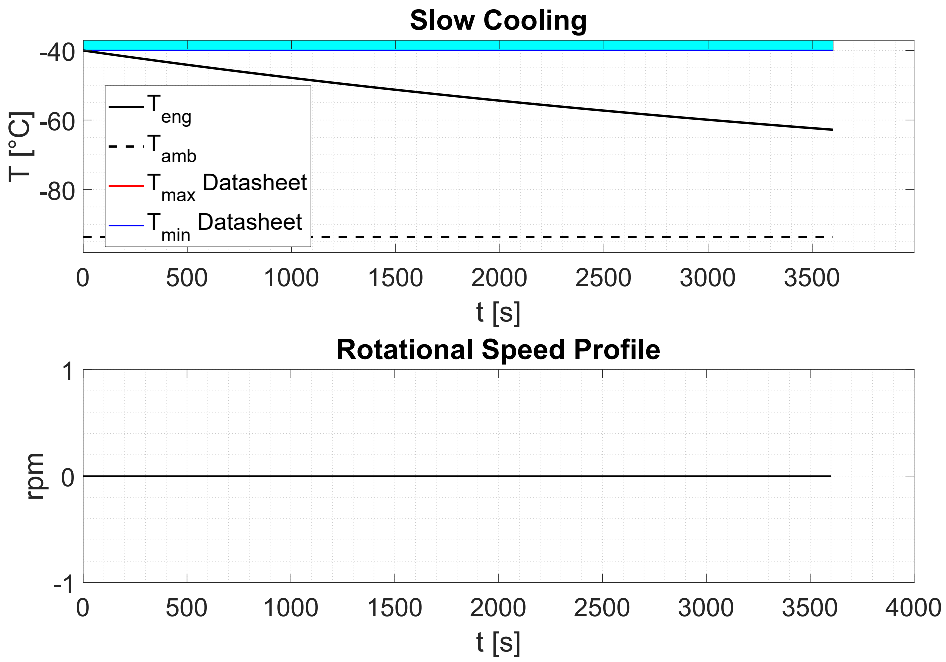

Figure 4.34: Slow Cooling Analysis.

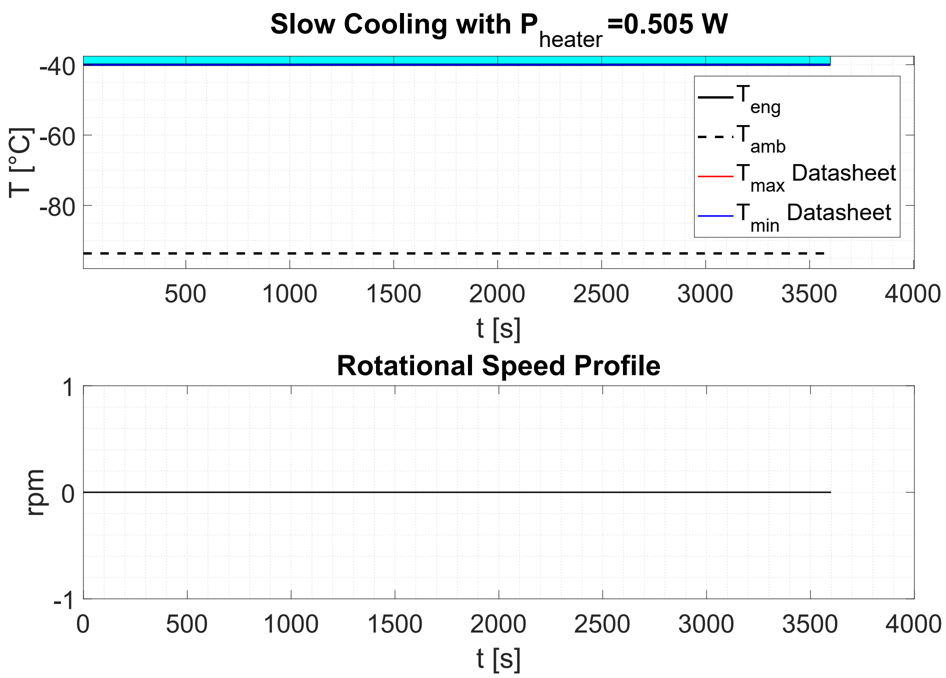

Figure 4.35: Slow Cooling Analysis with heater.

In this case the motor surface temperature after 1 hour in the coldest environment is -62.79 °C. To maintain the temperature to -40 °C it is necessary to heat the motor with an heater of 0.505 W of power.

Slow cooling results:

(a) $T_{min} = -62.79$ °C,

(b) $P_{heater} = 0.505$ W

The heater power requested to maintain the minimum allowable temperature is affected by the radiative heat transfer between motor surface and environment and by the natural convection heat transfer coefficient. From fast and slow cool down analyses it is possible to note that there is an important difference in heater power. An improvement in design can therefore be done.

4.4 Motor design improvements

A design improvement could be to insulate the motor (with some sort of aerogel) in order to require less heater power because the battery pack must be as small as possible to reduce drone weight.

This is possible only if with the insulated motor maximum temperature does not reach the max operating limit. To verify this a new analysis was performed and could be called "very worst hot case analysis" in which the convective heat transfer coefficient h is forced to 0, as if the insulation k would be 0. The parameters will be:

- $C = 0.9 \cdot C_{std}$ (case 3C Table 4.1),
- $\epsilon = 0.1$ (case 4C Table 4.1),
- $\alpha_S = 1.1 \cdot \alpha_{S_{std}}$ (case 5A Table 4.1),
- $Q_{in} = 1.1 \cdot Q_{in_{std}}$, (case 6A Table 4.1),
- $h = 0$ (impossible).

Results are shown in Figure 4.36.

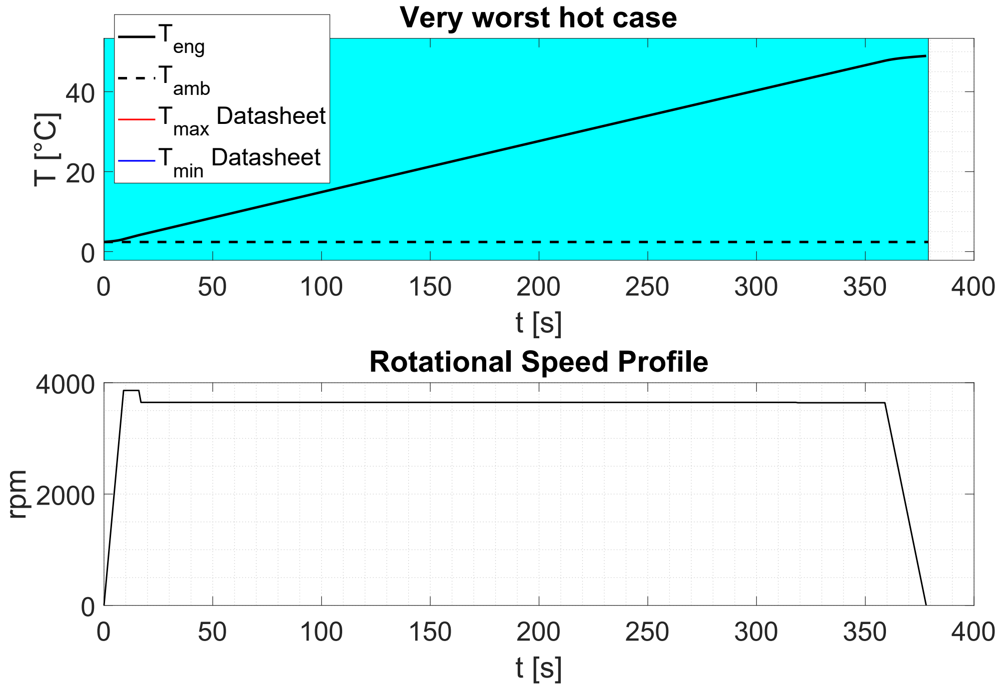

Figure 4.36: Insulated Motor. "Very Worst Hot Case".

Maximum temperature is $T_{max} = +48.962$ °C which is again lower than the maximum limit of +125 °C and 33.77% (12.36 °C) higher than the standard hot case analysis. Once verified that even with an insulated motor there is no overheating it is possible to simulate the motor cool down in coldest environment from the initial temperature of -40 °C and to compute the required heater power. In this case the natural convective heat transfer coefficient was reduced to 1/10 of its standard value.

Simulation parameters were those of slow cool down analysis plus the insulated motor parameter:

- $C = 1.1 \cdot C_{std}$,
- $\epsilon = 0.1$,
- $h = 0.1 \cdot h_{std}$.

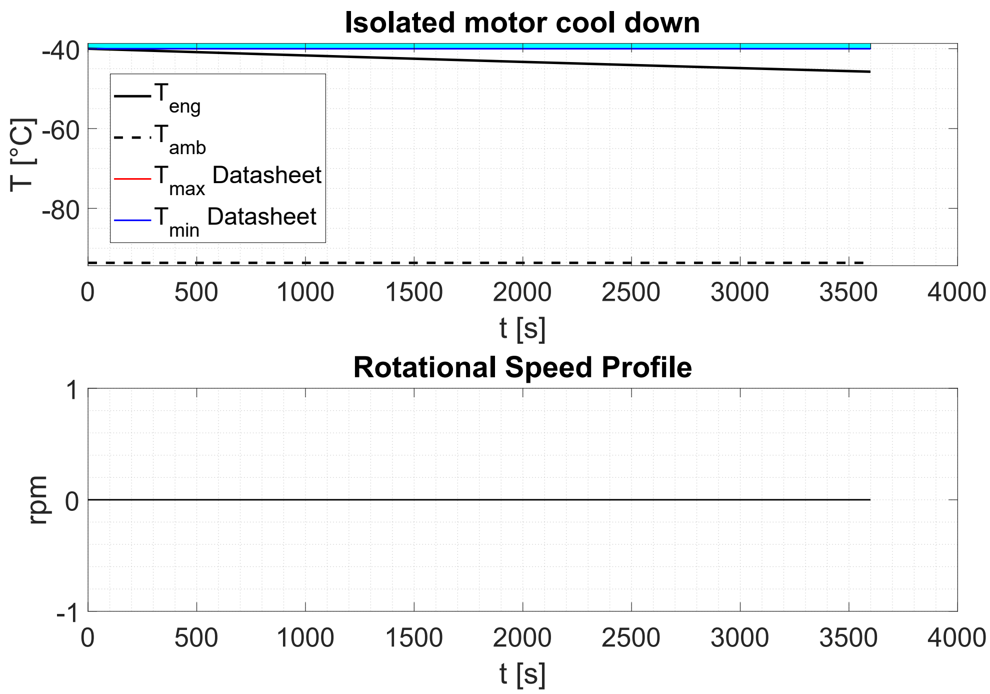

Figure 4.37: Insulated motor cool down analysis.

Minimum temperature is -45.76 °C, only 5.76 °C lower than initial value. This means that only 0.105 W are required to maintain the motor at its minimum allowable temperature.

Insulated motor cooling results:

1. $T_{min} = -45.76$ °C,
2. $P_{heater} = 0.105$ W

In conclusion, if motor temperature must be controlled, it would be useful to insulate the motor as much as possible but a sensitivity analysis about aerogel thickness has to be performed (it will be done in Chapter 6).

4.5 Motor analysis conclusion

The developed MATLAB model is a very useful tool to simulate the thermal behaviour of a BLDC motor requiring only a small tuning from experimental data to adjust forced convection heat transfer depending on rotor performances. It is also possible to simulate different environments such as Martian one and to test lots of different cases and motors easily and without changing any complex geometrical model so it is a helpful preliminary design tool. Of course it is not a final design model, that task is assigned to an ESATAN-TMS more detailed model once motor (and drone) geometry and features, mission profile and rotor performances will be finally determined.

In these first chapters we focused on the study of a given motor and its thermal behaviour depending on the rotor mechanical and aerodynamic performances. This allowed us to properly account the convective heat fluxes and the unknown thermal capacitances which were not known at the beginning of this thesis.
In the following chapters we will deal with the drone preliminary design and with its thermal and energetic analyses, in this way we will be able to give an answer to the question "*is it possible to fly on Mars?*".

4.6 Future model improvements

The development of both MATLAB and ESATAN-TMS models faced the problem of properly describe the forced convection without using CFD analysis. Since the field of motion is characterized by a very low Reynolds over a vertical cylinder geometry at different Prandtl numbers (air and CO_2), a study about this geometry in these field of motion would be very useful and it would be very interesting to study particular geometries in other-than-Earth environmental conditions. If in future such a work will be done the model could integrate that results and therefore be improved.

The MATLAB model could also be improved with the development of a new environmental routine which provides environmental parameters over time. At the moment they are supposed to be constant. The development of such a routine/function would allow to analyse cyclical missions, which are now analysable only with ESATAN-TMS or other thermal software.

Chapter 5

Drone Preliminary Design

With the purpose of choose the best engine to fit the drone rotors and the best thermal control solution it is important to define all the main constraints and requirements of the project such as rotor performances, drone dimensions and mass.
The main design drivers are the rotor performances in terms of delivered thrust, torque and power. In fact once known the rotational speed needed to hover (condition in which thrust equals weight) it is possible to extrapolate the associated torque and power. With these values we can choose a motor and a battery pack which provides energy for a given duration. The NASA's Mars Helicopter Scout (MHS) is designed to fly for only about 90 seconds [10]. In this Chapter we propose a preliminary design configuration and we want to understand if the MHS low flight time is due to the battery mass and consequently lack of storable energy (energy budget limit), a recharging time problem or a cold environment survival problem. In previous Chapter it has been demonstrated that it shouldn't be an overheating issue but a cold environment survival issue.
The following steps were followed to obtain the design configuration:

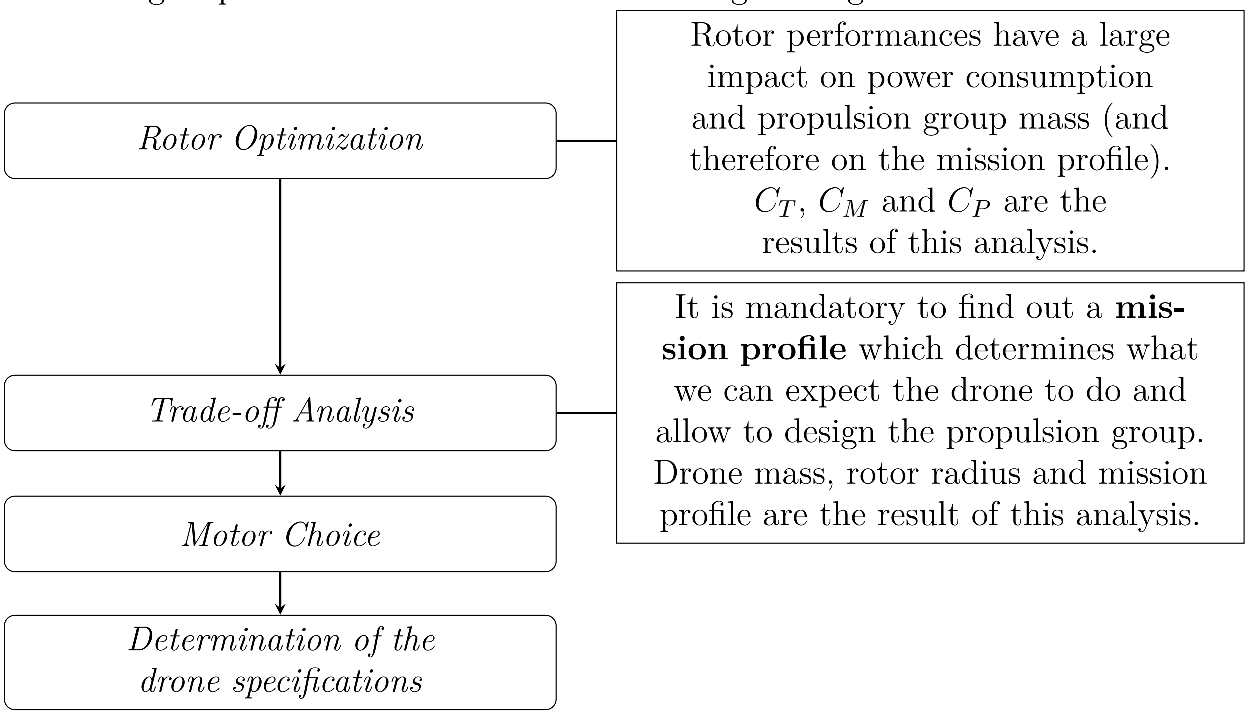

5.1 Rotor optimization

At the end of Section 3.3 it was introduced that the TAS-I rotor (Figure 3.17) as well as the Maryland ones (Figure 3.16) are not optimized in terms of efficiency, this means that they must rotate faster and/or absorb a higher amount of power in order to produce the required thrust. Since:

- the **power energy budget** determines the mass of the battery,
- a higher rotational speed stresses the blades more,
- a higher required torque means heavier motor,

⇒ it is mandatory to optimize the rotor.
The rotor is the main driver of the design.

An interesting work about rotor optimization has been done at Politecnico di Torino by Domenico Zaza [7] followed by Stronati's internship, whose results were introduced in Section 3.3.
The rotor proposed by D. Zaza is shown in Figure 3.20.
For a preliminary design purpose the performances of the above mentioned rotor in terms of thrust and torque are better than those of Maryland University and can represent a better starting point for the design of the drone.
Here are reported the characteristic coefficients of the Zaza-Stronati's rotor:

R [m]	C_T	C_M	C_P
0.313	0.184	0.0153	0.0963

Table 5.1: Results of on-design analysis [7].

These coefficients are not defined using the same definition of the Maryland ones.
In Maryland/TAS-I form coefficient values are:

R [m]	C_T	C_M	C_P
0.313	0.0237	0.00395	0.00395

Table 5.2: Results of on-design analysis (converted).

Note that $C_M = C_P$ in this form.

Comparing all the results we have:

	R [m]	C_T	C_M	C_P
PoliTO	0.313	0.0237	0.00395	0.00395
Maryland	0.2286	0.017693	0.0047744	0.0047744
TAS-I	0.2285	0.017900	0.0096818	0.0096818

Table 5.3: Compared coefficients.

From Table 5.3 the **PoliTO rotor presents better performances and therefore was taken fir the drone design instead of the Maryland one.**

Since characteristic coefficients can have a dependence with radius (tip losses for example are more and more important with the decreasing in radius) here we assume that they can decrease with rotor dimension but they can not exceed the on-design values (Table 5.2) to preserve the blade from structural problems. The trend is shown in Figure 5.1 and in Table 5.4.

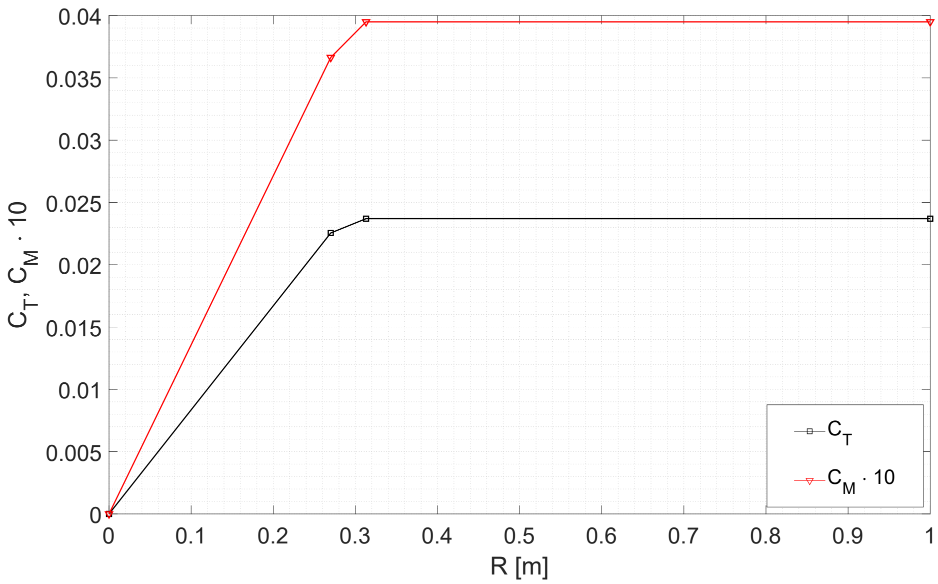

Figure 5.1: Characteristic coefficients dependence with radius.

R [m]	C_T	$C_M = C_P$
0	0	0
0.270	0.0226	0.00366
0.313	0.0237	0.00395
$\rightarrow \infty$	0.0237	0.00395

Table 5.4: Characteristic coefficients dependence with radius.

With these data we can plot Rotational Speed Ω, requested Torque M and requested

Power P needed to hover the same mass m with rotor of different radius but identical coefficients (Figure 5.2).
These curves are obtained imposing a thrust equal to $T = \frac{1.8}{4} \cdot g_M = 1.67\,N$ because the MHS will have a mass of 1.8 kg and we suppose to build a quadcopter, therefore each rotor has to supply 1/4 of the total thrust.
Of course the trends in Figure 5.2 do not take into account the fact that a bigger rotor will weight a lot more than a small one (Figure 5.3) so we must focus only on the first part of the curves ($R < 0.5m$).

- Imposing T and by varying R we can compute $\Omega(R) = \sqrt{\frac{T}{\rho A C_T}} \cdot \frac{1}{R} \propto \frac{1}{R^2}$
- Then $M(R) = \rho A \Omega^2 R^3 C_M \propto R$
- and $P(R) = M \cdot \Omega \propto \frac{1}{R}$

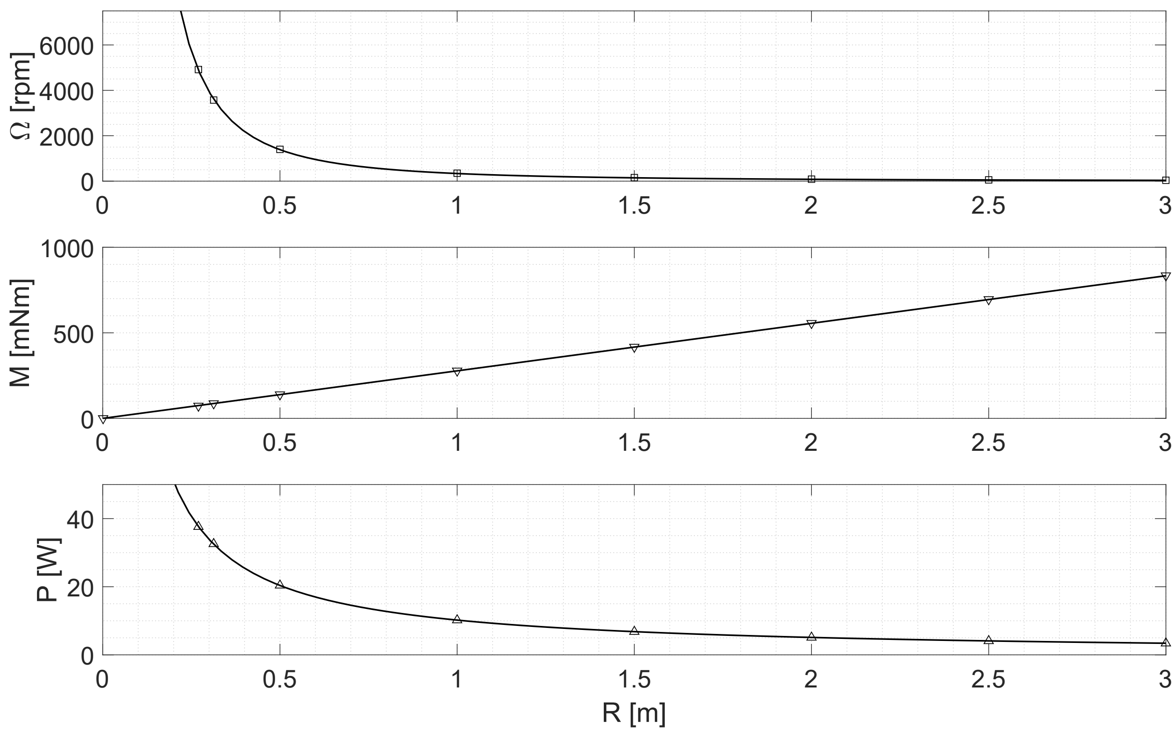

Figure 5.2: Ω, M, P dependence with radius.

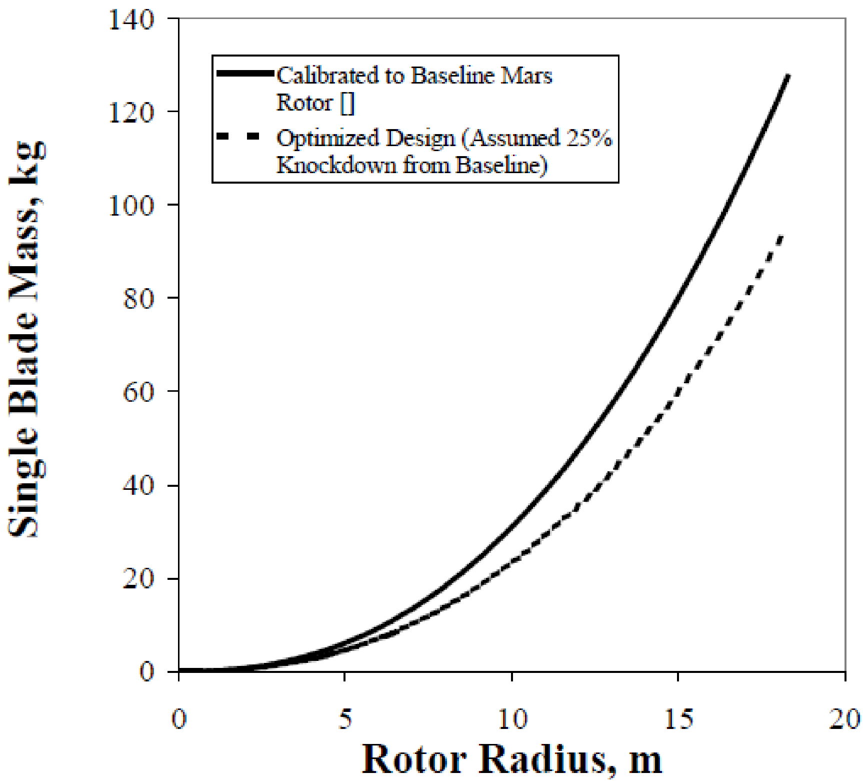

Figure 5.3: Rotor mass with increasing radius [11].

A bigger propeller can lift the same mass with reduced power, reduced rotational speed but with more torque requested to the engine. The latter two parameters are used to choose the motor. If one looks for a small and light motor the requested torque should not be too high because it is directly correlated with the absorbed current from the equation

$$M = k_M \cdot (I - I_0) \tag{5.1}$$

where:

- M is the output torque (equal to the rotor torque if no gearbox is used),
- I is the motor absorbed current [A],
- I_0 is the motor no-load current [A],
- k_M is the motor torque constant usually expressed in [mNm/A].

and a higher absorbed current means larger wires and, at the end, a bigger and heavier motor. A solution often consists in the use of a gearbox to reduce the motor requested torque (with an increased motor rotational speed).

5.2 Mission profile

All the considerations about time of flight and power budget must consider the **mission profile** ($\Omega(t)$). The NASA's MHS is supposed to fly for about 90 seconds [10]. In this section we assume a different, higher total flight duration broken up into 3 phases: ascent, hovering and landing.

In order to determine the duration of the flight we allocate a part of the drone mass for the battery pack and assume that all the flight will be carried out at full throttle. Moreover, to keep into account payload and electronics power consumption and power requested by possible heaters needed to survive in the cold Martian environment, the computed duration will be halved (when an actual design will be chosen the battery pack mass and energy will be better defined). The battery mass is assumed to be the same as the MHS ones (273 g [10]), so it's about the 15% of the drone mass, its maximum storage energy is 43 Wh.
Ascent time will be computed imposing a nominal altitude to reach at 90% throttle and descent/landing time will be computed imposing a maximum vertical landing velocity.

These hypothesis are here summarized:

- Battery pack mass $m_B = 15\%$ Drone mass
- Battery energy [6] $E_B = 0.1589\,\frac{Wh}{g} \cdot m_B\,[g]$
- Throttle in hovering $\xi_{hover} = 85\%$
- Throttle @ lift-off $\xi_{l.o.} = 90\%$
- Maximum vertical landing velocity $= 0.5\,m/s$

Once chosen rotor dimension and drone mass from the Trade-off Analysis it is possible to determine the mission profile in Figure 5.5.

5.2.1 Trade-off analysis

There are three main constraints that drive the design: the environmental properties, the drone mass and the drone dimensions, alternatively one can impose a flight duration as a requirement. The drone maximum dimension is given by the **rotor radius** (or diameter) that normally comes from space vehicle requirements (e.g. the launcher) but **we assume it is the maximum testable radius in the PHASE vacuum chamber** (Appendix C).
The atmospheric density is supposed to be constant in order to not affect the rotor characteristic coefficients obtained with that precise simulation density [7], even if they shouldn't change with density variations by definition.

Assuming that the rotor axis can be aligned with the PHASE chamber axis the maximum rotor diameter is 715 mm due to the breadboard support sledges. Here we assume a **maximum diameter of 600 mm** to avoid accidental contacts with the chamber walls during any oscillation and to have a little gap between blades tips and walls in order to not obstruct too much the generation of tip vortices that would misrepresent tip losses.

The assumed design data to test will be:

- Drone mass 1 kg $< m_D <$ 1.8 kg
- Number of rotors N = 4
- Rotor radius 200 mm < R < 300 mm
- Gap between two blades $l_{gap} = 50$ mm
- Hovering throttle $\xi_{hover} = 85\%$
- Throttle @ lift-off $\xi_{l.o.} = 90\%$
- Atmospheric density $\rho_M = 0.0167\ kg/m^3$
- Gravitational acceleration $g_M = 3.71\ m/s^2$
- Speed of sound $a_M = 232.26\ m/s$
- Max Mach @ tip $M_{tip} = 0.65$
- Battery pack mass $m_B = 15\%$ Drone mass
- Battery energy [6] $E_B = 0.1589\ \frac{Wh}{g} \cdot m_B\ [g]$
- Maximum vertical landing velocity $v_l = 0.5\,m/s$
- Nominal flight altitude z = 10 m

5.2.2 Trade-off analysis results

Assuming the above mentioned design data and by varying mass and rotor radius it is possible to compute the performances requested by the rotor itself to lift off a given drone mass. With these results it is possible to look for a motor and a gearbox (if needed) to match the rotor in order to allow it to work properly. The mass of the propulsion group must be as lower as possible. The solution which gives the largest mass budged will be chosen. Performances variations with mass and rotor radius are shown in Figure 5.4.

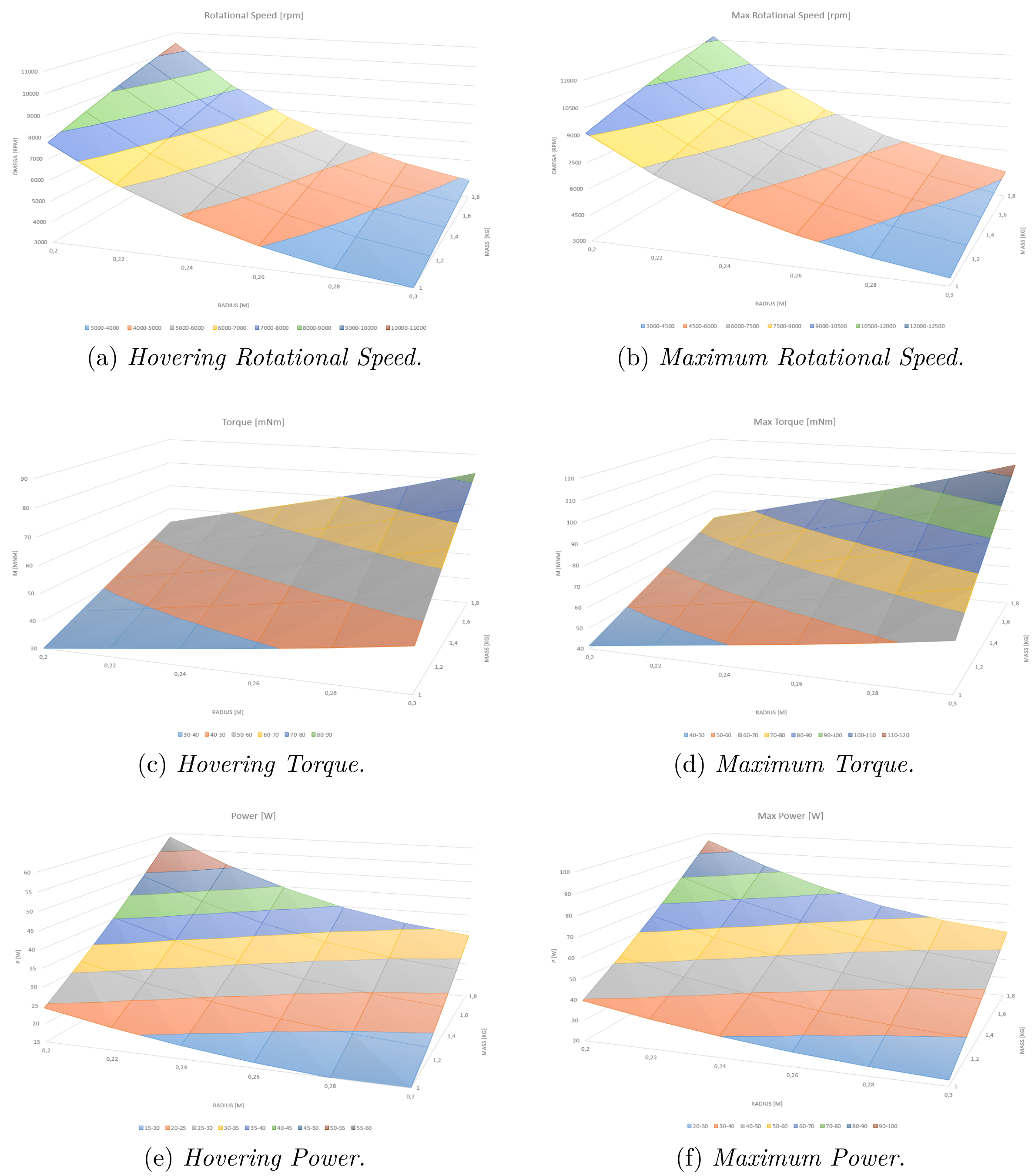

(a) *Hovering Rotational Speed.*

(b) *Maximum Rotational Speed.*

(c) *Hovering Torque.*

(d) *Maximum Torque.*

(e) *Hovering Power.*

(f) *Maximum Power.*

Figure 5.4: Trade-off Analysis Results.

A summary of the results in Figure 5.4 are reported in Table 5.5:

CASE	MIN	MAX
$\boldsymbol{\Omega_h}$ $\boldsymbol{\Omega_{max}}$	2915 rpm @ m = 1.0 kg , R = 0.3 m 3429 rpm @ m = 1.0 kg , R = 0.3 m	10400 rpm @ m = 1.8 kg , R = 0.2 m 12236 rpm @ m = 1.8 kg , R = 0.2 m
$\boldsymbol{M_h}$ $\boldsymbol{M_{max}}$	30 mNm @ m = 1.0 kg , R = 0.2 m 42 mNm @ m = 1.0 kg , R = 0.2 m	83 mNm @ m = 1.8 kg , R = 0.3 m 114 mNm @ m = 1.8 kg , R = 0.3 m
$\boldsymbol{P_h}$ $\boldsymbol{P_{max}}$	14 W @ m = 1.0 kg , R = 0.3 m 23 W @ m = 1.0 kg , R = 0.3 m	59 W @ m = 1.8 kg , R = 0.2 m 96 W @ m = 1.8 kg , R = 0.2 m

Table 5.5: Trade-off Results Table.

The most important parameter is the requested power (per rotor), high power means larger and heavier battery and motor. Since a larger rotor is more efficient than a smaller one and since the only requirement for dimension is given by the rotor diameter **a rotor radius equal to 0.3 m is adopted**.

Torque and rotational speed are both important in order to chose a motor once the motor power has been identified.
Power demand for the larger rotor (0.3 m) is 23 W for the 1.0 kg drone and goes up to 55 W for the larger one (1.8 kg). Unfortunately for the smallest configuration the weight of each motor is still too high (150 g the best solution found: MAXON EC-i 30 45 W) due to the high requested torque. Such a propulsion group weight would not leave enough mass budget for the other drone components so this solution has been discarded even if it doesn't need any gearbox.
All the other analysed solutions need a gearbox in order to reduce the motor requested torque. The necessity of using a planetary reduction do increment the motor requested power and torque due to the efficiency of the gearbox itself so the lightest solution found is the same for all the other analyses cases: 1.2, 1.4, 1.6 and 1.8 kg. So the best solution is that with the largest mass budget that is the 1.8 kg drone.
A drone mass of 1.8 kg will be adopted.

The detailed analysis of the motor solution found is shown in Section 5.3.

The rotational speed profile for the 1.8 kg, 0.3 m rotor radius drone is:

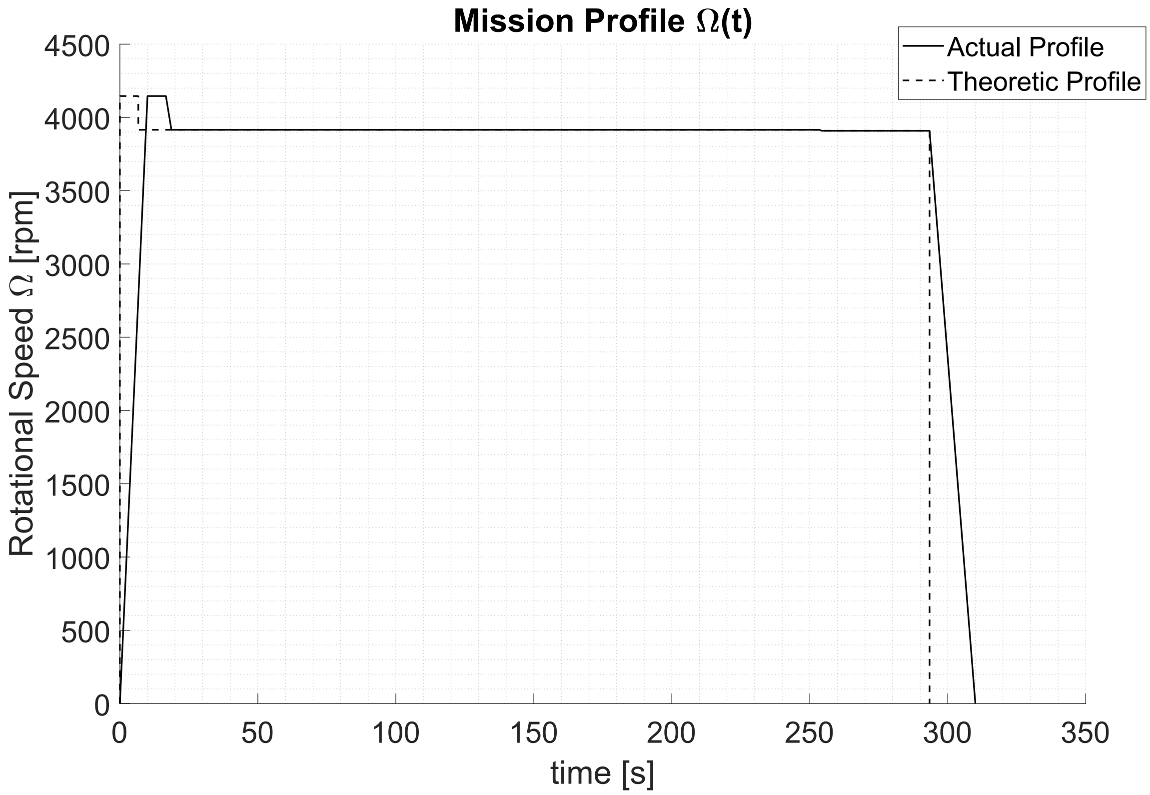

Figure 5.5: Mission profile.

This mission profile (Figure 5.5) is the one simulated in all the thermal analyses of Chapter 6.
The mission profile simulated in the MATLAB model (Chapter 4) is a little different because the detailed motor propulsion group design had not been done yet, in particular the greatest difference is given by the introduction of the gearbox.

5.3 Motor choice

In order to choose a motor the driver is the **load mechanical characteristics** (M-n curve). In our case the "load" is the rotor and its M-n curve is given by the equation

$$M = \rho A R^3 \Omega^2 C_M = \rho \pi R^5 \left(\frac{\pi \cdot n}{30}\right)^2 \cdot C_M \propto n^2 \tag{5.2}$$

The load curve for a given propeller changes only with density. For the PoliTO rotor the load curves are, for $\rho = [0.012 \ , \ 0.014 \ , \ 0.0167] \ kg/m^3$:

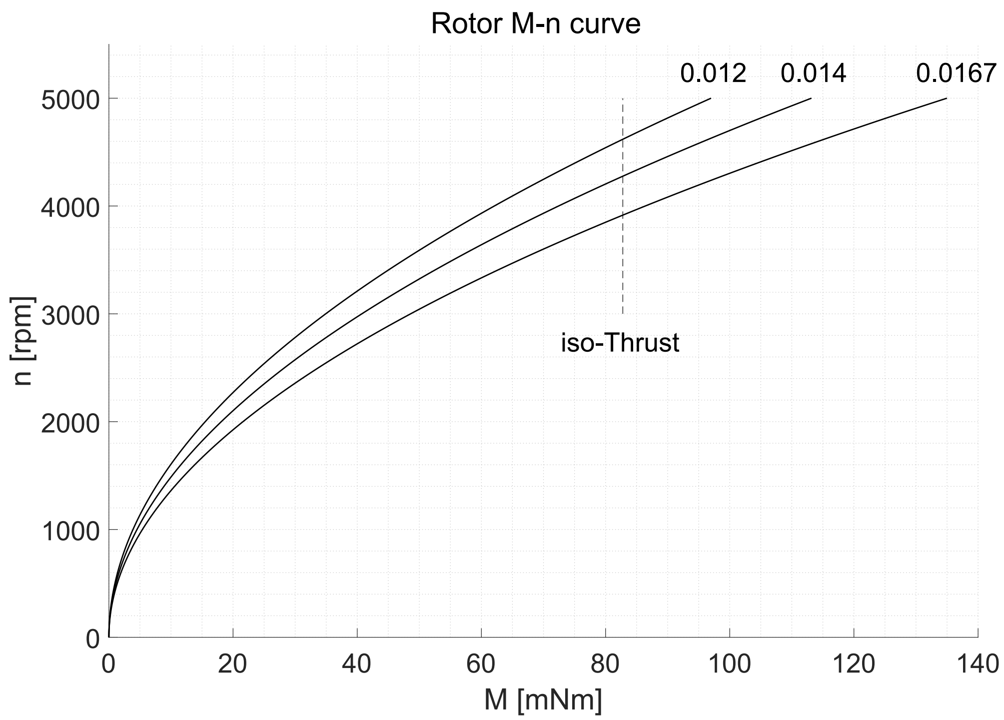

Figure 5.6: Rotors M-n curves.

The assumption of constant coefficients imposes that, for a given thrust, the required torque doesn't change with density variations (see Section 3.4).
Another way to see that torque is constant on iso-thrust lines is:

$$T = const = \rho \pi R^4 \left(\frac{\pi \cdot n}{30}\right)^2 \cdot C_T \ \Rightarrow \rho \cdot n^2 = const \ \Rightarrow n^2 = \frac{const}{\rho}$$

$$\text{so} \quad M = \rho \pi R^5 \left(\frac{\pi \cdot n}{30}\right)^2 \cdot C_M = \frac{\pi^3 R^5 C_M}{30^2} \cdot \boldsymbol{\rho} \cdot \frac{const}{\boldsymbol{\rho}} = constant$$

Once known the load M-n curve it is necessary to identify the **EXTREME OPERATION POINT (EOP)** which is the point where the motor is supposed to work only for a limited time at the maximum mechanical and thermal stresses.

For a rotor this point is represented by the maximum power point and, since it works on a monotone line, both M and n are at their maximum values so $M = M_{P_{max}}$ and $n = n_{P_{max}}$.
To be consistent with the previous chapter assumptions the extreme operation point is evaluated at $\rho = 0.0167\ kg/m^3$ so:

$$M^{(m)}_{EOP} = M^{(r)}_{P_{max}} = 114.6\, mNm \quad \text{EOP torque} \tag{5.3}$$
$$n^{(m)}_{EOP} = n^{(r)}_{P_{max}} = 4606.43\, rpm \quad \text{EOP rotational speed} \tag{5.4}$$

where:

- $^{(m)}$ indicates the motor shaft
- $^{(r)}$ indicates the rotor shaft

These values are the same for motor and rotor shaft if no gearbox (GB) is used. If instead it is necessary to use a reducer, those values are:

$$M^{(m)}_{EOP} = \frac{M^{(r)}_{P_{max}}}{\eta_{GB} \cdot i} \quad \text{EOP torque (GB)} \tag{5.5}$$
$$n^{(m)}_{EOP} = n^{(r)}_{P_{max}} \cdot i \quad \text{EOP rotational speed (GB)} \tag{5.6}$$

where:

- η_{GB} is the gearbox efficiency
- i is the gearbox reduction ratio

Reminding that the higher the torque the heavier the motor at fixed speed n, many motors from different supplier catalogues were discarded because too heavy for the 1.8 kg drone.
Many light BLDC motors are likely to spin faster then 5000 rpm with high efficiency but low torque so the introduction of a gearbox would allow to choose a lighter motor and usually this leads to a lighter solution even if the weight of the gearbox has to be accounted.

The motor we are looking for is an inrunner type instead of an outrunner. The latter is usually able to provide more torque at the same speed and is a little lighter, but is not protected enough from the external environment and Martian dust. Moreover the windings are placed on the stator that is inside the motor and they are more difficult to cool down during working phases, keeping in mind that no air intakes are allowed due to dust protection (see Appendix B for more information about BLDC motors).

Different MAXON and FAULHABER motor/gearbox solution were compared (comparison based on catalogues data):

		Reduction Ratio
Motor	**Maxon EC-4 pole 22, 22 mm, 90 W**	
Gearbox	GP 13 A, 13 mm, 0.2-0.35 Nm	4.1 : 1
Gearbox	GP 13 A, 13 mm, 0.2-0.35 Nm	5.1 : 1
Gearbox	GP 16 C, 16 mm, 0.2-0.6 Nm	4.4 : 1
Gearbox	GP 16 C, 16 mm, 0.2-0.6 Nm	5.4 : 1
Gearbox	GP 22 HP, 22 mm, 2.0-3.4 Nm	3.8 : 1
Gearbox	GP 22 HP, 22 mm, 2.0-3.4 Nm	4.4 : 1
Gearbox	GP 22 HP, 22 mm, 2.0-3.4 Nm	5.4 : 1
Motor	**Maxon EC-4 pole 22, 22 mm, 120 W**	
Gearbox	GP 13 A, 13 mm, 0.2-0.35 Nm	4.1 : 1
Gearbox	GP 13 A, 13 mm, 0.2-0.35 Nm	5.1 : 1
Gearbox	GP 16 C, 16 mm, 0.2-0.6 Nm	4.4 : 1
Gearbox	GP 16 C, 16 mm, 0.2-0.6 Nm	5.4 : 1
Gearbox	GP 22 HP, 22 mm, 2.0-3.4 Nm	3.8 : 1
Gearbox	GP 22 HP, 22 mm, 2.0-3.4 Nm	4.4 : 1
Gearbox	GP 22 HP, 22 mm, 2.0-3.4 Nm	5.4 : 1
Motor	**FAULHABER 2264...BP4**	
Gearbox	15/10, 0.35 Nm	3.33 : 1
Gearbox	15/10, 0.35 Nm	4.5 : 1
Gearbox	17/1, 0.55 Nm	3.33 : 1
Gearbox	17/1, 0.55 Nm	4.5 : 1
Gearbox	20/1 R, 0.8 Nm	3.71 : 1
Gearbox	26/1 R, 0.4 Nm	3.71 : 1

Table 5.6: Solutions tested.

The best solution seems to be:

- **Motor:** MAXON EC-4 pole 22, 22 mm, 90 W
- **Gearbox:** MAXON GP 22 HP, 22 mm, 2.0-3.4 Nm, $i = 3.8 : 1$

but it must be verified if this configuration is able to work at the EOP.

In order to validate the above mentioned solution it is necessary to match the motor with the load because a given motor could have enough nominal power, torque and speed but may be inadequate to work at the EXTREME OPERATION POINT represented by the rotor maximum power. In fact every motor usually may have different windings so could be able or unable to accomplish the task.
To choose the correct motor the following steps were followed:

1. Calculate $M_{EOP}^{(m)}$ and $n_{EOP}^{(m)}$ through equations 5.5, 5.6.

2. Compute
$$V_{EOP} = \frac{1}{k_n}\left(n_{EOP}^{(m)} + \frac{\Delta n}{\Delta M} \cdot M_{EOP}^{(m)}\right) \quad [V] \tag{5.7}$$
where:
   - V_{EOP} is the EOP motor tension [V]
   - k_n is the velocity constant [rpm/V]
   - $\frac{\Delta n}{\Delta M}$ is the M-n curve slope [rpm/mNm]

3. Chose a motor model with a similar (if possible higher) nominal voltage.

4. Set a maximum supplier voltage, possibly a little higher than the motor nominal voltage (it will be regulated by the motor ECU to the proper value).

5. Compute
$$k_{n_{min}} = \frac{n_{EOP}^{(m)} + \frac{\Delta n}{\Delta M} \cdot M_{EOP}^{(m)}}{V_{mot}} \quad [rpm/V] \tag{5.8}$$
where V_{mot} can be intended as the supplier voltage.

6. If $k_{n_{min}} \approx 0.8 \cdot k_n$ the motor is able to spin the load properly. If $k_{n_{min}} > k_n$ the motor can't be used, if $k_{n_{min}} << k_n$ the motor is oversized and would run with low efficiency and high drained current.

7. Once found the proper motor and supplier tension is must be check if the EOP is placed inside the *continuous operation zone* or at least in the *continuous operation with reduced thermal resistance zone*. It is not admitted to be placed in the *intermittent operation zone* because the rotor must spin smoothly.

8. Draw the matching M-n curve for the proposed solution.

The above mentioned steps were done for every combination in Table 5.6 and the MAXON solution introduced in the previous page was confirmed.

5.3.1 Motor-Rotor M-n matching graph

The matching M-n graph for the MAXON solution is:

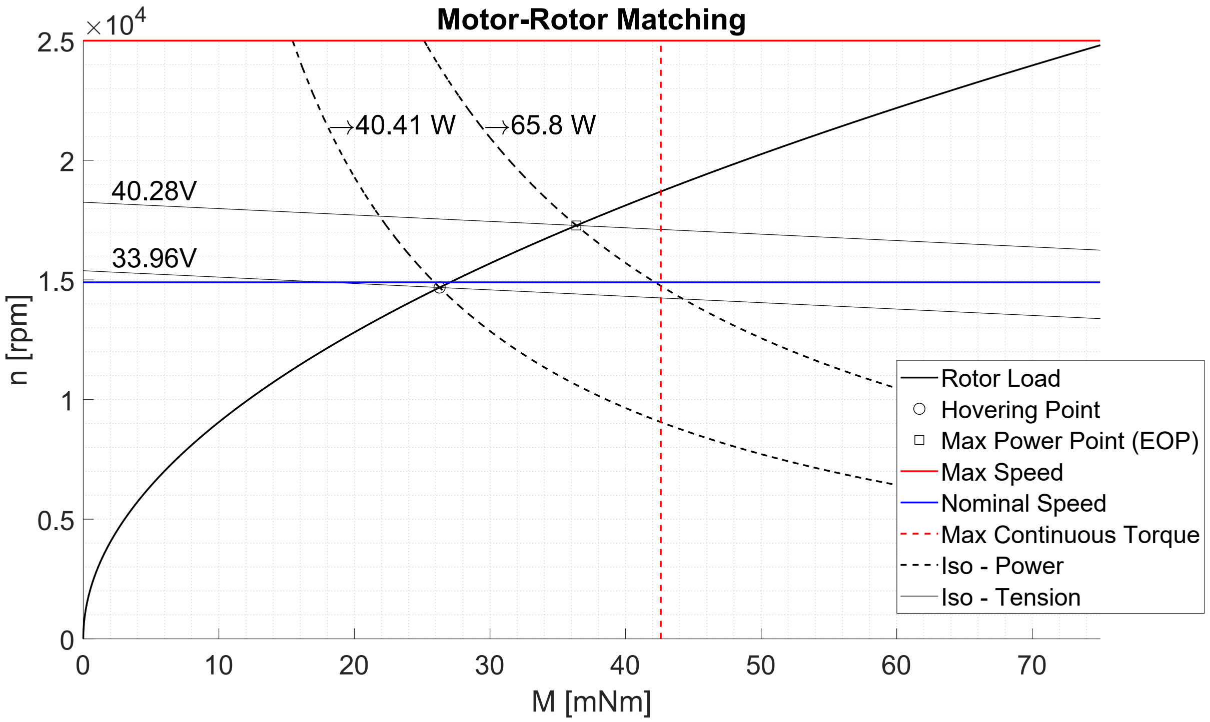

Figure 5.7: Rotor-Motor M-n matching.

The motor has a nominal tension of 36 V but needs more than 40.28 V to reach the EOP. A supplier voltage of 48 V is therefore necessary. Since $V_{EOP} > V_N$ it must be checked if the EOP is inside the *continuous operational zone* (Figure 5.8).

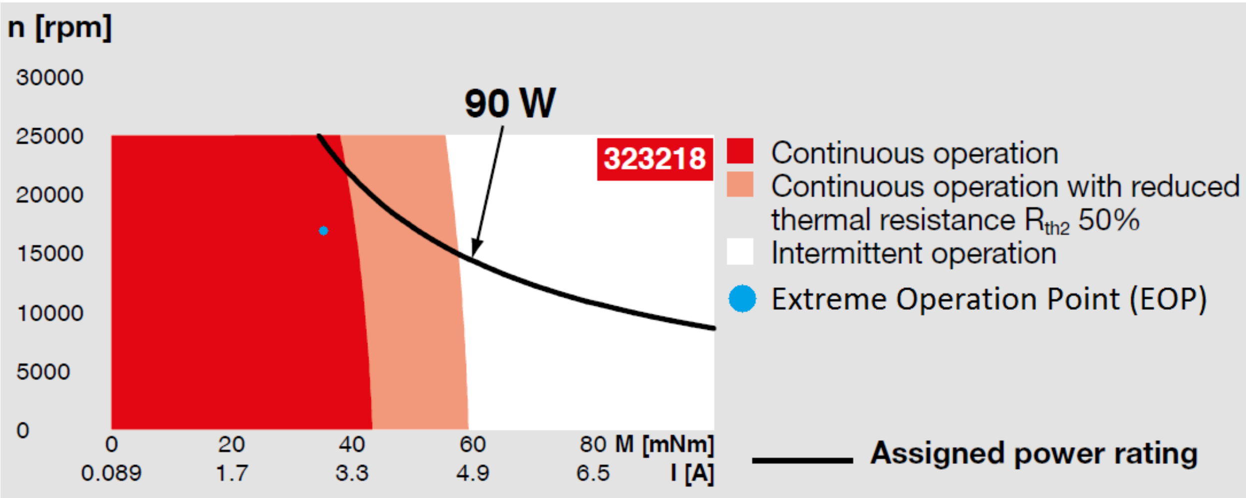

Figure 5.8: Motor absorbed current check.

Since the EOP is inside the red zone the motor is able to run the rotor properly.

A summary of motor and gearbox characteristics are here listed:

1. **Motor**

- Motor name: MAXON EC-4 pole 22
- Part number: 323219
- Diameter: 22 mm
- Nominal voltage: 36 V
- Nominal current: 2.16 A
- No load current: 0.109 A
- Nominal speed: 14900 rpm
- Max. speed: 25000 rpm
- Nominal torque: 43.7 mNm
- Max efficiency: 88%
- Torque constant: 21.1 mNm/A
- Speed constant: 453 rpm/V
- $\Delta n/\Delta M$: 26.7 rpm/mNm
- Thermal resistance housing-ambient (standard Earth conditions): 12.2 K/W
- Thermal resistance housing-winding (standard Earth conditions): 1.19 K/W
- Thermal time constant winding: 5.12 s
- Thermal time constant motor: 482 s
- Ambient temperature: -20...+100 °C
- Max. winding temperature: +155 °C
- Max. axial load (dynamic): 4 N
- Weight: 125 g

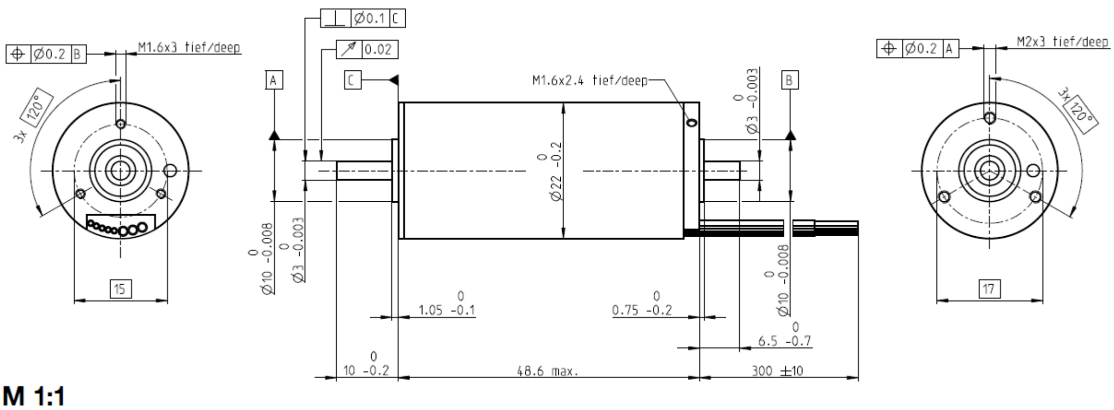

M 1:1

Figure 5.9: Motor dimensions.

2. **Gearbox**

- Gearbox name: Planetary Gearhead GP 22 HP
- Part number: 370683
- Diameter: 22 mm
- Max. transmittable power (continuous): 150 W
- Max. continuous torque: 2 Nm
- Max. continuous input speed: 12000 rpm
- Max. efficiency: 84%
- Max. axial load (dynamic): 100 N
- Recommended temperature range: -40...+100 °C
- Reduction: 3.8 : 1 (absolute reduction 15/4)
- Weight: 51 g

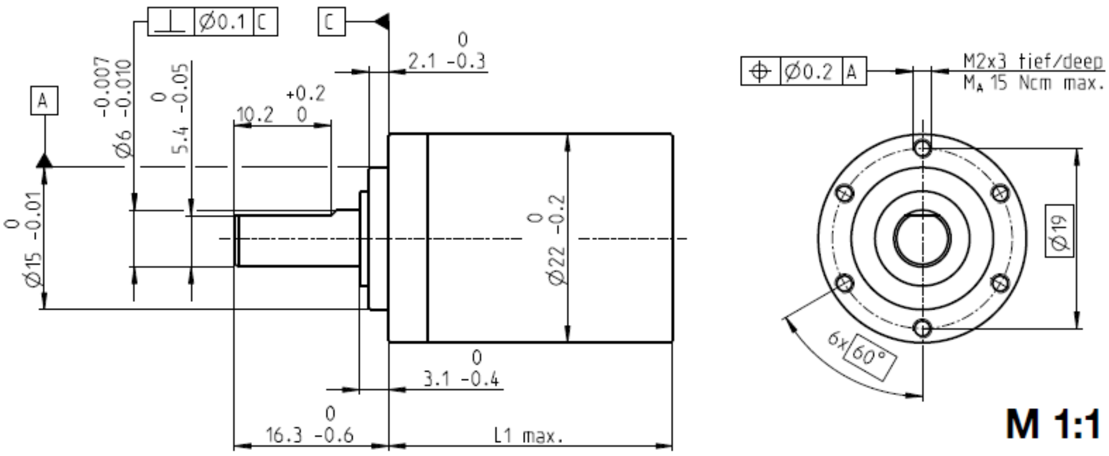

Figure 5.10: Gearbox dimensions.

5.3.2 Motor CAD

Here some images about motor and gearbox are shown.

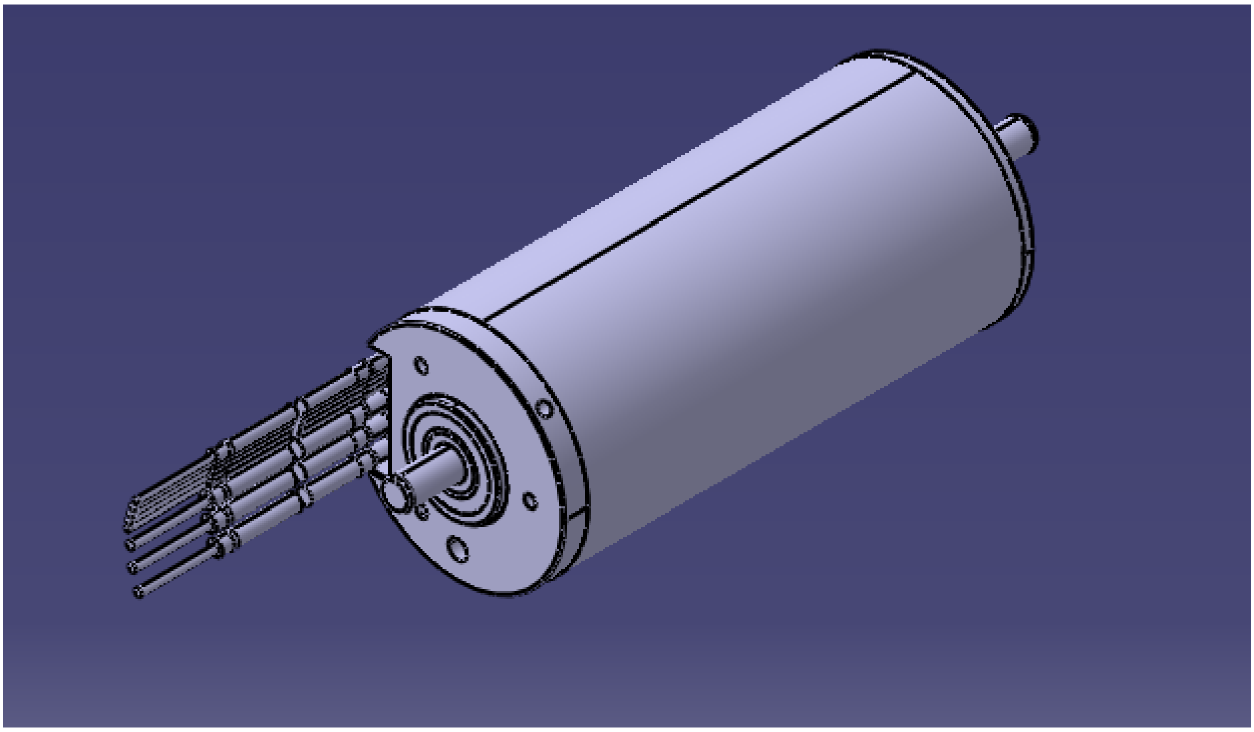

Figure 5.11: Motor CAD.

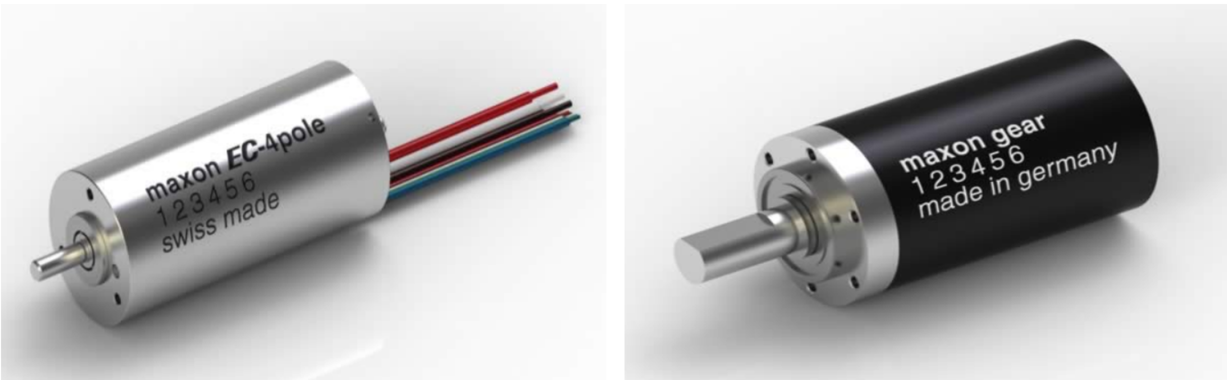

(a) *Motor image.*

(b) *Gearbox image.*

Figure 5.12: Motor and gearbox pictures.

5.4 Preliminary design results summary

In this section all the drone design parameters obtained from the trade-off and preliminary design analysis are summarized and synthesized in form of bullet list.

5.4.1 Drone and Rotor data

- Drone mass $m_D = 1.8$ kg
- Number of rotors $N = 4$
- Rotors radius $R = 0.3$ m
- $C_T = 0.0234$
- $C_M = C_P = 0.00386$
- Gap between rotors $l_{gap} = 5$ cm
- Maximum drone dimension

$$L_{max} = (4R + l_{gap}) \cdot \sqrt{2} = 1.768 \ m \tag{5.9}$$

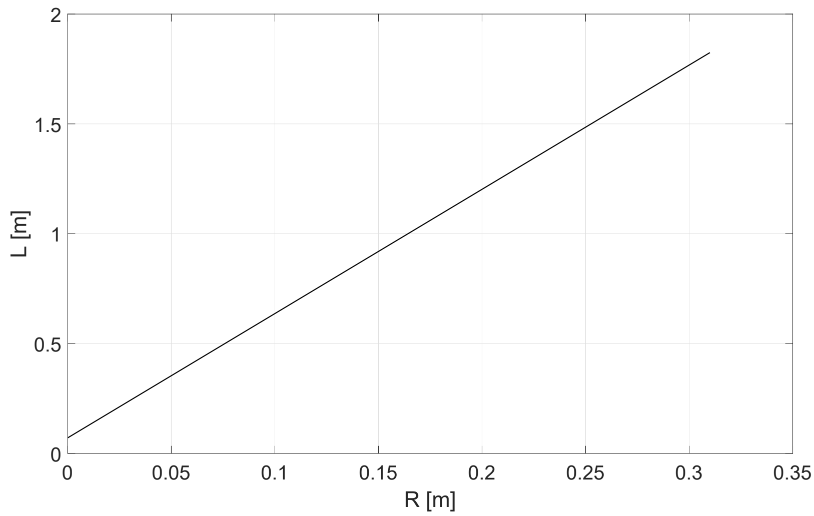

Figure 5.13: Quadcopter dimension increases with rotor radius.

- Battery mass $m_B = 270$ g
- Battery energy $E_B = 43$ Wh
- Hovering Altitude $z = 10$ m
- Touchdown velocity $v_l = 0.5$ m/s

- Thrust in hovering $T_{hover} = \frac{1.8 \cdot 3.71}{4} = 1.670$ N
- Hovering rotational speed $\Omega_{hover} = 410.03\ rad/s = 3915.5\ rpm$
- Lift-off rotational speed $\Omega_{l.o.} = 434.15\ rad/s = 4145.8\ rpm$
- Maximum rotational speed $\Omega_{max} = 482.38\ rad/s = 4606.43\ rpm$
- Thrust @ lift-off/ascent $T_{l.o.} = 1.872$ N
- Maximum Thrust $T_{max} = 2.311$ N
- Rotor Torque in hovering $M_{hover} = 82.8\ mNm$
- Rotor Torque @ lift-off/ascent $M_{l.o.} = 92.8\ mNm$
- Rotor Maximum Torque $M_{max} = 114.6\ mNm$
- Rotor Power in hovering $P_{hover} = 33.94\ W$
- Rotor Power @ lift-off/ascent $P_{l.o.} = 40.29\ W$
- Rotor Maximum Power $P_{max} = 55.27\ W$
- Total flight time (theoretical) $t_{flight} = \frac{\text{Battery Energy}}{2 \cdot \frac{P_{max}}{\eta_{GB}} \cdot N} = 4.89 \approx 5$ min
- Total flight time (actual) $t_{flight} = 310$ s
- Landing rotational speed $\Omega_{land} = 3908.9$ rpm
- Landing throttle $\xi_{land} = 0.8485$

Red results have been used in Section 5.3 to choose the BLDC motor and gearbox.

5.4.2 Motor and Gearbox data

A detailed explanation about how motor and gearbox have been chosen is presented in Section 5.3. In this subsection data about mass and main (mechanical) characteristics of motor and gearbox are reported in form of bullet list:

1. *Motor Data*

   - Motor Power: 90 W
   - Nominal Voltage: 36 V
   - Nominal Torque: 43.7 mNm
   - Max Speed: 25000 rpm
   - Nominal Speed: 14900 rpm
   - Max Efficiency η_{max} : 0.88
   - Weight: 125 g

2. *Gearbox Data*

   - Max Transmissible Power (continuous): 150 W
   - Max continuous Torque: 2 Nm
   - Max continuous input speed: 12000 rpm (can be exceeded if transmitted torque is lower then max continuous torque)
   - Max Efficiency η_{max} : 0.84
   - Weight: 51 g
   - Number of stages: 1
   - Absolute reduction: $15/4 \approx 3.8 : 1$

5.5 Mass breakdown

Drone mass breakdown gives an overview about how much mass it's possible to allocate in other-than-propulsion components such as structure, payload and CPU. Through the assumption in previous subsections we have:

	Value	
SINGLE MOTOR MASS	125	[g] +
SINGLE GEARBOX MASS	51	[g] +
SINGLE ROTOR MASS	35	[g] +
SUBTOTAL (4 rotors)	844	[g] =
BATTERY MASS	270	[g] +
PROPULSION GROUP MASS	1114	[g] =
OTHER ELEMENTS MASS BUDGET	686	[g]
GYRO MASS	32	[g] +
CPU MASS	250	[g] +
PAYLOAD MASS	40	[g] +
TCS	0	[g] +
STRUCTURE	350	[g] +
COMPUTED TOTAL MASS	1786	[g] =
HYPOTHESISED TOTAL MASS	1800	[g]

Table 5.7: Mass Breakdown

- Structure is supposed to be made of a main carbon fibre bulkhead which incorporates the four motor support arms and a main body (avionic bay) made of plastic walls and aerogel-filled inter space.
- Gyroscope is a small 2x2x2 cm tri-axis gyroscope, tri-axis accelerometer which weighs 16 g. It's weight has been doubled to keep into account a possible redundant unit.
- CPU mass is similar to the one used in actual Mars missions and includes the electronics and antenna to communicate with its base or with a rover.
- Payload consists of a HD camera shielded from radiations.
- TCS mass is not considered, it will be eventually proposed after analyses in Chapter 6.

Chapter 6

ESATAN-TMS Drone Thermal Analysis

In this Chapter is described a detailed thermal and energy balance analysis of the whole drone using the ESA's thermal analysis software **ESATAN-TMS** (**E**uropean **S**pace **A**gency **T**hermal **A**nalysis **N**etwork - **T**hermal **M**odelling **S**uite) .

ESATAN allows to simulate complex geometries in a dynamic environment both with Lumped Parameters and/or FEM approach and it is based on a simil-FORTRAN programming language called **MORTRAN** (**MO**dified fo**RTRAN**) which integrates an internal geometry modelling suite, the TMS, which allows to define the system geometry and to compute some **linear conductors (GL)** (conductive, convective conductors), **thermal capacitances** (**C**) and **radiative conductances (GR)**, the latter through the ray-tracing algorithm using the Monte Carlo method.

Heat transfers are computed in ESATAN as following:

- Conductive or convective heat transfer between nodes i and j:

$$Q_{i,j} = GL_{ij} \cdot (T_i - T_j) \tag{6.1}$$

where GL_{ij} [W/K] is defined as (example):

$$GL_{ij} = \frac{k \cdot A_c}{d_{i,j}} \qquad \text{for planar conduction}$$
$$GL_{ij} = h \cdot A \qquad \text{for convective heat transfer}$$

and

  - A_c is the contact area between nodes i and j
  - $d_{i,j}$ is the distance between the centres of mass of nodes i and j
  - A is the area in contact with the fluid

- Radiative infrared heat transfer between nodes i and j:

$$Q_{i,j} = \sigma \cdot GR_{ij} \cdot (T_i^4 - T_j^4) \tag{6.2}$$

  where σGR_{ij} $[W/K^4]$ is a complex function of the optical properties ϵ of nodes i,j and all the other nodes and accounts for the system geometry too.
  A good approximation is:

$$\sigma GR_{ij} = \sigma \cdot \epsilon_i \cdot \epsilon_j \cdot A_i \cdot FoV_{i,j}$$
$$\sigma \rightarrow \text{ Stephan-Boltzmann constant } [W/(m^2K^4)]$$

- Solar power absorbed by node i: QS_i
- Power dissipated by node i: QI_i
- Heater power applied on node i: QR_i

For the thermal analyses a Lumped Parameters approach was used considering the following steps:

1. Definition of motor geometry using manufacturer catalogue data (GMM)
2. Definition of a simple, thermally representative, drone geometry (GMM)
3. Definition of the Martian surface geometry (GMM)
4. Calculation of GR and solar absorbed power in a typical Martian Sol (GMM)
5. Definition of **drone and motor main conductors and thermal capacitances** (Input)
6. Integration of MATLAB model routines to calculate convective heat transfer and motor power consumption (TMM)
7. Integration of different TCS (Thermal Control System) solutions (TMM)

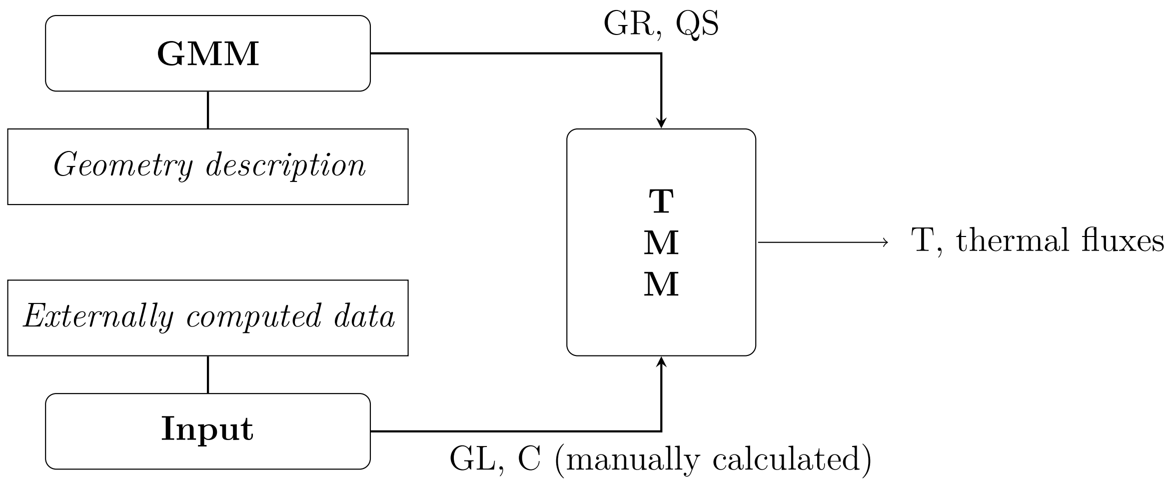

The purpose of this model is to better simulate the whole drone thermal behaviour in the dynamic Martian environment during both operational and non-operational mission phases. In fact the main driving factor in the NASA's Mars Helicopter Scout thermal design was minimizing survival heater energy while maintaining compliance with temperature requirements for all system components. This problem was introduced in Chapter 4 through different runs of the MATLAB model but it could not simulate properly the Martian time-variable thermal environment.
A simple verification of the MATLAB model routines was done in ESATAN (MORTRAN) (Figure 6.1).

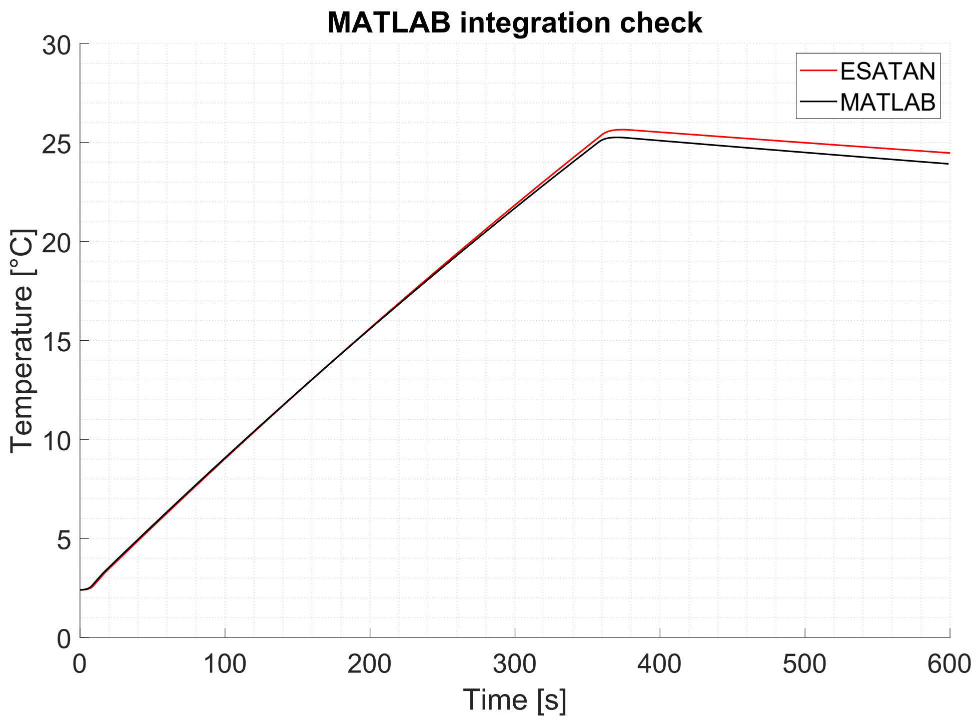

Figure 6.1: Routines check.

Results show that the maximum difference between the two runs is really small (about 0.54 °C due to the better environment simulation in ESATAN), this validates the integration method used in MATLAB model and its preliminary results.

6.1 Geometrical Mathematical Model (GMM)

The first step toward the thermal analysis with ESATAN-TMS was defining motor, drone and Mars geometry. It is important to note that an actual drone CAD was not available. However, from the thermal point of view, **an exact geometry representation was not needed because most of the lumped parameters network values were computed manually, externally or by functions/routines, then the geometry was important only for the radiative heat transfer in terms of GR and for solar absorbed power**. Therefore a thermally representative geometry was modelled in the TMS environment (Figure 6.4).
Results of GMM are GR and QS.

6.1.1 Motor geometry

Manufacturers do not usually supply internal motor features in a CAD because of product protection. To overcome the problem the manufacturer catalogue pictures were used in order to extrapolate main component dimensions such as magnet, housing and shaft.
In Figures 6.2 and 6.3 are shown respectively the real motor and the ESATAN-TMS geometrical representation.

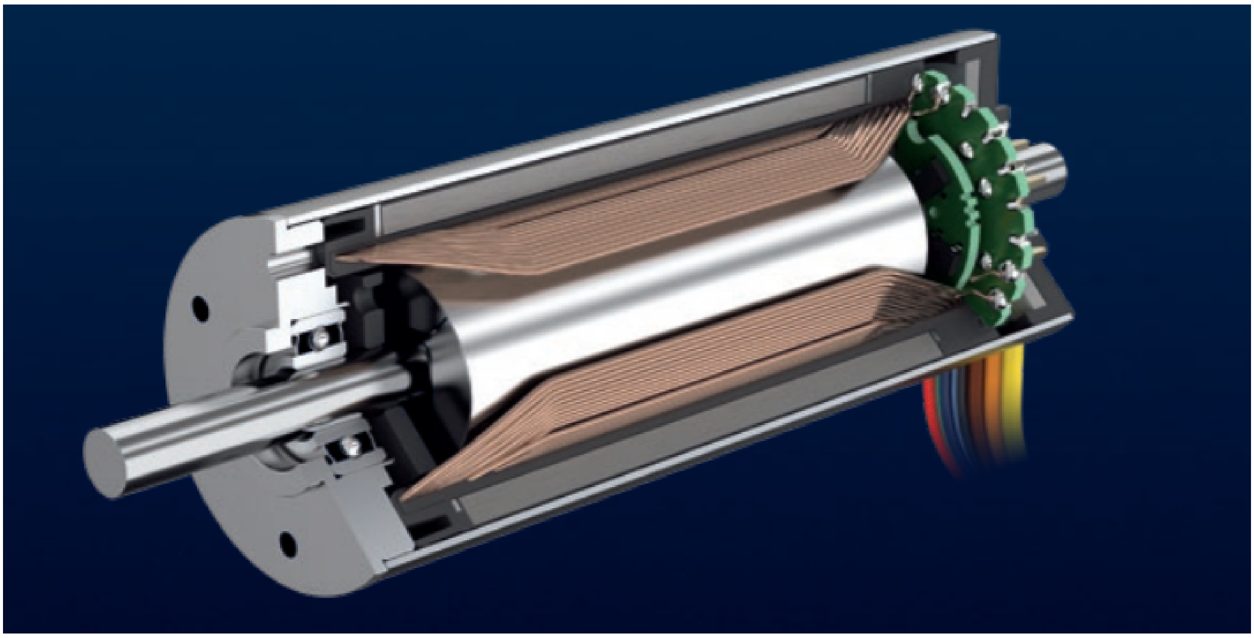

Figure 6.2: Catalogue motor picture.

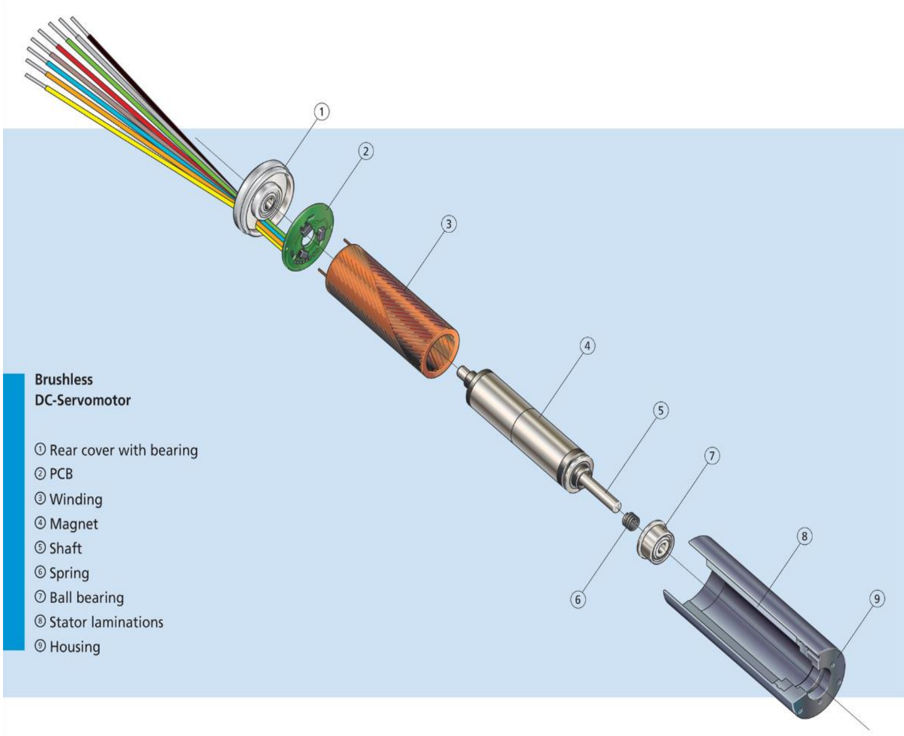

(a) Motor exploded view.

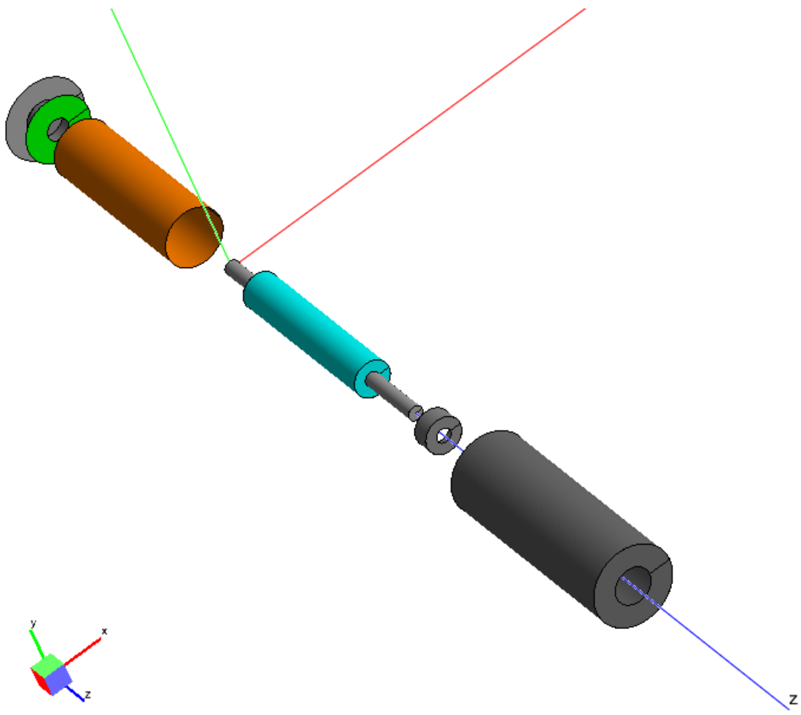

(b) ESATAN-TMS representation.

Figure 6.3: Motor geometry in ESATAN-TMS.

6.1.2 Drone geometry

Since an actual drone CAD configuration did not exist a simple, thermally representative geometry of a typical terrestrial quadcopter was modelled.

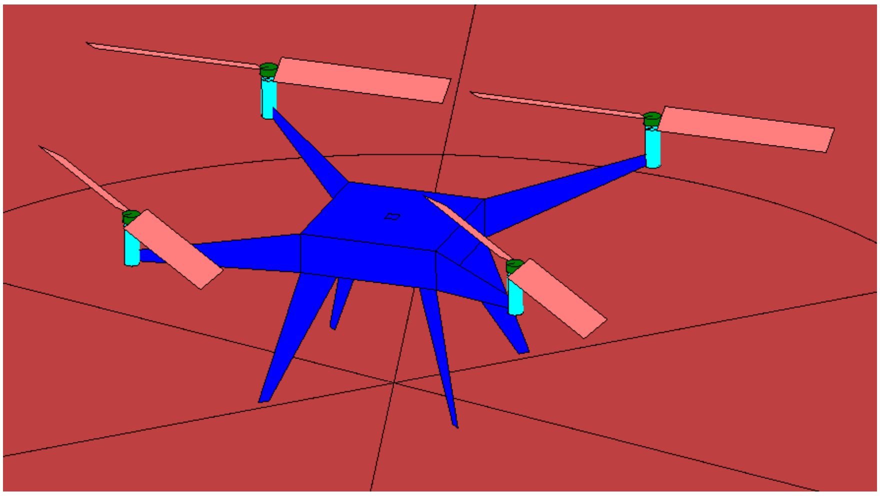

Figure 6.4: Drone thermal representative geometry.

6.1.3 Mars geometry

Martian surface was modelled with a radiative inactive sphere and a radiative active planar landing area, which represents the surface right below the drone extended almost to the horizon. In Figure 6.5(b) it is possible to see the landing area position of the drone during a Martian Sol (viewed from far Sun).

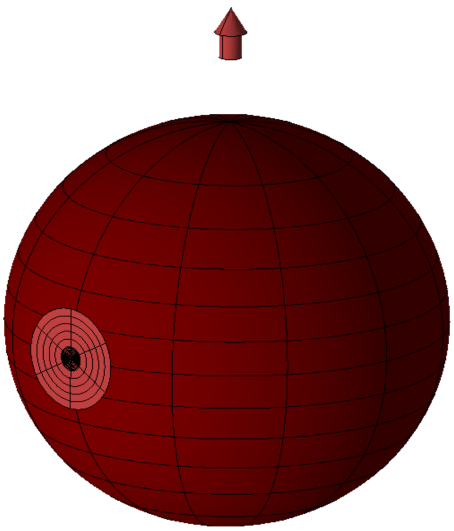

(a) Mars representation.

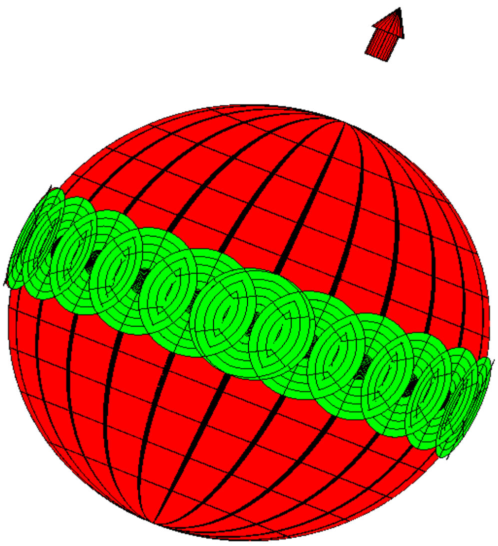

(b) Orbital representation (far Sun).

Figure 6.5: Mars thermal representative geometry.

6.2 Thermal Mathematical Model (TMM)

The TMM is the .d file where all the thermal informations, the call to the subroutines/functions and the output logic are placed. To be precise a pre-compiler generates a FORTRAN 77 executable .f file from the .d and then the .f is compiled by a FORTRAN compiler and linked to the ESATAN library.
The TMM is organized as follows:

$MODEL
- DATA BLOCKS
- OPERATION BLOCKS
$ENDMODEL

- DATA BLOCKS include all the informations from the GMM and Input data set manually or externally computed.
- OPERATION BLOCKS are:
  - $SUBROUTINES: all the MATLAB routines and the ones related to the drone are included in this block
  - $INITIAL: initial conditions
  - $VARIABLES1: parameters set at the start of each time step
  - $VARIABLES2: parameters set at the end of each time step
  - $EXECUTION: informations about solution parameters and different analyses cases are contained in this box
  - $OUTPUTS: how to write the results

The solution process for transient analysis is:

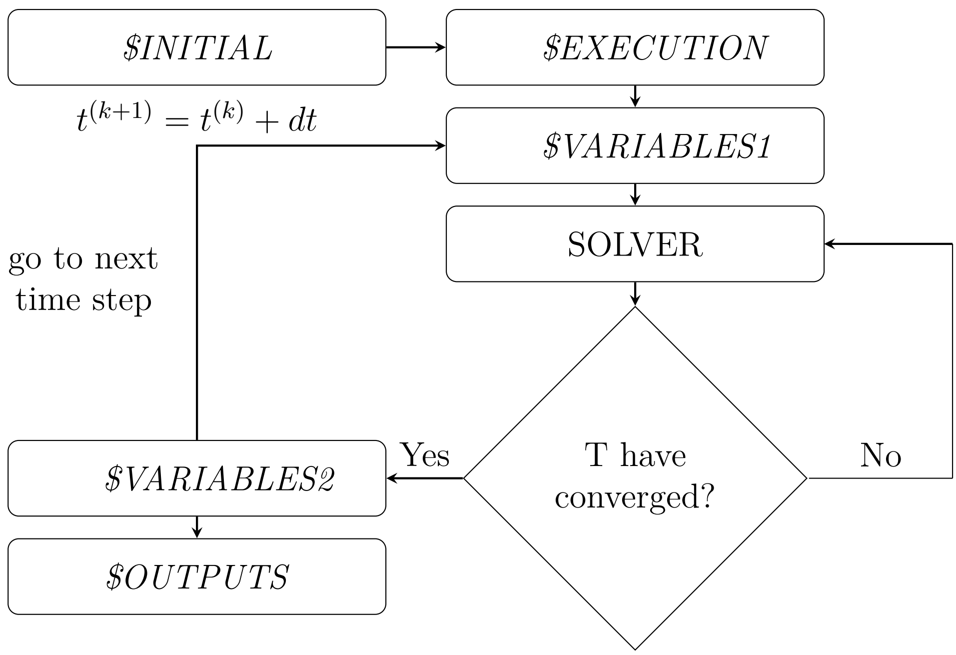

One of the most useful features of ESATAN is the possibility to build a model which includes submodels. A submodel is defined in the same way as the main model and it's included in the latter through a $INCLUDE. This hierarchy allows to better control the design and to separate different entities. Usually the most important routines are included only in the main model.

MAIN MODEL

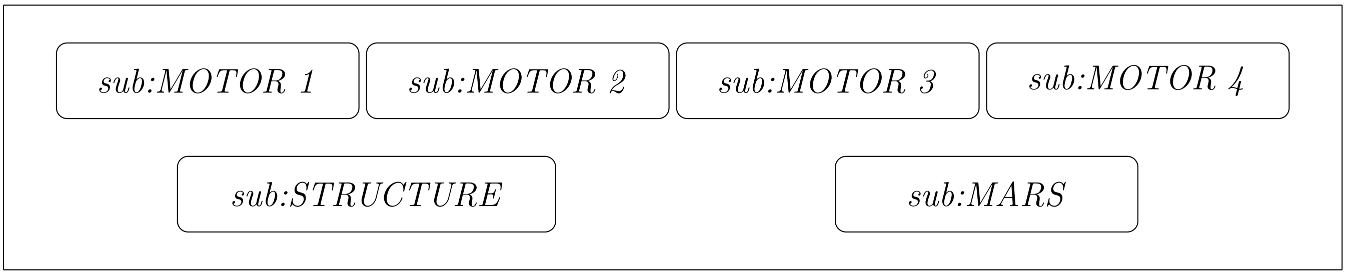

Inside each model/submodel there are different types of nodes:

- Diffusive nodes (D)
- Boundary nodes (B)
- Inactive nodes (X)
- FHTS (Fluid Heat Transfer System) nodes

For the purpose of our analyses only diffusive, boundary and inactive nodes are used.

Moreover, from the radiative point of view, a node can be defined as:

- Active: its surfaces are radiative and therefore radiative heat transfer is allowed. GR are calculated.
- Inactive: its surfaces are not allowed to transfer heat by radiation and therefore there are not GR involving these nodes.

6.2.1 Motor submodel

Since the actual dimensions of the internal components were not available it was chosen to compute the motor total thermal capacitance as explained in Chapter 4:

$$C_{housing} \approx \tau_m \cdot GL_{h-e} = 39.53 \ [J/K]$$
$$C_{winding} \approx \tau_w \cdot GL_{w-h} = 4.30 \ [J/K]$$
$$C_{tot} \approx C_h + C_w = 43.83 \ [J/K]$$

where:

- $\tau_m = 482$ [s] (Section 5.3)
- $\tau_w = 5.12$ [s] (Section 5.3)
- $GL_{h-e} = GL_{housing-environment} = 0.082$ [W/K] (Section 5.3)
- $GL_{w-h} = GL_{winding-housing} = 0.840$ [W/K] (Section 5.3)
- $C_{housing} = C_h$ is intended to be the thermal capacitance of all the components attached to the housing.

Those capacitance values were distributed among the 8 motor main components weighing them with the hypothetical thermal capacitance of each component computed with the extrapolated geometry dimensions and materials.
Results are:

NODE	Component	C [J/K]
1	Rear cover	2.1
2	PCB	1.4
3	Winding	4.3
4	Magnet	5.5
5	Shaft	7.4
6	Rear cover bearing	1.2
7	Housing bearing	1.2
8	Housing with laminations	20.73
		= 43.83

Table 6.1: Motor components thermal capacitance.

These values were set manually inside the motor TMM.
Other important parameters included in the motor TMM $VARIABLES1 are the convective heat transfer, power dissipation and heater control calls to the routines which set the proper parameters for the current time step with regard to QI and heat fluxes about motor components. If enabled, motor heaters power is $QR_{motor} = 1 \ W$.

The Lumped Parameters Thermal Network (LPTN) of the BLDC motor is shown Figure 6.6 and was introduced in Chapter 4.

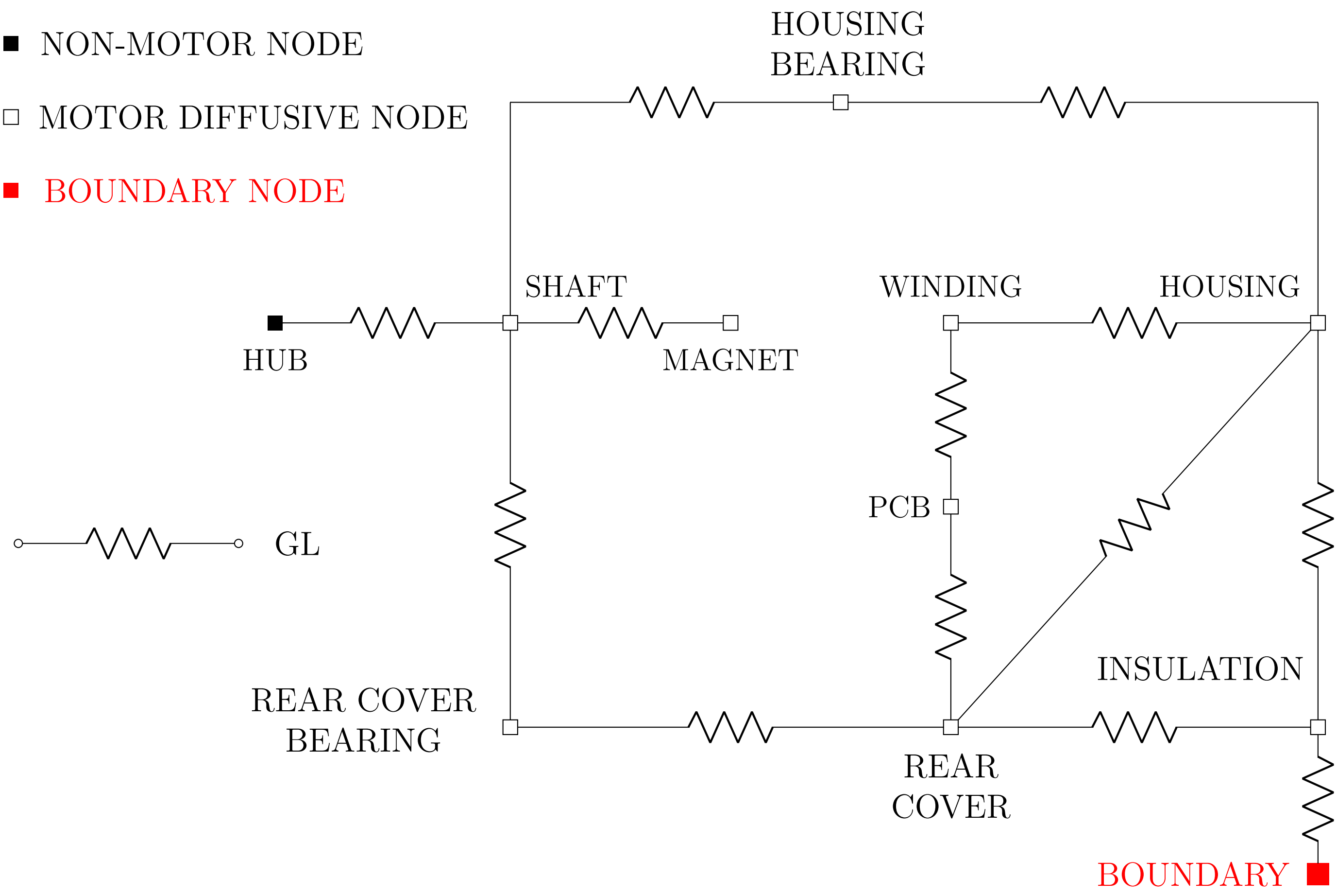

Figure 6.6: Motor Lumped Parameter Thermal Network.

Motor LPTN linear conductances (GL) values are:

Linear Conductor	**Value** (* from datasheet)	
GL(shaft, magnet)	29.77	[W/K]
GL(shaft, housing bearing)	0.005	[W/K]
GL(shaft, rear cover bearing)	0.005	[W/K]
GL(rear cover bearing, rear cover)	0.005	[W/K]
GL(rear cover, PCB)	0.086	[W/K]
GL(winding, PCB)	0.001	[W/K]
GL(winding, housing)	0.834*	[W/K]
GL(housing, housing bearing)	0.005	[W/K]
GL(housing, rear cover)	9.71	[W/K]
GL(rear cover, insulation)	variable	[W/K]
GL(housing, insulation)	variable	[W/K]
GL(insulation, boundary)	variable	[W/K]

6.2.2 Drone submodel

Drone TMM contains thermal capacitances, GL, QI, QR, power dissipation/convection/ control routines about every drone component except for the motor.
The most important parameters are the avionic thermal capacitances ($C_i = m_i\ [kg] \cdot 1000\ [J/(kgK)]$), the avionic control logic, avionics power dissipation, convection routines and the variable thickness of the aerogel insulation and its properties.

For contacts avionics-walls TAS-I GL values are used, air gap convection is evaluated with a dedicated routine. In fact all the components of these submodel are connected to the external environment or to the internal air gap with forced or natural convection.

Power dissipations and heaters power for avionics are parametrized and can be changed easily:

- $QI_{gyro} = 1\ W$
- $QI_{CPU} = 10\ W$
- $QI_{payload} = 5\ W$
- $QR_{battery} = 8\ W$
- $QR_{gyro} = QR_{CPU} = QR_{payload} = 1.5\ W$

Control logic switches on CPU, gyro and camera 180 s before the lift-off in order to perform pre-flight tests. Once landed only the CPU keeps working for other 180 s in order to transmit the acquired data. Heaters (QR) are simulated if they are enabled.

6.2.3 Mars submodel

Boundary nodes are included in this submodel.
Boundary nodes are: sky, ground and external environment. Those data are provided by ESA's LMD tool to simulate the Martian dynamic environment.
If enabled another boundary node is represented by the walls of a support platform where the drone sits when non operative and can be used to exchange data and to provide power and thermal control.
The only active node is the landing area connected to the drone through the radiative conductors computed by the GMM.

6.3 Simulated TCS solutions

Since from the MATLAB model was evident that the drone could not survive the cold Martian environment some thermal control system (TCS) solutions were already simulated with ESATAN from the beginning. The simplest solution was to protect the drone critical components with aerogel insulation of different thickness. Therefore the first simulation was a insulation thickness sensitivity analysis. Once found the best insulation solution further different TCS were simulated:

1. RHU (radioactive heating unit) inside avionic bay
2. Support platform with warm walls
3. Internal heaters on motors and avionics

The Aerogel properties used for the sensitivity analysis were:

- Aerogel name: Aeroflex by Active Aerogels
- Thermal conductivity: $k_{isol} = 0.031$ $[W/mK]$
- Density: $\rho_{isol} = 100$ $[kg/m^3]$
- Specific thermal capacitance: $c_{isol} = 1800$ $[J/kgK]$

Five different analyses were run:

1. Insulation thickness sensitivity
2. Basic TCS (only insulation)
3. RHU inside avionic bay
4. Support platform with warm walls
5. Internal heaters on motors and avionics

Results are shown in Section 6.5.

6.4 Boundary conditions

In any simulation the solution is strictly correlated with the boundary conditions. In thermal analyses the boundaries are represented by the temperatures which are not affected by the presence of the body inside the domain and have a specific time behaviour. As above mentioned in subsection 6.2.3 there are 3(+1) boundary temperatures (the +1 represents the warm walls of the support platform if enabled) and a boundary power flux.
Boundary temperatures from LMD tool are:

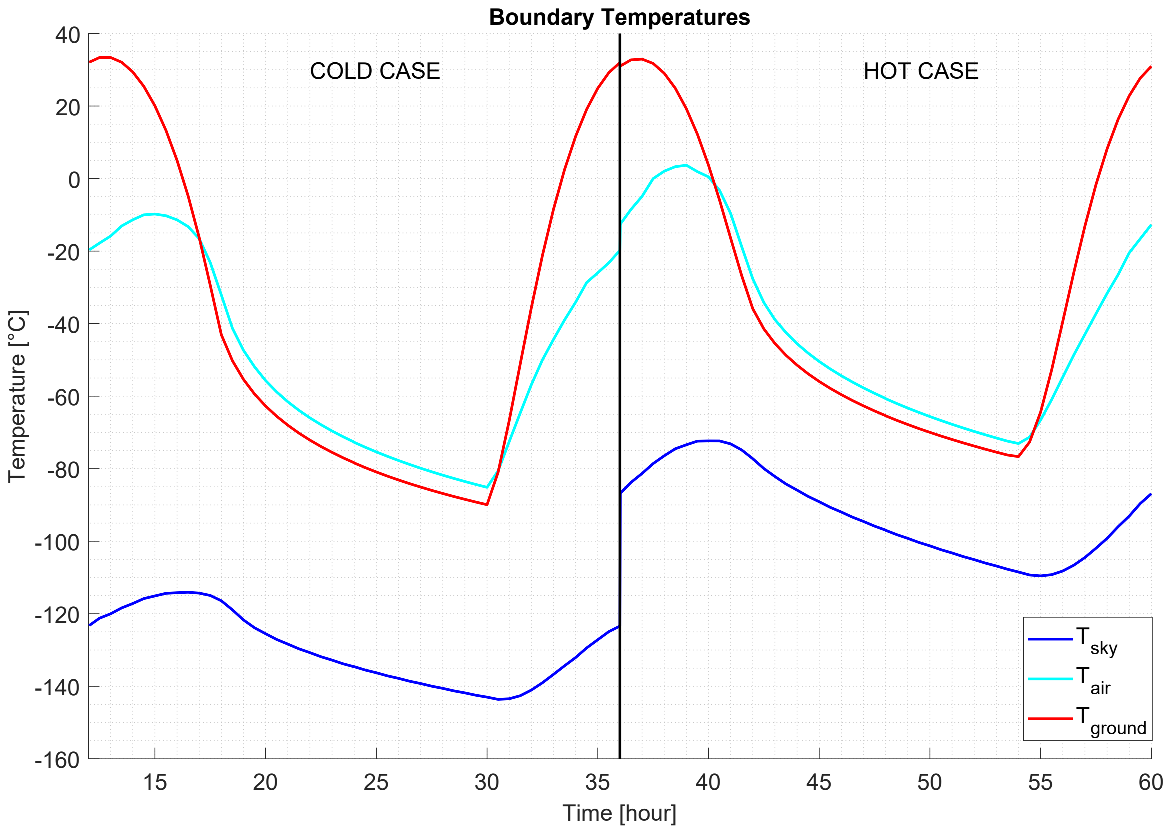

Figure 6.7: ESATAN Boundary temperatures.

The results start from the mid day and are different for the cold and hot cases.
The fourth boundary temperature is not shown in a dedicated picture because it is supposed to be constant for all the time the drone sits on the support platform. This temperature is +15 °C and is accounted in the simulation only if the platform is enabled.

Another important boundary condition is represented by the incident solar flux (solar intensity).
On Earth the averaged solar intensity is 1362 W/m^2 whilst on Mars it's lower due to the greater distance from the Sun. It varies with the solar longitude LS which is the position of the planet on its orbital path. LMD tool was used to find the environmental properties at LS=244, just before winter solstice (LS=270), at equatorial latitude. The incident solar flux is:

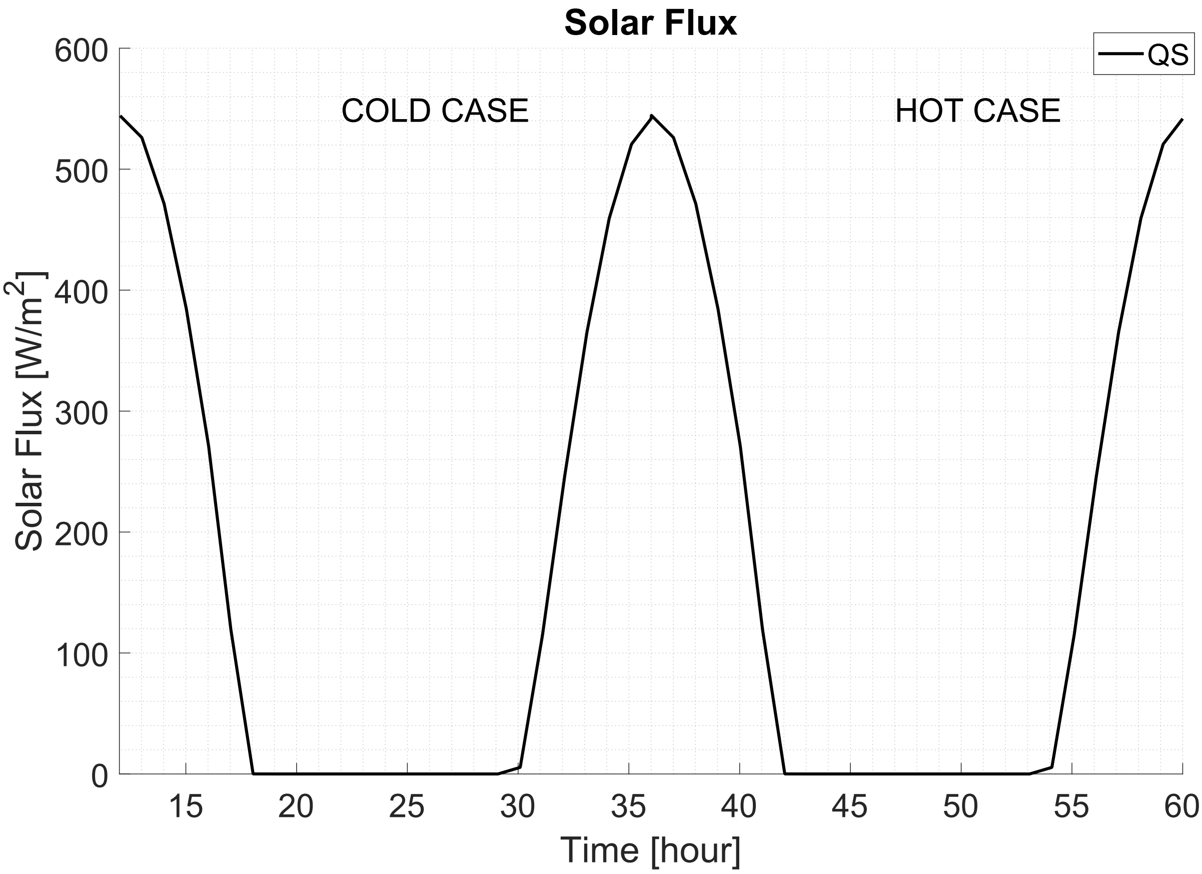

Figure 6.8: ESATAN Solar flux (boundary).

Cold case and Hot case results are identical because, for a given day, the incident solar flux on the planet is the same. Differences on an object QS may be given by the transparency of the atmosphere, described by the optical depth.

The third important boundary parameter which influences the solution is the dissipated power.
The dissipated power for each drone electrical/electronic component is:

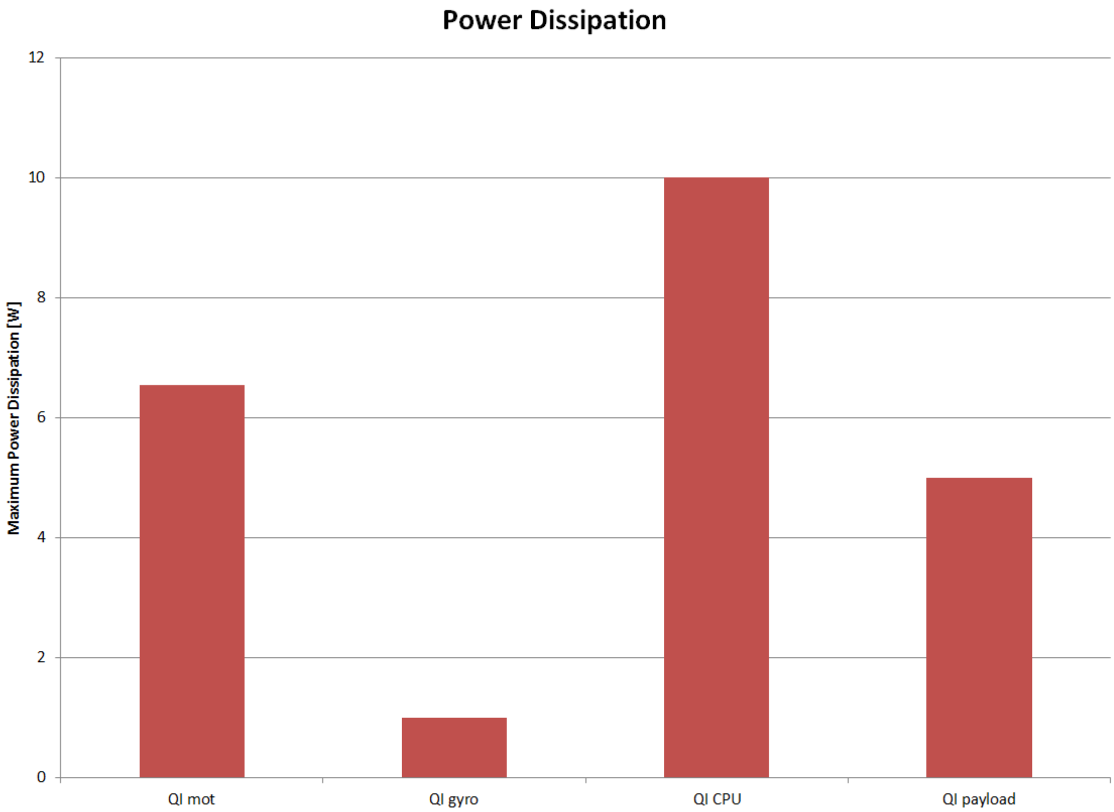

Figure 6.9: ESATAN Dissipated power.

The motor dissipated power is computed as a function of the mission profile $\Omega(t)$ using motor, gearbox and rotor specifications and can vary from 0 to 6.3 W.
Avionics dissipated power is assumed from TAS-I experience and datasheets.

6.5 Results

6.5.1 Insulation thickness sensitivity

As for all past missions on Mars, the thermal insulation is the first TCS solution. Different thickness for the top insulation (the one facing the sky), lateral insulation and motor insulation were tried. They are summarized in Table 6.2.
For the avionic bay the first number represents the top thickness and the second one the lateral thickness; for the motor there is no differences between top and lateral insulation dimensions.

CASE N	Avionics	Motor
1	10 - 10 mm (COLD)	1 mm (COLD)
2	30 - 30 mm (COLD)	2 mm (COLD)
3	50 - 50 mm (COLD)	5 mm (COLD)
4	30 - 10 mm (COLD)	1000 mm (COLD)
5	10 - 10 mm (HOT)	1 mm (HOT)
6	30 - 30 mm (HOT)	2 mm (HOT)
7	50 - 50 mm (HOT)	5 mm (HOT)
8	30 - 10 mm (HOT)	1000 mm (HOT)

Table 6.2: ESATAN Insulation sensitivity cases.

In Table 6.2 some solutions are not possible to be used because there is not enough space in the avionic bay (50 - 50 mm) of because they are an extremism used to show that the model works properly (1000 mm). Their presence inside the table is useful in order to determine if there is an improvement in the thermal behaviour.

Insulation Sensitivity Results

The following tables (6.3, 6.4) summarize the extreme temperatures achieved by the main motor and avionic components during a Sol.

	Motor winding T_{min}/T_{max}	**Motor housing** T_{min}/T_{max}
CASE 1	-86,44/+41,98	-86,44/+35,07
CASE 2	-86,43/+44,77	-86,43/+37,96
CASE 3	-86,39/+48,70	-86,39/+42,05
CASE 4	-43,21/+57,63	-43,21/+51,30
CASE 5	-73,79/+50,53	-73,79/+43,66
CASE 6	-73,75/+53,03	-73,75/+46,27
CASE 7	-73,64/+56,36	-73,64/+49,75
CASE 8	-34,44/+62,86	-34,44/+56,64

Table 6.3: Motor sensitivity results.

	CPU T_{min}/T_{max}	**Battery** T_{min}/T_{max}	**Payload** T_{min}/T_{max}	$\boldsymbol{\Delta E}$ **(w SP)** [Wh]
CASE 1	-97,20/+45,19	-97,57/+32,34	-101,60/+45,05	-
CASE 2	-92,59/+28,27	-92,89/+22,3	-96,26/+28,97	-80,13
CASE 3	-82,01/+7,63	-82,26/+7,82	-85,06/+9,77	-
CASE 4	-95,65/+39,42	-95,96/+26,97	-99,91/+39,47	-183,40
CASE 5	-81,49/+48,25	-81,82/+35,95	-84,76/+48,75	-
CASE 6	-77,36/+32,02	-77,62/+26,60	-80,02/+32,87	-48,27
CASE 7	-67,97/+12,95	-68,19/+13,20	-70,22/+15,17	-
CASE 8	-80,11/+41,98	-80,38/+30,10	-83,27/+42,67	-83,03

Table 6.4: Avionics sensitivity results.

From Tables 6.3, 6.4 it is possible to note that there is an improvement by increasing the avionic bay insulation thickness whilst the motor insulation thickness is irrelevant (the 1000 mm case shows that it would be possible to protect the motor with aerogel only with a lot of material, meaning that this is not a way to follow in order to protect the motor).
Moreover it seems that the 30 - 10 mm avionic insulation gives almost the same results as the 30 - 30 mm but, aiming to maintain the avionic components at their required non operative temperatures, more heater energy would be used. This is demonstrated by the ΔE results: the lower the value, the higher the heater power will be.
The energy requested to the battery is shown in Figure 6.10.
A negative ΔE means that the 43 Wh battery is not able to provide enough energy to heat up the drone components and therefore a different solution must be found.

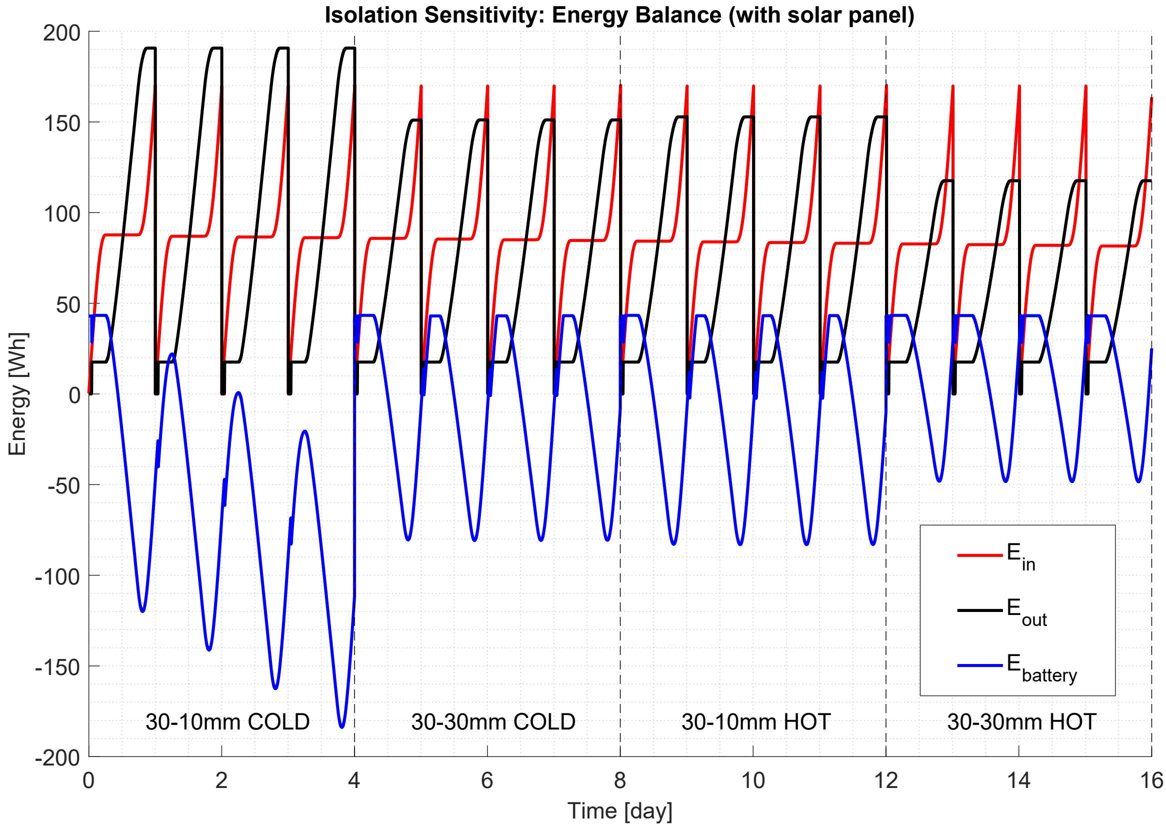

Figure 6.10: ESATAN Insulation sensitivity (cases: 2, 4, 5, 8).

This sensitivity analysis showed that the best insulation thickness is 30 - 30 mm for the avionic bay and 1 mm for the motor, but other TCS solutions must be added in order to maintain compliance with temperature requirements.

6.5.2 Thermal Control Systems analyses

In order to improve the basic thermal control system and maintain compliance with the temperature limits, 10 analyses were run (5 for HOT and 5 for COLD environment):

CASE N	Name
1	**insulation only (COLD)**
2	**insulation only (HOT)**
3	radioactive heating unit (COLD)
4	radioactive heating unit (HOT)
5	support platform (COLD)
6	support platform (HOT)
7	avionics and motor electrical heaters (COLD)
8	avionics and motor electrical heaters (HOT)
9	avionic electrical heaters only (COLD)
10	avionic electrical heaters only (HOT)

Table 6.5: ESATAN Cases.

From the sensitivity analysis the selected insulation thickness is 30 - 30 mm for the avionic bay (except for the support platform where the avionic bay insulation thickness is 30 - 10 mm) and 1 mm for the motors.
Electrical heaters maintain the component temperatures within its temperature limits using a on-off logic. They are placed on avionic components and on the BLDC motors in cases 7 and 8.
NASA's home made BLDC motors are not heated during non operational phases but only before the flight if the measured motor temperature is too low to operate [10]. This information is the reason why the cases 9 and 10 were simulated.
Since avionics always need to be maintained at required temperatures even during non-operational phases, the avionic bay heaters were kept into account even in cases 9 and 10.
The analysed main components are: motor winding, motor housing, gyro, CPU, battery and payload. Their temperature requirements are obtained from datasheets or from TAS-I experience.
Results are shown both with images and tables in order to highlight the maximum and minimum operational and non-operational temperatures (OP = operational, NOP = non-operational) and to compare them with the required ones for each main component.

Cases 1 and 2 are the **reference cases**, those including only the basic insulation. Every improved TCS must be compared with case 1 for cold environment and with case 2 for hot environment.

Motor thermal behaviour

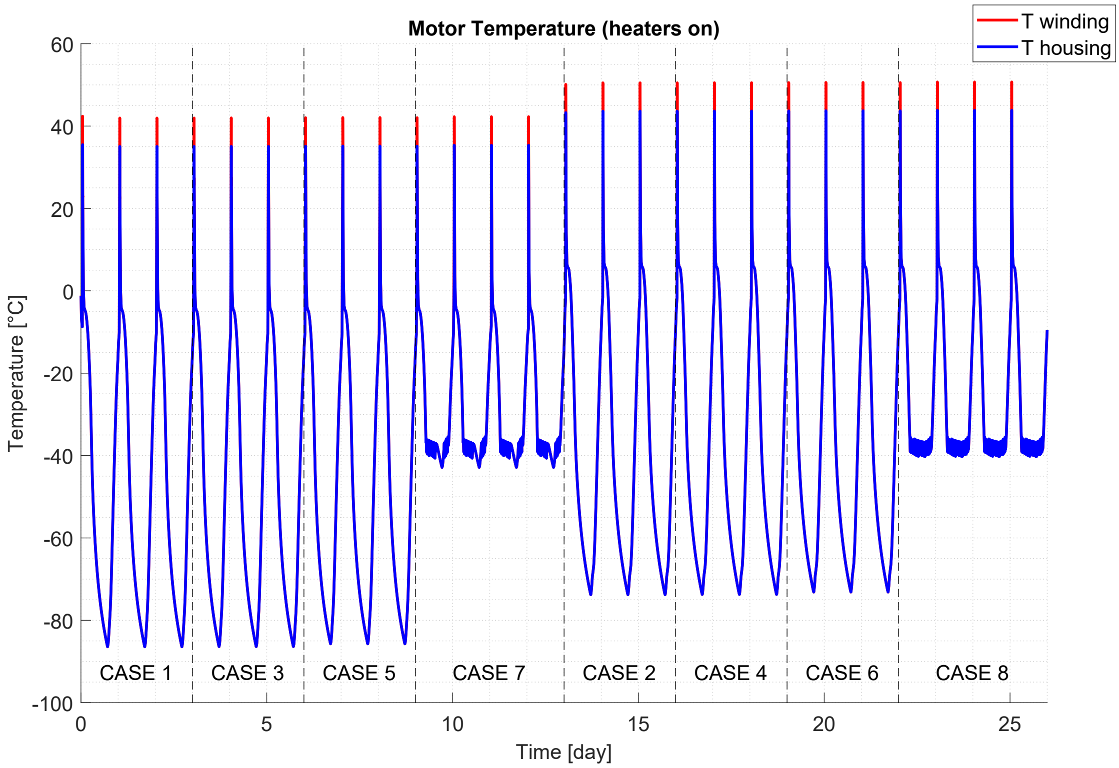

Figure 6.11: ESATAN Motor temperatures (heaters on).

RHU and support platform (cases 3, 4, 5 and 6) do not influence the motor temperature because they are intended to heat up only the avionic bay (support platform) or are placed inside of it (RHU). The only way to heat up the motor is with a dedicated electrical heater (cases 7 and 8). Case 7, which is a COLD environment, shows that the motor heater has not enough power ($QR_{motor} = 1\ W$) to maintain the motor temperature at -40 °C so a more powerful one would be necessary if the motor must be heated. This does not happen in the HOT case (8) because the boundary temperatures are higher. Alternatively a thicker motor insulation could be used.
The maximum temperature limit for both winding and housing is never reached meaning that there is no motor overheating, as previously assessed with the MATLAB model.

Avionics thermal behaviour

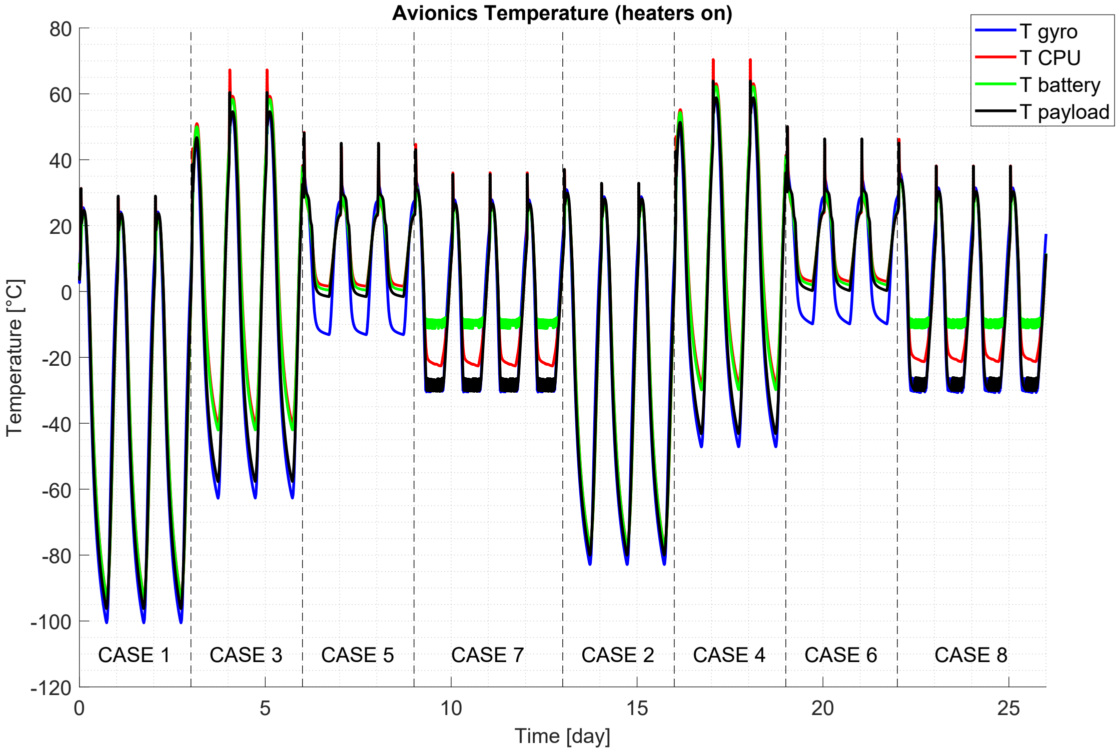

Figure 6.12: ESATAN Avionic temperatures (heaters on).

About avionics, the only insulation solution (cases 1 and 2) is not enough for maintaining required temperature limits both for COLD and HOT cases as assessed with the sensitivity analysis.
The RHU (cases 3 and 4) is the worst solution because both minimum and maximum temperature limits aren't satisfied, causing overheating during the day and overcooling at night. A smaller RHU would be useless for night survival and a bigger one would overheat the avionics.
The support platform with warm walls which heat up the avionic bay during non-operational phases (cases 5 and 6) is a good solution because it is able to maintain compliance with minimum non-operational temperatures even if a little oversized for maximum operational limits. This is not a problem since the walls have a boundary temperature of +15 °C and it is possible to decrease this value and easily maintain compliance with temperature limits, requiring less energy for heating up the walls. Moreover less aerogel is needed (30-10 mm instead of 30 - 30 mm) and no heaters are placed inside the drone so, if a support platform can be used, this is the best solution because the drone would be lighter, less complicated and therefore more reliable.
Active thermal control with heaters (cases 7 and 8) is capable of maintaining temperature requirements but uses too much energy as showed in Figures 6.13 and 6.14. This means that with the actual design, even with a 0.5 m^2 solar panel attached to the drone, it would be impossible to provide enough energy to survive and fly again

without an external support. This solution can be useful if a support platform with warm walls can't be used but the battery can be recharged externally (draining energy from a rover), for example with a wireless recharging similar to the one used with smart phones. With an improved thermal design it may be possible to use this active TCS solution to design a stand alone quadcopter similar to the MHS.

Energy balance

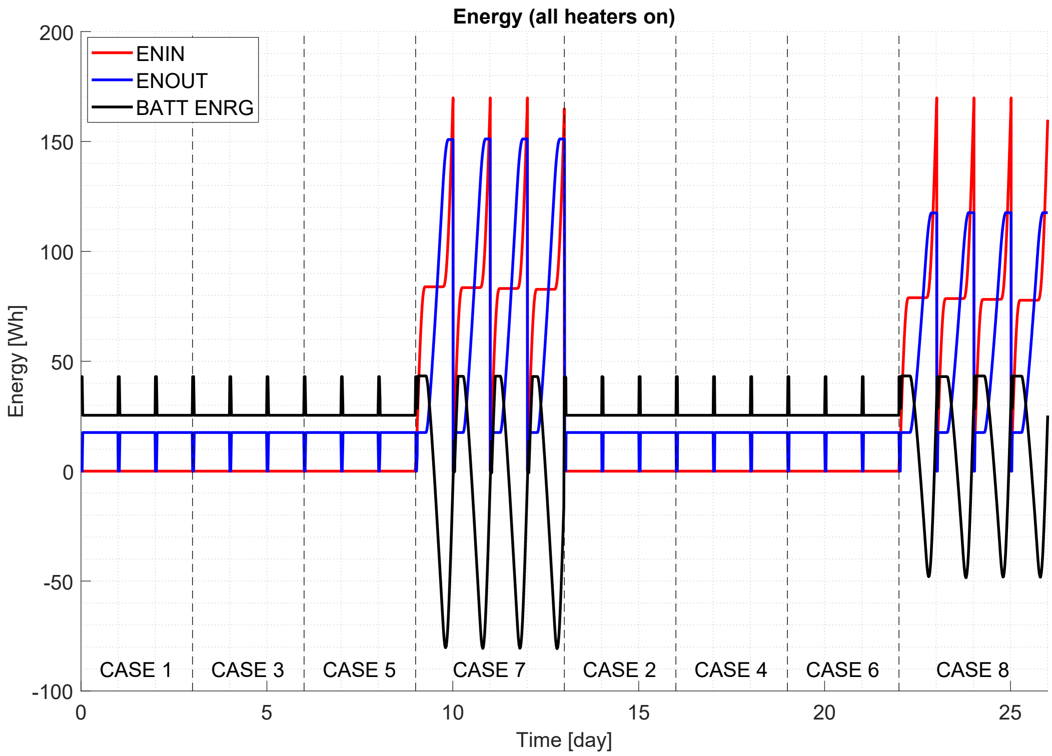

Figure 6.13: ESATAN Energy consumption (heaters on).

Figure 6.13 shows the energy balance for the drone with both avionic and motor heaters enabled, providing energy with a 0.5 m^2 solar panel attached to the drone (cases 7 and 8). The other cases shows the energy consumption without solar panel and assuming that the battery is fully recharged at the end of each Sol, before the flight. With this assumption the battery is oversized because only 17 Wh are used for operations. If an external recharging support can be used the battery pack can be reduced saving more than 100 g (the 43 Wh battery weighs about 270 g).
Cases 7 and 8 show that an external support must have a battery pack dedicated to the drone with a capacity of about 100 Wh and a 0.5 m^2 solar panel dedicated to the drone. The weigh of a 100 Wh battery is about 0.6 kg. With such a solution the solar panel would be attached to the support system instead of to the drone. Moreover if a larger solar panel is available and the battery is fast enough in recharging it would be possible to use the drone battery only.

In order to try to reduce energy consumption it was tried to switch off the motor heaters such as NASA's procedure. This was possible because external temperature at mission time was higher than the minimum one required for the motor to operate, but it must be assessed if it is possible to leave the motor at ambient temperature during the night. Results are shown in Figure 6.14:

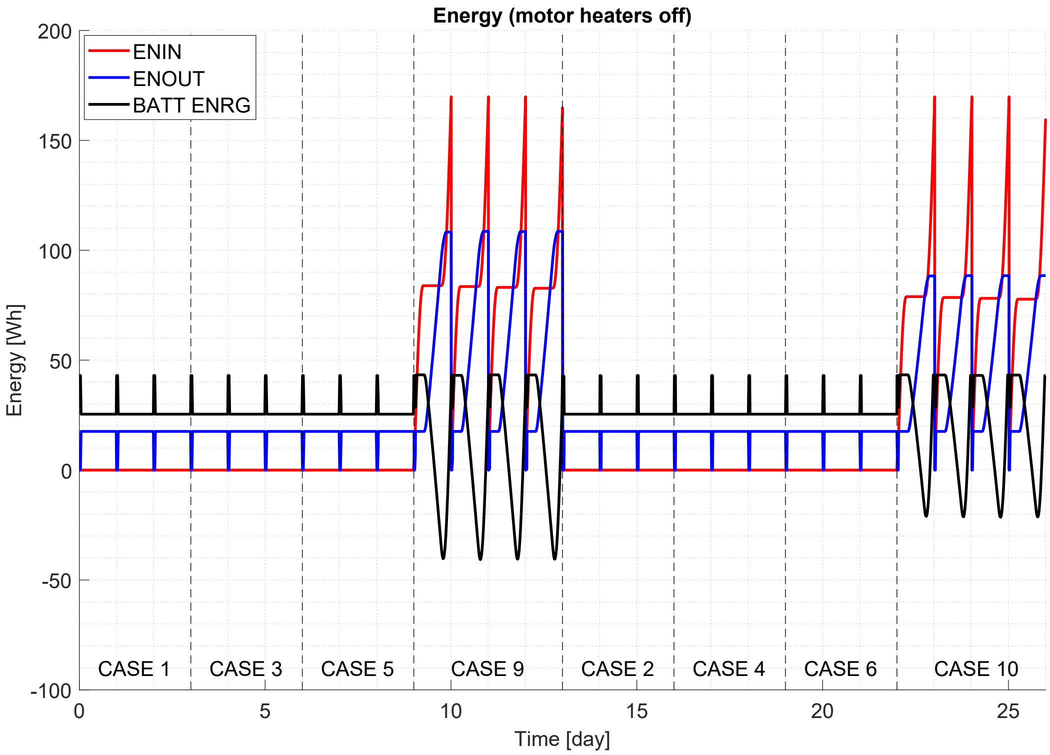

Figure 6.14: ESATAN Energy consumption (motor heaters off).

Figure 6.14 shows that even in this case there isn't enough battery energy for allowing the drone to survive on its own, but a 50 Wh instead of 100 Wh support battery would be enough, saving 300 g on the support system.
The $\Delta Energy$ for cases 7, 8, 9 and 10 is here summarized:

	ΔE [Wh]
CASE 7	-80.7
CASE 8	-48.4
CASE 9	-40.6
CASE 10	-21.4

Table 6.6: ESATAN Energy results.

Of course the best result is achieved with motor heaters off and in the warmer environment (case 10).

The motor thermal behaviour with no heaters applied on it is shown in Figure 6.15:

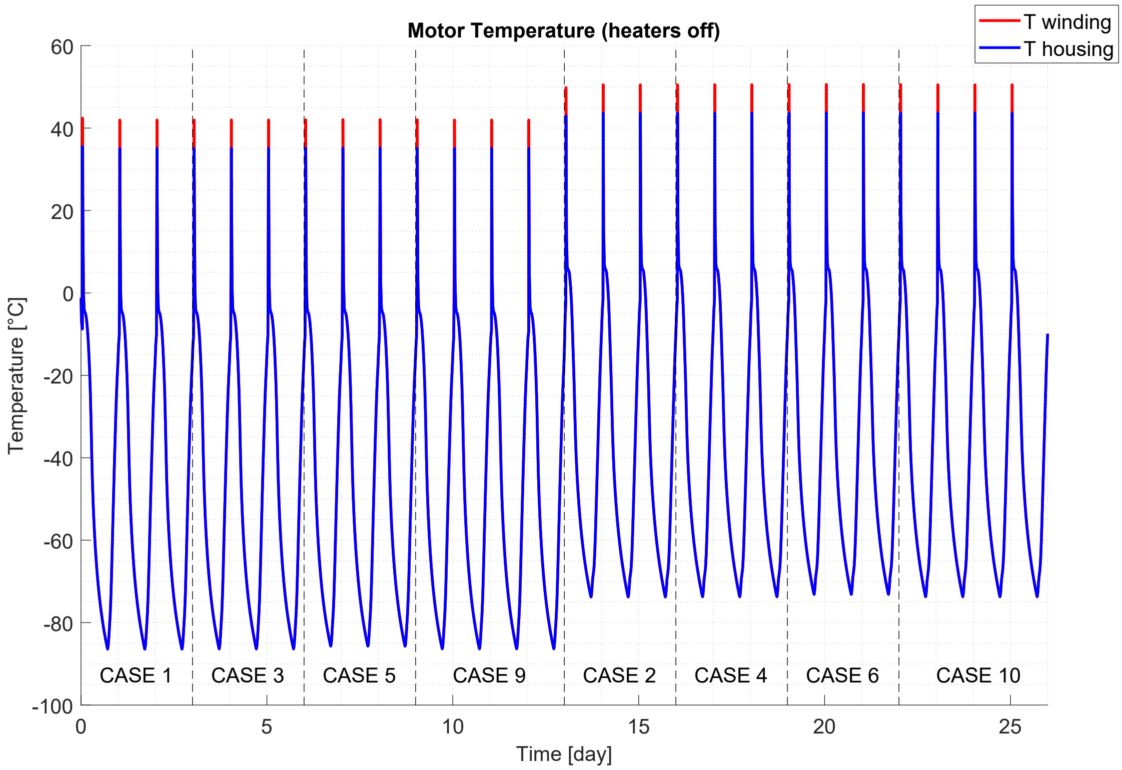

Figure 6.15: ESATAN Motor temperatures (heaters off).

As expected there is no difference between the COLD cases and HOT cases without motor heaters.

Main components maximum/minimum operational and maximum/minimum non-operational temperatures are summarized in Table 6.7 in the following page.

		Motor winding T_{min}/T_{max}	**Motor housing** T_{min}/T_{max}	**Gyro** T_{min}/T_{max}	**CPU** T_{min}/T_{max}	**Battery** T_{min}/T_{max}	**Payload** T_{min}/T_{max}
REQUIREMENTS	OP	-40/+155*	-40/+100*	-40/+105*	-30/+45*	-10/+30	-30/+45
	NOP	NA	NA	-65/+105*	-40/+85*	-20/+40	-40/+55
CASE 1	OP	-9,5/42,0	-9,5/35,1	13,3/24,2	6,5/28,3	7,3/22,3	8,3/29,0
	NOP	-86,4/-9,5	-86,4/-9,5	-100,6/13,3	-92,9/6,5	-92,9/7,3	-96,19/8,30
CASE 2	OP	-1,5/50,5	-1,5/43,6	17,3/28,8	10,3/32,1	11,1/26,6	12,3/32,9
	NOP	-73,8/-1,5	-73,8/-1,5	-82,9/17,3	-77,4/10,3	-77,6/11,1	-80,0/12,3
CASE 3	OP	-9,5/42,0	-9,5/35,1	43,4/54,0	46,3/67,3	45,8/58,3	41,2/60,4
	NOP	-86,4/-9,5	-86,4/-9,5	-62,7/43,4	-40,2/46,3	-42,0/45,8	-57,7/41,2
CASE 4	OP	-1,5/50,5	-1,5/43,7	47,0/58,3	49,7/70,4	49,0/62,2	44,7/63,9
	NOP	-73,7/-1,5	-73,7 /-1,5	-47,1/47,0	-28,1/49,5	-29,8/49,0	-43,1/44,7
CASE 5	OP	-9,4/42,1	-9,4/35,2	27,8/32,8	23,4/43,9	23,9/30,1	24,8/45,0
	NOP	-85,7/-9,4	-85,7/-9,4	-13,1/27,8	1,7/23,4	0,4/23,9	-1,6/24,8
CASE 6	OP	-1,4/50,6	-1,4/43,7	29,2/33,9	24,1/44,4	24,7/31,1	25,7/46,3
	NOP	-73,2/-1,4	-73,2/-1,4	-9,9/29,2	3,0/24,1	2,0/24,7	0,3/25,7
CASE 7	OP	-9,2/42,3	-9,2/35,4	20,0/27,9	15,1/36,1	15,6/25,9	15,6/35,6
	NOP	-42,9/-9,2	-42,9/-9,2	-30,5/20,0	-22,5/15,1	-11,2/15,6	-30,5/15,6
CASE 8	OP	-1,3/50,7	-1,3/43,8	22,6/31,5	17,1/38,1	17,7/29,3	18,1/38,1
	NOP	-40,2/-1,3	-40,2/-1,3	-30,5/22,6	-21,3/17,1	-11,1/17,7	-30,2/18,1
CASE 9	OP	-9,5/42,0	-9,5/35,1	20,0/27,9	15,1/36,1	15,6/25,9	15,6/35,6
	NOP	-86,4/-9,5	-86,4/-9,5	-30,5/20,0	-22,5/15,1	-11,2/15,6	-30,5/15,6
CASE 10	OP	-1,5/50,5	-1,5/43,7	22,6/31,5	17,1/38,1	17,7/29,3	18,1/38,1
	NOP	-73,7/-1,5	-73,7/-1,5	-30,5/22,6	-21,3/17,1	-11,1/17,7	-30,2/18,1

Table 6.7: ESATAN Simulation results.

6.6 Conclusions

The aim of this work was to assess the feasibility of multiple flight of a quadcopter drone on Mars from the thermal point of view.
In order to achieve this result a motor-rotor couple was found, starting from the University of Maryland rotor performances, TAS-I tests and PoliTO work about Martian rotors. A preliminary drone design was proposed together with the propulsive group design (MAXON BLDC motor and gearbox). Afterwards, a thermal representative geometry was simulated with the software ESATAN-TMS in order to study the drone thermal behaviour. The model included the natural and forced convection routines developed and validated with MATLAB and took into account the drone mission profile $\Omega(t)$ for a better evaluation of the heat fluxes, power consumption and energy balance.
Different analyses were run, starting from the simplest possible TCS solution (only insulation) to an active TCS with several electrical heaters.
Results are in accordance with NASA's Mars Helicopter Scout design specifications found in the paper "Mars Helicopter Technology Demonstrator" [10], confirming that the main driving factor for the thermal design is to minimize the survival heater energy while maintaining compliance with allowable flight temperatures for all system components in a dynamic thermal environment.
The analyses demonstrated that it is actually possible to design a quadcopter drone able to fly on Mars.

The best solution found for the proposed drone is a support platform (BASE) with warm walls which heat up the drone avionic bay during non-operational phases while recharging the quadcopter battery. In this case the drone would be lighter and the actual design would be sufficient to allow the drone to operate on Mars.
Alternatively, if a support platform is available only for battery recharging, the solution could be the active TCS with electrical heaters on board.

However, if the drone is considered as a stand alone system able to operate without external support as the NASA's Mars Helicopter Scout, a different design has to be developed, since the presented one requires too much energy to survive during the cold Martian nights.

Several improvements could be made to the current ESATAN model and to the current drone design. Concerning the ESATAN model, a more detailed geometry discretization for larger and critical components could be used, based on a drone CAD to be developed. Moreover, a more accurate definition of some avionic components power consumption and geometry is needed.

Regarding the drone design, some improvements could be introduced, concerning:

- Battery mass allocation, depending on the actual requested energy and recharging time, and energy breakdown for different phases
- Geometry optimization of the avionic bay, support arms and drone legs
- Optimization of insulation thickness and aerogel position inside the avionic bay
- Optimization of heaters power
- Optimization of solar panel position and dimension (for a stand alone drone)

With such an optimization process it would be possible to assess the feasibility of the survivability and operation of a Martian quadcopter even without external support.

Finally, the design process followed within this thesis can be applied to any flying drone for terrestrial and extraterrestrial application.

Appendix A

MATLAB Model

Here is reported the MATLAB code. It is composed of three files:

1. The main program.
2. The time march function.
3. The Induced Axial Speed function.

MAIN PROGRAM

```
clear all
close all force
clc

%% INPUT DATA
N=3+1;               %[-]      Nuber of axial node discretization (+1 is for
boundary node)
t_max=300;           %[s]      Max Operative Time (600s=10min)
R_CO2=188.9;         %[J/kg/K] Specific Gas Constant
D_prop=0.457;        %[m]      Propeller Diameter
D=0.022;             %[m]      Engine Diameter
L=0.064;             %[m]      Engine Length
C_tot=0.140*380;     %[J/K]    Engine Thermal Capacitance (Calculated as
m_engine*c_copper)
T_max=125;           %[°C]     Max Engine Temperature - DATASHEET
T_min=-40;           %[°C]     Min Engine Temperature - DATASHEET
k_eng=16.3;          %[J/m/K]  Mass-Averaged Thermal Conductivity
k=sum(ki*mi)/sum(mi) (setted as k_steel << k_copper)
eps=0.11;            %[-]      Surface Radiant Emittance (standard eps=0.11)
alpha_S=0.39;        %[-]      Solar Absorptance (standard alpha_S=0.39)
I0=0.261;            %[A]      No-load Current - DATASHEET
k_m=11.8;            %[mNm/A]  Torque Constant - DATASHEET
k_v=809;             %[rpm/V]  Speed Constant - DATASHEET
dn_dM=14.8;          %[min-1/mNm] M-n slope - DATASHEET
sigma=5.67051e-8;    %[W/m2/K4]   Stephan-Boltzmann Constant

%% MISSION PROFILE RPM(t) %%

rpm_raw=[0 4145.8 4145.8 3915.5 3915.5 3908.9 3908.9 0]';

time_rpm_raw=[0 10 16.67 18.67 253.4 254.4 293.4 310]';

ramp1=linspace(rpm_raw(1),rpm_raw(2),floor(time_rpm_raw(2)-
time_rpm_raw(1)))';
ramp2=linspace(rpm_raw(2),rpm_raw(3),floor(time_rpm_raw(3)-
time_rpm_raw(2)))';
ramp3=linspace(rpm_raw(3),rpm_raw(4),floor(time_rpm_raw(4)-
time_rpm_raw(3)))';
ramp4=linspace(rpm_raw(4),rpm_raw(5),floor(time_rpm_raw(5)-
time_rpm_raw(4)))';
ramp5=linspace(rpm_raw(5),rpm_raw(6),floor(time_rpm_raw(6)-
time_rpm_raw(5)))';
ramp6=linspace(rpm_raw(6),rpm_raw(7),floor(time_rpm_raw(7)-
time_rpm_raw(6)))';
ramp7=linspace(rpm_raw(7),rpm_raw(8),floor(time_rpm_raw(8)-
time_rpm_raw(7)))';

rpm=[ramp1; ramp2; ramp3; ramp4; ramp5; ramp6; ramp7];
dt=1; %[s]
```

```
%rpm=zeros(t_max,1); % decomment for cooling only analysis

lung=length(rpm);
if t_max>lung
    rpm=[rpm; zeros(t_max-lung,1)];
else
    t_max=lung;
end

%%%%%%%%%%

%% DEFINING ANALYSIS %%

% Velocity field: laminar or turbulent
field=input('Velocity field type? (lam or turb allowed) ','s');

if strcmp('lam',field)~=1 && strcmp('turb',field)~=1
    disp('Error in velocity fiel type')
    return
end

t_case=input('Case type? (hot or cold allowed) ','s');

if strcmp('cold',t_case)~=1 && strcmp('hot',t_case)~=1
    disp('Error in case of analysis')
    return
end

if strcmp(t_case,'hot')
    T0=0;                          %[°C]    Initial BLDC Motor Temperature - if
controlled
    T0=T0+273.15;
    T_amb=2.4;                     %[°C]    Ambient Temperature
    T_amb=T_amb+273.15;            %[K]
    a=sqrt(1.3*R_CO2*T_amb);       %[m/s]   Speed of sound
    p=6.60;                        %[mbar]  Ambient pressure
    p=p*1e2;                       %[Pa]
    rho_eff=p/(R_CO2*T_amb);       %[kg/m3] Mars' atmosphere Density - supposed
to be constant
    rho=0.0167;
    mu=1.38205e-5;                   %[Pa*s]  Dynamic Viscosity
    Pr=0.765954;                     %[-]     Prandtl Number
    k=0.0147941;                     %[W/m/K] CO2 thermal conducivity
    Q_solar=885.65;                  %[W/m2]  Solar Flux + Scatter
    S_mot=pi*D*L+2*pi*D^2/4;         %[m2]    Motor surface
    Q_ext=Q_solar*S_mot*alpha_S;     %[W]     Engine immited power from other
sources (solar flux etc)
else
    T0=T_min;                      %[°C]    Initial Temperature - if controlled
    T0=T0+273.15;
    T_amb=-93.65;                  %[°C]
    T_amb=T_amb+273.15;            %[K]
    a=sqrt(1.36*192*T_amb);        %[m/s]   Speed of sound
```

```
    p=6.60;                   %[mbar]   Ambient pressure
    p=p*1e2;                  %[Pa]
    rho_eff=p/(R_CO2*T_amb);  %[kg/m3]  Mars' atmosphere Density -
supposed to be constant
    rho=0.0167;
    mu=9.00817e-6;              %[Pa*s]   Dynamic Viscosity
    Pr=0.792054;                %[-]      Prandtl Number
    k=0.00812201;               %[W/m/K]  CO2 thermal conductivity
    Q_solar=0;                  %[W/m2]   Solar Flux - Scatter
    S_mot=pi*D*L+2*pi*D^2/4;    %[m2]     Motor surface
    Q_ext=Q_solar*S_mot*alpha_S; %[W]     Engine immited power from other
sources (solar flux etc)
end

n_step=t_max/dt;     %[-] Number of time steps

T=zeros(n_step,N);   %[K] Temperature Vector

quest=input('T0 controlled? (y/n Default=n) ','s');
if strcmp(quest,'y')==1
    %T0=T0 controlled
    T(1,:)=T0*ones(1,N);
    T(1,N)=T_amb;
    T_stamp=T0;
else
    % T0 non-controlled
    T0=T_amb;
    T(1,:)=T_amb*ones(1,N);
    T_stamp=T_amb;
end

%%%%% FILES OPENING

analysis_case=input('Analysis case name: ','s');

fid1=fopen(strcat('Results_CO2/Results_CO2_vs_',analysis_case,'.log'),'w');
%Results file
    fprintf(fid1,'T[°C]\tQ_i[W]\tQ_conv[W]\tQ_rad[W]\n');

fid2=fopen(strcat('Results_CO2/Conductances_CO2_vs_',analysis_case,'.log'),
'w'); %Conductances file
    fprintf(fid2,'GL_cond \tGL_conv \tGR \n');

fid3=fopen(strcat('Results_CO2/Initial_CO2_vs_',analysis_case,'.log'),'w');
%Initial condition reminder file
    fprintf(fid3,'INITIAL
VALUES\nT_amb[°C]\tT0[°C]\tt_max[s]\tC[J/K]\trho[kg/m3]\n');
    fprintf(fid3,'%5.2f\t\t%5.2f\t%5.1f\t\t%5.2f\t%5.4f',T_amb-
273.15,T_stamp-273.15,t_max-1,C_tot,rho);
fclose(fid3);
```

```matlab
%% PRE-PROCESSING

S_up=0.25*pi*D^2;            %[m2] engine top surface
S_lat=pi*D*L;                %[m2] engine lateral surface
S_down=0.25*pi*D^2;          %[m2] engine bottom surface
S_tot=S_up+S_lat+S_down;     %[m2] total engine exposed area
dx=L/(N-1);                  %[m]  length of axial nodes
dS_lat=pi*D*dx*ones(N,1);    %[m2] partialized lateral surface
dS_lat(N)=0;                 %Boundary has no surface

A=zeros(N,1);
A(1)=dS_lat(1)+S_up;
A(N-1)=dS_lat(N-1)+S_down;
A(2:N-2)=dS_lat(2:N-2);

Volume=0.25*pi*D^2*L;
dVol=Volume/(N-1);
Vol=dVol*ones(N,1);
Vol(N)=0;                    %Boundary has no volume

C=Vol/Volume*C_tot;          %[J/K] Capacitance Vector
C(N)=Inf;

% MATRIX OF INNER CONDUCTANCES (linear) - only axial discretization

K=zeros(N,N);
for i=1:N-1
    if i==1
        K(i,2)=k_eng*(pi*D^2/4)/dx;
    elseif i==N-1
        K(i,N-2)=k_eng*(pi*D^2/4)/dx;
    else
        for j=i-1:2:i+1
            K(i,j)=k_eng*(pi*D^2/4)/dx;
        end
    end
end

%% TIME MARCH

v_IAS(1,1)=0;
for i=2:n_step

    [T,coeff_conv(i-1),V] =
time_march_CO2(i,rpm(i),rho,D_prop,D,mu,dx,field,k,k_eng,I0,k_m,k_v,dn_dM,Q
_ext,T,T_amb,N,K,eps,sigma,A,C,dt,fid1,fid2,Pr,L);

    v_IAS(i,1) = V;

end  %end time march routine

fclose(fid1);
fclose(fid2);
```

```
%% OUTPUTS

%%%%%% PRINTING FIGURES

figure(1)
for i=1:n_step
    T_plot(i,1)=mean(T(i,1:end-1))-273.15;
end
t_plot=0:dt:t_max-dt;
t_fill=[0 t_max];
T_min=[T_min T_min];
T_max=[T_max T_max];

t_fill2 = [t_fill, fliplr(t_fill)];
inBetween = [T_min, fliplr(T_max)];

subplot(2,1,1)
fill(t_fill2, inBetween, 'c');

hold on
pl1=plot(t_plot,T_plot,'k','linewidth',2);
pl2=plot(t_fill,[T_amb-273.15 T_amb-273.15],'k--','linewidth',2);
pl3=plot(t_fill,T_max,'r-','linewidth',1.3);
pl4=plot(t_fill,T_min,'b-','linewidth',1.3);

legend([pl1 pl2 pl3 pl4],'T_{eng}','T_{amb}','T_{max} Datasheet','T_{min}
Datasheet')
grid minor
xlabel('t [s]')
ylabel('T [°C]')

%%%%% Velocity profile plot

if t_max>lung

subplot(2,1,2)
plot(0:dt:lung-1,rpm(1:lung),'k','linewidth',1.2)
xlabel('t [s]')
ylabel('rpm')
title('Rotational Speed Profile')
grid minor

else

subplot(2,1,2)
plot(0:length(rpm)-1,rpm,'k','linewidth',1.2)
xlabel('t [s]')
ylabel('rpm')
title('Rotational Speed Profile')
grid minor

end
```

```
%%%%% DISP T MAX AND DELTA T

for i=1:N
    tmax(i)=max(T(:,i));
end
    TMAX=max(tmax);

disp('-------------------------------------------------------------------')
disp('-------------------------------------------------------------------')
disp(strcat('Temperatura ambiente=', num2str(T_amb-273.15),' °C'))
disp(strcat('Temperatura iniziale=', num2str(T0-273.15),' °C'))
disp(strcat('Temperatura massima modello=', num2str(TMAX-273.15),' °C'))
disp(strcat('Massimo Delta_T (T_max - T_amb)=',num2str(abs(TMAX-T_amb)),'
°C'))
disp(strcat('Massimo Delta_T (T_max - T0)=',num2str(abs(TMAX-T0)),' °C'))
disp('NOTE: If T0 is not controlled -> T0=T_amb -> T_max-T_amb = T_max-T0')
disp('-------------------------------------------------------------------')
disp('-------------------------------------------------------------------')
```

TIME MARCH

```
function
[T,coeff_conv,V]=time_march_CO2(i,rpm,rho,D_prop,D,mu,dx,field,k,k_eng,I0,k
_m,k_v,dn_dM,Q_ext,T,T_amb,N,K,eps,sigma,A,C,dt,fid1,fid2,Pr,L)

Thrust=2.692e-8*rpm^2.005;    %[n]   Rotor Characteristic Thrust Equation
(EXPERIMENTAL)

M=2.6e-5*rpm^1.736;           %[mNm] Rotor Characteristic Torque Equation
(EXPERIMENTAL)

V_adt=sqrt(Thrust/(2*rho*0.25*pi*D_prop^2));  %[m/s]   Propeller-induced
axial speed from Actuator Disc Theory

%%%%%%%%%%%%%%%%%%%%%%%%%%%%%%%%%%%%%%%%%%%%%%%%%%%%%%%%%%%%%%%%%%%%%%%%%%%%%
% IAS=Induced Axial Speed = FUNZIONE CHE DETERMINA LA VELOCITà ASSIALE DEL
ROTORE DI OTTIMO SECONDO LA
% TEORIA DEI VORTICI CORRETTA

[u,v]=IAS_vs(rho,D_prop,rpm,Thrust);

V=mean(v);

%%%%%%%%%%%%%%%%%%%%%%%%%%%%%%%%%%%%%%%%%%%%%%%%%%%%%%%%%%%%%%%%%%%%%%%%%%%%%

% CONVEZIONE FORZATA

Re_D=rho*D*V/mu;

% for p=1:N
%     Re_x(p,1)=(0.5*dx+(p-1)*dx)*rho*V/mu; %[-] Reynolds number along
engine axes
% end
% Re_x(N,1)=0;

if strcmp(field,'lam')==1
    CORREZIONE=1.8671629+2.7071e-5*rpm;
    %Nu=0.06*Re_x.^(4/5)*Pr^(1/3); TAS-I
    Nu=0.134*Re_D^0.668*CORREZIONE;
else
    CORREZIONE=1.636875+1.08284e-5*rpm;
    %Nu=0.23*Re_x.^(4/5)*Pr^(0.4); TAS-I
    Nu=0.155*Re_D^0.674*CORREZIONE;
end
%h=Nu*k/D;
h_forz=Nu.*k./D.*ones(N,1); %[W/m2/K] heat transfer factor vector
h_forz(N)=0;

%%%%%%%%%%%%%%%%%%%%%%%%%%%%%%%%%%%%%%%%%%%%%%%%%%%%%%%%%%%%%%%%%%%%%%%%%%%%%
```

```matlab
% CONVEZIONE NATURALE

    nu=mu/rho;
    T_cyl=mean(T(i-1,1:N-1));
    Tm=0.5*(T_cyl+T_amb);
    beta=1/Tm;
    %beta=1/T_amb;
    g=3.71; %[m/s^2]
    Grash_L=g*beta*abs(T_cyl-T_amb)*L^3/nu^2;
    Ra=Grash_L*Pr;

    %if Ra<10^2
    %%% TAS-I %%%
    %Nu=(0.8*Ra^(0.25))*(1+(1+1/sqrt(Pr))^2)^(-0.25);
    %else
    %%% Le Fevre & Ede %%%

Nu=4/3*((7*Grash_L*Pr^2)/(5*(20+21*Pr)))^0.25+(4*(272+315*Pr)*L)/(35*(64+63
*Pr)*D);
    %end

    h_nat=Nu.*k./D.*ones(N,1); %[W/m2/K] global heat transfer factor
    h_nat(N)=0;
    if abs(T_cyl-T_amb)<0.1
        h_nat=zeros(N,1);
    end

h=max(h_nat,h_forz);
coeff_conv=mean(h(1:end-1));

%%%%%%%%%%%%%%%%%%%%%%%%%%%%%%%%%%%%%%%%%%%%%%%%%%%%%%%%%%%%%%%%%%%%%%%%%%%%%

% POWER DISSIPATION

    P_prop=M/1000*(pi*rpm/30);       %[W]
    I=I0+1/k_m*M;                    %[A]   Drained Current
    V_s=1/k_v*(rpm+dn_dM*M);         %[V]   Supplier Voltage
    %eta(i-1,1)=P_prop/(V_s*I);      %[-]   Motor efficiency
    Q_heater = 0;
    Q_eng=(V_s*I-P_prop)+Q_heater;   %[W]   ENGINE DISSIPATED POWER
    Q_in=Q_eng+Q_ext;                %[W]   Total immitted power
    Q=Q_in/(N-1)*ones(N,1);          %[W]   IMMITTED POWER VECTOR
    Q(N)=0;

%%%%%%%%%%%%%%%%%%%%%%%%%%%%%%%%%%%%%%%%%%%%%%%%%%%%%%%%%%%%%%%%%%%%%%%%%%%%%

    % Conductive heat transfer between motor nodes
    for j=1:N
        for k=1:N
            TT(j,k)=T(i-1,j)-T(i-1,k);
        end
    end
```

```matlab
    for j=1:N
       KT(j,1)=K(j,:)*TT(:,j);
    end

    % Radiative exchange between nodes and environment
    qr=eps*sigma*A.*(T(i-1,:)'.^4-T_amb^4); %[W]=[J/s] -> q*dt=[J]

    q_rad(i-1,:)=qr'; %radiative rejected/recived power backup

    % Convective exchange between nodes and environment
    qc= h .* A .* (T(i-1,:)'-T_amb);

%%%%%%%%%%%%%%%%%%%%%%%%%%%%%%%%%%%%%%%%%%%%%%%%%%%%%%%%%%%%%%%%%%%%%%%%%%%%
%%%%%%%%%% TIME STEP %%%%%%%%% TIME STEP %%%%%%%%%% TIME STEP %%%%%%%%%%%%
%%%%%%%%%%%%%%%%%%%%%%%%%%%%%%%%%%%%%%%%%%%%%%%%%%%%%%%%%%%%%%%%%%%%%%%%%%%%
    T(i,:) = T(i-1,:)'    ...
            + dt./C .* KT ...
            + dt./C .* Q  ...
            - dt./C .* qc ...
            - dt./C .* qr ;
%%%%%%%%%%%%%%%%%%%%%%%%%%%%%%%%%%%%%%%%%%%%%%%%%%%%%%%%%%%%%%%%%%%%%%%%%%%%
%%%%%%%%%%%%%%%%%%%%%%%%%%%%%%%%%%%%%%%%%%%%%%%%%%%%%%%%%%%%%%%%%%%%%%%%%%%%
%                                                                          %
%    % KT represent linear conductance between inside motor nodes,         %
%    % h represent convective flux between nodes and AIR ("air")           %
%    % Q represent inner-node dissipated power due to Joule effect         %
%    % q represent rejected (if positive) heat due to radiative exchange   %
%                                                                          %
%%%%%%%%%%%%%%%%%%%%%%%%%%%%%%%%%%%%%%%%%%%%%%%%%%%%%%%%%%%%%%%%%%%%%%%%%%%%

    % boundary imposition - the last node is a boundary @ T=T_amb
    T(i,N)=T_amb;

%%%%%%%%%%%%%%%%%%%%%%%%%%%%%%%%%%%%%%%%%%%%%%%%%%%%%%%%%%%%%%%%%%%%%%%%%%%%

% TEMPERATURE & FLUXES FPRINTF

    temp=(i-1)*dt;
    %Unbal=Q-qc-qr; %[W] Power unbalance

    fprintf(fid1,'t= %5.1f s \n',temp);
    for k=1:N
        fprintf(fid1,'%5.2f %9.7f %9.7f %9.7f \n',T(i,k)-273.15,Q(k),-
qc(k),-qr(k));
    end

%%%%%%%%%%%%%%%%%%%%%%%%%%%%%%%%%%%%%%%%%%%%%%%%%%%%%%%%%%%%%%%%%%%%%%%%%%%%
```

```matlab
% CONDUCTANCES FPRINTF

GL_i = k_eng*(pi*D^2/4)/dx*ones(N,1); % linear conductances related to
conductive mode
GL_i(N)=0;

GL_e = h.*A; % linear conductances related to convective mode

GR = eps*A*1; % 1 = FoV % conductances related to radiative mode

stamp=[GL_i GL_e GR];

    fprintf(fid2,'t= %5.1f s \n',temp);
    for i=1:N
    for j=1:3
        if j==3
            fprintf(fid2,'%9.7f \n',stamp(i,j));
        else
            fprintf(fid2,'%9.7f \t',stamp(i,j));
        end
    end
    end

%%%%%%%%%%%%%%%%%%%%%%%%%%%%%%%%%%%%%%%%%%%%%%%%%%%%%%%%%%%%%%%%%%%%%%%%%%%%%%%

end %function
```

IAS FUNCTION

```
% Codice per la determinazione del campo di velocità di ottimo (secondo
Glauert)
% sul disco attuatore secondo la teoria dei vortici corretta tramite
fattore di Prandtl

function [u,v]=IAS_vs(rho,Diam,Omega_rpm,Thrust)

R=Diam*.5;                  %[m]        raggio del rotore
Omega=pi*Omega_rpm/30;      %[rad s-1]
A=pi*R^2;                   %[m2]       superficie disco rotore
N=2;                        %[]         numero di pale per rotore
if Omega_rpm==0
    u=0;
    v=0;
    return
end

% coefficiente di spinta ottenuto dalle prove sperimentali @ 3060 rpm
C_T_reale=0.25*pi^2*Thrust/(rho*R^4*Omega^2);

%% Calcolo della distribuzione di circuitazione

r=linspace(0.00001,R,100); % discretizzazione uniforme della coordinata
radiale (non partire da 0!)
NN=length(r);
lungh=NN;
dr=r(5)-r(4); %tanto è uniforme e qualsiasi prendo va bene

% CICLO PER DETERMINAZIONE PARAMETRO DI GLAUERT G

G(1)=0.0001; %parametro adimensionale (parametro di carico di Glauert) di
primo tentativo
count=1;
Tnew(count)=0;

while Tnew(count)<Thrust

r_tilde=r/(R*G(count)); % coordinata radiale adimensionalizzata
theta=acos(((r_tilde).^6+3*(r_tilde).^4+3*(r_tilde).^2-
ones(1,NN))./((r_tilde).^6+4*(r_tilde).^4+3*(r_tilde).^2+ones(1,NN)));
omega_bar=6./(5*ones(1,NN)+(r_tilde).^2+2*(ones(1,NN)+(r_tilde).^2).*cos(th
eta/3));
omega=omega_bar.*Omega; % velocità angolare della particella fluida nel
sistema di riferimento fisso

v0=Omega.*r.*sqrt(omega_bar./(2-omega_bar));
phi=atan(v0./(Omega*r));
Gamma_bar_corr=2/pi*acos(exp((r-R)./(r.*phi))).*omega_bar.*r_tilde.^2;
f=N/2.*(R-r)./(r.*phi);                     % esponente per il calcolo del
fattore di Prandtl
```

```
F=2/pi*acos(exp(-f));                          % fattore di Prandtl
Gamma_bar=omega_bar.*r_tilde.^2;               % distrubuzione di
circuitazione adimensionale
Gamma=Gamma_bar.*2*pi*Omega*R^2*G(count)^2; % distrubuzione di
circuitazione
Gamma_corr=F.*Gamma;                           % distribuzione di
circuitazione corretta

u=Gamma_corr./(2*pi*r);                  %velocità tangenziale
v=0.5*sqrt(Gamma_corr*Omega/pi);         %velocità assiale

dT=0.5*rho*sqrt((Omega*r-u/2).^2+v.^2).*Gamma_corr*dr;
Tnew(count+1)=sum(N*dT);
if G(count)>1
    disp('Errore: G>1')
    break
end
count=count+1;
G(count)=G(count-1)+0.0001;

end %fine del ciclo while

Thrust_modello=Tnew(end);
G=G(end);

v_ADT=sqrt(Thrust/(2*rho*A)); %velocità assiale secondo la teoria del disco
attuatore semplice

% figure(100)
% plot(r/R,v,'k','linewidth',1.2)
% hold on
% plot([0 1],[v_ADT v_ADT],'k--')
% title('Velocità indotta assiale al disco')
% xlabel('r/R')
% ylabel('v_i(r)  [m/s]')
% legend('Corrected Vortex Theory (opt. design)','Actuator Disc
Theory','location','best')
% grid minor

% figure
% plot(r/R,u,'k','linewidth',1.2)
% title('Velocità indotta tangenziale al disco')
% xlabel('r/R')
% ylabel('u(r) [m/s]')
% legend('Corrected Vortex Theory (opt. design)','location','best')
% grid minor

%disp(strcat('Spinta modello= ',num2str(Thrust_modello),'[N]'))
%disp(strcat('Spinta sperimentale=',num2str(Thrust),'[N]'))

end %end function
```

Appendix B

Introduction to BLDC Motor

To drive the drone rotors the electrical motors chosen are called "Brushless Direct Current Motor" (BLDC motor). This kind of motors have many of the benefits of classic direct current (DC) motor with permanent magnets but without the drawback represented by the brushes. Thanks to this they are very competitive compared to normal direct current motor and induction or asynchronous motors (AC motors).
The friction contact between brushes and commutator, in fact, leads to heat generation (dissipation of energy $\rightarrow$ less efficiency and higher temperatures) and need for maintenance. Moreover when the commutation takes place an electric arc is fired and it can be dangerous in some kind of environments such as fuel tanks (in low pressure pumps AC motors are usually used); this electric arc causes also an electromagnetic disturbance which could interfere with the transmitted signals, in our case signals between drone and rover or a possible landing platform.
With the development of solid state electronic commutator devices it has been natural to try to substitute mechanical commutation with electronic commutation, at this point BLDC motors were born.

BLDC Motor architecture

Brushless motors consists of:

- **Permanent magnet rotor.**
- **Stator, on which windings are placed.**

  This architecture looks like the AC synchronous motor ones. The difference lies on the rotor magnetization.
- An angular position transducer for the rotor position (usually 3 Hall sensors).
- An electronic commutator which feeds the proper stator winding at each time.

With these components the motor works like a synchronous machine.
There is another component essential to the proper work of the BLDC motor: the **MOTOR CONTROLLER** or **ECU** (Engine Control Unit).

Typically powered by a six-MOSFET bridge controlled using Pulse-Width Modulation (PWM), the windings are commutated in a controlled sequence to produce a rotating magnetic field that drags the rotor around and drives an attached load. The sequence is determined by the relative positions between stator and rotor estimated by the electronic control unit (ECU) through measurements by either position sensors or the magnitude of the back electromagnetic force (EMF) generated as the motor rotates (in a "sensor-less" unit).

There are three control schemes for electronic commutation:

- Sinusoidal.
- **Trapezoidal** (or six-step).
- FOC = Field Oriented Control (or vectorial control).

The sinusoidal control scheme has its main pro in the output torque profile which is smoother than the trapezoidal one (Figure B.1). In fact with the trapezoidal scheme it is impossible to generate a perfect trapezoidal counter electromotive force and the effect of windings inductances gives a non-regular current profile during commutation and therefore in the output torque.
As usual better performances means higher complexity and higher costs, therefore to perform a sinusoidal control scheme a high precision angular position transducer is needed in order to drive the stator magnetic field 90° ahead to the rotor one to obtain the maximum torque. Instead, for a trapezoidal scheme, three Hall sensors are enough to perform the task.

For many applications the trapezoidal controlled BLDC motor is the best solution. It is compact, reliable and is rapidly falling in price, making it particularly suitable for many small motor applications including automotive and computers. Additionally, the trapezoidal technique is the easiest to implement and therefore the most popular. Each phase of the motor is powered by direct current which is commutated every 60°. The phase is either driven "high", "low", or is left floating. The current waveform for each winding is therefore a staircase from zero, to positive current, to zero, and then to negative current: this produces a current space vector that approximates smooth rotation as it steps among six distinct directions as the rotor turns. In theory such a system can generate a smooth and constant torque but in practice it is impossible for the current of a given phase to instantaneously change from low to high. Instead, the resulting rise time generates a ripple in the output that coincides with the commutation timing and it can be seen in Figure B.1.

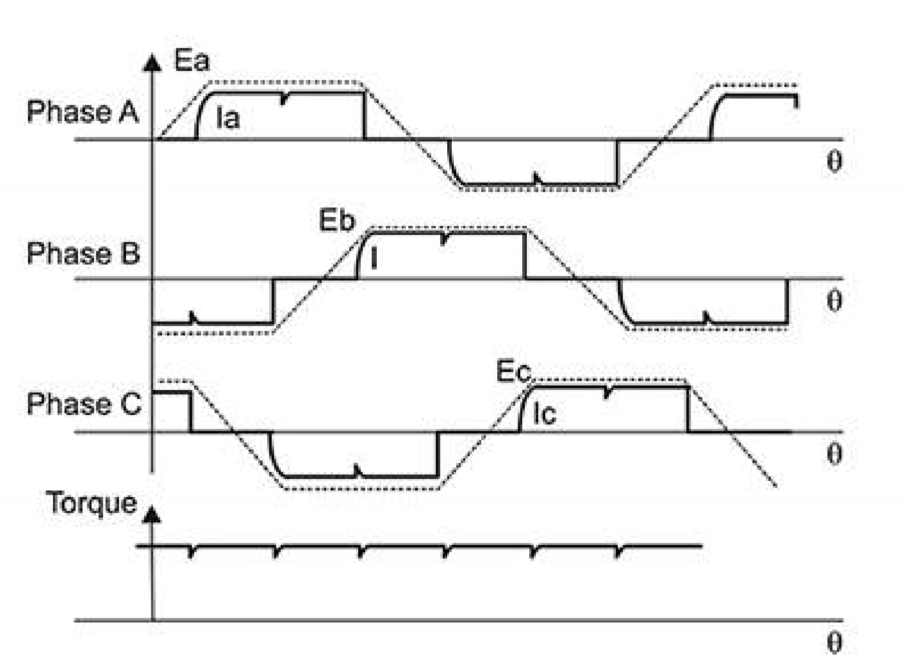

Figure B.1: Electrical waveform for a 3-phase BLDC motor using trapezoidal control.

Through all these considerations it is possible to state that BLDC motors with trapezoidal control are most suitable for velocity control (we want to archive a given rotational speed) and low budgets. For high precision position control, such as servomechanisms, AC motors are the best solution instead.

Here are listed the advantages of BLDC motors:

- **There are no brushes.**
  It has been already discussed about the main advantage of this feature, but there are other pros to keep in mind: the mechanic commutator does not exist in a BLDC motor so the engine is lighter, shorter and the bearings are closer to each other so the motor shaft is stiffer and it can rotate faster. A lighter shaft means that it's moment of inertia is lower so the response time during transient is shorter.

- **No rotor losses in terms of back-EMF.**
  The BLDC motor is synchronous, this means that the rotor magnetic flux is constant in time giving no rotor losses. The only eddy currents losses due to magnetic flux variations in time occurs in the windings supports. This is **very important from a thermal point of view** because it's easier to transfer heat from the motor to the environment if this is generated in the motor stator (for an IN-RUNNER architecture). Furthermore the efficiency benefits from the low losses, allowing to reach higher η values.

- **Windings on the stator.**
  This feature gives benefits in terms of motor cooling as already mentioned, but another benefit is that the higher cross-sectional area gives more space for the windings placement so they can generate a higher magnetic flux resulting in a high output torque. The high current allowed from the motor cooling performances leads to the highest power density of any kind of electrical motor.

- **Use of ferromagnetic metals with a high flux density.**
  This leads to a very high specific power. The NdFeB is a classic material used for the rotor magnets.

- **High output torque at no speed.**
  In fact in a mechanic commutator its plates would fast be damaged if a high current would flow through them continuously (no speed means that the same plate remains below the brush for a long time), this does not happen in a BLDC motor since the commutator is electronic.

In order to conclude this introduction to the BLDC motor word another classification is possible to be made. This kind of motors can be divided into two big categories:

1. IN-RUNNER BLDC Motors
2. OUT-RUNNER BLDC Motors

The most common architecture is the IN-RUNNER one, in fact they are widely diffused and the rotor part is inside the stator one which does not rotate; this is the classic motor one can think about.
OUT-RUNNER motors, instead, have the stator placed inside the rotor, so the external part of the motor does rotate. This architecture is diffused for small and very small applications such as drone motors, CD drivers, hard discs, and the advantage of this architecture is that it can output a greater torque then an IN-RUNNER one at a fixed rotational speed and with the same overall dimensions thanks to the greater distance between magnets and rotational axis; this feature can sometimes avoid the use of a gearbox. On the other hand the efficiency is lower then an IN-RUNNER solution because of the worse electromagnetic coupling and there is lower protection from moisture, dust and foreign objects. These drawbacks are the reason why an IN-RUNNER motor has been chosen.

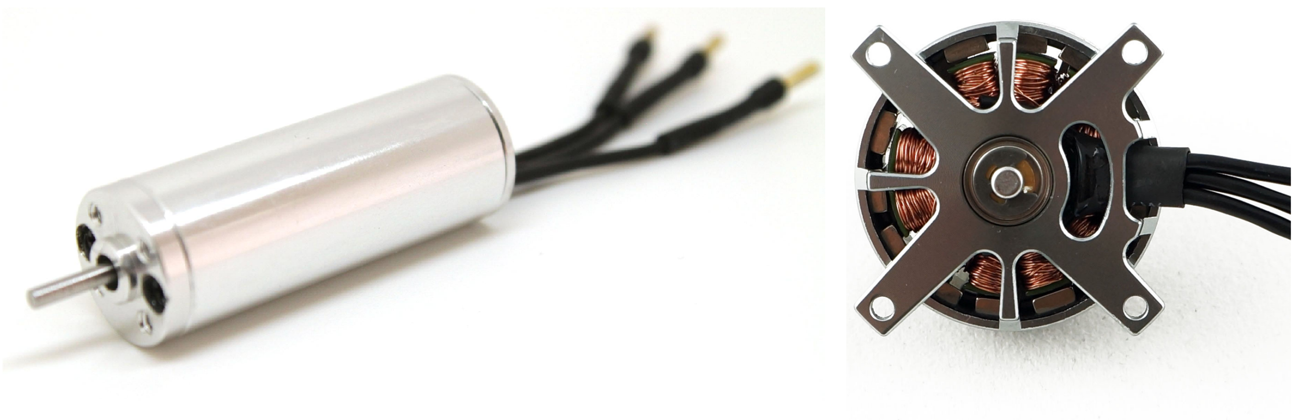

Figure B.2: IN-RUNNER on the left, OUT-RUNNER on the right.

Here it is represented an exploded view of a generic BLDC motor:

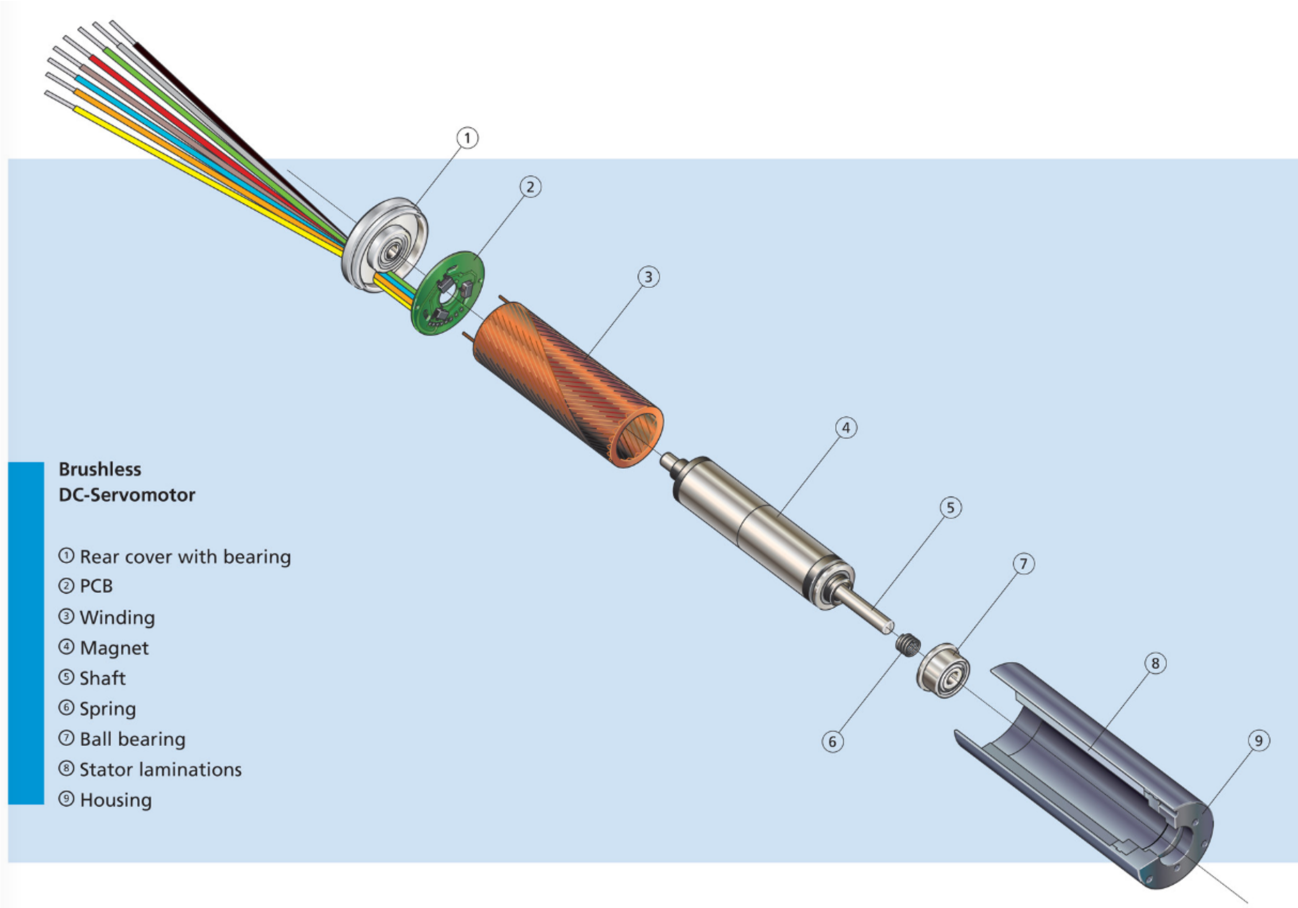

Figure B.3: Exploded view of a generic trapezoidal, IN-RUNNER BLDC motor.

Appendix C

PHASE vacuum chamber

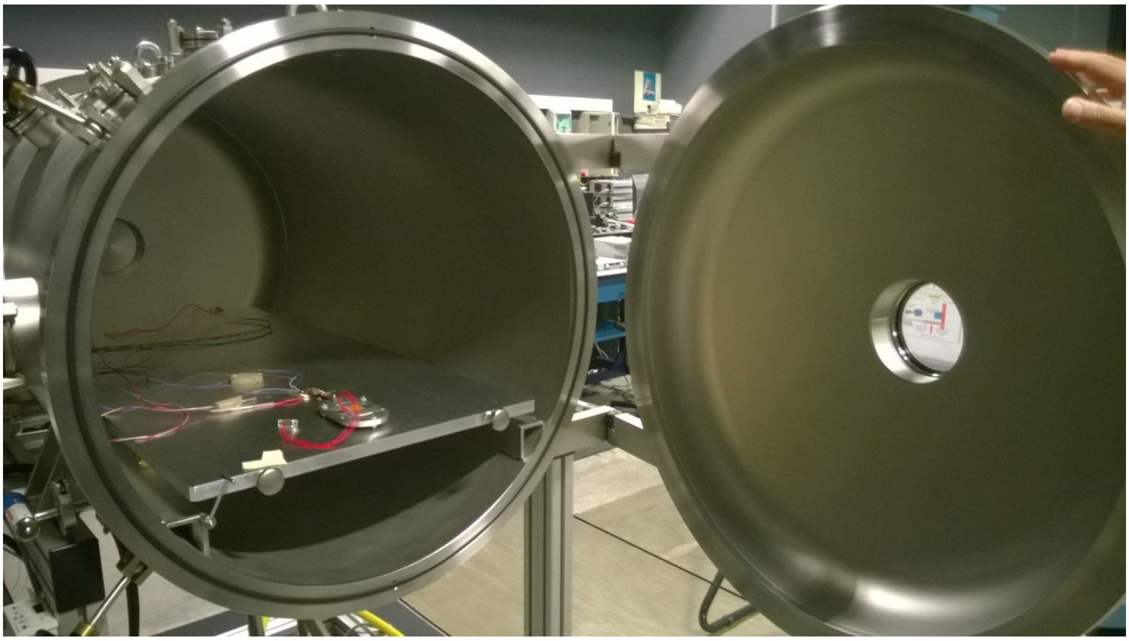

Figure C.1: PHASE vacuum chamber (TAS-I).

PHASE is a stainless steel, horizontal axis, cylindrical vacuum chamber (Figure C.1). Its vacuum pump, a Pfeiffer Duo 20 rotatory vane pump, can get the chamber to about $1 \cdot 10^{-1}$ mbar (medium vacuum) and it is connected with the chamber itself through a ball valve and a filter. Inside there are two movable 600×600 mm steel plates mounted on sliding rails, to ease articles positioning. The chamber has a window and pass-through flanges for the cables. Its features are listed below in Table C.1 and its internal dimensions are shown in Figure C.2.

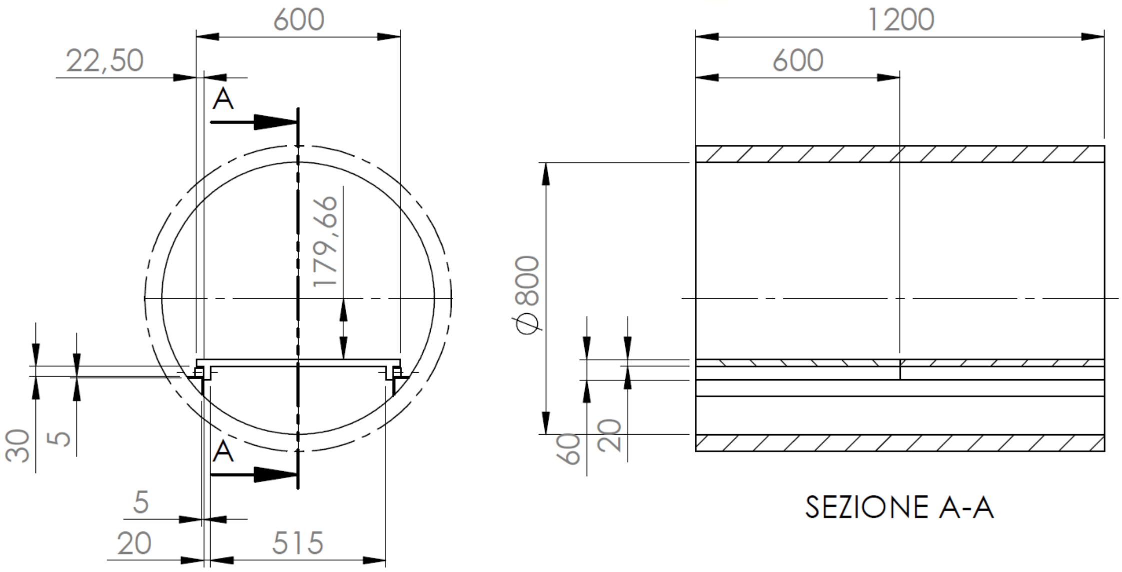

Figure C.2: PHASE vacuum chamber internal dimensions.

Dimension	
Internal Diameter	800 mm
Available Space	600×1200×570 mm
Vacuum Pump	
Model	PFEIFFER DUO 20
Final Pressure	$1 \cdot 10^{-1}$ mbar
Flow Rate	20 m^3/h
Pressure Sensor	
Model	Granville Philips 375 Convectron
Type	Gauge (Relative)
Min. Measurable Pressure	$1 \cdot 10^{-3}$ mbar
Thermocouples	4 available
Connectors	8 Connectors with 9 pin
	9 Connectors with 15 pin
	1 Connectors with 25 pin
	4 BNC Connectors

Table C.1: PHASE characteristics.

PHASE chamber already comes with 4 thermocouples (used for thermal tests) and a pressure sensor. More instruments can be mounted through multiple available ports. Data are processed using a dedicated external PC.

Ringraziamenti

Varcata la soglia del Politecnico ormai cinque anni e mezzo fa non mi sarei aspettato di intraprendere un viaggio che mi avrebbe portato così lontano dalla persona che ero. Questa condivisa odissea fatta di esami, progetti e piccole sfide della vita quotidiana è arrivata dunque a compimento grazie e soprattutto alle persone che con me hanno scelto di remare per arrivare alla tanto agognata conclusione. Tra tutte spiccano i miei genitori che, con il loro supporto, mi hanno permesso di prendere un po' più alla leggera i momenti di sconforto e di conservare parte del ragazzino che è entrato pensando di dover affrontare solo anni di sacrificio. La mia sorellina Gaia, perché anche se si nasconde so che ha fatto sempre il tifo per me come io lo faccio per lei. I miei compagni di avventura che, seppur avendo scelto percorsi diversi, sono riusciti comunque a condividere con il sottoscritto la stragrande maggioranza della lezioni, delle serate, dei divertimenti e delle complicazioni che ci si sono parate davanti. La mia super ragazza, che pur così lontana dall'ambiente ingegneristico ha sempre cercato di capire e sopportare quello che le raccontavo, non facendomi mai mancare il suo supporto che più di tutto è stato indispensabile in questi ultimi due difficili anni e, non di meno, è stata sempre al mio fianco in ogni altra occasione, di gioia o di tristezza e mi ha un po' cambiato dentro, rendendomi meno "ingegnere" di quanto non fossi prima. I miei nonni, che con le loro sagge parole mi hanno rassicurato nei confronti di quello che verrà, e infine un sentito ringraziamento a tutti coloro che, nella mia famiglia o non, mi hanno fatto sentire il loro supporto morale durante questi anni.

Un ringraziamento a parte va invece fatto a coloro i quali mi hanno permesso di lavorare su un progetto tanto interessante quanto inusuale quale quello contenuto in questa tesi. In primis il Professor Paolo Maggiore per essere sempre disponibile con gli studenti senza mai fargli pesare la loro inesperienza ma, al contrario, fornendogli sempre un reale supporto per quello che avviene e per quello che avverrà durante e successivamente alla carriera universitaria. Poi come non citare i dottori, manager ed ingegneri che si sono resi disponibili per insegnarmi ad affrontare un lavoro difficile come quello di uno studente alla prima esperienza in una grossa azienda come Thales Alenia Space, dandomi la possibilità di mettermi alla prova e dimostrare che effettivamente questi anni hanno dato frutti importanti e avendo la pazienza di sopperire a tutte le mie inesperienze. Tra tutti voglio citare il grande capo Massimo Antonacci perché nonostante i sui milioni di impegni ha sempre trovato qualche minuto per parlare con me e darmi le dritte giuste; Carlo Paccagnini per avere combattuto e reso possibile la nascita di un progetto come quello del drone marziano e avermi

dato fiducia in questi mesi, sopportando le mie ansie da esame di laurea; il mitico Sergio Mannu che per primo mi ha iniziato ai segreti del design termico e per avermi raccontato una quantità infinita di aneddoti interessantissimi; Savino De Palo per la quantità di informazioni, testi e consigli che mi ha dato sin dall'inizio del mio lavoro, quando ancora dovevo capire in che luogo mi trovavo. Inoltre tutti i colleghi del quinto piano sono stati mitici a non farmi sentire troppo un pesce fuor d'acqua.
Ultimo ma non ultimo il guru Valter Perotto, senza il quale non so come avrei fatto a completare un lavoro così appagante, per essere stato in grado di dedicarmi del tempo anche quando il tempo non c'era e per essere stato in grado di mantenere la calma e spiegarsi in una maniera ammirevole pure con uno "sbarbato" con appena una briciola della conoscenza che il buon Valter è in grado di trasmettere.
Spero che questo percorso mi faccia da vento per permettermi di spiegare le ali e decollare in un mondo così complesso e complicato come quello in cui viviamo.

Grazie sentitamente ad ognuno di voi.

Fabio Acquaviva, 27 Marzo 2019.

Bibliography

[1] T. D'ésert, J.M. Moschetta, H. B'ézard, *Aerodynamic Design of a Martian Micro Air Vehicle*, ONERA and ISAE-SUPAERO, 2017.

[2] International Civil Aviation Organization. *Manual of the ICAO Standard Atmosphere* ,1993, ISBN 92-9194-004-6, Doc 7488-CD.

[3] J. Balaram, P. T. Tokumaru, *Rotorcrafts for Mars Exploration*, in 11th International Planetary Probe Workshop, 2014.

[4] Witold J. F. Koning, Wayne Johnson, Brian G. Allan, *Generation of Mars Helicopter Rotor Model for Comprehensive Analyses*, NASA, 2018.

[5] *Mars Fact Sheet*, https://nssdc.gsfc.nasa.gov/planetary/factsheet/marsfact.html, NASA.

[6] R. Shrestha, Moble Benedict, Vikram Hrishikeshavan and Inderjit Chopra, *Hover Performance of a Small-Scale Helicopter Rotor for Flying on Mars*, University of Maryland, 2015.

[7] D. Zaza, D. D'Ambrosio, *Analisi delle prestazioni e del campo di moto indotto da un'elica in ambiente marziano*, Politecnico di Torino, 2017.

[8] A. Botta, M. Chiaberge *MARS DRONE Rotors & Engines testing in Mars-like atmosphere*, TAS-I & Politecnico di Torino, 2017.

[9] J.H. Lienhard IV, J.H. Lienhard V, *A Heat Transfer Textbook*, Phlogiston Press.

[10] J. Balaram, T. Canham, C. Duncan, M. Golombek, H.F. Grip, W. Johnson, J. Maki, A. Quon, R. Stern, and D. Zhu, *Mars Helicopter Technology Demonstrator*, 2018 AIAA Guidance, Navigation, and Control Conference, AIAA SciTech Forum, 8–12 January 2018, Kissimmee, Florida.

[11] L. A. Young, E. Aiken, P. Lee, G. Briggs, *Mars Rotorcraft: Possibilities, Limitations, and Implications For Human/Robotic Exploration*, NASA Ames Research Center.

[12] Sandra K. S. Boetcher, *Natural Convection from Circular Cylinders*, Springer.

[13] E. J. Le Fevre, A. J. Ede, *"Laminar Free Convection From the Outer Surface of a Vertical Cylinder*, 1956, In Proceedings of the 9th International Congress on Applied Mechanics, pp. 175–183.

[14] A. J. Ede, *Advances in Free Convection*, 1967, Advances in Heat Transfer, Academic Press, New York, pp. 1–64.

[15] J. Day, *Laminar Natural Convection from Isothermal Vertical Cylinders*, University of North Texas, 2012.

[16] R. Wiberg, N. Lior, *Heat transfer from a cylinder in axial turbulent flows*, International Journal of Heat and Mass Transfer 48 (2005) 1505–1517.

[17] W. Johnson, *Helicopter Theory*, editore

[18] M. Knight, R. A. Hefner, *Static Thrust Analysis of the Lifting Airscrew*, 1973.

[19] W. Z. Stepniewski, *Rotary-Wing Aerodynamics*, Vol. I. Philadelphia, Pennsylvania, January 1979.

[20] J. T. Conway, *Exact actuator disk solutions for non-uniform heavy loading and slipstream contraction*, Journal of Fluid Mechanics, vol. 365, 1998.

[21] A. Betz, with L. Prandtl appendix, *Screw Propellers with Minimum Energy Loss*, Gottingen Reports, 1919.

[22] H. Glauert, *Airplane Propellers, Aerodynamic Theory*, New York: Dover Publications, 1980. p251-8-310-4.

[23] R. Morrades, D. Peters, *Closed-form solutions for optimum rotor in hover and climb*, Washington University in St. Luois, Missouri. 22 February 2016.

[24] R. Modarres, D. A. Peters, *Optimum blade loading for a powered rotor in descent*, Department of Mechanical Engineering & Materials Science, Washington University in St. Louis, St. Louis, MO 63130, USA.

[25] *Mars Helicopter Scout*, video presentation at Caltech.

[26] S. Clarke, *Helicopter to accompany NASA's next Mars rover to Red Planet*, Spaceflight Now. 14 May 2018.

[27] K. Northon, *Mars Helicopter to Fly on NASA's Next Red Planet Rover Mission*, NASA News. 11 May 2018.